

Politecnico di Bari

Repository Istituzionale dei Prodotti della Ricerca del Politecnico di Bari

Lithium niobate on insulator devices for photonic integrated circuits

This is a PhD Thesis

Original Citation:
Lithium niobate on insulator devices for photonic integrated circuits / Yousefi, P.. - ELETTRONICO. - (2026).

Availability:
This version is available at http://hdl.handle.net/11589/308720 since: 2026-10-18

Published version
DOI:

Publisher: Politecnico di Bari

Terms of use:

(Article begins on next page)

25 October 2026

DOCTOR OF PHILOSOPHY (Ph.D.)

Research carried out within the RESTART Project (Spoke 1)
Funded by the Italian National Recovery and Resilience Plan (PNRR)



POLITECNICO DI BARI

DEPARTMENT OF ELECTRICAL AND INFORMATION ENGINEERING
(DEI)

Ph.D. Program in Electrical and Information Engineering

Ph.D. Thesis

Lithium Niobate on Insulator Devices for Photonic Integrated Circuits

Supervisor
Prof. Vincenzo Petruzzelli

Co-Supervisor
Prof. Giovanna Calò

Coordinator
Prof. Nicola Giaquinto

Ph.D. Candidate
Pezhman Yousefi

XXXVIII Cycle
Academic Year 2025–2026

Abstract

Passive photonic components play a central role in photonic integrated circuits (PICs), where optical power distribution, power combining, and wavelength-selective routing must be achieved within compact, low-loss, and fabrication-aware platforms. This thesis addresses the design, analysis, and experimental assessment of passive integrated Multimode Interference (MMI) devices based on thin-film lithium niobate (TFLN). Moreover, hybrid silicon nitride–thin-film lithium niobate (SiN–TFLN) add drop filters are designed and analyzed.

A major part of this work is devoted to multimode interference (MMI) couplers as broadband passive splitters and combiners. A systematic design methodology is developed for $1 \times N$ and $N \times 1$ configurations with $2 \leq N \leq 8$, starting from the self-imaging principle and extending to a detailed numerical investigation of geometrical design parameters and performance metrics. The analysis includes insertion loss, output power uniformity, broadband behavior, and combined performance evaluation, together with the role of output-port spacing and taper geometry. The study is further extended from splitter operation to combiner operation, where inter-port phase relations, wavelength stability of the phase, ideal combining performance, and sensitivity to amplitude and phase errors are examined. In addition, fabrication tolerance is assessed through thickness-related variations, providing a broader view of the practical design space of TFLN-based MMI devices.

The numerical design study is complemented by the fabrication and experimental characterization of selected MMI structures. The fabricated devices are analyzed within the technological constraints of the adopted TFLN platform, including actual fabrication conditions and thickness-induced geometrical variations. Experimental measurements are performed using grating-coupled configurations in the C-band, outside the original O-band design range. The measured responses are interpreted together with the corresponding numerical predictions in order to clarify the effects of off-design operation, coupling and normalization uncertainties, and fabrication-induced deviations, thereby establishing a direct link between idealized design and realistic device performance.

The thesis also investigates wavelength-selective routing through a grating-assisted add–drop filter implemented on a hybrid SiN–TFLN platform. Starting from a single-channel reference configuration, the study develops dual-channel and multi-channel structures based on superimposed gratings, enabling multiple wavelength-selective drop operations within a single device footprint. The analysis addresses spectral response, field distribution, effect of grating-period separation, inter-drop crosstalk, wavelength positioning, bandwidth stability, and the optimization of the number of grating periods. Fabrication-oriented considerations, including duty-cycle sensitivity, tolerance analysis, and minimum feature-size constraints, are also incorporated.

Overall, this thesis establishes a fabrication-aware design perspective for passive photonic devices in lithium-niobate-based platforms, combining systematic numerical design, experimental characterization, and multi-channel wavelength-routing concepts to provide robust building blocks for integrated photonic systems.

This research was carried out within the framework of the RESTART project (Spoke 1), funded by the Italian National Recovery and Resilience Plan (PNRR).

مەبزوە مەحویا لەم ڕێگەدا تا دەبیە خاکی ڕێ
ئومێدە دەستی گەردت هەر دەگا ئاخر بە داوێنێ
مەحوی

Do not falter, Mahwi, on this path, even if you become the dust of the road; there is hope that your dust-covered hand will at last reach the beloved's hem.

Mahwi
Translated from Kurdish

Contents

Preface vi

List of Papers Written by the Author vi

1 Photonic Integrated Circuits 1
- 1.1 Photonic Integrated Circuits: Context and Motivation . . . 1
- 1.2 Materials Platforms for Large-Scale PICs . . . 2
  - 1.2.1 Silicon-on-Insulator (SOI) . . . 3
  - 1.2.2 Indium Phosphide (InP) . . . 4
  - 1.2.3 Silicon Nitride (Si_3N_4) . . . 7
  - 1.2.4 Thin-Film Lithium Niobate (TFLN/LNOI) . . . 9
  - 1.2.5 Hybrid and Heterogeneous Integration in Photonic Integrated Circuits . . . 11
- 1.3 PIC Devices . . . 12
  - 1.3.1 Multimode-Interference (MMI) Couplers . . . 12
  - 1.3.2 Directional Couplers . . . 14
  - 1.3.3 Grating-Assisted Contra-Directional Couplers (GACDCs) 16
  - 1.3.4 Microring Resonators . . . 18
  - 1.3.5 Arrayed Waveguide Gratings (AWGs) . . . 19
  - 1.3.6 Mach–Zehnder Modulators (MZMs) . . . 21
  - 1.3.7 Periodically Poled Lithium Niobate (PPLN) Devices . . . 23
- 1.4 Summary . . . 25

2 Design of MMI Splitters and Combiners 27
- 2.1 Introduction . . . 27
- 2.2 Multimode Interference devices based on TFLN platform . . . 27
- 2.3 Multimode Interference Coupler . . . 29
  - 2.3.1 Numerical Modeling and Simulation Framework . . . 29
  - 2.3.2 Operating Principle of Multimode Interference Couplers . 30
    - 2.3.2.1 Self-Imaging Conditions and Design Lengths . 31
    - 2.3.2.2 Generalized N-Fold Imaging and 1×N Splitter Design . . . 31
    - 2.3.2.3 Physical Interpretation of Self-Imaging . . . 32
  - 2.3.3 Design Parameters and Figures of Merit . . . 33
    - 2.3.3.1 Geometrical Design Parameters . . . 33
    - 2.3.3.2 Figures of Merit . . . 34
  - 2.3.4 Broadband Performance and Robustness . . . 35
  - 2.3.5 Multiport MMI Splitters and Combiners . . . 36
    - 2.3.5.1 Design Space Exploration and Scaling Trends 37
    - 2.3.5.2 Field Evolution and Physical Interpretation . 39
    - 2.3.5.3 Uniformity Analysis at the Design Wavelength 41
    - 2.3.5.4 Combined Performance Factor at the Design Wavelength . . . 42
    - 2.3.5.5 Effect of Inter-Taper Gap and Output Taper Geometry . . . 43
    - 2.3.5.6 Broadband Insertion Loss Analysis . . . 45
    - 2.3.5.7 Broadband Uniformity Analysis . . . 47
    - 2.3.5.8 Broadband Performance Factor . . . 47
  - 2.3.6 Combiner Design Derived from the Splitter Geometry . . 50

2.3.6.1 Wavelength Stability of Inter-Port Phase Relations 51
2.3.6.2 Output Phase Difference Across the Feasible Design Space . . . 52
2.3.6.3 Ideal Combiner Operation and Insertion Loss Performance . . . 54
2.3.6.4 Sensitivity to Amplitude and Phase Errors in Combiner Operation . . . 55
2.3.7 Fabrication Tolerance Analysis . . . 56
2.3.8 Conclusion . . . 57

3 Design Refinement, Fabrication, and Characterization of Multimode Interference Couplers 59
3.1 Introduction . . . 59
3.2 Experimental Overview . . . 59
3.3 Overview of Fabricated MMI Devices . . . 60
3.4 Platform Description and Design Procedure . . . 61
3.4.1 Adopted TFLN Platform . . . 61
3.4.2 Foundry-Defined Parameters and Device Optimization . . . 61
3.4.3 Single-Wavelength Design Optimization at 1310 nm . . . 62
3.4.4 Broadband Evaluation of the Optimized Designs in the O-band . . . 64
3.5 Numerical Analysis of MMI Topologies . . . 66
3.5.1 Performance analysis in the Design Band . . . 66
3.5.2 Off-Design Spectral Response Toward the C-Band . . . 67
3.5.3 Combined Impact of Thickness and Wavelength Variations 69
3.5.3.1 Realized Fabrication Conditions . . . 69
3.5.3.2 1×2 MMI: Thickness and Wavelength Sensitivity 69
3.5.3.3 1×4 MMI: Thickness and Wavelength Sensitivity 70
3.5.3.4 2×2 MMI: Thickness and Wavelength Sensitivity 72
3.6 Device Layout, Fabrication and Chip Organization . . . 73
3.6.1 Device Layout . . . 73
3.6.2 Chip Organization and Measurement Repeatability . . . 74
3.7 Measurement Setup and Experimental Methodology . . . 74
3.7.1 General Measurement Strategy . . . 76
3.7.2 Laboratory Setup . . . 76
3.7.3 Injection Configurations . . . 77
3.7.4 Polarization Control . . . 78
3.7.5 Practical Measurement Considerations . . . 78
3.8 Experimental Results . . . 79
3.9 Conclusion . . . 81

4 Design of Wavelength-Selective Add Drop Filters 82
4.1 Introduction . . . 82
4.2 Contra-Directional Coupling Principle . . . 82
4.3 Hybrid SiN–TFLN platform for grating-assisted add–drop filters . . . 85
4.4 FDTD Simulation Model . . . 85
4.5 Figures of Merit for Add–Drop Operation . . . 87
4.6 Single-Channel Add–Drop Filter Design . . . 88
4.6.1 Optimization of the Gap between the waveguides . . . 91
4.6.2 Spectral Response of the single channel filter . . . 92
4.7 Dual-Channel Add–Drop Filter Design . . . 93
4.7.1 Effect of Grating-Period Separation in Dual-Channel Operation . . . 94
4.7.2 Dual-Channel Spectral Response with Optimized Grating Separation . . . 96
4.8 Four-Channel Add–Drop Filter Design . . . 97

4.8.1 Effect of Grating-Period Separation in Four-Channel Operation . . . 98
4.8.2 Crosstalk Between Drop Ports in Four-Channel Operation 100
4.8.3 Drop Channel Wavelength and Bandwidth Stability . . . 101
4.8.4 Optimization of the Number of Grating Periods 102
4.8.5 Optimized Four-Channel Spectral Response 103
4.9 Fabrication Tolerance Analysis 104
4.9.1 Sensitivity to Duty-Cycle Variations 104
4.9.2 Effect of Waveguide Thickness and Width Variations . . . 106
4.9.3 Minimum Feature Size and Edge-Spacing Constraints . . 107
4.10 Discussion 108
4.11 Summary 109

Conclusions **111**

References **113**

Preface

This thesis is submitted in partial fulfillment of the requirements for the degree of *Philosophiae Doctor* in Electrical and Information Engineering at the Politecnico di Bari.

The research presented in this dissertation was carried out within the framework of the National Ph.D. Program and the RESTART project (Spoke 1), and was conducted at Politecnico di Bari and in collaboration with the University of Aveiro.

Parts of the results presented in this work have been published or submitted to international peer-reviewed journals and conferences. The full list of papers written by the author is reported hereafter.

List of Papers Written by the Author

International Journal Articles

[1] Yousefi, P., Khalid, M., Petruzzelli, V., and Calò, G., "Design of thin-film lithium niobate power splitters and combiners based on multimode interference," *Optical and Quantum Electronics*, vol. 57, no. 3, p. 198, 2025. DOI: 10.1007/s11082-025-08060-z

[2] Yousefi, P., Khalid, M., Petruzzelli, V., and Calò, G., "Multi-channel add-drop filter using superimposed gratings in hybrid sin-tfln platform," *Optics Communications*, vol. 591, p. 132 164, 2025. DOI: https://doi.org/10.1016/j.optcom.2025.132164 [Online]. Available: https://www.sciencedirect.com/science/article/pii/S0030401825006923

[3] Yousefi, P., Khajeh, A., Yahaghi, A., and Hosseini, K., "Inverse design of a wide-angle wideband programmable thz reflectarray through generative adversarial networks," *International Journal of Information & Communication Technology Research*, vol. 17, pp. 1–8, Sep. 2025.

International Conference Proceedings

[4] Khalid, M., Simone, M., Ferraresi, S., Bellanca, G., Yousefi, P., Petruzzelli, V., and Calò, G., "Lithium niobate electro-optic phase shifters for reconfigurable beam steering," in *2025 25th Anniversary International Conference on Transparent Optical Networks (ICTON)*, 2025, pp. 1–4. DOI: 10.1109/ICTON67126.2025.11125211

[5] Yousefi, P., Khalid, M., Petruzzelli, V., and Calò, G., "Dual-wavelength add-drop filters with aperiodic gratings on a hybrid sin-tfln platform," in *2025 25th Anniversary International Conference on Transparent Optical Networks (ICTON)*, 2025, pp. 1–4. DOI: 10.1109/ICTON67126.2025.11125232

[6] Yousefi, P., Khajeh, A., Yahaghi, A., and Hosseini, K., "Rhc-based systematic design of a wide-angle periodic coded thz reflectarray," in *2024 11th International Symposium on Telecommunications (IST)*, 2024, pp. 1–5. DOI: 10.1109/IST64061.2024.10843591

[7] Yousefi, P., Khalid, M., Petruzzelli, V., and Calò, G., "Thin film lithium niobate 1xn multimode interference splitters," in *2024 24th International Conference on Transparent Optical Networks (ICTON)*, 2024, pp. 1–4. DOI: 10.1109/ICTON62926.2024.10648216

Acknowledgements

This work would not have been possible without the support and guidance of several individuals and institutions.

First and foremost, I would like to express my sincere gratitude to my supervisor, Prof. Giovanna Calò, for her continuous guidance, insightful discussions, and support throughout my Ph.D. Her expertise and perspective have been essential in shaping this work.

I am also deeply grateful to Prof. Vincenzo Petruzzelli and Dr. Muhammad Khalid for their valuable feedback, technical discussions, and collaboration during the development of this research.

I would like to acknowledge the collaboration with PICadvanced and the University of Aveiro, where part of the experimental work was carried out. In particular, I thank Prof. António Teixeira and the engineering team for their support during chip characterization and measurements.

This work has been partially supported by the RESTART project (Spoke 1) within the framework of the Italian National Recovery and Resilience Plan (PNRR).

Finally, I would like to thank my wife for her constant support, patience, and encouragement throughout this journey. Her support has been fundamental to completing this work.

Chapter 1

Photonic Integrated Circuits

1.1 Photonic Integrated Circuits: Context and Motivation

Photonic integrated circuits (PICs) enable the co-integration of optical waveguides and fundamental photonic functions on a single substrate, providing a scalable solution for high-bandwidth, low-latency, and energy-efficient data transmission at the chip level. As electronic interconnects approach fundamental limits imposed by electromagnetic crosstalk, resistive losses, and the increasing RC cost associated with metal wiring, photonic integration has emerged as a key technology for sustaining performance scaling in modern information systems. By exploiting optical degrees of freedom such as wavelength, spatial mode, and polarization, PICs support dense multiplexing, thereby increasing the information capacity of integrated optical links. They also enable high-speed optical modulation and detection. Furthermore, the compatibility of many PIC platforms with wafer-scale CMOS fabrication facilitates scalable and cost-effective manufacturing [1]. These characteristics have favoured a growing interest in highly integrated photonic platforms for communication, computing, and sensing applications.

The rapid growth of global data traffic in datacenter and metro networks, together with the emergence of co-packaged and chip-to-chip optical interconnects, is now pushing integrated photonic systems toward aggregate capacity targets well beyond the multi-terabit-per-second regime. Recent scalability analyses identify ambitious yet concrete benchmarks for the coming decade, aimed at enabling future petabit-per-second optical interconnects, including approximately two orders of magnitude increase in transmission capacity, a fivefold improvement in bandwidth density, and an order-of-magnitude reduction in energy consumption per transmitted bit [2]. Achieving these targets in future petabit-per-second optical links will require module-level energy efficiencies of approximately 100 fJ/bit. Such efficiency levels correspond to total optical–electrical power budgets of around 100 W. While state-of-the-art multiplexed photonic chips currently demonstrate aggregate capacities on the order of tens of terabits per second, closing the gap toward petabit-scale operation requires a fundamental rethinking of how bandwidth, footprint, and power efficiency are simultaneously scaled at the device and platform levels.

From a capacity-scaling perspective, wavelength-division multiplexing alone becomes increasingly impractical at extreme aggregate data rates. Although additional multiplexing dimensions, including spatial modes and polarization, can alleviate this limitation, they require photonic components that simultaneously provide low insertion loss, broad operating bandwidth, compact footprints, and high fabrication tolerance. Such characteristics are essential for realizing dense photonic integration while minimizing crosstalk, optical losses, and footprint penalties. Consequently, components for power splitting, routing, filtering, and wavelength manipulation play a central role in scalable PIC architectures.

These scaling pressures highlight the central role of integrated photonic device architectures and material platforms in determining the ultimate performance of large-scale PICs. As capacity, bandwidth density, and energy efficiency targets continue to rise, the limited transparency window of silicon, the absence of a linear electro-optic (Pockels) effect, and the difficulty of efficiently integrating active functionalities motivate the exploration of alternative and hybrid integration strategies capable of supporting wide transparency windows, low-loss passive routing, and efficient active and nonlinear functionalities within a unified photonic platform.

Figure 1.1 illustrates a conceptual heterogeneous photonic integration platform for scalable photonic integrated circuits (PICs), highlighting the combination of wavelength-, mode-, and polarization-division multiplexing together with compact active and passive

photonic devices.

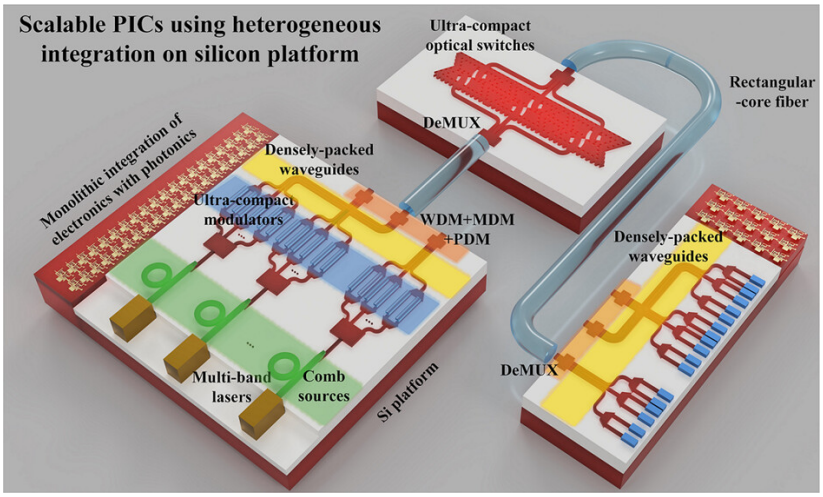


Figure 1.1: Conceptual illustration of heterogeneous photonic integration for scalable photonic integrated circuits (PICs). The architecture combines wavelength-division multiplexing (WDM), mode-division multiplexing (MDM), and polarization-division multiplexing (PDM), together with demultiplexers (DeMUX), compact modulators, optical switches, and densely packed waveguides to increase integration density and transmission capacity. Adapted from [2].

Meeting these system-level targets requires PICs to simultaneously satisfy constraints on footprint, optical loss, crosstalk, and power consumption.

Scaling PICs toward petabit-per-second-class operation requires increasing bandwidth density while maintaining a practical chip footprint. Even optimistic roadmaps estimate that a 1-Pb/s optical module may occupy approximately 200 mm^2 unless compact photonic architectures are employed. At the same time, finite waveguide dimensions and evanescent coupling between adjacent waveguides limit how closely optical channels can be packed without introducing excessive crosstalk. These constraints make compact, low-loss building blocks and crosstalk-aware routing strategies essential for dense photonic integration.

Power efficiency and packaging impose additional limits on large-scale PICs. Although current integrated optical links operate at energy efficiencies on the order of 1 pJ/bit, future roadmaps target values close to 100 fJ/bit. Achieving such efficiencies requires not only energy-efficient active devices, but also passive components with low insertion loss and reduced thermal tuning requirements. As photonic circuits become more densely integrated, thermal management, electrical I/O density, and chip-to-chip interconnect architectures increasingly determine the overall scalability of the system [2].

Taken together, recent device-level advances such as those reported in [1], [2] suggest a broader trend in which photonic integrated circuits increasingly function as an integration platform, where compactness, low loss, and architectural efficiency become as critical as individual component performance.

These system-level constraints are ultimately rooted in the properties of the underlying material platform, which defines the achievable performance limits of large-scale PICs.

1.2 Materials Platforms for Large-Scale PICs

As photonic integrated circuits evolve from laboratory-scale multi-terabit-per-second prototypes toward petabit-class systems, the choice of material platform becomes increasingly important in determining overall system performance and scalability. While individual photonic functions can often be realized on multiple platforms, large-scale integration exposes fundamental trade-offs that cannot be resolved through device design alone. In large-scale photonic systems, the material platform determines how much bandwidth can be integrated within a limited chip area, how efficiently data can be

transmitted under practical thermal conditions, and how stable the overall architecture remains without requiring continuous active reference.

As the required capacity and integration density of PICs continue to increase, the choice of material platform becomes increasingly important. Material properties directly influence optical propagation loss, achievable integration density, energy efficiency, and long-term stability. Consequently, different material platforms have been developed to balance passive performance, active functionality, and fabrication compatibility according to the requirements of specific applications.

From this perspective, no single material platform simultaneously optimizes all system requirements. Instead, PICs increasingly rely on a division of roles across complementary materials. Silicon-on-insulator provides unmatched integration density and a mature CMOS-compatible ecosystem for routing and modulation, but faces challenges related to thermal sensitivity and nonlinear effects. Indium phosphide provides native optical gain, light generation, and high-speed detection, making it essential for active transmitter and receiver integration. Silicon nitride offers ultra-low propagation loss, wide transparency, and improved phase stability, making it well suited for wavelength-selective and path-length–critical functions. However, it lacks an efficient intrinsic electro-optic tuning mechanism, often requiring hybrid integration with active materials. Thin-film lithium niobate exhibits a high-speed Pockels electro-optic effect and strong second-order nonlinearity, enabling efficient modulation and wavelength conversion within a compact footprint.

Hybrid and heterogeneous integration strategies emerge naturally from this materials-driven view. By combining complementary material platforms, hybrid photonic integration enables system-level performance that cannot be achieved using a single monolithic material platform. The system-level challenges discussed above are presented to motivate the physical constraints that future PICs must address, such as compactness, low optical loss, and fabrication tolerance. Within this context, the following sections review the principal integrated photonic material platforms, with particular emphasis on thin-film lithium niobate and its integration with complementary platforms, such as silicon nitride, which form the basis of the devices investigated in this thesis.

1.2.1 Silicon-on-Insulator (SOI)

Silicon-on-insulator (SOI) has become the dominant platform for large-scale photonic integration by combining the maturity of CMOS fabrication with the high refractive-index contrast between silicon and its silicon-dioxide layer. This combination enables strong optical confinement, allowing for compact waveguide bends and dense routing, while simultaneously benefiting from a well-established fabrication processes that provides process design kits, advanced lithography and etching control, and scalable co-integration pathways with electronic circuits such as drivers, transimpedance amplifiers, and digital signal processing blocks [1], [3]. As a result, SOI has emerged as the default technological platform for integrated transmitter and receiver architectures in wavelength-division-multiplexed (WDM) optical links and short-reach optical interconnects.

On the transmitter side, silicon photonic implementations typically follow one of two established architectural approaches. In the first, broadband Mach–Zehnder modulators are combined with wavelength multiplexers such as arrayed-waveguide gratings, echelle gratings, cascaded Mach–Zehnder interferometers, or microring filter arrays, enabling modulation that is largely independent of wavelength selection. In the second approach, wavelength-selective microring modulators are directly integrated along a shared bus waveguide. This approach is particularly attractive when multi-wavelength optical sources are available and extreme footprint reduction is required [3]. On the receiver side, the strong birefringence inherent to submicron silicon waveguides necessitates explicit polarization-handling strategies. Consequently, polarization-diverse front-end architectures employing polarization beam splitters and polarization rotators are commonly adopted to restore polarization-insensitive operation in WDM receivers [3]. From a packaging and testing perspective, SOI platforms support both vertical grating

couplers, which are advantageous for wafer-level testing and relaxed alignment tolerances, and edge (butt) couplers based on inverse tapers, which are preferred in applications requiring low coupling loss and broad optical bandwidth [4].

The technological value of SOI thus primarily stems from its ability to support high integration density, tight electrical–photonic co-design, and a rich library of well-characterized passive and active building blocks. High-index contrast enables compact waveguide crossings, resonators, and multiplexing structures, while close proximity to CMOS electronics facilitates efficient electro-optic interfaces and traveling-wave modulator designs [1], [3].

Despite these advantages, several intrinsic characteristics of SOI impose practical constraints on the scalability and robustness of silicon-based photonic circuits, particularly in dense WDM systems. The effective refractive index of submicron silicon waveguides exhibits a strong sensitivity to nanometer-scale variations in waveguide width and thickness, leading to accumulated phase errors over millimeter-scale propagation lengths and posing challenges for narrowband interferometric filters and resonant devices [3]. In addition, the pronounced birefringence between transverse-electric and transverse-magnetic modes complicates the realization of inherently polarization-insensitive passive components, often necessitating polarization-diversity schemes that increase circuit complexity and footprint. Furthermore, silicon's large thermo-optic coefficient results in significant resonance wavelength drift with temperature, while intensity-dependent nonlinear effects at telecom power levels can further constrain stable operation in densely multiplexed systems unless active thermal stabilization or careful power management is employed [1], [3].

Together, these considerations motivate the growing adoption of hybrid and heterogeneous photonic integration approaches in which SOI serves as a high-density routing and modulation layer, while complementary material platforms are employed to mitigate loss, enhance thermal stability, or provide efficient electro-optic and nonlinear optical functionalities beyond the intrinsic capabilities of silicon.

Lower-index-contrast waveguide layers, most notably silicon nitride, are often employed for path-length–critical wavelength-processing functions such as arrayed-waveguide gratings, where improved phase stability and reduced thermal sensitivity are required. Heterogeneous and hybrid integration strategies then enable efficient optical coupling between these functional layers, combining their respective strengths within a single photonic system. This functional separation has been widely reported in WDM PIC demonstrations [1], [3], [4].

In recent years, demonstrations have further illustrated the continued expansion of silicon-on-insulator beyond its traditional role as a CMOS-compatible routing and modulation platform. These works demonstrate the integration of phase-engineered elements, wafer-scale polarization control for quantum transmitters, enhanced sensing interfaces via electrokinetic actuation, and large-scale coherent signal processing on silicon, collectively highlighting the architectural flexibility and maturity of the SOI platform across diverse application domains [5], [6], [7], [8]. Representative passive silicon photonic building blocks are illustrated in Fig. 1.2.

1.2.2 Indium Phosphide (InP)

Indium phosphide (InP) is one of the most established III–V material platforms for photonic integrated circuits, particularly in applications where optical gain and high-speed optoelectronic functionality must be integrated on the same chip. In contrast to silicon and silicon nitride, which primarily rely on external or heterogeneous light sources, the InP material system provides direct-bandgap semiconductors compatible with native light generation, optical amplification, modulation, and photodetection in the main telecommunication windows around 1310 and 1550 nm [10], [11]. This intrinsic active functionality has made InP a reference platform for optical transceivers, coherent communication systems, semiconductor optical amplifiers, tunable lasers, and sensing-oriented photonic circuits.

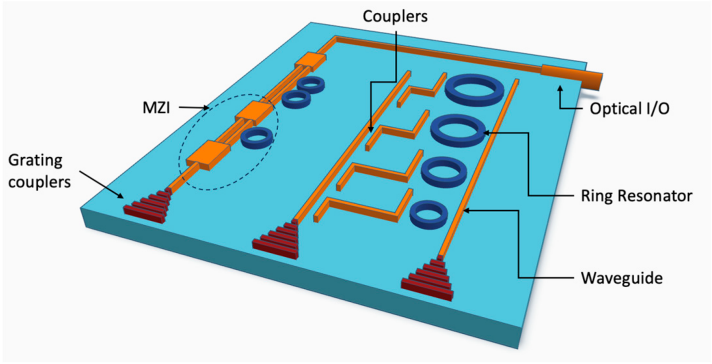


Figure 1.2: Examples of common silicon photonic passive devices. Adapted from [9].

A central advantage of InP-based photonic integration is the possibility of monolithically combining active and passive components within a single material system. Lasers, semiconductor optical amplifiers (SOAs), electro-absorption modulators, phase modulators, photodiodes, waveguides, filters, couplers, and wavelength multiplexers can all be implemented using related InP/InGaAsP epitaxial layer stacks [10], [11]. This functional completeness distinguishes InP from platforms such as SOI, where passive routing and compactness are excellent but efficient light generation generally requires external, hybrid, or heterogeneous III–V integration.

Several active–passive integration strategies have been developed for InP PICs, including quantum-well intermixing, selective-area growth, vertical twin-guide integration, and butt-joint regrowth [10], [12]. Butt-joint regrowth provides high design flexibility because the active and passive regions can be optimized separately in terms of material composition, quantum-well structure, and doping. However, this flexibility comes at the cost of additional epitaxial regrowth steps and increased process complexity. Quantum-well intermixing and selective-area growth reduce some regrowth requirements, but may introduce compromises in absorption loss, bandgap control, or material uniformity. Therefore, the main design challenge in conventional InP integration is not the absence of active functionality, but the need to balance device-level optimization against fabrication complexity and yield.

From a system perspective, InP is especially attractive when the photonic circuit requires compact on-chip sources or optical gain. This includes wavelength-tunable transmitters, coherent transceiver PICs, optical phase-locked loops, beam-steering systems, and optoelectronic circuits for millimeter-wave or terahertz signal generation [10], [13]. In such systems, the ability to integrate lasers, SOAs, modulators, and photodiodes on the same substrate can reduce coupling losses, packaging complexity, parasitic electrical interconnects, and system footprint. These advantages explain why InP-based solutions have remained commercially important in optical communication modules despite the rapid growth of silicon photonics.

At the same time, conventional InP platforms are generally less attractive than SOI for extremely dense passive routing, because the index contrast and fabrication ecosystem differ from mature CMOS silicon photonics. To address this limitation, InP membrane platforms, especially InP-membrane-on-silicon (IMOS), have been developed as a route toward combining the functional completeness of InP with the compactness of high-index-contrast nanophotonic waveguides [11], [12]. In IMOS, a thin InP membrane is bonded to a silicon substrate wafer and optically isolated using a low-index bonding or oxide layer. After removal of the original InP substrate, the thin membrane supports strongly confined optical modes, enabling submicrometer-scale waveguides and compact passive devices comparable in footprint to silicon photonics.

The IMOS concept also supports close integration with electronic circuits. Since the InP membrane can be placed on a silicon substrate containing driver or control electronics, short vertical electrical interconnects can reduce parasitic effects compared

with conventional multi-chip optoelectronic assemblies [11]. Recent IMOS developments further demonstrate a broad portfolio of passive and active building blocks, including compact reflectors, polarization converters, grating antennas, native light sources, SOAs, modulators, and detectors [11].

The IMOS concept is schematically illustrated in Fig. 1.3. In this architecture, active and passive InP-based devices are integrated within a thin photonic membrane bonded onto a silicon substrate. The passive waveguide layer acts as the common optical backbone, while active sections such as lasers, modulators, and photodetectors are locally introduced to provide full transmitter and receiver functionality. This integration strategy enables compact photonic circuits with short electrical interconnects to the underlying silicon electronics, making InP membrane platforms attractive for high-density electronic–photonic co-integration.

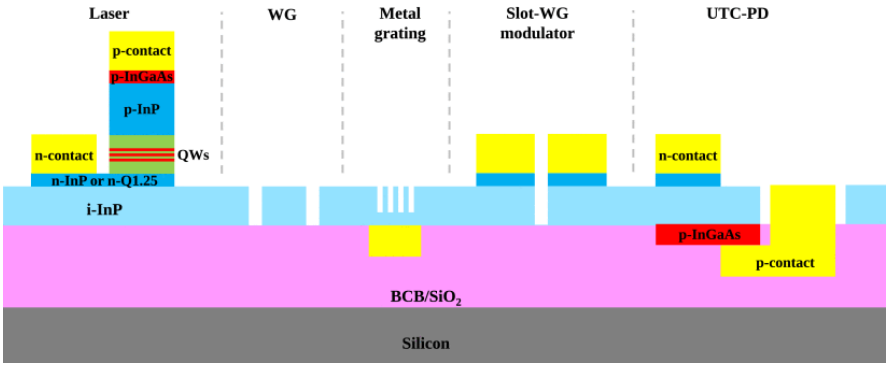


Figure 1.3: Schematic illustration of the active–passive integration scheme in an InP membrane-on-silicon (IMOS) platform. The platform enables the integration of multiple photonic functions, including lasers, passive waveguides, metal gratings, slot-waveguide modulators, and photodetectors, within a common InP-based membrane bonded to a silicon substrate through a BCB/SiO_2 layer. This architecture highlights the capability of InP membrane platforms to combine light generation, modulation, routing, and detection in a compact heterogeneous photonic layer. Adapted from [11].

Nevertheless, InP platforms still involve important practical trade-offs. Active–passive integration requires careful epitaxial design, bandgap engineering, and control of optical absorption in passive regions. In membrane platforms, thermal management becomes particularly important because bonding layers such as benzocyclobutene (BCB) can increase thermal resistance, while lasers and SOAs generate heat during operation [11], [12]. Therefore, InP is considered not as a universal replacement for silicon, silicon nitride, or lithium niobate, but as a highly capable active photonic platform whose strongest role lies in circuits requiring native gain, light generation, high-speed detection, and compact optoelectronic integration.

Within the materials for large-scale PICs, InP therefore occupies a complementary position. Silicon provides high-density CMOS-compatible routing and modulation, silicon nitride offers ultra-low-loss and phase-stable passive processing, and thin-film lithium niobate provides efficient Pockels electro-optic and $\chi^{(2)}$ nonlinear functionality. InP, by contrast, supplies the active optoelectronic functions that are difficult to realize natively in these passive or weakly active platforms. For this reason, modern PIC architectures increasingly treat InP either as a monolithic active platform for transmitter and receiver integration, or as a heterogeneous gain and detection layer combined with silicon, silicon nitride, or other low-loss passive platforms.

In recent years, several works have further confirmed the continuing relevance of InP-based photonics beyond conventional monolithic transmitter and receiver PICs. On the integration-technology side, room-temperature InP/Si surface-activated wafer bonding has recently been demonstrated as a promising route for electronic–photonic system integration. In this approach, a void-free and ultrathin bonding interface below 3 nm was obtained, with a room-temperature tensile strength of about 3 MPa and values exceeding 7 MPa after a short 300 °C thermal treatment [14]. Importantly, this work

also highlights that bonding-interface quality, plasma-induced InP oxidation, electrical conduction across the bonded interface, and thermal/mechanical stress must be treated as key design parameters rather than secondary process details.

At the system level, hybrid InP/Si_3N_4 integration has recently enabled ultra-low-noise chip-scale photonic microwave generation. Reference [15] demonstrates the combination of an InP distributed-feedback laser with a low-loss Si_3N_4 external cavity to realize a self-injection-locked optical comb laser, achieving individual comb-line linewidths around 35 Hz and an RF intrinsic linewidth of 0.8 Hz after optic–electro–optic feedback. This result illustrates the complementary role of InP and SiN. The InP provides compact optical gain and direct laser functionality, while the SiN supplies the low-loss, high-Q passive cavity required for linewidth narrowing and phase-noise reduction.

Recent InP transceiver developments also show that the platform remains highly competitive for next-generation optical interconnects. InP externally modulated lasers, Mach–Zehnder modulators, coherent receiver PICs, and AWG-integrated photodetectors have been reported for both direct-detection and coherent-detection links, including demonstrations targeting 100–200 GBaud-class operation and coherent receiver bandwidths above 75 GHz [16]. These results emphasize that InP continues to offer practical advantages in high-speed operation, efficient fiber-to-chip coupling, monolithic integration of active components, and reduced module complexity.

1.2.3 Silicon Nitride (Si_3N_4)

Silicon nitride (Si_3N_4) has emerged as a key passive photonic platform due to its exceptionally low propagation loss, wide optical transparency window spanning the visible to mid-infrared, moderate refractive-index contrast with SiO_2, and high optical power handling. In addition, its thermo-optic coefficient is approximately an order of magnitude smaller than that of silicon, enabling phase-stable interferometric circuits and nearly athermal operation without extensive thermal control [17], [18]. Compared with silicon-on-insulator, the reduced index contrast mitigates sensitivity to sidewall roughness and fabrication-induced dimensional variations, while still allowing compact routing and dense functional layouts when waveguide thickness is appropriately engineered. These properties have positioned Si_3N_4 as the preferred platform for ultra-high-Q resonators, low-noise wavelength-selective filtering, precision metrology, Kerr frequency-comb generation, and broadband WDM networks across a wide spectral range [17], [18].

State-of-the-art Si_3N_4 fabrication relies primarily on two process families: subtractive etching of LPCVD or PECVD films and the photonic Damascene reflow approach combined with chemical–mechanical polishing. Subtractive flows, developed and refined through stress-relief strategies and thermal cycling, routinely achieve telecom-band propagation losses on the order of 10^{-2} dB/cm and support resonators with quality factors exceeding 10^7. The Damascene reflow process enables thicker waveguide cores suitable for dispersion engineering, while maintaining losses below 0.01 dB/cm and Q factors in the multi-million regime, at the cost of increased process complexity and tighter control of oxide quality [17], [18]. Waveguide geometry acts as a primary design parameter: thin cores favor ultra-low loss and long photon lifetimes but impose large bend radii, whereas thicker cores enable anomalous group-velocity dispersion required for Kerr nonlinear processes while demanding stricter control of stress and sidewall quality.

Beyond stoichiometric silicon nitride, silicon-rich nitride compositions provide an expanded nonlinear design space. Silicon-rich and ultra-silicon-rich nitride films exhibit significantly enhanced Kerr nonlinearity—up to two orders of magnitude larger than stoichiometric Si_3N_4—while remaining effectively free of two-photon absorption at telecom wavelengths [19]. Through controlled CVD growth, the refractive index and dispersion can be tuned to balance nonlinear efficiency, absorption from residual N–H bonds, and fabrication robustness. In practice, these materials are attractive for compact nonlinear devices such as optical parametric amplifiers, supercontinuum sources, and soliton dynamics, where ultra-low linear loss is not the dominant constraint [19].

From a device perspective, Si_3N_4 supports a broad range of passive and nonlinear photonic functions. Low-loss rings and arrayed-waveguide gratings enable phase-stable and athermal wavelength filtering for dense WDM systems, while high-Q resonators provide narrow-linewidth feedback in hybrid laser cavities [18]. Thick-core Si_3N_4 waveguides with engineered dispersion have enabled Kerr frequency combs and optical parametric oscillation with experimentally demonstrated pump thresholds in the sub-watt regime, with residual absorption mitigated through high-temperature annealing or crack-free anneal-free processes [17]. In sensing and ranging applications, the visible and near-infrared transparency of Si_3N_4 enables low-noise interferometric architectures and nonlinear processing near 800–1000 nm, while integrated heaters allow fine phase trimming without incurring large thermal penalties [20].

At the system level, silicon nitride increasingly serves as the low-loss routing and wavelength-processing layer within heterogeneous and hybrid photonic stacks. In such architectures, silicon or III–V materials provide active functions such as modulation, detection, and gain, while lithium niobate contributes high-speed electro-optic and second-order nonlinear capabilities. Foundry-accessible Si_3N_4 process design kits and multi-project wafer services have enabled large-scale integration of SiN filters with hybrid lasers and nonlinear elements, supporting robust athermal WDM fabrics, ultra-narrow-linewidth sources, and scalable frequency-comb systems [18], [20].

Figure 1.4 summarizes representative silicon nitride photonic platforms and device implementations that support its role as a low-loss, phase-stable, and versatile passive layer in large-scale PICs.

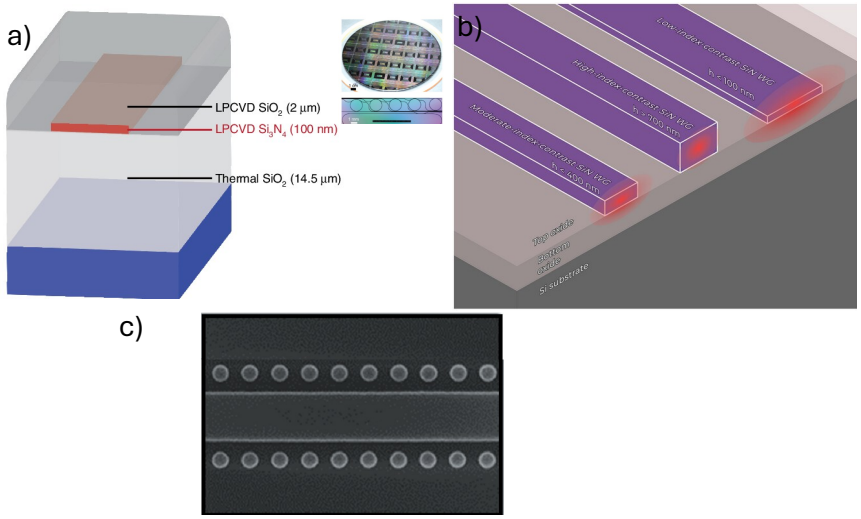


Figure 1.4: Representative silicon nitride (Si_3N_4) photonic platforms illustrating the breadth of the SiN design space. (a) Schematic view of a low-loss Si_3N_4 platform and wafer-scale integration enabled by mature deposition and processing. (b) Illustration of silicon nitride waveguide geometries spanning low- to high-index contrast and thin to thick cores, highlighting the trade-offs between confinement, dispersion, and loss. (c) Scanning electron micrograph of a representative nonlinear silicon-rich nitride structure, demonstrating the use of composition-engineered SiN for compact Kerr-based photonic devices. Adapted from Refs. [23,24,21].

In recent years, work has continued to consolidate silicon nitride (Si_3N_4) as a versatile and application-ready passive platform, spanning fiber–chip interfacing, low-loss linear routing, and power-scalable nonlinear processing. On the coupling side, single-etch and MPW-compatible multiband grating couplers operating simultaneously around 950, 1310, and 1550 nm have demonstrated fiber–chip insertion losses approaching ∼2.5 dB, enabled by subwavelength apodization and focused-beam engineering without resorting to multi-step fabrication flows [21]. These results reinforce the suitability of SiN for broadband and multi-band photonic systems.

Beyond coupling, compact resonant and delay-line structures fabricated in standard foundry processes have achieved intrinsic quality factors in the 10^6–10^7 range, with

propagation losses well below 0.1 dB/cm. Such performance confirms that low-loss SiN platforms do not inherently require exotic processing or custom material stacks to reach state-of-the-art metrics [22]. In parallel, passive power-distribution elements have progressed toward polarization robustness: broadband 1×2 splitters based on hybrid $Si/SiN_x/Si$ slot-MMI concepts have demonstrated polarization-independent operation with sub-0.2 dB insertion loss across bandwidths exceeding 100 nm, which is particularly attractive for wavelength routing in dense photonic integrated circuits [23].

Recent demonstrations have also highlighted the growing maturity of silicon nitride for nonlinear and parametric signal processing. Dispersion-engineered SiN waveguides supporting dual-polarization traveling-wave four-wave mixing have enabled comparable optical parametric amplification and wavelength-conversion performance for TE_0 and TM_0 modes near the C-band, including high-speed (25 Gbaud) coherent signal processing without polarization-diversity overhead [24]. This capability addresses a long-standing limitation of integrated nonlinear platforms and extends the relevance of SiN to advanced coherent communication systems.

Finally, application-driven advances in photonic beam forming and LiDAR have underscored the power-handling capability and phase stability of SiN. Optical phased-array radiators implemented on TriPleX-based platforms, using flat-emission grating designs, have achieved sub-degree beam divergence and peak directivities approaching 35 dBi in compact arrays. These results illustrate the suitability of silicon nitride for robust solid-state beam steering under high optical power conditions and dynamic operation [25].

1.2.4 Thin-Film Lithium Niobate (TFLN/LNOI)

Thin-film lithium niobate on insulator (LNOI or TFLN) combines a wide optical transparency window with exceptionally strong second-order nonlinearity and a large Pockels electro-optic effect, while enabling tight optical confinement through submicron waveguide geometries. This transition from conventional, weakly guiding lithium niobate waveguides to high-index-contrast thin films has fundamentally expanded the design space of integrated photonics, making compact bends, dense routing, and low-loss resonant structures compatible with high-speed electro-optic modulation and efficient $\chi^{(2)}$ frequency conversion on a single crystalline platform [26], [27], [28].

Commercial LNOI wafers are typically fabricated using ion implantation, direct bonding, and exfoliation processes (smart-cut), as illustrated in Fig. 1.5, where the formation of the thin-film LN layer on a buried oxide is achieved through successive bonding, annealing, and polishing steps.

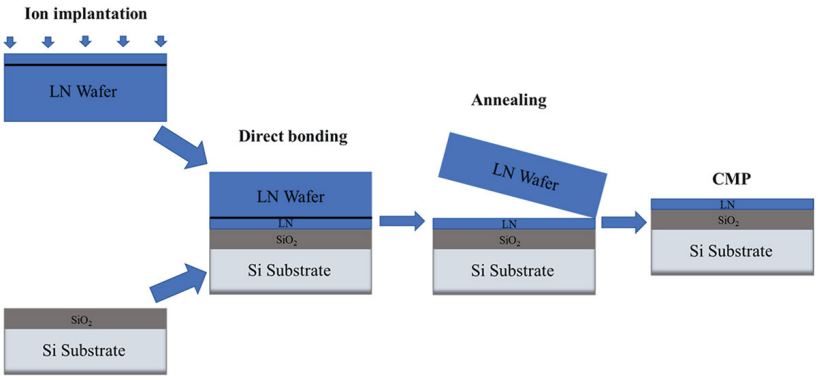


Figure 1.5: Schematic overview of a typical lithium-niobate-on-insulator (LNOI) fabrication flow based on ion implantation, wafer bonding, and exfoliation (smart-cut), followed by annealing and chemical–mechanical polishing to define the thin-film LN device layer on a buried oxide [26].

After bonding to a handle substrate through a buried SiO_2 layer and subsequent annealing and chemical–mechanical polishing, high-quality single-crystal LN films with thicknesses of a few hundred nanometers are obtained. Both X-cut and Z-cut orientations

are widely available, allowing device designers to access specific electro-optic and nonlinear tensor elements through appropriate waveguide orientation and electrode placement. The buried oxide layer not only provides optical isolation but also enhances the overlap between radio-frequency and optical fields in traveling-wave electro-optic devices [26], [28].

Early TFLN devices relied on shallow ridge or rib-loaded waveguides to mitigate fabrication challenges associated with dry etching of ferroelectric materials. These geometries typically exhibited strongly slanted sidewalls and ridge-to-slab ratios close to unity, which constrained achievable bend radii and integration density. Continued process development—including argon-ion milling, deep-UV lithography, chemo-mechanical polishing, and photo-lithography-assisted chemo-mechanical etching (PLACE)—has progressively reduced propagation losses while improving reproducibility at the wafer scale. Intrinsic cavity quality factors exceeding 10^8 and propagation losses approaching the 10^{-1} dB/cm regime have been demonstrated on 6- to 8-inch wafers [26], [27]. More recently, diamond-like-carbon hard-mask processes have enabled fully etched strip waveguides with near-vertical sidewalls and losses below a few dB/m, yielding more than an order-of-magnitude increase in area density compared to shallow ridge approaches while preserving electro-optic efficiency [29].

Lithium niobate is a uniaxial, ferroelectric crystal, and the optical and electro-optic behavior of TFLN devices is strongly influenced by crystal cut, propagation direction, and modal polarization. In practice, etched waveguides often exhibit mildly trapezoidal cross-sections due to finite sidewall angles, a feature that must be accounted for when estimating effective waveguide widths, dispersion, and phase-matching conditions in preliminary designs. Figure 1.6 schematically shows this non-ideal but systematic geometry, where the finite sidewall angle γ leads to a trapezoidal cross-section with distinct top and bottom widths. In practical designs, the optical mode samples the entire cross-section rather than a nominal lithographic width, making the concept of an effective waveguide width essential. Neglecting this geometry can result in systematic errors in effective-index estimation, dispersion engineering, and phase-matching calculations, particularly in submicron TFLN waveguides where confinement is strong and modal sensitivity is high.

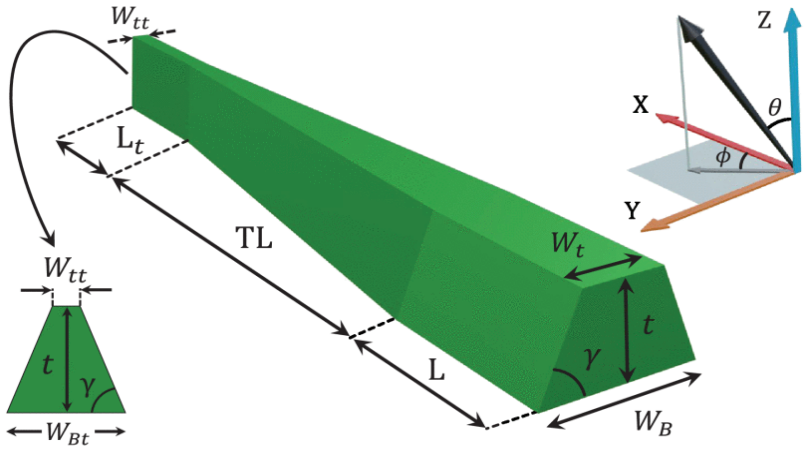


Figure 1.6: Schematic illustration of a trapezoidal thin-film lithium niobate waveguide cross-section, highlighting the finite sidewall angle γ that arises from practical dry-etching processes. The resulting difference between top and bottom widths (W_t and W_B) defines an effective waveguide width that directly influences modal confinement, dispersion, and phase-matching behavior in integrated TFLN devices.

As a result, realistic trapezoidal waveguide geometries, together with polarization-dependent refractive indices, are routinely incorporated at early design stages using preliminary mode solvers and numerical simulations. This fabrication-aware modeling approach provides reliable starting points for electro-optic devices, multimode interferometers, grating-assisted couplers, and nonlinear wavelength-conversion structures, prior to full three-dimensional optimization [26]. By accounting for non-ideal cross-sections, discrepancies between simulated and fabricated devices are reduced, leading to improved

predictability of key performance metrics such as modulation efficiency, bandwidth, and nonlinear conversion efficiency.

Electro-optic modulators on TFLN exploit the large Pockels effect using traveling-wave electrode configurations integrated with tightly confined optical modes. Such devices routinely demonstrate a combination of low drive voltage, very high modulation bandwidth, and improved thermal stability compared to thermo-optic platforms, with reported bandwidths approaching or exceeding 100 GHz at sub-volt operation [26], [27]. The strong confinement and the presence of the buried oxide layer enhance radio-frequency–optical mode overlap, provided that metal-induced optical losses are carefully managed through electrode spacing and dielectric buffering.

In parallel, thin-film lithium niobate has revitalized integrated second-order nonlinear optics. Efficient second-harmonic, sum- and difference-frequency generation, optical parametric amplification and oscillation, and spontaneous parametric downconversion have all been demonstrated in straight waveguides and high-Q microresonators. Phase matching can be achieved either through periodic poling for quasi-phase matching or through modal phase matching enabled by dispersion engineering in submicron waveguides. Compared to bulk lithium niobate, the reduced mode area and enhanced field overlap in TFLN significantly increase normalized nonlinear efficiencies, enabling practical wavelength conversion and parametric gain with milliwatt- to watt-level pump powers [26], [27], [30].

From a system perspective, fiber interfacing on TFLN platforms commonly relies on edge couplers based on inverse or three-dimensional tapers to achieve low insertion loss and broad bandwidth, with surface grating couplers increasingly explored for specific packaging scenarios. Hybrid integration strategies, such as SiN–LN or III–V-on-LN stacks, further extend functionality by combining ultra-low-loss routing or on-chip gain with lithium niobate's electro-optic and $\chi^{(2)}$ capabilities, at the cost of added bonding and transition complexity [28].

Recent advances further position thin-film lithium niobate (TFLN/LNOI) as a technologically mature and application-ready photonic platform, extending beyond isolated device demonstrations toward system-level completeness. Advances in fiber–chip interfacing, such as ultra-thin suspended LNOI grating couplers, address long-standing coupling bottlenecks while remaining compatible with fully etched waveguide stacks [31]. In parallel, dispersion-engineered TFLN waveguides have enabled continuous-wave optical parametric amplification with double-digit on-chip gain across the C and L bands using wafer-scale fabrication flows, indicating viable paths toward integrated amplification without external optical amplifiers [32].

Beyond interfacing and gain, recent demonstrations highlight the scalability of LN-based electro-optic control for complex photonic architectures. Hyper-multiplexed photonic processors combining co-integrated sources with high-speed TFLN electro-optics illustrate how space–time–wavelength parallelism can be realized within a single platform [33]. Complementary characterization studies, including integrated electric-field sensors on LNOI and in-situ measurements of effective electro-optic coefficients in Ti:PPLN channel waveguides, provide useful insight into how crystal orientation and domain engineering influence practical device performance [34], [35].

At a broader level, recent review work synthesizes progress across modulators, nonlinear converters, and coupling strategies while identifying remaining challenges in packaging, heterogeneous integration, and large-scale manufacturability [36]. In a closely related ferroelectric platform, triply resonant electro-optic frequency-comb generation on thin-film lithium tantalate demonstrates how resonance engineering can dramatically extend comb span while reducing microwave drive power, offering concepts that are directly transferable to future LNOI-based electro-optic systems [37].

1.2.5 Hybrid and Heterogeneous Integration in Photonic Integrated Circuits

As photonic integrated circuits scale toward higher functional density and system-level complexity, the limitations of monolithic material platforms increasingly motivate hybrid

and heterogeneous integration strategies. While individual photonic materials can deliver excellent performance in specific roles, no single platform simultaneously optimizes low-loss routing, high-speed electro-optic modulation, efficient nonlinear conversion, and optical gain. Hybrid and heterogeneous integration therefore emerge as enabling approaches for combining complementary material properties within a single photonic system.

In the context of silicon photonics, heterogeneous integration is commonly defined as the wafer- or die-level bonding of dissimilar materials—most notably III–V semiconductors, dielectric waveguides, or functional oxides—onto a silicon substrate, followed by lithographic definition of the photonic devices [38]. This approach differs from conventional hybrid assembly, where fully fabricated chips are aligned and coupled post-fabrication, by enabling tighter optical coupling, relaxed alignment tolerances, and improved scalability through CMOS-compatible processing. As a result, heterogeneous integration has become a key pathway for overcoming silicon's intrinsic limitations, particularly the absence of native optical gain and weak electro-optic effects.

Recent system-level reviews highlight heterogeneous integration as a central enabler of high-performance silicon photonics, supporting dense integration of lasers, modulators, detectors, and low-loss passive circuits on large-diameter wafers [39]. By selectively incorporating materials such as III–V gain media, ultra-low-loss silicon nitride waveguides, or ferroelectric films, heterogeneous platforms allow performance optimization beyond what is achievable with monolithic silicon alone. From a scalability perspective, this functional partitioning is increasingly viewed as essential for future photonic systems targeting co-packaged optics, high-bandwidth datacenter interconnects, and energy-efficient chip-scale signal processing.

Within this broader landscape, lithium niobate has attracted significant attention for a heterogeneous or hybrid integration due to its strong Pockels electro-optic response and large second-order nonlinearity. Review studies on lithium-niobate-on-insulator (LNOI) emphasize that heterogeneous integration with silicon or silicon nitride platforms enables the combination of high-speed electro-optic control and efficient $\chi^{(2)}$ processes with low-loss routing and wavelength-selective filtering [40]. In particular, SiN–LN hybrid stacks exploit the wide transparency and phase stability of silicon nitride together with the active functionality of lithium niobate, offering an attractive route for integrated modulation and wavelength conversion without sacrificing passive performance.

1.3 PIC Devices

This section introduces representative photonic building blocks relevant to the devices and functionalities considered throughout this thesis. Rather than providing an exhaustive survey of all possible photonic components, the discussion focuses on device classes that illustrate the main functional roles required in integrated photonic circuits, including optical power distribution, wavelength-selective routing, electro-optic modulation, and nonlinear frequency conversion.

The section first discusses passive power-distribution elements, including multimode-interference (MMI) couplers and directional couplers, which are widely used for splitting, combining, and controlled power transfer. It then introduces wavelength-selective devices, including grating-assisted contra-directional couplers, microring resonators, and arrayed waveguide gratings, which provide different approaches to filtering, add–drop routing, and wavelength multiplexing. Finally, Mach–Zehnder modulators and periodically poled lithium niobate (PPLN) devices are considered as representative examples of active electro-optic and nonlinear photonic components, respectively. This organization clarifies the role of each device class within the broader architecture of integrated photonic systems.

1.3.1 Multimode-Interference (MMI) Couplers

Multimode-interference (MMI) couplers are well-established building blocks in photonic integrated circuits for broadband power splitting and combining. Their operation is based

on the self-imaging principle, whereby the constructive interference of multiple laterally propagating modes in a multimode waveguide reproduces one or more replicas of an input field at periodic propagation distances. In comparison with directional couplers, MMIs exhibit reduced sensitivity to fabrication-induced dimensional variations and naturally scale to $1\times N$ and $N\times 1$ configurations, which makes them attractive for power distribution and combining functions in large-scale PICs [9], [41].

In a typical MMI geometry, a single-mode access waveguide excites several transverse modes in a uniform multimode section of width W_{MMI} and effective refractive index n_{eff}. The fundamental beat length that governs the self-imaging periodicity can be approximated as

$$L_\pi \approx \frac{4\, n_{\mathrm{eff}}\, W_e^2}{3\,\lambda}, \tag{1.1}$$

where W_e denotes an effective width that accounts for modal field penetration into the cladding. For a $1\times N$ splitter, the multimode section length is typically chosen as a suitable fraction of L_π to generate N equally spaced images at the output plane. These expressions provide a first design guideline, while accurate performance assessment generally relies on numerical mode analysis and full-wave simulations [9], [41].

Beyond uniform-width implementations, generalized-interference MMI (GIMMI) concepts introduce controlled width variations or short tapers within the multimode region to tailor the imaging condition. Such approaches can reduce device footprint, improve spectral flatness, or relax polarization-dependent behavior, while preserving the inherent broadband nature of the MMI operation [41]. As a result, MMIs offer a flexible design space that can be adapted to different integration platforms and system-level requirements.

The practical behavior of MMIs is strongly influenced by the underlying material platform and waveguide cross-section. In thin-film lithium niobate (TFLN/LNOI), etched waveguides typically exhibit trapezoidal profiles and optical anisotropy, requiring effective-width and imaging conditions to be evaluated using polarization- and dispersion-aware models. Silicon nitride (Si_3N_4) platforms, characterized by lower refractive-index contrast, lead to larger MMI footprints but benefit from excellent broadband uniformity and low excess loss. Conversely, silicon-on-insulator (SOI) enables very compact MMIs at the expense of increased sensitivity to nanometer-scale dimensional variations, which can be critical in uniformity-limited applications [9].

To connect the general self-imaging principle to a specific device, Fig. 1.7 summarizes the representative 1×2 TFLN MMI designed, fabricated, and experimentally characterized in this thesis. The device was implemented using a trapezoidal TFLN rib-waveguide cross-section comprising a 200-nm-thick slab and a nominal rib height of 400 nm, with a sidewall angle of approximately 55°. The multimode section was designed with a bottom width of $W_{\mathrm{MMI}}^{(B)} = 4\ \mu$m and a length of $L_{\mathrm{MMI}} = 10.6\ \mu$m, while the bottom width of each output taper was $W_{\mathrm{taper}}^{(B)} = 2\ \mu$m. The corresponding top widths are determined by the rib height and sidewall angle. The geometry was optimized to achieve low-loss and balanced power splitting across the O-band.

As shown in Fig. 1.7(b), the optimized design provides nearly identical responses at the two output ports throughout the O-band. Around the central wavelength of the investigated range, the simulated transmittance is approximately 0.489 at each port, corresponding to a total transmitted power of approximately 97.8% and an excess insertion loss of approximately 0.10 dB. The close overlap between the two responses confirms the balanced operation of the geometrically symmetric 1×2 configuration.

The device was subsequently fabricated as part of a TFLN photonic chip, as shown in Fig. 1.7(c). Post-fabrication information indicated that the realized rib height was approximately 300 nm rather than the nominal value of 400 nm used in the original O-band design. Moreover, the available grating couplers were designed for C-band operation. Consequently, the fabricated MMI was experimentally characterized between 1500 and 1600 nm, outside its intended design band.

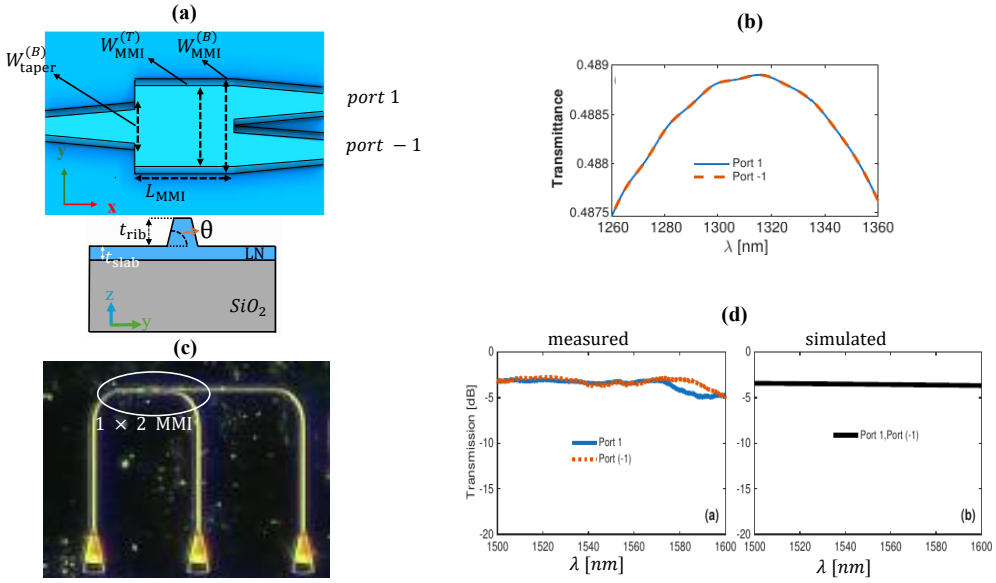


Figure 1.7: Representative 1 × 2 TFLN MMI investigated in this thesis. (a) Top-view schematic of the MMI and cross-sectional representation of the trapezoidal TFLN rib waveguide, showing the top and bottom widths, multimode-section length, rib height, slab thickness, and sidewall angle. (b) Simulated transmittance at the two output ports over the intended O-band operating range. (c) Optical micrograph of the fabricated device, with the 1 × 2 MMI region highlighted. (d) Measured and simulated per-port transmission over the available C-band wavelength range. The nominal design assumed a 400-nm rib height, whereas post-fabrication information indicated an actual rib height of approximately 300 nm. The C-band response was therefore recalculated using the fabricated cross-section for comparison with the experimental results.

Figure 1.7(d) compares the measured transmission with the numerical response recalculated using the fabricated cross-section. Around 1550 nm, the measured per-port transmission level is consistent with the simulated value of approximately −3.5 dB. Nevertheless, the measured spectra exhibit additional wavelength dependence, particularly toward longer wavelengths, which is not reproduced by the device-only numerical model. The remaining discrepancy may reflect the combined effects of the wavelength-dependent coupling response, fabrication-induced dimensional variations, and measurement uncertainty. Detailed discussions of the design optimization, fabrication-tolerance analysis, fabrication process, and experimental characterization are provided in Chapters 2 and 3.

1.3.2 Directional Couplers

Directional couplers (DCs) are among the most fundamental building blocks in photonic integrated circuits, enabling controlled power transfer between adjacent waveguides through evanescent field coupling. They are extensively employed in power splitting, optical switching, wavelength filtering, interferometric circuits, and programmable photonic architectures [42], [43].

The operation of a directional coupler is governed by coupled-mode theory (CMT), which describes the interaction between two closely spaced waveguides through evanescent field coupling. Under the assumption of single-mode propagation in each waveguide and negligible loss in the coupling region, the evolution of the complex modal amplitudes can be expressed as

$$\begin{pmatrix} A_3(L) \\ A_4(L) \end{pmatrix} = \begin{pmatrix} \cos(\gamma L) - i\dfrac{\Delta\beta}{\gamma}\sin(\gamma L) & -i\dfrac{\kappa}{\gamma}\sin(\gamma L) \\ -i\dfrac{\kappa}{\gamma}\sin(\gamma L) & \cos(\gamma L) + i\dfrac{\Delta\beta}{\gamma}\sin(\gamma L) \end{pmatrix} \begin{pmatrix} A_1(0) \\ A_2(0) \end{pmatrix}. \tag{1.2}$$

Here, A_1 and A_2 denote the complex optical field amplitudes at the input ports, while A_3 and A_4 correspond to the output ports. The amplitudes are typically normalized such that total optical power is conserved, i.e., $|A_1|^2 + |A_2|^2 = |A_3|^2 + |A_4|^2$, reflecting the unitary nature of the coupling process in the absence of loss.

The parameter κ is the coupling coefficient, determined by the overlap of the evanescent fields of the two waveguides, and is strongly dependent on the gap G, waveguide dimensions, and refractive-index contrast. The term $\Delta\beta = \beta_1 - \beta_2$ represents the propagation constant mismatch between the two waveguides, arising from structural asymmetry or wavelength-dependent dispersion. The interaction length L corresponds to the physical length of the coupling region.

The generalized coupling coefficient is defined as

$$\gamma = \sqrt{\kappa^2 + \Delta\beta^2}, \tag{1.3}$$

which governs both the oscillation period and amplitude of power transfer between the waveguides. In the phase-matched case ($\Delta\beta = 0$), complete power transfer can occur, whereas a nonzero mismatch reduces the maximum achievable coupling efficiency.

The corresponding power transfer ratio is given by

$$T = \frac{\kappa^2}{\kappa^2 + \Delta\beta^2} \sin^2(\gamma L), \tag{1.4}$$

demonstrating that the coupling efficiency depends critically on the waveguide geometry, operating wavelength, and refractive-index distribution.

The schematic representation of a conventional directional coupler is shown in Fig. 1.8. A typical DC consists of two parallel waveguides with identical width W, brought into close proximity over a coupling region of length L_c.

Optical power transfer occurs due to evanescent coupling between the guided modes of the two waveguides. While the straight interaction region primarily determines the coupling behavior, the adjacent S-bend sections also contribute to the effective coupling length, leading to a total interaction length larger than the nominal L_c.

The coupling strength is strongly dependent on geometrical parameters, including the waveguide width W, the gap G between the waveguides, and the vertical dimensions defined by the rib height H and slab thickness h. Careful optimization of these parameters is required to achieve the desired coupling ratio and spectral response.

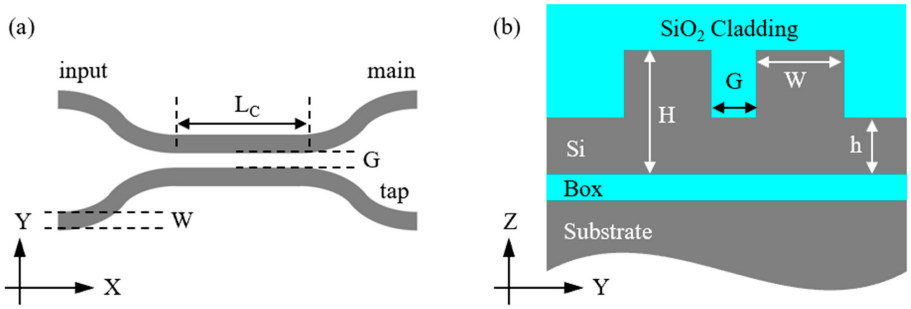


Figure 1.8: Schematic representation of a conventional directional coupler (DC). (a) Top view showing two parallel waveguides coupled over a length L_c, including S-bend sections for input and output routing. The coupling occurs primarily in the straight interaction region, with additional contributions from the adjacent transition regions. (b) Cross-sectional view of the rib waveguide geometry, highlighting key design parameters, including waveguide width W, gap G, rib height H, and slab thickness h, which collectively determine the coupling strength and modal overlap. Adapted from [43].

Despite their simplicity, conventional directional couplers suffer from several limitations, including wavelength sensitivity, fabrication-induced variations, and limited bandwidth. In particular, the dependence of the coupling coefficient on effective index difference leads to significant spectral variation in the splitting ratio, which is undesirable for broadband applications [43]. To mitigate this, several design strategies have been explored.

One approach involves broadband and low-loss coupler design using modified geometries, such as asymmetric or curved coupling regions. For example, replacing one straight waveguide with an arc-shaped structure reduces the effective coupling length and improves spectral stability, achieving power variation below 1.5% over a wide wavelength range with excess loss below 0.3 dB [43]. Similarly, suspended directional couplers have been proposed to enhance confinement contrast and reduce footprint, enabling compact designs with dimensions as small as 20×30 μm and insertion losses around 0.5 dB [44].

Another important direction is the development of tunable directional couplers, where active control is introduced through phase shifters. Dual-drive directional couplers (DD-DCs) incorporate phase actuators in both arms, allowing independent control of the splitting ratio and output phase. The phase shift induced by thermo-optic tuning can be expressed as

$$\Delta\phi = \frac{2\pi}{\lambda}\Delta n_{\text{eff}} L, \tag{1.5}$$

where Δn_{eff} is the effective index change induced by temperature variations [45]. Such devices enable reconfigurable photonic circuits and form the basis of tunable basic units (TBUs) in programmable waveguide mesh architectures.

Recent advances have also explored polarization-selective directional couplers, where asymmetry is introduced to achieve phase matching for only one polarization. Asymmetric directional couplers (ADCs) and bent coupler configurations have demonstrated ultra-low insertion losses below 0.02 dB with extinction ratios exceeding 25 dB, highlighting their suitability for polarization beam splitting in dense PICs [46]. These designs carefully balance mode mismatch and coupling efficiency, addressing the trade-off between insertion loss and extinction ratio.

Beyond conventional designs, emerging concepts such as topological directional couplers have introduced fundamentally new mechanisms for light coupling. By exploiting topological photonic crystal interfaces, these devices enable robust, backscattering-immune coupling with reduced device length. In such systems, coupling occurs through controlled hybridization of topological edge states, analogous to Rabi oscillations, allowing compact and tunable beam splitting with enhanced robustness [47].

Overall, directional couplers remain indispensable in PIC design due to their versatility and compatibility with a wide range of platforms, including SOI, SiN, and hybrid systems. While traditional designs are limited by wavelength sensitivity and fabrication tolerances, recent developments in broadband, tunable, polarization-selective, and topological couplers demonstrate that these limitations are increasingly being addressed. Consequently, directional couplers continue to evolve from simple passive splitters toward highly engineered and multifunctional components in modern photonic integrated circuits.

1.3.3 Grating-Assisted Contra-Directional Couplers (GACDCs)

Grating-assisted contra-directional couplers (GACDCs) are wavelength-selective devices in which a periodic refractive-index perturbation enables coupling between forward- and backward-propagating modes of two adjacent waveguides. In contrast to conventional co-directional couplers, the power transfer is restricted to wavelengths satisfying a Bragg-type phase-matching condition. Consequently, GACDCs can provide compact and free-spectral-range-free add–drop filtering without relying on resonant cavity buildup [48], [49], [50].

For the configuration considered in this thesis, an optical signal launched into the input port propagates along the uniform SiN waveguide. At wavelengths away from the phase-matching condition, the signal remains in the same waveguide and exits through the through port. At the Bragg wavelength, however, the periodic SiN grating couples the input mode to the backward-propagating mode of the adjacent waveguide, directing the selected wavelength toward the drop port. The first-order contra-directional phase-matching condition is expressed as

$$\beta_{\text{fwd}}(\lambda_0) + \beta_{\text{bwd}}(\lambda_0) = \frac{2\pi}{\Lambda}, \tag{1.6}$$

where β_{fwd} and β_{bwd} are the propagation constants of the forward-propagating mode in the input waveguide and the backward-propagating mode in the grating waveguide, respectively, Λ is the grating period, and λ_0 denotes the phase-matched wavelength. The grating period primarily determines the wavelength position of the drop channel, whereas the coupling gap, grating duty cycle, waveguide dimensions, and interaction length control the coupling strength, bandwidth, and extinction at the through port.

Figure 1.9 presents the representative hybrid SiN–TFLN add–drop filter numerically investigated in this thesis. The device consists of a uniform SiN input waveguide and an adjacent periodically patterned SiN waveguide placed on a thin-film lithium niobate layer and embedded in a SiO_2 cladding. The principal geometrical parameters are the grating period Λ, coupling gap g, grating-waveguide width W_{G}, input-waveguide width W_{in}, SiN thickness t_{SiN}, and LN thickness t_{LN}.

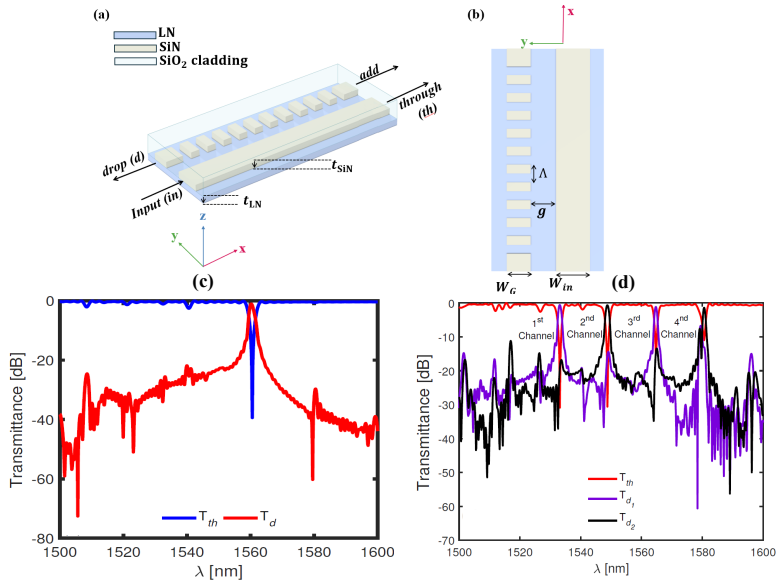


Figure 1.9: Representative hybrid SiN–TFLN grating-assisted contra-directional add–drop filter investigated in this thesis. (a) Three-dimensional schematic showing the SiN waveguides, TFLN layer, SiO_2 cladding, and input, through, add, and drop ports. (b) Top view of the coupling region showing the grating period Λ, coupling gap g, grating-waveguide width W_{G}, and input-waveguide width W_{in}. (c) Simulated through- and drop-port responses of the single-channel reference design with $\Lambda = 422$ nm and $N = 1200$ periods. (d) Simulated four-channel response obtained using two superimposed-period grating pairs, with two wavelength channels routed to each drop port.

The single-channel reference configuration shown in Fig. 1.9(c) was designed with a grating period of $\Lambda = 422$ nm, $N = 1200$ periods, a duty cycle of 0.5, and a coupling gap of $g = 900$ nm. The resulting interaction length is approximately 506.4 μm. At the phase-matched wavelength of approximately 1560 nm, the simulated drop-port transmittance is $T_{\mathrm{d}} \simeq -1.08$ dB, while the through-port transmittance decreases to $T_{\mathrm{th}} \simeq -39.34$ dB. These values indicate efficient wavelength transfer to the drop port together with strong suppression at the through port.

The single-channel concept was subsequently extended to multi-wavelength operation by superimposing grating periodicities within the same physical coupling region. As shown in Fig. 1.9(d), the period pairs $(412, 422)$ nm and $(417, 427)$ nm generate four drop channels located at approximately 1533, 1549, 1565, and 1581 nm. The resulting channels have a nearly uniform spacing of approximately 16 nm and are routed to two drop ports, with each port collecting two wavelengths. The multi-channel configurations provide drop-port insertion losses of approximately 1 dB and 3-dB bandwidths ranging from approximately 1 to 2.2 nm.

Fabrication-tolerance analysis further showed that the spectral response remains robust for grating duty cycles between 0.48 and 0.52 and coupling gaps between 600

and 1100 nm, with $g = 900$ nm selected as the nominal design value. Variations in the SiN waveguide dimensions and layer thickness primarily shift the Bragg wavelength and modify the coupling strength because they change the effective indices and modal overlap of the interacting modes. All responses reported in Fig. 1.9 were obtained numerically. The proposed add–drop filters were not fabricated or experimentally characterized within this thesis. The complete design procedure, multi-period analysis, spectral-performance assessment, and fabrication-tolerance study are presented in Chapter 4.

1.3.4 Microring Resonators

Microring resonators (MRRs) are among the most widely used building blocks in photonic integrated circuits due to their compact footprint, wavelength selectivity, and strong field confinement. These devices consist of a closed-loop waveguide coupled to one or more bus waveguides, enabling resonant enhancement of optical signals at specific wavelengths [51], [52].

The resonance condition in an MRR is governed by the round-trip phase matching requirement, which can be expressed as

$$\lambda_R = \frac{2\pi R}{m} n_{\text{eff}}, \tag{1.7}$$

where R is the ring radius, m is an integer mode number, and n_{eff} is the effective refractive index of the guided mode [51]. This relation indicates that the resonant wavelength is highly sensitive to both geometrical and material parameters.

MRRs exhibit sharp resonance peaks characterized by the quality factor (Q), defined as

$$Q = \frac{\lambda_{\text{res}}}{\text{FWHM}}, \tag{1.8}$$

where FWHM is the full-width at half-maximum of the resonance [53]. High-Q resonators enable strong light-matter interaction and improved spectral selectivity, making them suitable for filtering, sensing, and nonlinear applications.

The schematic of an add–drop microring resonator is shown in Fig. 1.10. The device consists of a closed-loop waveguide coupled to two bus waveguides, forming an input (through) and output (drop) channel.

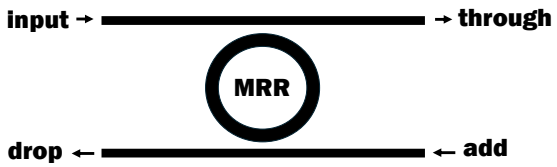


Figure 1.10: Schematic of an add–drop microring resonator (MRR). An input optical signal is coupled into a ring cavity through a bus waveguide. At resonance, constructive interference leads to efficient power transfer into the ring, resulting in wavelength-selective routing to the drop port, while off-resonant wavelengths propagate to the through port. The add port enables reverse injection into the resonator, supporting bidirectional operation.

When an optical signal is injected into the input waveguide, a portion of the light is evanescently coupled into the ring. At specific wavelengths satisfying the resonance condition, the circulating field inside the ring constructively interferes after each round trip, leading to strong field enhancement within the cavity. As a result, optical power is efficiently transferred to the drop port.

In contrast, off-resonant wavelengths do not satisfy the phase-matching condition and therefore remain in the through port with minimal coupling into the ring. This wavelength-selective behavior makes MRRs highly suitable for filtering and add–drop multiplexing in WDM systems.

One of the key advantages of MRRs is their ability to achieve strong optical confinement within a small footprint (typically a few micrometers in radius), which results in enhanced interaction between light and the surrounding medium [52]. This property makes MRRs particularly attractive for sensing applications, where changes in the refractive index lead to measurable shifts in the resonance wavelength. Compared to other resonant structures such as Fabry–Pérot cavities, MRRs do not require mirrors and are more compatible with integrated photonic platforms [52].

Despite their advantages, MRRs are highly sensitive to fabrication-process variations (FPVs), such as deviations in waveguide width, thickness, and radius. Even nanometer-scale variations can result in significant resonance shifts, which is critical in dense wavelength-division multiplexing (DWDM) systems where channel spacing is on the order of sub-nanometers [51]. Analytical models show that the resonance shift can be approximated as a function of variations in geometrical parameters and effective index, highlighting the importance of robust design optimization.

To address these challenges, recent works have focused on optimization of MRRs under fabrication variations. By carefully selecting design parameters such as waveguide dimensions and coupling conditions, it is possible to improve tolerance to FPVs by up to 70% while maintaining high performance metrics such as Q-factor and bandwidth [51].

In addition to passive filtering applications, MRRs play a crucial role in nonlinear photonics. The resonant enhancement inside the cavity significantly increases the effective optical intensity, enabling efficient nonlinear processes such as second-harmonic generation (SHG) and frequency conversion [54]. For instance, hybrid TFLN-on-SiN racetrack resonators have demonstrated loaded Q-factors on the order of 10^5 and efficient SHG via modal phase matching, highlighting the potential of integrated resonators for nonlinear and electro-optic functionalities [54].

Furthermore, MRRs can be used in microwave photonics, where their spectral selectivity enables the realization of high-resolution microwave photonic filters. By exploiting the resonance characteristics of silicon MRRs, tunable filters with rejection ratios exceeding 60 dB and high frequency resolution can be achieved, enabling accurate microwave frequency measurement with low error [55].

Overall, microring resonators provide a versatile platform for a wide range of applications, including filtering, modulation, sensing, nonlinear optics, and microwave photonics. While their strong sensitivity to fabrication variations presents a design challenge, recent advances in optimization techniques and hybrid material platforms continue to enhance their robustness and functionality, making them indispensable components in modern photonic integrated circuits.

1.3.5 Arrayed Waveguide Gratings (AWGs)

Arrayed waveguide gratings (AWGs) are key wavelength-selective components in photonic integrated circuits, widely used for multiplexing and demultiplexing optical signals in wavelength-division multiplexing (WDM) systems. Their ability to simultaneously process multiple wavelength channels with high spectral resolution has made them fundamental building blocks in optical communication, sensing, and signal-processing applications [56], [57].

The schematic structure of an arrayed waveguide grating is shown in Fig. 1.11. An optical signal entering the input waveguide spreads into the first free propagation region (FPR), also referred to as the input coupler. The optical field is then coupled into an array of waveguides, each having a constant path-length difference with respect to its adjacent waveguide.

This path-length difference introduces a progressive phase shift between the propagating modes, forming a phased-array structure. As the light propagates into

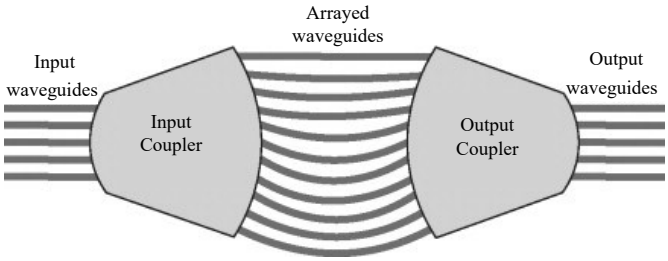


Figure 1.11: Schematic diagram of an arrayed waveguide grating (AWG). The device consists of an input waveguide coupled to a free propagation region (input coupler), followed by an array of waveguides with incremental path-length differences, and a second free propagation region (output coupler) that focuses different wavelengths to distinct output ports. The phased-array interference in the waveguide array enables wavelength-dependent spatial separation. Adapted from [58].

the second FPR (output coupler), constructive interference occurs at wavelength-dependent spatial positions, effectively focusing different wavelengths into separate output waveguides.

This spatial separation mechanism enables AWGs to perform wavelength multiplexing and demultiplexing functions, making them key components in dense WDM systems.

The operating principle of an AWG is based on phased-array interference. An input optical signal is first expanded in a free propagation region (FPR) and then coupled into an array of waveguides with a constant path-length difference ΔL. This path-length difference introduces a wavelength-dependent phase shift between adjacent waveguides, leading to constructive interference at different spatial positions in the output FPR. The central wavelength λ_c for a given diffraction order m satisfies the phase-matching condition

$$m\lambda_c = n_{\text{eff}}\Delta L, \tag{1.9}$$

where n_{eff} is the effective refractive index of the arrayed waveguides. As a result, different wavelengths are spatially separated at the output ports, enabling wavelength routing and filtering functionalities [57].

From a design perspective, several key parameters determine the spectral response of an AWG, including the channel spacing $\Delta\lambda$, the free spectral range (FSR), and the number of arrayed waveguides. For instance, integrated InP-based AWGs designed for WDM-PON systems typically exhibit channel spacings on the order of 0.8 nm and FSR values of several nanometers, enabling multi-channel transmission in dense wavelength grids [59]. The cyclic AWG configuration further introduces periodic spectral responses, which can be exploited to improve robustness against wavelength misalignment in multi-channel systems [59].

Performance metrics such as insertion loss and crosstalk are critical in evaluating AWG devices. Silicon nanowire AWGs fabricated using CMOS-compatible processes have demonstrated insertion losses in the range of 2–3 dB and crosstalk levels below -20 dB, making them suitable for dense WDM applications [56]. These results highlight the importance of design optimization techniques, including waveguide geometry engineering and tapering strategies, to improve spectral uniformity and reduce inter-channel interference.

Beyond telecommunications, AWGs have also emerged as enabling components in sensing systems, particularly in fiber Bragg grating (FBG) interrogation. In such systems, AWGs act as wavelength demodulators by converting spectral shifts into intensity variations across multiple output channels. Recent integrated AWG-based interrogators achieve sub-10 pm wavelength accuracy and high-speed sampling rates up to 10 kHz,

demonstrating their suitability for real-time sensing in harsh environments [60], [61]. These results illustrate the versatility of AWGs beyond conventional filtering applications.

Despite their advantages, AWGs also exhibit certain limitations. Their performance is sensitive to fabrication-induced variations in effective refractive index and waveguide dimensions, which can lead to phase errors and degraded spectral response. In addition, their footprint is generally larger than resonant devices such as microring resonators, due to the requirement of multiple arrayed waveguides and free propagation regions.

Overall, AWGs provide a robust and scalable solution for multi-channel wavelength routing in photonic integrated circuits. Compared to resonant devices, they offer broadband operation and reduced sensitivity to temperature-induced resonance drift, while enabling simultaneous processing of multiple wavelength channels. These characteristics make AWGs particularly attractive for large-scale WDM systems and integrated sensing platforms.

1.3.6 Mach–Zehnder Modulators (MZMs)

Mach–Zehnder modulators (MZMs) are among the most important active components in photonic integrated circuits, serving as the primary interface between electrical and optical domains for high-speed signal encoding. Their widespread adoption in optical communication systems stems from their capability to provide linear, chirp-controlled amplitude modulation, broadband operation, and compatibility with advanced modulation formats [62], [63].

The schematic of a Mach–Zehnder modulator is shown in Fig. 1.12. The device operates by splitting an input continuous-wave (CW) optical signal into two arms, where phase modulation is induced through externally applied voltages.

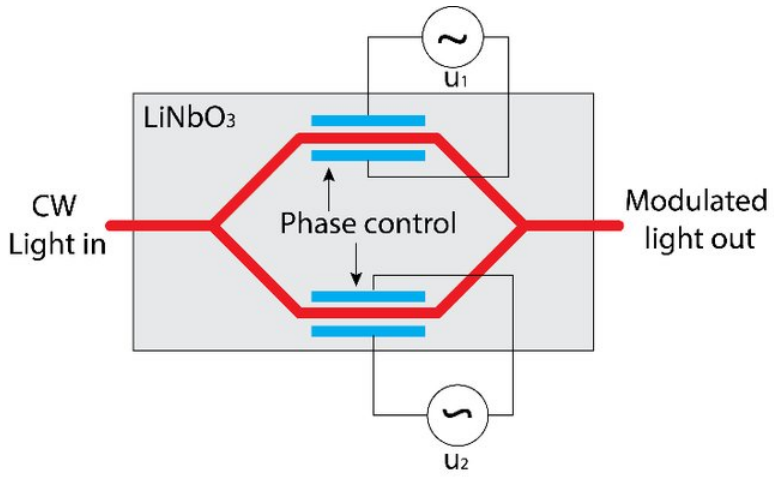


Figure 1.12: Schematic representation of a Mach–Zehnder modulator (MZM) based on a lithium niobate platform. The input continuous-wave (CW) optical signal is split into two arms, where phase modulation is induced via applied electrical voltages. The resulting phase difference leads to constructive or destructive interference at the output, enabling intensity modulation of the optical signal. Adapted from [64].

Depending on the applied electrical signals, different phase shifts are introduced in the two arms, which leads to interference at the output coupler. This interference can be constructive or destructive, resulting in modulation of the output optical intensity.

MZMs can operate in different configurations depending on the applied voltages. In the push–push mode, identical voltages are applied to both arms, resulting in pure phase modulation. In contrast, in the push–pull mode, opposite voltages are applied to the two arms, producing chirp-free intensity modulation, which is particularly desirable in high-speed optical communication systems.

The operating principle of an MZM is based on optical interference. An input optical field is split into two arms, where an externally applied electric field induces a phase shift

in one or both arms. The output intensity is determined by the phase difference $\Delta\phi$ between the two arms:

$$I_{\text{out}} = I_{\text{in}} \cos^2\left(\frac{\Delta\phi}{2}\right), \tag{1.10}$$

where $\Delta\phi$ is typically controlled via electro-optic or plasma dispersion effects. In phase modulators, the efficiency is commonly quantified by the half-wave voltage V_π, defined as the voltage required to induce a π phase shift, with a figure of merit given by $V_\pi \cdot L$, where L is the interaction length [62].

MZMs can be implemented on various material platforms, each offering distinct trade-offs. Silicon photonics MZMs rely on the plasma dispersion effect, where carrier injection or depletion modifies the refractive index. These devices are compatible with CMOS fabrication and enable high integration density, but suffer from relatively weak electro-optic efficiency and nonlinear response [62]. As a result, phase shifters typically extend over millimeter-scale lengths, limiting compactness and increasing power consumption.

To overcome these limitations, alternative material platforms have been explored. Thin-film lithium niobate (TFLN) MZMs make use of the strong Pockels effect to achieve high linearity, low chirp, and high modulation bandwidth. Recent demonstrations report electro-optic bandwidths exceeding 40 GHz with half-wave voltages as low as 1.45 V, enabled by optimized traveling-wave electrode designs and velocity matching between RF and optical signals [65]. Furthermore, plasmonic-enhanced TFLN MZMs have achieved record-high modulation efficiencies as low as 0.070 V·cm and bandwidths beyond 110 GHz with ultra-compact device lengths of only tens of micrometers, by exploiting strong field confinement in subwavelength slot waveguides [66].

From an architectural perspective, MZMs are widely used in advanced transmitter configurations. In silicon photonics, Mach–Zehnder-based transmitters support high-data-rate operation through multistage or traveling-wave electrode designs, achieving data rates up to tens of gigabits per second with improved power efficiency and extinction ratio performance [63]. The traveling-wave architecture is particularly important for high-speed operation, as it enables efficient RF–optical interaction over extended lengths while minimizing bandwidth limitations.

In addition to conventional intensity modulation, MZMs enable advanced modulation schemes through parallel and nested configurations. Dual-parallel MZMs (DPMZMs) allow independent control of in-phase (I) and quadrature (Q) components, enabling coherent modulation formats such as QPSK and QAM. These architectures are essential for high-capacity communication systems, including emerging terahertz wireless links, where silicon photonic integrated circuits based on dual-parallel MZMs have demonstrated data rates up to 50 Gbps with low bit-error rates [67].

Recent developments also extend MZM operation to new wavelength regimes. For instance, silicon-based MZMs operating at 2 μm have demonstrated high-speed modulation up to 80 Gbps using PAM-4 formats, highlighting the potential of MZMs for next-generation communication windows beyond the conventional C-band [68].

From a system perspective, MZMs remain the preferred solution for high-linearity modulation, particularly in coherent communication systems and microwave photonics. Their intrinsic linear transfer function and push–pull operation enable low-chirp signal generation, which is critical for high-order modulation formats and dispersion-tolerant transmission [62].

Despite these advantages, MZMs also exhibit limitations. Their relatively large footprint compared to resonant modulators, as well as the trade-off between modulation efficiency, bandwidth, and power consumption, remain key design challenges. Nevertheless, ongoing advances in hybrid material integration, plasmonic enhancement, and device architecture continue to push the performance of MZMs toward ultra-compact, high-speed, and energy-efficient operation.

Overall, Mach–Zehnder modulators represent a versatile and mature platform for optical modulation, supporting a wide range of applications from data communications and sensing to microwave photonics and emerging terahertz systems.

1.3.7 Periodically Poled Lithium Niobate (PPLN) Devices

Periodically poled lithium niobate (PPLN) devices are introduced in this section as representative second-order nonlinear building blocks for frequency conversion in integrated photonic systems. Rather than focusing on a specific device geometry, the discussion emphasizes the underlying physical principles, material considerations, and nonlinear interaction mechanisms that make PPLN particularly relevant for on-chip wavelength conversion. This section introduces periodically poled lithium niobate (PPLN) as a $\chi^{(2)}$ nonlinear platform for integrated wavelength conversion, with a primary focus on SHG, SFG, and DFG processes. The discussion centers on physical principles and material considerations, while references to bulk implementations are included solely for contextual completeness.

Periodically poled lithium niobate (PPLN) is one of the most established platforms for second-order ($\chi^{(2)}$) nonlinear frequency conversion, primarily due to its ability to implement quasi-phase-matching (QPM). In QPM, the sign of the effective nonlinear coefficient is periodically inverted through ferroelectric domain reversal, compensating for the phase mismatch accumulated between interacting optical waves and thereby enabling coherent nonlinear interactions over extended propagation lengths.

Compared with conventional birefringent phase matching, quasi-phase matching relaxes constraints on polarization and propagation direction, reduces spatial walk-off, and enables direct access to the largest nonlinear tensor element of lithium niobate, d_{33}. These characteristics allow efficient frequency conversion across a wide spectral range spanning the visible, near-infrared, and mid-infrared regions within a single material system [69], [70]. As a result, PPLN has become the workhorse of nonlinear optics in bulk and guided-wave laser systems, while simultaneously providing a natural conceptual and technological bridge toward integrated implementations on thin-film lithium niobate platforms.

Figure 1.13 illustrates the basic structure of a periodically poled lithium niobate device, where ferroelectric domains are arranged with a fixed spatial period to enforce quasi-phase matching for a target nonlinear interaction. The same principle underlies both bulk and waveguide-based PPLN devices.

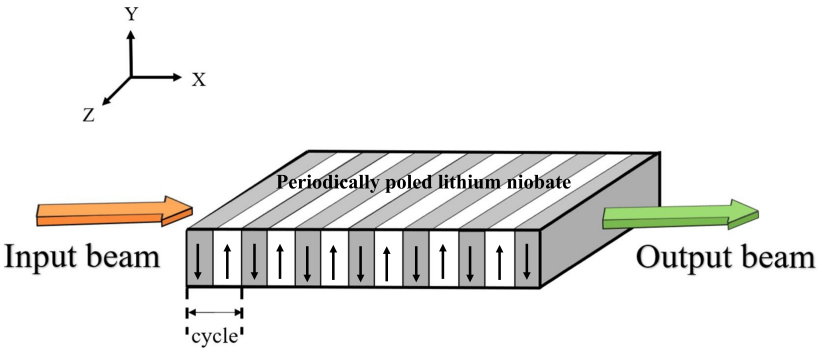


Figure 1.13: Schematic illustration of a periodically poled lithium niobate (PPLN) structure implementing quasi-phase-matching through periodic ferroelectric domain inversion [70].

The fabrication of PPLN has matured significantly over the past decades, transitioning from early high-temperature and electron-beam-based techniques to reliable room-temperature electric-field poling processes. Modern poling approaches provide high yield, accurate control of the domain duty cycle, and reproducible poling periods on the micron scale. Together with temperature tuning, the poling period offers a practical degree of freedom for precise phase-matching control. The introduction of waveguides within PPLN further increases optical intensity and modal overlap, reducing conversion

thresholds and enhancing efficiency. This technological evolution establishes a continuous pathway from bulk PPLN crystals to guided-wave and thin-film lithium niobate devices.

A practical limitation of undoped PPLN is its susceptibility to photorefractive damage under visible or near-infrared excitation, particularly at elevated optical intensities. Photorefractive effects can induce refractive-index changes, beam distortion, and long-term instability, thereby constraining the maximum usable pump power and operational reliability of nonlinear devices.

Doping lithium niobate with magnesium oxide, typically at concentrations of approximately 5 mol%, substantially increases the photorefractive damage threshold while largely preserving the high effective nonlinear coefficient. MgO-doped PPLN therefore enables stable operation at higher optical intensities and over broader wavelength ranges, often without the need for aggressive crystal heating [69], [71]. These advantages have been demonstrated in both ultrafast and continuous-wave optical parametric oscillators, where MgO:PPLN supports broadband tunability, high conversion efficiency, and watt-level output powers under demanding intracavity conditions [69], [71]. Consequently, MgO:PPLN has become the preferred material choice for high-power and broadband quasi-phase-matched nonlinear devices.

The quasi-phase-matched structure of PPLN enables efficient implementation of several second-order nonlinear processes that are directly relevant to integrated photonic systems. Among these, second-harmonic generation (SHG), sum-frequency generation (SFG), and difference-frequency generation (DFG) constitute the fundamental interaction mechanisms.

In SHG, two photons at a fundamental frequency ω are converted into a single photon at twice the frequency, 2ω. In PPLN, the use of quasi-phase matching allows SHG to exploit the d_{33} nonlinear coefficient, resulting in high conversion efficiency in both bulk and guided-wave configurations. While bulk PPLN implementations typically rely on long interaction lengths or resonant enhancement, waveguide-based and thin-film PPLN devices achieve comparable or higher normalized efficiencies through strong optical confinement. Recent demonstrations in thin-film PPLN waveguides have reported substantial pump depletion within millimeter-scale devices, confirming the suitability of integrated PPLN for compact and efficient frequency doubling [72], [73].

Sum-frequency generation extends the concept of SHG by enabling frequency conversion between two non-degenerate input waves. In PPLN, quasi-phase matching accommodates multiple interacting wavelengths while maintaining access to the largest nonlinear tensor element. Bulk PPLN systems have achieved visible-wavelength outputs across a wide spectral range using long crystals and high pump powers, whereas waveguide-based PPLN architectures provide enhanced efficiency and scalability through improved modal overlap. In integrated platforms, SFG often serves as an intermediate step in cascaded $\chi^{(2)}$ schemes, enabling broadband and modulation-format-transparent wavelength translation [73].

Difference-frequency generation produces radiation at the frequency difference of two input waves and has been widely employed for mid-infrared generation in PPLN. In addition to its role as a tunable mid-infrared source, DFG has recently been exploited as a high-fidelity wavelength-conversion mechanism when combined with SHG in cascaded configurations. Thin-film PPLN waveguides have demonstrated efficient DFG-based wavelength translation with broad conversion bandwidths and negligible signal degradation, even for advanced modulation formats, highlighting the versatility of PPLN-based $\chi^{(2)}$ processes for integrated nonlinear signal processing [72].

Figure 1.14 schematically illustrates the frequency-mixing pathways and the periodically poled domain configuration used to provide quasi-phase matching for SHG, SFG, and DFG. For each nonlinear process, the poling period Λ is selected to compensate for the corresponding phase mismatch. Accordingly, Λ_{SHG}, Λ_{SFG}, and Λ_{DFG} denote the process-specific poling periods for SHG, SFG, and DFG, respectively.

The physical principles governing quasi-phase-matched $\chi^{(2)}$ interactions in bulk PPLN directly translate to thin-film lithium niobate (TFLN) platforms. However, the transition to a thin-film geometry fundamentally enhances nonlinear interaction strength through

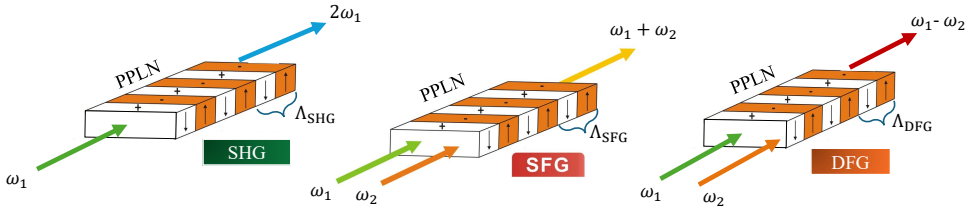


Figure 1.14: Schematic illustration of SHG, SFG, and DFG in periodically poled lithium-niobate waveguides. Periodic inversion of the ferroelectric domains with process-specific poling periods Λ_{SHG}, Λ_{SFG}, and Λ_{DFG} provides quasi-phase matching for the corresponding nonlinear frequency-conversion processes [70].

strong optical confinement, reduced mode areas, and improved modal overlap, enabling normalized conversion efficiencies that exceed those of bulk or weakly guiding waveguides by orders of magnitude.

In TFLN, phase matching can be realized not only through periodic poling but also via birefringent phase matching, modal phase matching, grating-assisted quasi-phase matching, and cyclic or natural quasi-phase matching in resonant structures. Each approach presents different trade-offs in bandwidth, nonlinear tensor utilization, and fabrication complexity [72]. Periodic poling and cyclic schemes enable access to d_{33}, while birefringent and modal phase matching may rely on reduced tensor elements depending on crystal orientation and polarization configuration.

As a consequence, TFLN ridge, ring, and disk devices provide compact, low-loss, and highly efficient nonlinear building blocks that can be co-fabricated alongside electro-optic modulators, filters, and passive routing elements. This co-integration allows PPLN-inspired SHG, SFG, and DFG sections to be placed in close proximity to components such as MMI splitters and grating-assisted add–drop filters, forming a practical foundation for fully integrated photonic transceivers and nonlinear signal-processing systems [73].

1.4 Summary

This chapter has established the system-level and technological context for the development of scalable photonic integrated circuits. The discussion highlighted how emerging requirements in bandwidth density, energy efficiency, and integration complexity impose coupled constraints on device architecture, material selection, and overall system design.

A materials-oriented perspective was adopted to analyze the complementary roles of silicon-on-insulator, silicon nitride, thin-film lithium niobate, and III–V platforms. Rather than viewing these technologies as competing solutions, the analysis emphasized their functional specialization and the increasing importance of hybrid and heterogeneous integration in addressing system-level limitations.

Within this framework, representative photonic building blocks for power distribution, wavelength-selective routing, electro-optic modulation, and nonlinear processing were reviewed, highlighting their operating principles, design trade-offs, and platform dependencies in large-scale integration.

Among these, particular emphasis is placed on multimode interference couplers and grating-assisted contra-directional devices, which form the primary focus of this thesis in addressing broadband power distribution and wavelength-selective routing.

This perspective motivates the focus of the following chapters, where MMI-based power distribution and grating-assisted wavelength-selective routing are investigated as

complementary building blocks with particular emphasis on robustness, scalability, and experimental validation.

Thesis Contributions

The main contributions of this thesis can be summarized as follows:

- A systematic design-space exploration of multimode interference (MMI) couplers on thin-film lithium niobate, including insertion loss, uniformity, and phase behavior across multiport configurations. The identification of geometry-invariant and broadband inter-port phase relations, enabling the realization of multiport combiners based on passive MMI structures.
- Experimental validation of the proposed designs, including fabrication-aware analysis and characterization under off-design wavelength conditions.
- The design and analysis of grating-assisted add–drop filters on a hybrid SiN–TFLN platform, enabling wavelength-selective routing within the same passive-design framework.

Together, these contributions establish a consistent methodology for designing robust, fabrication-tolerant passive components that address both power-domain and wavelength-domain functionalities in integrated photonic systems.

Chapter 2

Design of MMI Splitters and Combiners

2.1 Introduction

Photonic Integrated Circuits (PICs) rely on passive optical components as basic building blocks, defining how optical signals are routed, distributed, combined, and spectrally processed on chip. These elements establish the physical connectivity required for higher-level functionalities, including modulation, detection, and nonlinear processing.

Among the functionalities of PICs, three fundamental operations are considered here: optical power splitting, combining, and wavelength-selective filtering. These operations allow the internal signal flow of the PIC and play a role analogous to interconnect networks in electronic integrated circuits [74].

In particular, this chapter is devoted to the systematic design and analysis of multimode interference (MMI) devices, which serve as broadband passive components for optical power splitting and coherent combining. MMI couplers are selected due to their inherent fabrication tolerance, compactness, and weak sensitivity to wavelength variations, making them suitable for scalable photonic integration [75], [76].

Rather than providing an exhaustive survey of passive photonic devices, this chapter focuses on MMI structures as representative building blocks that allow interference-based signal manipulation. In contrast to strongly wavelength-selective devices, MMI operation is governed by geometry-driven self-imaging mechanisms, enabling broadband behavior and relaxed phase-matching requirements.

The analysis is carried out within a fabrication-aware design framework, where device performance is evaluated not only under ideal conditions but also under realistic geometrical variations. This approach enables the identification of robust design regions rather than isolated optimal configurations, consistent with scalable PIC design strategies [1], [77].

The remainder of this chapter therefore addresses the operating principles, systematic design, multiport behavior, broadband performance, and robustness of MMI couplers, including their extension from splitter to coherent combiner configurations.

This chapter investigates multimode interference (MMI) couplers as broadband passive building blocks for optical power splitting and combining on a thin-film lithium niobate (TFLN) platform.

A systematic design methodology is developed for $1 \times N$ multiport MMI splitters, based on parametric exploration of the multimode section geometry and output-port configuration. The device performance is evaluated in terms of insertion loss, uniformity of power at the output ports, and a combined figure of merit, enabling the identification of design regions rather than isolated optimal points.

Broadband analysis over the C-band demonstrates that MMI couplers maintain low insertion loss in a wide wavelength range, whereas, power uniformity becomes the primary limiting factor as the number of output ports increases. The same structures are further analyzed in the Nx1 combiner configuration, where inter-port phase relations enable coherent multiport combining using optimized phase offsets.

Finally, fabrication tolerance analysis confirms that the proposed designs exhibit gradual performance degradation under realistic variations in geometry, preserving functionality even for high N values.

2.2 Multimode Interference devices based on TFLN platform

The use of TFLN for the MMI devices considered in this chapter is motivated by the broader objective of developing passive building blocks that are directly compatible with

lithium-niobate photonic integrated circuits. Although multimode-interference couplers can also be implemented on other integrated-photonics platforms, such as silicon and silicon nitride [1], [17], [18], TFLN provides the additional advantage of combining passive waveguiding with the strong electro-optic and nonlinear properties of lithium niobate within the same integrated platform [26], [27], [28]. Therefore, the MMI structures investigated here are not intended to exploit a material-specific requirement of the self-imaging mechanism, but rather to provide broadband splitting and combining functions that can be directly integrated with active and nonlinear TFLN devices.

At the same time, the use of TFLN introduces additional fabrication constraints that must be considered during device design. In particular, the realized rib-waveguide geometry, including the etched depth and sidewall profile, directly affects the modal propagation constants and therefore the self-imaging condition. For this reason, the actual TFLN cross-section is explicitly included in the numerical model, and the sensitivity of the MMI performance to fabrication-related dimensional variations is investigated later in this chapter [28], [82].

All devices analyzed in this chapter are implemented on a thin-film lithium niobate on insulator (TFLN) also referred to as Lithium Niobate on Insulator (LNOI) platform. The material properties of the platform are treated as fixed technological parameters throughout the study.

All MMI couplers discussed in Sec. 2.3 are implemented considering a silica (SiO_2) as both the upper and lower cladding. As shown in Fig. 2.1(a), only the lower silica layer is illustrated for clarity.

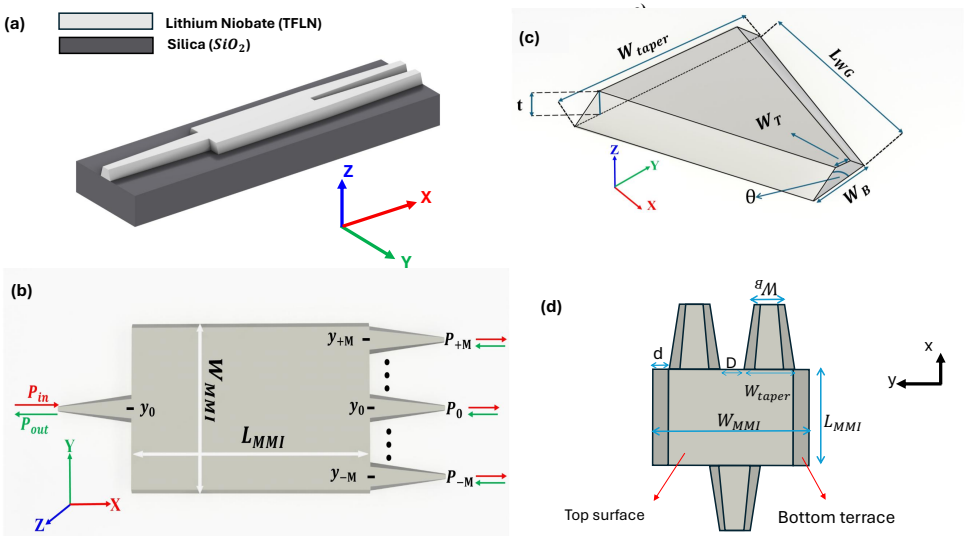


Figure 2.1: Geometrical definition of the multimode interference (MMI) coupler implemented on the TFLN platform. (a) Three-dimensional schematic of the adopted TFLN waveguide platform, showing the lithium-niobate waveguide on a silica (SiO_2) lower cladding. For clarity, only the lower silica layer is illustrated, although silica is used as both the upper and lower cladding in the numerical model. (b) Three-dimensional view of the tapered access waveguide highlighting the trapezoidal cross-section resulting from the etching process, characterized by the waveguide thickness t, bottom width W_B, top width W_T, taper length L_{WG}, and sidewall angle θ. (c) Top view of the MMI device showing the input waveguide, the multimode section of width W_{MMI} and length L_{MMI}, and the output ports symmetrically positioned with respect to the central axis. The transverse coordinates y_0 and $y_{\pm M}$ define the port locations. (d) Top-view schematic of a 1×2 MMI coupler indicating the MMI region, the output tapers, the bottom terrace, the top surface, the taper width W_{taper}, the inter-port separation D, and the offset d from the MMI edges. The coordinate system used throughout this work is also indicated.

The guiding region is defined directly within the lithium-niobate layer, while the silica cladding ensures vertical optical confinement and mechanical protection.

The thickness of the lithium-niobate film is fixed to $t = 400$ nm, consistently with commercially available TFLN wafers. Unless otherwise specified, the waveguides are modeled as fully etched structures with trapezoidal cross-sections, with finite sidewall

angles typically introduced by dry-etch fabrication processes. A nominal sidewall angle of $\theta = 70°$ is adopted, in agreement with experimentally reported values for etched LN waveguides [65].

The trapezoidal geometry is explicitly taken into account in the numerical simulations by considering the relation between the top width W_{T} and the bottom width W_{B} of the LN waveguides:

$$W_{\mathrm{B}} = W_{\mathrm{T}} + 2t \cot \theta, \tag{2.1}$$

which is used to accurately model modal confinement and effective index values in the MMI region and access waveguides. Unless otherwise specified, a top waveguide width of $W_{\mathrm{T}} = 600$ nm is considered, which ensures single-mode operation for the fundamental TE polarization.

The trapezoidal waveguide cross-section, defined by the top width W_T, bottom width W_B, thickness t, and sidewall angle θ, is illustrated in Fig. 2.1.

Material anisotropy and wavelength dispersion of lithium niobate are included in the simulations by suitably defining the permittivity tensor. As shown in Fig. 2.1, light propagates along the x-axis, while the optical axis of the TFLN layer is oriented along the y-axis. Throughout this work, the devices operate with the fundamental TE mode.

The platform parameters, i.e., the LN layer thickness t, the sidewall angle θ, and the SiO_2 cladding, are treated as fixed technological constraints and are not included as optimization variables in the MMI design process. The performance trends reported in the following sections are therefore obtained by varying only device-level geometrical parameters, namely the MMI width W_{MMI}, the MMI length L_{MMI}, and the relative positioning of the input/output access waveguides.

This choice ensures that the extracted design rules and performance trends are robust, fabrication-oriented, and directly transferable to experimentally realizable TFLN platforms.

2.3 Multimode Interference Coupler

2.3.1 Numerical Modeling and Simulation Framework

The numerical analysis of all MMI devices in this chapter is carried out using a three-dimensional finite-difference time-domain (FDTD) solver implemented in Lumerical [78].

The simulation domain which is shown in Fig. 2.2 is defined to fully encompass the multimode section and access waveguides, with perfectly matched layer (PML) boundary conditions applied along all directions to suppress artificial reflections. A mesh accuracy of 6 is adopted to accurately resolve the waveguide cross-section and modal field evolution within the TFLN platform.

For the splitter configurations, optical excitation is performed using waveguide ports, which enable direct injection of the fundamental TE guided mode at the input waveguide and simultaneous extraction of transmitted power at the output ports. The use of ports ensures proper mode normalization and allows direct computation of scattering parameters.

The optical properties of lithium niobate are modeled by importing a dispersive and anisotropic material model into the simulation environment [79]. The refractive indices are defined through Sellmeier equations, providing wavelength-dependent permittivity tensors along the principal crystal axes [79]. This approach ensures accurate representation of both material dispersion and birefringence of the LN material.

The device response is evaluated in terms of scattering parameters (S-parameters), which can be used to quantify the power transmission from the input port to each output port across the wavelength range of interest. These parameters form the basis for the extraction of insertion loss, uniformity, and phase relations discussed in subsequent sections.

For the combiner configurations, the same physical geometry used for the splitter is retained, consistent with the reciprocity of passive photonic structures. However,

the excitation scheme is modified. Instead of using ports for simultaneous multi-input excitation, multiple mode sources are employed to inject optical signals into the input waveguides with controlled amplitude and phase. Due to the limitations of simultaneous multi-port excitation in the FDTD framework, this approach allows independent phase tuning of each input signal, which is required to realize constructive interference at the combiner output. Field monitors are also used at the output waveguide to evaluate the transmitted power and phase under multi-source excitation conditions.

The combination of port-based S-parameter analysis for splitters and multi-source excitation for combiners provides a consistent and physically accurate model for analyzing both device functionalities within the same simulation environment.

To clarify the numerical modeling approach, a representative 1×8 MMI splitter is shown in the FDTD simulation setup in Fig. 2.2.

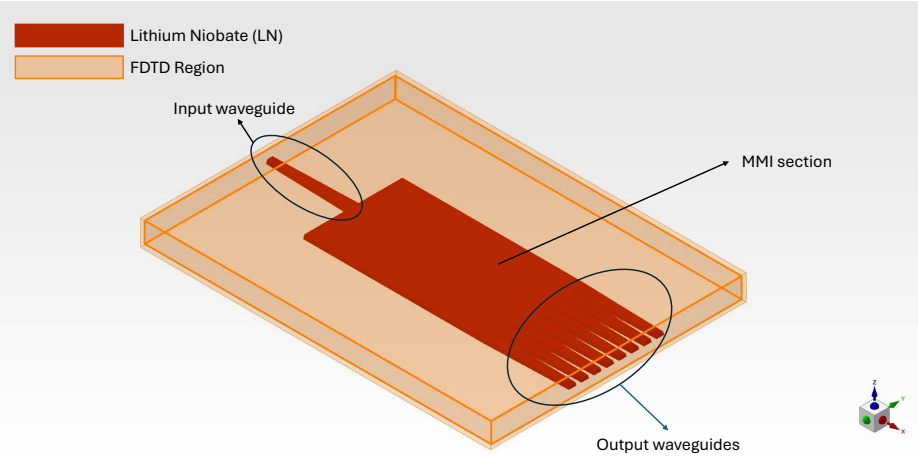


Figure 2.2: Three-dimensional view of the 1×8 MMI splitter implemented on the TFLN platform, as modeled in the FDTD simulation environment. The multimode interference region, input waveguide, and output waveguides are shown. The simulation domain (FDTD region) is also indicated, enclosing the entire device structure.

The figure highlights the geometrical definition of the device, including the input waveguide, the multimode section, and the output waveguides, as well as the simulation domain used for electromagnetic analysis. This visualization serves as a reference for the simulation results described in this section.

2.3.2 Operating Principle of Multimode Interference Couplers

Multimode interference (MMI) couplers are based on the self-imaging phenomenon in multimode waveguides, where an input field is reproduced in single or multiple replicas at specific propagation distances [75], [76]. The operation relies on the coherent interference of the guided modes supported by the multimode section.

Here, y and z denote the transverse coordinates of the multimode waveguide cross-section, while x represents the propagation direction.

An input field injected into the multimode region excites a multiple guided modes, which can be written as

$$E(0, y, z) = \sum_{l} c_l \psi_l(y, z), \tag{2.2}$$

where ψ_l are the modal field profiles and c_l are excitation coefficients, and l denotes the mode index. The propagated field is then

$$E(x, y, z) = \sum_{l} c_l \psi_l(y, z) e^{-j\beta_l x}. \tag{2.3}$$

Self-imaging requires a structured phase evolution among modes. For step-index multimode waveguides, the propagation constants follow an approximate quadratic dependence [75]:

$$\beta_l \approx \beta_0 - \alpha l(l+2), \tag{2.4}$$

This approximate quadratic dependence of the modal propagation constants is responsible for the periodic modal rephasing underlying the self-imaging phenomenon.

The parameter α is a proportionality constant determined by the waveguide geometry and modal dispersion characteristics.

Substituting the quadratic approximation into the propagated field expression gives

$$E(x,y,z) = e^{-j\beta_0 x} \sum_l c_l \psi_l(y,z) \exp\left[j\alpha l(l+2)x\right], \tag{2.5}$$

Self-imaging occurs when the relative phase evolution among the excited modes reconstructs the input-field distribution.

This behavior occurs at the so-called beat length between the two lowest-order modes:

$$L_\pi = \frac{\pi}{\beta_0 - \beta_1}. \tag{2.6}$$

The beat length represents the characteristic distance over which the relative phase difference between the two lowest-order modes accumulates to π, governing the periodic modal interference responsible for self-imaging.

2.3.2.1 Self-Imaging Conditions and Design Lengths

Using the quadratic phase relation, the general self-imaging condition is obtained when

$$x = n \cdot 3L_\pi, \quad n \in \mathbb{Z}, \tag{2.7}$$

which defines the *general interference* regime [75]. At these lengths, the input field is reproduced either as a direct or mirrored image.

For practical MMI devices, reduced imaging lengths are achieved by controlling modal excitation:

Symmetric excitation When the input is centered, only even modes are excited due to symmetry. The imaging length becomes

$$L_{\text{symmetric}} = n \cdot \frac{3}{4} L_\pi. \tag{2.8}$$

Paired excitation When the input is positioned at fractional locations (e.g., $W_{\text{MMI}}/3$; see Fig. 2.1(b)), modes are excited in correlated pairs, yielding

$$L_{\text{paired}} = n \cdot L_\pi. \tag{2.9}$$

These regimes satisfy

$$L_{\text{general}} = 3L_{\text{paired}} = 4L_{\text{symmetric}}, \tag{2.10}$$

which provides a direct scaling rule for compact device design [75].

2.3.2.2 Generalized N-Fold Imaging and 1×N Splitter Design

A key property of MMI devices is the ability to generate multiple replicas of the input field across the multimode section. The field at the imaging plane can be expressed as a superposition of shifted images [75]:

$$E(y,x) = \sum_{q=0}^{N-1} E_{\text{in}}(y - y_q), e^{j\phi_q}, \tag{2.11}$$

where y_q and ϕ_q denote the position and phase of the q-th image.

For simplicity, the generalized imaging description is commonly expressed using a reduced two-dimensional representation, where the dominant self-imaging behavior is analyzed in the lateral transverse direction y and along the propagation direction x. The vertical field confinement is assumed to remain approximately unchanged.

From the general self-imaging theory, N-fold images occur for device lengths given by

$$L = \frac{3L_\pi}{N}, \tag{2.12}$$

or more generally

$$L = \frac{M}{N} \cdot 3L_\pi, \quad M, N \in \mathbb{Z}, \tag{2.13}$$

where N corresponds to the number of images (i.e., output ports) [75].

This relation directly provides the design rule for a $1 \times N$ splitter. Therefore, the design of a $1 \times N$ splitter typically involves selecting the desired number of output ports N, choosing the minimum imaging order $M = 1$ for compact operation, and determining the corresponding multimode-section length from the self-imaging relation.

This formulation also explains why increasing N requires shorter imaging periods but wider multimode sections capable of supporting a larger number of guided lateral modes.

A larger number of output images requires the excitation and controlled interference of a larger modal set. Consequently, the multimode section width must generally increase to support the required number of guided modes for stable image formation.

2.3.2.3 Physical Interpretation of Self-Imaging

The self-imaging mechanism can be interpreted physically as a distributed interference process. After injection into the multimode section, the optical field expands laterally and excites multiple guided modes. Each mode accumulates phase according to its propagation constant, resulting in an evolving interference pattern along the propagation direction.

At specific propagation distances, the relative phase evolution among the excited modes reconstructs the input-field distribution through constructive interference. Unlike directional couplers, where power transfer is primarily governed by local evanescent coupling between adjacent waveguides, MMI devices rely on the collective interference of multiple guided modes across the entire multimode section.

As a result, MMI devices generally exhibit improved tolerance to wavelength variations and fabrication imperfections compared to phase-sensitive coupling structures. In addition, their operation does not require the strict phase-matching conditions typically associated with directional couplers, contributing to broadband and fabrication-robust performance.

These characteristics make MMI couplers particularly attractive for broadband integrated photonic applications requiring compactness, relaxed fabrication tolerances, and stable power splitting behavior over a wide wavelength range.

The self-imaging behavior of MMI devices is strongly influenced by the waveguide geometry, operating wavelength, and refractive-index contrast. In general, increasing the width of the multimode section allows a larger number of guided modes to participate in the interference process, enabling multiport image formation. However, wider multimode sections also lead to longer imaging lengths and larger device footprints.

The operating wavelength similarly affects the modal phase evolution and the corresponding self-imaging distance. Shorter wavelengths generally reduce the required imaging length, whereas longer wavelengths increase the overall interference period.

In high-index-contrast integrated photonic platforms, stronger optical confinement enables more compact MMI structures while maintaining efficient modal interference. These scaling trends provide important physical intuition for the practical device optimization strategies discussed in the following sections.

2.3.3 Design Parameters and Figures of Merit

The performance of multimode interference (MMI) couplers is governed by a limited set of geometrical and modal parameters, which jointly determine imaging quality, insertion loss, wavelength stability of the relative phase, and robustness. Although the self-imaging principle provides a clear theoretical foundation, practical MMI design requires explicit geometrical rules to translate the underlying interference mechanism into reproducible and fabrication-aware layouts.

2.3.3.1 Geometrical Design Parameters

The width of the multimode section, W_{MMI}, represents a primary design parameter, as it directly controls the number of guided modes supported by the multimode region and, consequently, the structure of the interference pattern. Increasing W_{MMI} enables a higher modal capacity, which is beneficial for multiport configurations and power uniformity. However, wider multimode sections result in larger footprints and may increase sensitivity to fabrication-induced width variations [80]. Conversely, reducing W_{MMI} improves compactness but limits the number of achievable output ports and may degrade imaging fidelity.

The length of the multimode section, L_{MMI}, is selected to satisfy the self-imaging condition associated with the chosen interference regime. Small deviations from the nominal imaging length lead to incomplete field reconstruction at the output plane, resulting in excess insertion loss, output imbalance, and phase errors among the ports. For this reason, L_{MMI} is treated as a critical parameter during both layout optimization and tolerance analysis.

Access waveguides and their associated taper sections play a key role in controlling modal excitation at the entrance of the multimode region. The taper geometry influences the excitation coefficients of the supported modes and can be exploited to suppress unwanted higher-order or vertically confined modes, particularly in high-index-contrast platforms [81]. Proper taper design therefore improves imaging fidelity and reduces insertion loss without modifying the multimode section itself.

In multiport MMI devices, the lateral placement of the output waveguides constitutes an additional geometrical degree of freedom, as it determines how the self-imaged field is sampled at the output plane. Throughout this work, the parameter D denotes the spacing between adjacent output ports at the interface with the multimode section, while the parameter d represents the distance between the outermost output ports and the lateral boundaries of the multimode region (Fig. 2.1).

To preserve symmetry and ensure balanced optical paths, the output ports are positioned symmetrically with respect to the centerline of the multimode section. For an odd number of ports ($N = 2M + 1$), one output waveguide is placed on the centerline of the MMI region, while the remaining ports are located in symmetric pairs. For an even number of ports ($N = 2M$), no waveguide is placed at the center, and all output ports are arranged symmetrically around the centerline.

Following the design rule adopted in the associated MMI study and used consistently throughout this thesis, the multimode width W_{MMI} is conceptually divided into N equal lateral regions. The center of each region is used as the nominal center position of the corresponding output port. Accordingly, the transverse coordinates y_n of the port centers are defined as

$$y_n = \begin{cases} \frac{n.W_{MMI}}{2\mathrm{M}+1} & n = 0, \pm 1, .., \pm \mathrm{M} \quad \text{for} \quad \mathrm{N} = 2\mathrm{M}+1 \\ \frac{(2n \mp 1).W_{MMI}}{4.\mathrm{M}} & n = \pm 1, .., \pm \mathrm{M} \quad \text{for} \quad \mathrm{N} = 2\mathrm{M} \end{cases} \tag{2.14}$$

where N denotes the total number of output ports. This formulation ensures uniform sampling of the self-imaged field, preserves symmetry, and yields predictable amplitude and phase relations at the output plane.

In addition to the analytical port-positioning rule written above, practical layout constraints are enforced to guarantee fabrication robustness. In particular, the lateral spacing parameters D and d are not treated as independent quantities. In this work, a simple geometrical constraint is imposed by design, namely

$$D = \frac{d}{2}, \tag{2.15}$$

which ensures sufficient clearance between the outermost output ports and the multimode sidewalls while maintaining compact port packing. This relation represents a layout choice adopted consistently throughout the thesis to enforce symmetry and edge clearance, rather than a universal design rule.

The combined use of the analytical port-placement formulation and the constraint imposed on D and d provides a systematic and scalable definition of the output geometry across different ports. This approach avoids ad-hoc port positioning and enables consistent exploration of the MMI design space while preserving imaging quality, phase accuracy, and fabrication tolerance.

2.3.3.2 Figures of Merit

The performance of multimode interference (MMI) couplers in this work is assessed using a set of figures of merit (FoMs) that quantify optical efficiency, output balance, phase accuracy, and robustness. These metrics are defined once in this subsection and are subsequently used throughout the chapter to evaluate and compare different MMI configurations across wavelength and under geometrical variations.

Total transmittance. Let $T_n(\lambda)$ denote the optical transmittance from the input port to the n-th output port at wavelength λ. The total transmitted power is defined as the sum of the individual port transmittances,

$$T_{\mathrm{tot}}(\lambda) = \sum_{n=1}^{N} T_n(\lambda), \tag{2.16}$$

where N is the total number of output ports.

Insertion loss (IL). Insertion loss is used as the primary efficiency metric and is defined in terms of the total transmittance as

$$\mathrm{IL}(\lambda) = -10 \log_{10} \left[T_{\mathrm{tot}}(\lambda) \right]. \tag{2.17}$$

When broadband performance is considered, the worst-case insertion loss over the wavelength range of interest is employed,

$$\mathrm{IL}_{\mathrm{max}} = \max_{\lambda} \mathrm{IL}(\lambda), \tag{2.18}$$

ensuring conservative evaluation of the device performance.

Uniformity (UF). Power uniformity among the output ports is quantified by the ratio between the maximum and minimum transmittances,

$$\mathrm{UF}(\lambda) = 10 \log_{10} \left(\frac{\max\limits_{n} T_n(\lambda)}{\min\limits_{n} T_n(\lambda)} \right). \tag{2.19}$$

A lower UF value (i.e., closer to 0 dB) indicates a more balanced power distribution across the output ports.

For broadband analysis, the maximum value of $\mathrm{UF}(\lambda)$ over the investigated wavelength range is considered, since it represents the worst-case output imbalance across the operating band. This criterion provides a more stringent assessment of broadband transmittance uniformity across the ports than average spectral values alone.

Performance factor (PF). To jointly capture the trade-off between low insertion loss and high output uniformity, a combined performance indicator, referred to as the performance factor (PF), is defined as

$$\mathrm{PF}(\lambda) = \log_{10}\left(\frac{10^{-\mathrm{IL}(\lambda)/10}}{10^{\mathrm{UF}(\lambda)/10}}\right). \tag{2.20}$$

This quantity provides a compact design-level metric for ranking alternative MMI configurations under identical operating conditions. PF is not introduced as a universal figure of merit, but rather as a convenient internal indicator used consistently throughout this work.

Phase relations and phase stability. In addition to amplitude-related metrics, the relative phase relationships between output ports are analyzed. Let $\phi_n(\lambda)$ denote the optical phase at the n-th output port. The relative phase difference between ports i and j is defined as

$$\Delta\phi_{i,j}(\lambda) = \phi_i(\lambda) - \phi_j(\lambda). \tag{2.21}$$

To quantify wavelength-dependent phase stability, the phase variation range is introduced as

$$\sigma_{\Delta\phi_{i,j}} = \max_{\lambda} \Delta\phi_{i,j}(\lambda) - \min_{\lambda} \Delta\phi_{i,j}(\lambda), \tag{2.22}$$

evaluated over the wavelength interval of interest. Smaller values of $r_{\Delta\phi_{i,j}}$ indicate more stable relative phase behavior.

Footprint and fabrication tolerance. Finally, device footprint and fabrication tolerance are treated as higher-level figures of merit. The footprint is primarily determined by the multimode section length and the access regions, and reflects the trade-off between compactness and robustness. Fabrication tolerance is assessed by monitoring the sensitivity of IL, UF, and phase-related metrics to variations in critical geometrical parameters, such as MMI width, thickness, and sidewall angle.

2.3.4 Broadband Performance and Robustness

One of the main reasons for the widespread adoption of multimode interference (MMI) couplers in photonic integrated circuits is their inherently broadband operation and high tolerance to geometrical variations. Unlike directional couplers, whose power splitting ratio relies on phase-matched evanescent coupling over a well-defined interaction length, MMI devices exploit self-imaging in a multimode waveguide, resulting in reduced sensitivity to wavelength detuning and fabrication-induced parameter deviations.

The broadband behavior of MMI couplers is primarily reflected in the spectral flatness of the figures of merit defined in Sec. 2.3.3.2. Because self-imaging arises from the collective interference of multiple guided modes, moderate changes in wavelength do not significantly perturb the relative modal phase accumulation. As a result, both the total insertion loss $\mathrm{IL}(\lambda)$ and the output power uniformity $\mathrm{UF}(\lambda)$ exhibit weak wavelength dependence around the design point.

In this work, broadband performance is evaluated through wavelength sweeps over the C-band, typically spanning from 1.5 to 1.6 µm. The analysis focuses on the worst-case insertion loss $\mathrm{IL}_{\max}$ and the maximum uniformity deviation within the considered spectral range. The results presented in this chapter, which have also been published in [82], demonstrate that optimized MMI configurations maintain low $\mathrm{IL}_{\max}$ and limited wavelength-dependent imbalance even as the number of output ports increases. This behavior contrasts with directional couplers, where the splitting ratio and excess loss are strongly affected by wavelength detuning from the nominal phase-matching condition [43].

Beyond spectral behavior, robustness against fabrication imperfections represents a key advantage of MMI-based architectures. Geometrical variations, such as deviations

in the multimode section width or thickness, primarily shift the longitudinal position of the self-imaging planes rather than suppressing the interference mechanism itself. Consequently, performance degradation manifests as gradual increases in insertion loss and output imbalance, rather than abrupt failure of the splitting functionality.

Numerical tolerance analyses presented in [82] indicate that realistic variations in the multimode width and core thickness introduce limited changes in $\mathrm{IL}(\lambda)$ over the operational wavelength range. Power uniformity is found to be more sensitive at the spectral edges, while remaining relatively stable near the central operating wavelength. This behavior highlights the intrinsic robustness of the self-imaging mechanism and contrasts with the strong dimensional sensitivity typically observed in evanescently coupled structures.

Additional robustness considerations concern the spacing between output waveguides and the geometry of the access regions. While these parameters influence modal excitation and field sampling at the output plane, their impact on broadband performance is generally secondary, provided that symmetry and sufficient separation are preserved. Overall, the results confirm that MMI-based splitters offer a favorable trade-off between compactness, broadband operation, and fabrication tolerance.

As it will be detailed in the following, these properties establish MMI couplers as a robust and scalable alternative to directional couplers for multiport power distribution in broadband photonic integrated circuits.

2.3.5 Multiport MMI Splitters and Combiners

While 1×2 MMI couplers represent the most basic realization of the self-imaging principle, many practical photonic integrated circuits require power distribution and recombination across multiple ports. Extending MMI operation to multiport configurations introduces additional architectural constraints that go beyond simple length scaling and require careful control of geometry, symmetry, and phase relationships.

The 1×2 MMI coupler represents the simplest practical realization of the self-imaging principle, where a single input field is reproduced as two symmetric replicas at a specific propagation distance. While this configuration already illustrates the robustness and broadband nature of multimode interference, many integrated photonic systems require power distribution and recombination across a larger number of ports. Extending MMI operation to multiport architectures therefore constitutes a natural and important generalization of the fundamental 1×2 case.

From a conceptual standpoint, the extension from 1×2 to $1 \times N$ and more general $N \times M$ MMI devices does not rely on introducing new physical mechanisms. Instead, it is achieved by exploiting higher-order self-imaging conditions in wider multimode waveguides that support a larger number of guided modes. In this context, multiport operation can be interpreted as the formation of an N-fold transverse image of the input field, which is subsequently sampled by appropriately positioned access waveguides at the output plane.

As the number of output ports increases, two fundamental requirements emerge. First, the multimode section must provide a sufficient number of modes to sustain the formation of well-defined multiple self-images with minimal distortion. Second, the lateral symmetry of both the multimode region and the output port placement must be preserved in order to ensure balanced optical paths and predictable relative phase relationships. These constraints highlight that multiport MMI design is not obtained by simple scaling of the 1×2 geometry, but requires coordinated control of width, length, and output waveguide positions.

In practical terms, the design objective of a multiport MMI splitter is to identify a multimode waveguide geometry that simultaneously enables low excess loss, uniform power distribution among the output ports, and controlled phase behavior across the generated self-images.

While analytical self-imaging theory provides guidance on the existence and periodicity of such imaging conditions, it does not uniquely determine a fabrication-ready device layout. Consequently, the transition from conceptual self-imaging to practical multiport MMI splitters necessitates parametric exploration of the geometrical design space.

The same conceptual framework also applies to MMI combiners, where multiple input signals are coherently recombined into a smaller number of output ports. In this case, reciprocity ensures that the self-imaging-based design principles remain valid, provided that symmetry and suitable input phase conditions are satisfied. As a result, splitter and combiner functionalities can be treated within a unified multiport MMI architecture, differing primarily in the excitation conditions rather than in the underlying physical mechanism.

2.3.5.1 Design Space Exploration and Scaling Trends

To identify suitable geometries for multiport $1 \times N$ MMI splitters, a systematic exploration of the multimode-section design space was carried out by varying the multimode width W_{MMI} and length L_{MMI} (see Fig. 2.1(b)). For each $1 \times N$ configuration, with N ranging from 2 to 8, the investigated width interval was selected according to

$$2N\ \mu\mathrm{m} \leq W_{\mathrm{MMI}} \leq 4.5N\ \mu\mathrm{m}.$$

This N-dependent range was chosen to provide, for each splitting order, a sufficiently wide multimode region to support the modal content required for the formation of the corresponding N-fold self-image, while avoiding unnecessarily large multimode sections.

Once the W_{MMI} range was defined for each configuration, L_{MMI} was swept from 10 to 500 μm for each considered width. This longitudinal sweep was used to identify the propagation lengths for which multimode interference resulted in efficient power transfer to the output waveguides for each $1 \times N$ configuration. In this way, suitable L_{MMI} values were determined numerically for the different investigated widths rather than being fixed a priori.

For each investigated $(W_{\mathrm{MMI}}, L_{\mathrm{MMI}})$ combination, the insertion loss (IL), defined in eq. 2.17, was evaluated at the design wavelength $\lambda = 1.55$ μm using 3D FDTD simulations, resulting in the two-dimensional IL maps shown in Fig. 2.3 for $1 \times N$ MMI splitters with $N = 2$ to 8.

Rather than exhibiting isolated optimum points, the IL maps exhibit extended low-loss bands across the $(W_{\mathrm{MMI}}, L_{\mathrm{MMI}})$ design space. These bands identify combinations of multimode width and propagation length for which the multimode interference pattern is reconstructed efficiently at the output plane and a large fraction of the injected optical power is transferred to the output waveguides.

For the symmetric $1 \times N$ structures considered here, the multimode section and output-port arrangement are symmetric with respect to the propagation axis, and the fundamental input mode is injected along the center of the device. Consequently, geometrically symmetric output ports exhibit equal transmittance. Around the appropriate self-imaging conditions, this symmetry, together with the formation of the required N-fold image, also leads to an approximately balanced distribution of power among the output channels. Accordingly, the regions with IL approaching 0 dB largely correspond to the well-balanced operating regions subsequently identified through the uniformity analysis.

It should nevertheless be noted that insertion loss and uniformity quantify different aspects of device performance. According to eq. 2.17, IL depends on the total transmitted power collected by all output ports, whereas UF explicitly quantifies the difference between the individual output-port transmittances. Therefore, an increase in IL does not necessarily correspond to an equal reduction of power at all output ports. Although mirror-symmetric port pairs remain equally excited because of the structural symmetry, different symmetric pairs, or the central port in odd-N configurations, may carry different power levels when the device operates away from the optimum self-imaging condition.

The extended low-loss bands therefore represent families of geometries providing efficient multimode interference rather than isolated design points. From a practical perspective, this provides flexibility in selecting geometries within the low-loss regions and reduces the need to operate at a sharply defined combination of W_{MMI} and L_{MMI}.

As the number of output ports increases, the low-loss regions systematically shift toward larger multimode widths and longer interaction lengths. This trend reflects the

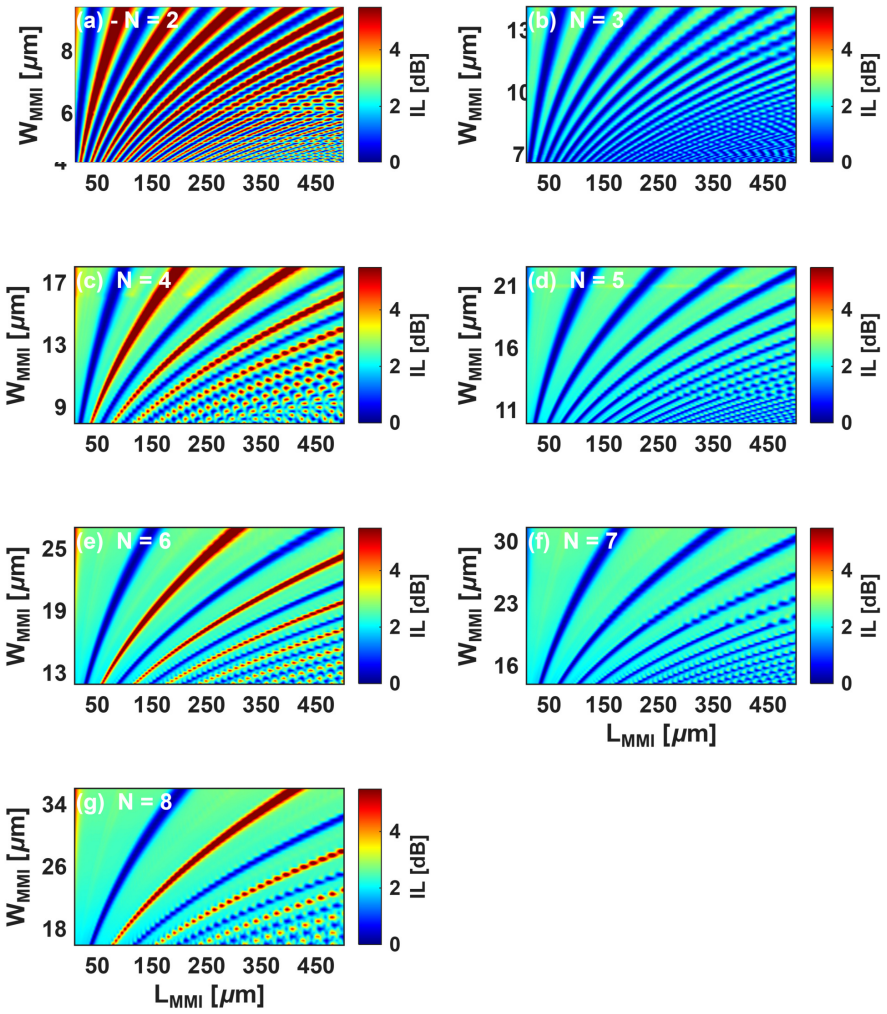


Figure 2.3: Insertion-loss (IL) maps at $\lambda = 1.55$ μm as a function of the multimode-section width W_{MMI} and length L_{MMI} for different $1 \times N$ MMI splitter configurations: (a) 1×2, (b) 1×3, (c) 1×4, (d) 1×5, (e) 1×6, (f) 1×7, and (g) 1×8. For each configuration, W_{MMI} is explored over the N-dependent interval $2N$–$4.5N$ μm, while L_{MMI} is swept over the corresponding range covering the relevant self-imaging lengths. Lower IL values indicate geometries providing higher total power transmission through the MMI section.

increased modes required to support higher-order multiport self-images with acceptable fidelity. Consequently, increasing the splitting ratio in MMI splitters inherently involves a trade-off between device footprint and the achievable number of output ports.

Based on the insertion-loss maps of Fig. 2.3, representative combinations of W_{MMI} and L_{MMI} were selected for each port configuration. Combinations near the center of the low-loss bands were preferred over those close to the band edges, thereby providing greater tolerance to fabrication-induced dimensional variations.

Starting from these selected MMI dimensions, additional optimization of the access tapers was subsequently performed while keeping the main multimode-section dimensions approximately unchanged.

Considering the different $1 \times N$ configurations analyzed in Fig. 2.3, the existence of extended low-loss regions enables scaling to higher N values while maintaining acceptable

insertion loss, provided that increases in footprint are acceptable.

A further distinction can be observed between configurations with odd and even values of N. This difference is reflected in the insertion-loss maps of Fig. 2.3, where odd-N configurations generally exhibit lower insertion loss over a wider portion of the design space, including regions away from the optimum geometries. Conversely, configurations with even values of N show larger variations in insertion loss under off-design conditions.

From a physical perspective, this behavior originates from the position of the output waveguides with respect to the self-imaged field at the output plane. The presence of a centrally aligned port in odd-N devices provides a direct coupling pathway that partially preserves transmission even under imperfect imaging, whereas even-N devices rely entirely on symmetric field redistribution among multiple ports.

It is important to emphasize that this effect does not alter the optimal insertion-loss values, which remain close to zero for both even and odd configurations, but rather influences the IL value under non-ideal geometrical conditions.

2.3.5.2 Field Evolution and Physical Interpretation

To complement the quantitative design-space exploration presented in the previous subsection, the electromagnetic field evolution of selected multiport MMI splitters is examined in this section. The objective here is not to optimize device dimensions, but rather to provide physical intuition on how the self-imaging mechanism adapts as the number of output ports increases.

Figure 2.4 shows the normalized steady-state electric field intensity distributions inside representative $1 \times N$ MMI splitters, with N ranging from 2 to 8. The geometries shown in this figure correspond to reference designs selected from the low-loss regions identified in the $(W_{\mathrm{MMI}}, L_{\mathrm{MMI}})$ maps, and are therefore representative of efficient multiport operation. The corresponding $(W_{\mathrm{MMI}}, L_{\mathrm{MMI}})$ values for the representative geometries are listed in Table 2.1.

Table 2.1: Representative values of W_{MMI} and L_{MMI} selected from the low-loss regions of the $(W_{\mathrm{MMI}}, L_{\mathrm{MMI}})$ maps for the $1 \times N$ MMI splitters shown in Fig. 2.4.

N	W_{MMI} [μm]	L_{MMI} [μm]
2	4	9.6
3	9	32.6
4	13	51.6
5	15	55.8
6	18	67.3
7	21	78.7
8	24	90.1

Starting from the fundamental 1×2 configuration, the self-imaging process leads to the formation of two symmetric field-intensity lobes at the output imaging plane.

As the number of output ports increases, the interference pattern inside the multimode section becomes progressively richer, reflecting the participation of a larger number of guided modes. Despite this increased modal complexity, the self-imaging process remains clearly identifiable, leading to the formation of well-separated intensity lobes at the output plane.

The emergence of these multi-lobed field profiles provides direct physical insight into the scalability of MMI-based splitters. A higher number of output ports can be considered thanks to the redistribution of the optical signal due to multimode interference.

It is important to emphasize that, at this stage, the field distributions are used for a qualitative analysis. Although the formation of clearly separated self-images indicates efficient multimode interference and field reconstruction, it does not by itself guarantee uniform power distribution among the output ports. In particular, small variations in

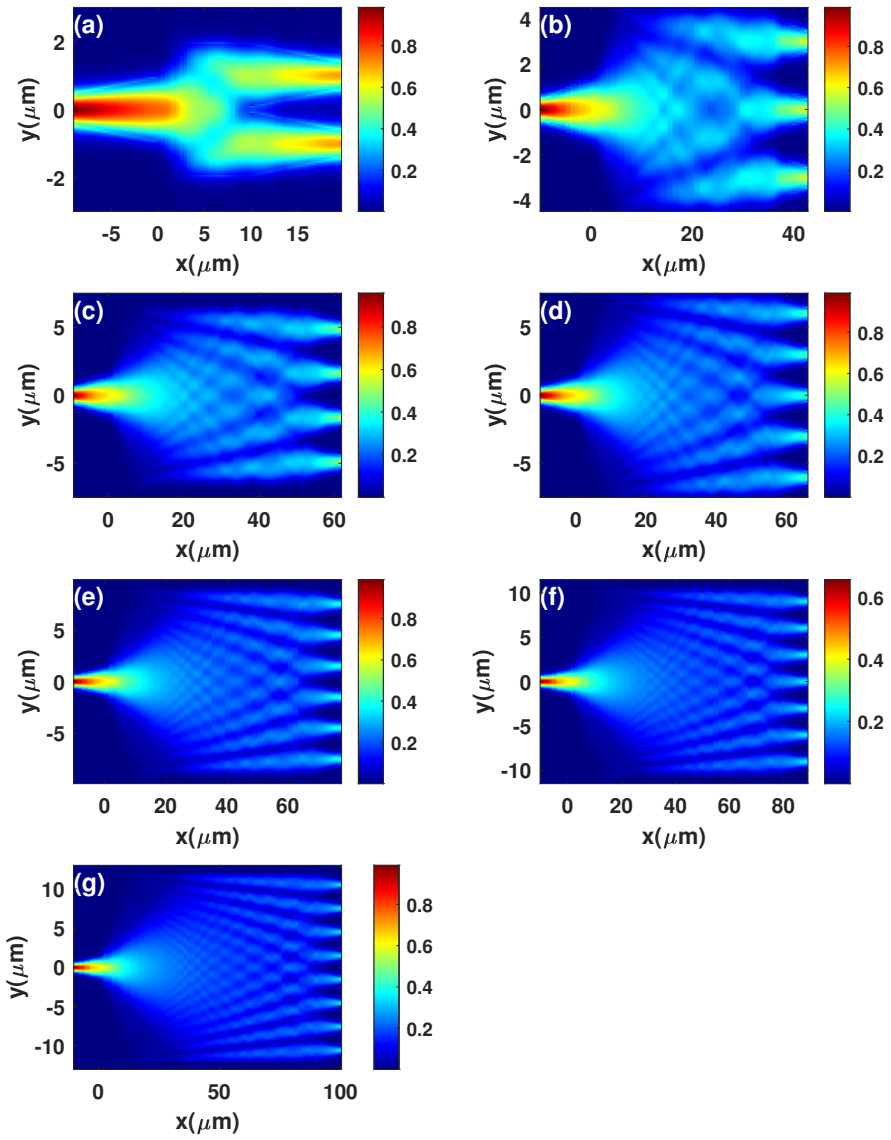


Figure 2.4: Normalized electric field intensity distributions inside optimized $1\times N$ MMI splitters, illustrating the scaling of the self-imaging phenomenon with increasing number of output ports. Subfigure (a) shows the fundamental 1×2 MMI configuration, serving as a reference case. Subfigures (b)–(g) correspond to multiport MMI splitters with N increasing from 3 to 8, respectively. At this stage, the figures are used to provide a qualitative visualization of the internal field evolution and N-fold self-image formation, while detailed geometrical parameters and quantitative performance metrics are discussed subsequently.

the intensity distribution and field profile, which may not be immediately evident from qualitative field plots alone, can still produce measurable output imbalance.

For this reason, a quantitative assessment of output balance requires explicit evaluation of the transmittance uniformity figure of merit. Accordingly, the next subsection analyzes the output power uniformity using uniformity (UF) maps, which quantitatively assess how the optical power is distributed among the output waveguides for different MMI geometries in the center wavelength 1550 nm .

2.3.5.3 Uniformity Analysis at the Design Wavelength

Following the insertion-loss-based design-space exploration, the uniformity of power distribution among the output ports was investigated as an additional figure of merit. Uniformity (UF), as defined in eq. 2.19, provides a quantitative measure of how the optical power is distributed across the output waveguides and is particularly relevant for multiport MMI splitters, where imbalance can accumulate in cascaded architectures.

The uniformity analysis was performed at the design wavelength $\lambda = 1.55$ μm for $1 \times N$ MMI splitters with N ranging from 3 to 8. The 1×2 configuration was excluded from this analysis, as its intrinsic mirror symmetry enforces equal power splitting by construction, resulting in UF= 0 dB.

Figure 2.5 reports the uniformity maps as a function of the multimode section width W_{MMI} and length L_{MMI} for each of the considered $1 \times N$ configurations. Regions of low

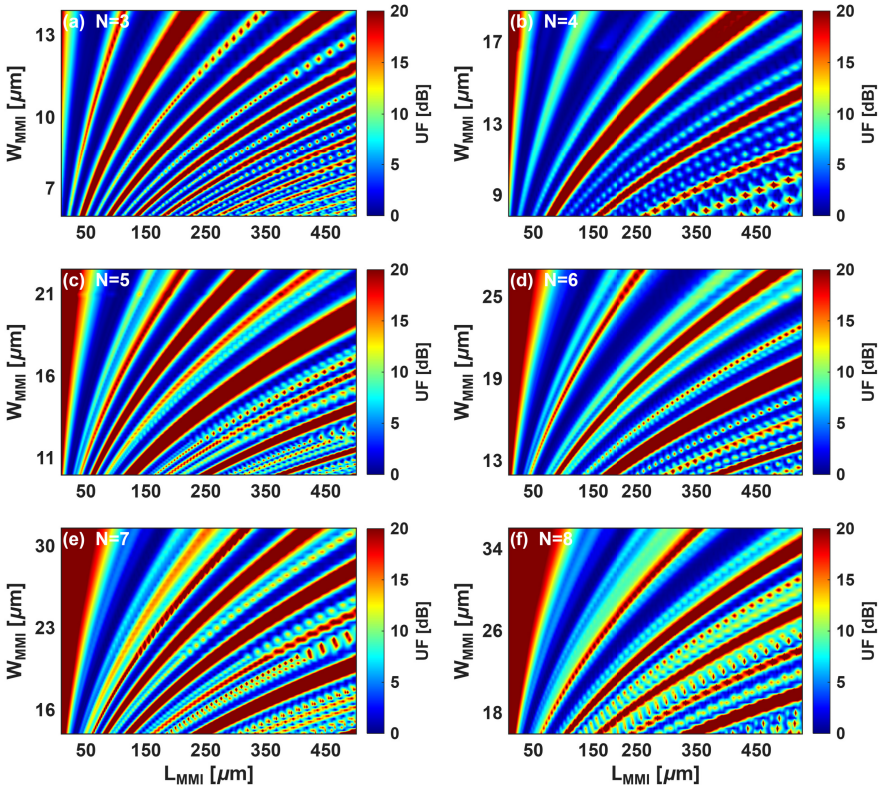


Figure 2.5: Uniformity (UF) maps at $\lambda = 1.55$ μm as a function of the multimode-section width W_{MMI} and length L_{MMI} for: (a) 1×3 ($N = 3$), (b) 1×4 ($N = 4$), (c) 1×5 ($N = 5$), (d) 1×6 ($N = 6$), (e) 1×7 ($N = 7$), and (f) 1×8 ($N = 8$). Lower UF values, approaching 0 dB, indicate a more uniform distribution of transmitted power among the output ports.

UF correspond to geometries where the self-imaged field is sampled symmetrically and with comparable intensity across all output ports.

Similar to the insertion-loss, the UF maps do not exhibit isolated optimal points, but rather extended regions in the $(W_{\mathrm{MMI}}, L_{\mathrm{MMI}})$ plane where highly uniform power distribution is achieved. These regions indicate that uniformity, like insertion loss, is achieved by families of geometries rather than by sharply defined optima.

A key observation is the partial overlap between the low-uniformity regions shown in Fig. 2.5 and the low-insertion-loss bands of Fig. 2.3. For example, in the 1×3 and 1×4 configurations (Figs. 2.5(a,b) and Figs. 2.3(b,c)), the regions of minimum UF largely

coincide with the low-insertion-loss bands, indicating that low IL and low UF can be achieved simultaneously over the same range of $(W_{\mathrm{MMI}}, L_{\mathrm{MMI}})$ values.

This overlap exhibits that, within certain areas of the design space, both efficiency and output balance can be simultaneously optimized. This behavior indicates that minimizing insertion loss alone is not sufficient for optimal MMI design, since low-loss geometries do not always provide the most uniform output power distribution.

At this stage, the analysis is intentionally restricted to the design operating wavelength. The purpose of this subsection is therefore not to establish broadband uniformity, but to identify candidate geometries that provide a favorable balance between insertion loss and power uniformity under reference conditions. While strict uniformity at the design wavelength does not guarantee optimal broadband behavior,it identifies initial efficient designs that can be further optimized considering their wavelength behaviour.

These candidate geometries form the basis for the subsequent combined performance analysis, where insertion loss and uniformity are jointly evaluated using a composite figure of merit, as detailed in the following subsection. This approach enables the identification of designs that maintain a robust balance between efficiency and uniformity in a broad wavelength range.

2.3.5.4 Combined Performance Factor at the Design Wavelength

To jointly assess insertion loss and output power uniformity within a single design-oriented metric, the performance factor (PF) defined in eq. 2.20 was evaluated across the $(W_{\mathrm{MMI}}, L_{\mathrm{MMI}})$ design space. PF provides a compact representation of the trade-off between insertion loss and uniformity, and is therefore particularly suitable for comparing multiport MMI configurations. PF ranges from 0 to 1, where higher values indicate better overall performance, corresponding to lower insertion loss and higher transmittance uniformity.

Figure 2.6 reports the PF maps as a function of the multimode section width W_{MMI} and length L_{MMI} at the design wavelength $\lambda = 1.55$ μm for $1 \times N$ MMI splitters with N ranging from 2 to 8.

For each $1 \times N$ configuration, PF is computed from the corresponding insertion loss and uniformity values obtained in the previous analyses, enabling a direct visualization of the combined performance.

A distinctive behavior is observed for the 1×2 configuration. Due to the intrinsic mirror symmetry of the device and the port-placement rules adopted in this work, the output power uniformity is identically zero by construction. As a result, the PF map for $N = 2$ effectively reduces to an insertion-loss-dominated function, leading to a comparatively larger number of geometries exhibiting high PF values. This behavior reflects the reduced design constraints in the two-port case, where IL alone governs the overall performance.

As the number of output ports increases, the PF maps exhibit a progressive reduction in the extent of high-performance regions. For $N \geq 3$, PF is jointly influenced by insertion loss and uniformity, resulting in more selective optimal regions within the design space. In particular, high-PF regions correspond to parameter regions where the low-insertion-loss regions in the IL maps largely coincide with the high-uniformity regions (low UF values) in the corresponding UF maps, demonstrating that high PF can only be achieved when both insertion loss and uniformity are simultaneously optimized.

The comparison across different $1 \times N$ configurations shows a clear scalability trend. While configurations with a lower number of ports admit a broader range of multimode widths and lengths with high PF, the design space progressively narrows as the number of output ports increases, leaving fewer geometries that simultaneously satisfy the IL and UF requirements. This behavior reflects the increasing sensitivity of power splitting to the relative position of the output waveguides with respect to the self-images formed inside the multimode region, making accurate image sampling more critical as the number of output ports increases.

The PF analysis at the design wavelength provides reference geometries for the subsequent investigation of output-port spacing and broadband performance.

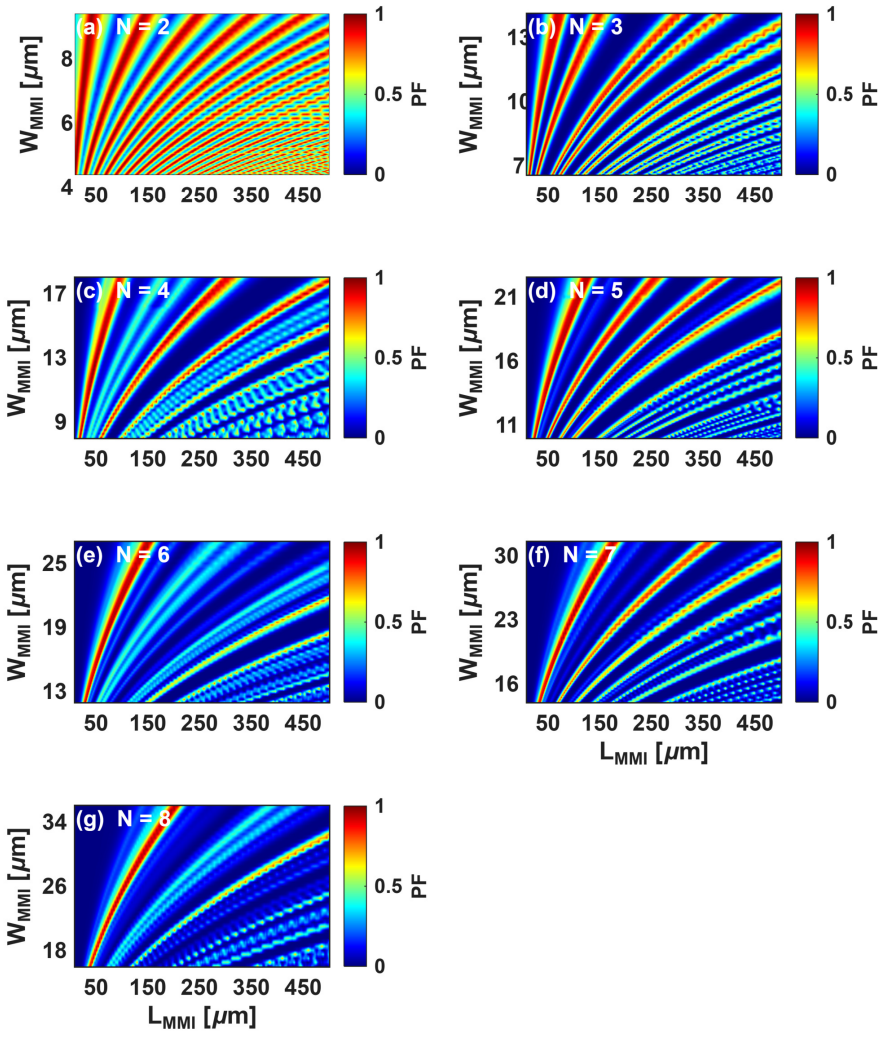


Figure 2.6: Performance-factor (PF) maps at $\lambda = 1.55$ μm as a function of the multimode-section width W_{MMI} and length L_{MMI} for: (a) 1×2 ($N = 2$), (b) 1×3 ($N = 3$), (c) 1×4 ($N = 4$), (d) 1×5 ($N = 5$), (e) 1×6 ($N = 6$), (f) 1×7 ($N = 7$), and (g) 1×8 ($N = 8$). The PF jointly accounts for insertion loss and output-power uniformity and is used to identify regions of the $(W_{\mathrm{MMI}}, L_{\mathrm{MMI}})$ design space providing the best combined performance.

2.3.5.5 Effect of Inter-Taper Gap and Output Taper Geometry

Following the $(W_{\mathrm{MMI}}, L_{\mathrm{MMI}})$ design-space analysis, the output taper geometry was further refined at the design wavelength $\lambda = 1.55$ μm. For each $1 \times N$ configuration, six candidate multimode widths were considered, ranging from $W_{\mathrm{MMI}} = 2N$ μm to $W_{\mathrm{MMI}} = 4.5N$ μm in steps of $0.5N$ μm. For each value of W_{MMI}, the corresponding L_{MMI} had already been selected from the preceding $(W_{\mathrm{MMI}}, L_{\mathrm{MMI}})$ design-space analysis. Therefore, during the present refinement step, each selected $(W_{\mathrm{MMI}}, L_{\mathrm{MMI}})$ pair was kept fixed while only the output taper geometry was varied. For clarity, these six reference geometries are denoted G1–G6 and are summarized in Table 2.2 for each value of N. Each table entry reports the corresponding $(W_{\mathrm{MMI}}, L_{\mathrm{MMI}})$ pair in μm. The same geometry labels are used consistently in the subsequent output-taper and broadband analyses to avoid repeatedly reporting the same geometrical parameters.

Table 2.2: Reference $(W_{\mathrm{MMI}}, L_{\mathrm{MMI}})$ geometries used in the output-taper optimization and subsequent broadband analyses. Geometries G1–G6 correspond to the six candidate designs selected from the single-wavelength design-space analysis for each $1 \times N$ configuration. Each entry reports $(W_{\mathrm{MMI}}, L_{\mathrm{MMI}})$ in μm.

Geometry	$N = 2$	$N = 3$	$N = 4$	$N = 5$	$N = 6$	$N = 7$	$N = 8$
G1	(4, 9.6)	(6, 14.4)	(8, 19.4)	(10, 24.4)	(12, 29.0)	(14, 34.3)	(16, 39.3)
G2	(5, 14.7)	(7.5, 22.6)	(10, 30.4)	(12.5, 38.7)	(15, 46.5)	(17.5, 54.4)	(20, 62.3)
G3	(6, 21.5)	(9, 32.6)	(12, 43.9)	(15, 55.8)	(18, 60.1)	(21, 78.7)	(24, 90.1)
G4	(7, 27.6)	(10.5, 44.1)	(14, 60.0)	(17.5, 76.0)	(21, 91.6)	(24.5, 107.2)	(28, 122.8)
G5	(8, 34.1)	(12, 59.0)	(16, 78.2)	(20, 99.4)	(24, 119.7)	(28, 140.9)	(32, 161.4)
G6	(9, 41.5)	(13.5, 68.0)	(18, 97.1)	(22.5, 126.0)	(27, 151.7)	(31.5, 177.4)	(36, 203.1)

The parameter D denotes the edge-to-edge gap between adjacent output tapers at their interface with the multimode section, as illustrated in Fig. 2.1(d). According to the adopted symmetric port arrangement, the multimode width is related to the taper width and inter-taper gap through

$$W_{\mathrm{MMI}} = N\,(W_{\mathrm{taper}} + D)\,, \tag{2.23}$$

or equivalently,

$$W_{\mathrm{taper}} = \frac{W_{\mathrm{MMI}}}{N} - D. \tag{2.24}$$

Consequently, for a fixed W_{MMI} and N, varying D directly changes the taper width at the MMI output interface without modifying the nominal transverse positions of the output ports defined by Eq. 2.14. Smaller values of D correspond to wider taper apertures, whereas increasing D results in narrower output tapers.

The purpose of this analysis is therefore not to re-optimize the multimode section, but to refine the coupling between the self-imaged field at the end of the MMI region and the output access waveguides. For each fixed $(W_{\mathrm{MMI}}, L_{\mathrm{MMI}})$ pair, D was swept and the corresponding insertion loss was calculated. The optimum value D_{opt} was defined as the value providing the minimum insertion loss at $\lambda = 1.55$ μm.

$$D_{\mathrm{opt}} = \arg\min_{D} \mathrm{IL}(D)\big|_{\lambda=1.55\ \mu\mathrm{m}}. \tag{2.25}$$

Figure 2.7 presents the resulting insertion loss as a function of D for the G1–G6 reference geometries of each investigated $1 \times N$ configuration. For each G1–G6 reference geometry, the value of D_{opt} was extracted from the D coordinate of the minimum-IL point marked in Fig. 2.7. The optimized inter-taper gaps D_{opt}, together with the corresponding insertion-loss values $\mathrm{IL}(D_{\mathrm{opt}})$, are summarized in Table 2.3, with D_{opt} identified from the minimum of each IL curve in Fig. 2.7.

The results show that the loss-minimizing value of D depends on the selected $(W_{\mathrm{MMI}}, L_{\mathrm{MMI}})$ geometry and does not follow a unique scaling rule with either N or W_{MMI}. In many of the investigated cases, the minimum IL is obtained for relatively small values of D. According to Eq. 2.23, this corresponds to wider taper apertures at the MMI output interface, which provide efficient collection of the self-imaged optical field.

However, the optimum does not always occur at $D = 0$, indicating that maximizing the taper width alone is not sufficient to guarantee minimum insertion loss. The optimum taper aperture depends on the spatial distribution of the self-imaged field and its coupling to the output access waveguides. Therefore, D_{opt} is extracted numerically for each investigated $(W_{\mathrm{MMI}}, L_{\mathrm{MMI}})$ pair from the minimum of the corresponding IL curve in Fig. 2.7.

At this stage, the analysis establishes the optimized inter-taper gap D_{opt} for each reference MMI geometry at $\lambda = 1.55$ μm. The wavelength dependence and broadband robustness of the resulting designs are evaluated in the following sections over the considered spectral range.

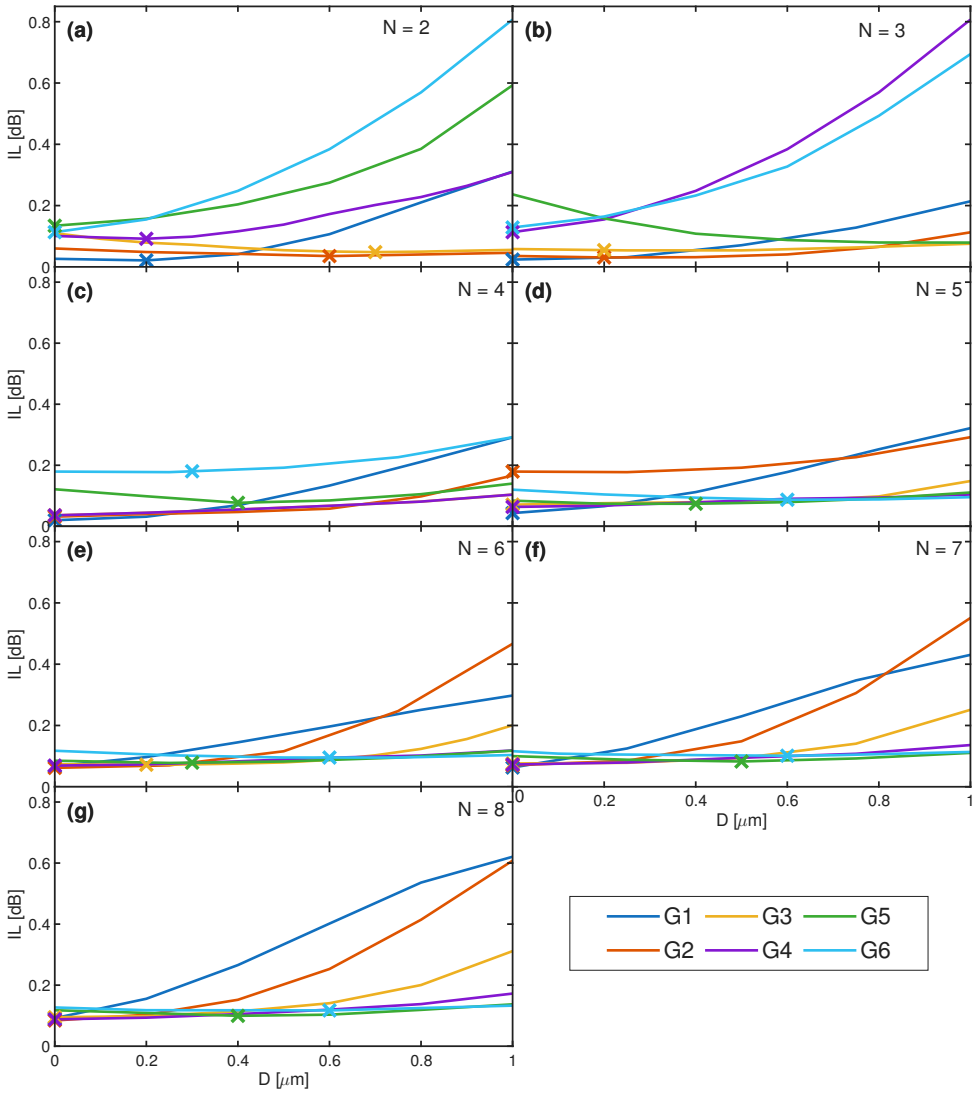


Figure 2.7: Insertion loss at $\lambda = 1.55$ μm as a function of the inter-taper gap D for: (a) $N = 2$, (b) $N = 3$, (c) $N = 4$, (d) $N = 5$, (e) $N = 6$, (f) $N = 7$, and (g) $N = 8$. Curves G1–G6 correspond to the fixed $(W_{\mathrm{MMI}}, L_{\mathrm{MMI}})$ reference geometries defined in Table 2.2. For each curve, only D, and consequently W_{taper}, is varied. The markers indicate the minimum-IL points from which the corresponding D_{opt} values are extracted.

Table 2.3: Optimized inter-taper gap D_{opt} and the corresponding insertion loss $\mathrm{IL}(D_{\mathrm{opt}})$ at $\lambda = 1.55$ μm for the G1–G6 reference geometries defined in Table 2.2. Each entry reports D_{opt} [μm] followed by $\mathrm{IL}(D_{\mathrm{opt}})$ [dB] in parentheses. The values are extracted from the minima of the corresponding curves in Fig. 2.7.

Geometry	$N = 2$	$N = 3$	$N = 4$	$N = 5$	$N = 6$	$N = 7$	$N = 8$
G1	0.2 (0.0211)	0.0 (0.0238)	0.0 (0.0199)	0.0 (0.0433)	0.0 (0.0670)	0.0 (0.0628)	0.0 (0.0919)
G2	0.6 (0.0352)	0.2 (0.0307)	0.0 (0.0316)	0.0 (0.1793)	0.0 (0.0617)	0.0 (0.0699)	0.0 (0.0843)
G3	0.7 (0.0482)	0.2 (0.0547)	0.0 (0.0359)	0.0 (0.0710)	0.2 (0.0720)	0.0 (0.0760)	0.0 (0.0947)
G4	0.2 (0.0918)	0.0 (0.1133)	0.0 (0.0359)	0.0 (0.0634)	0.0 (0.0691)	0.0 (0.0726)	0.0 (0.0879)
G5	0.0 (0.1343)	1.1 (0.0779)	0.4 (0.0770)	0.4 (0.0738)	0.3 (0.0787)	0.5 (0.0824)	0.4 (0.0995)
G6	0.0 (0.1133)	0.0 (0.1284)	0.3 (0.1803)	0.6 (0.0870)	0.6 (0.0954)	0.6 (0.1013)	0.6 (0.1172)

2.3.5.6 Broadband Insertion Loss Analysis

After identifying low-insertion-loss and low-uniformity regions at the design wavelength $\lambda_0 = 1.55$ μm, the next step is to assess the wavelength-dependent behavior of the selected

MMI geometries. This analysis is essential to verify whether designs optimized under single-wavelength conditions retain acceptable efficiency over a broader spectral range.

Figure 2.8 reports the broadband insertion loss as a function of wavelength for the G1–G6 reference geometries of the $1 \times N$ MMI splitters, with N ranging from 2 to 8 (subfigures (a)–(g)). For each value of N, multiple curves are shown, corresponding to

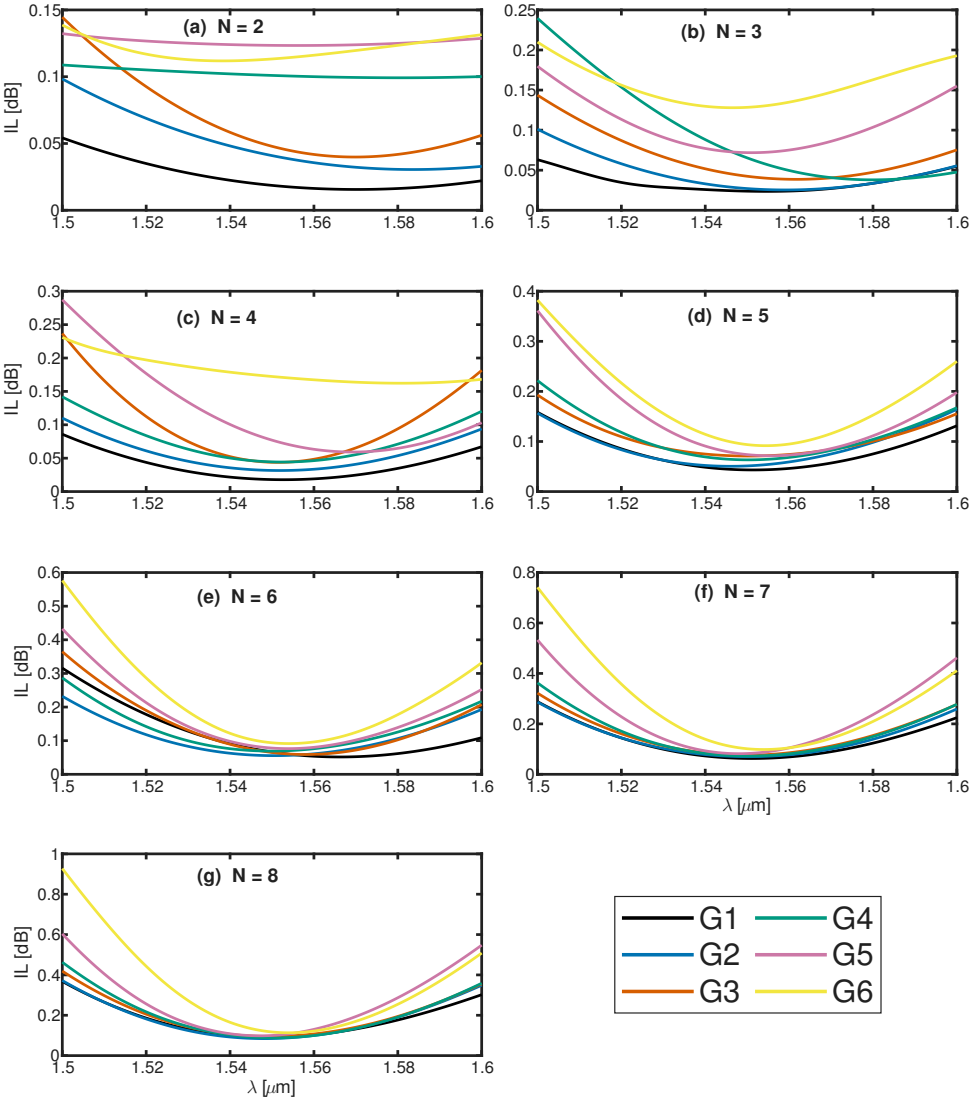


Figure 2.8: Broadband insertion loss (IL) as a function of wavelength for the $1 \times N$ MMI splitters: (a) $N = 2$, (b) $N = 3$, (c) $N = 4$, (d) $N = 5$, (e) $N = 6$, (f) $N = 7$, and (g) $N = 8$. Curves G1–G6 correspond to the reference $(W_{\mathrm{MMI}}, L_{\mathrm{MMI}})$ geometries defined in Table 2.2.

different $(W_{\mathrm{MMI}}, L_{\mathrm{MMI}})$ combinations extracted from the low-loss regions of the single-wavelength IL maps at $\lambda_0 = 1.55$ μm. All simulations include the optimized access taper geometries identified during the single-wavelength refinement stage.

In all configurations, the insertion loss exhibits a minimum around the central wavelength, as expected from the single-wavelength optimization criterion. As the wavelength moves away from λ_0, the insertion loss gradually increases toward the edges of the considered spectral range. This behavior reflects the intrinsic wavelength dependence of the self-imaging condition, which is exactly satisfied only at the design wavelength and progressively degrades as the accumulated modal phase mismatch increases.

As the number of output ports increases, two systematic trends become apparent. First, the overall insertion loss level increases, reflecting the higher modal complexity and

larger multimode sections required for high-N devices. Second, the spectral curvature of the IL response becomes more pronounced, indicating a reduced tolerance to wavelength detuning as the number of outputs (N) grows. Nevertheless, for all investigated values of N, the insertion loss remains below a few tenths of a decibel across the entire C-band, confirming the inherently broadband nature of the optimized MMI architectures.

It is important to emphasize that this subsection focuses exclusively on broadband insertion-loss performance. While low insertion loss is essential for practical operation, it does not by itself guarantee uniform power distribution among the output ports. The results presented here therefore establish a baseline for broadband transmission efficiency, motivating the subsequent wavelength-dependent uniformity analysis, which evaluates how evenly the optical power is distributed across the outputs over the same spectral range.

2.3.5.7 Broadband Uniformity Analysis

In addition to insertion loss, the broadband performance of multiport MMI splitters must be assessed in terms of output power uniformity, as wavelength-dependent imbalance can severely impact cascaded and coherent photonic architectures. Following the broadband insertion-loss analysis, the wavelength dependence of the uniformity metric was therefore evaluated for the same set of geometries.

Figure 2.9 reports the broadband uniformity as a function of wavelength for the G1–G6 reference geometries of the $1 \times N$ MMI splitters, with N ranging from 3 to 8 (subfigures (a)–(f)). The 1×2 configuration is excluded from this analysis, since its intrinsic mirror symmetry guarantees equal power splitting between the two output ports, resulting in UF=0 dB across the entire wavelength range.

For all investigated $1 \times N$ configurations, the uniformity exhibits a clear wavelength dependence, with minimum imbalance typically occurring in the vicinity of the design wavelength $\lambda_0 = 1.55\ \mu$m. This behavior is consistent with the self-imaging condition being exactly satisfied at the design wavelength, while wavelength detuning progressively modifies the relative modal interference pattern in correspondence of the output waveguides.

Compared to insertion loss, uniformity generally shows a stronger sensitivity to wavelength variations, particularly for $1 \times N$ configurations with higher N values. As N increases, relatively small changes in the transverse field distribution can lead to noticeable redistribution of power among the output waveguides, resulting in increased imbalance toward the wavelength range edges. This trend indicates that broadband uniformity, rather than insertion loss, often becomes the limiting factor in the design of MMI splitters with a high number of output ports.

The results further show that the multimode width plays a critical role in determining the wavelength stability of the uniformity. For each value of N, the broadband UF response depends strongly on the selected multimode width. For example, this behavior is particularly evident in the 1×3 configuration, where $W_{\mathrm{MMI}} = 12\ \mu$m provides a relatively flat UF response over the considered wavelength range, whereas neighboring widths exhibit more pronounced wavelength-dependent oscillations. Importantly, geometries that provide low insertion loss over wavelength do not necessarily guarantee optimal broadband uniformity, confirming that broadband optimization cannot be performed based on a single figure of merit.

At this stage, the broadband uniformity analysis serves to identify subsets of geometries that jointly offer acceptable insertion loss and controlled wavelength-dependent imbalance. When combined with the broadband insertion-loss trends discussed previously, these results enable the selection of designs suitable for broadband operation, which are summarized and quantitatively compared in the following section.

2.3.5.8 Broadband Performance Factor

To provide a unified assessment of broadband behavior, the performance factor (PF), previously defined as a combination of insertion loss (IL) and output power uniformity

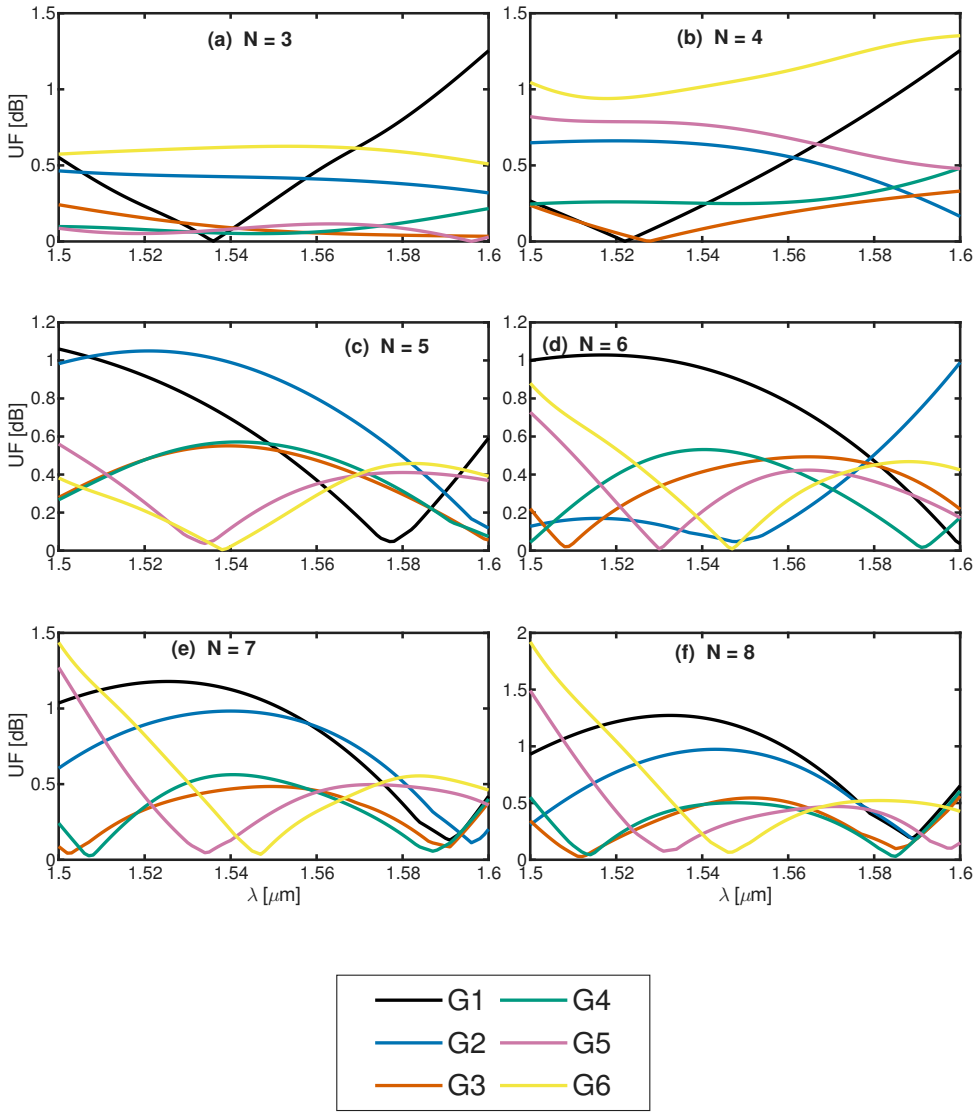


Figure 2.9: Broadband uniformity (UF) as a function of wavelength for the $1 \times N$ MMI splitters: (a) $N = 3$, (b) $N = 4$, (c) $N = 5$, (d) $N = 6$, (e) $N = 7$, and (f) $N = 8$. Curves G1–G6 correspond to the reference $(W_{\mathrm{MMI}}, L_{\mathrm{MMI}})$ geometries defined in Table 2.2.

(UF), is employed to evaluate the wavelength-dependent performance of the investigated MMI geometries. By jointly accounting for insertion loss and uniformity, PF enables a direct comparison of different splitter configurations over a broad spectral range.

Figure 2.10 reports the wavelength-dependent PF for the G1–G6 reference geometries of the $1 \times N$ MMI splitters, with N ranging from 2 to 8, over the 1.50–1.60 μm wavelength range. A clear and systematic trend emerges from these results. Only the 1×2 MMI splitter exhibits a performance factor that remains close to unity across the entire spectral range. This behavior is primarily attributed to the intrinsic symmetry of the two-port configuration, which guarantees perfectly balanced power splitting. As a consequence, the uniformity contribution is identically zero and the PF is effectively governed by insertion loss alone.

For higher N values ($N > 2$), the performance factor exhibits a pronounced wavelength dependence and a systematic reduction with respect to the 1×2 case. This degradation is not driven by a dramatic increase in insertion loss, which remains relatively moderate for many geometries, but rather by the emergence of non-zero uniformity. In multiport MMI splitters, small wavelength-dependent variations in the self-imaging condition translate

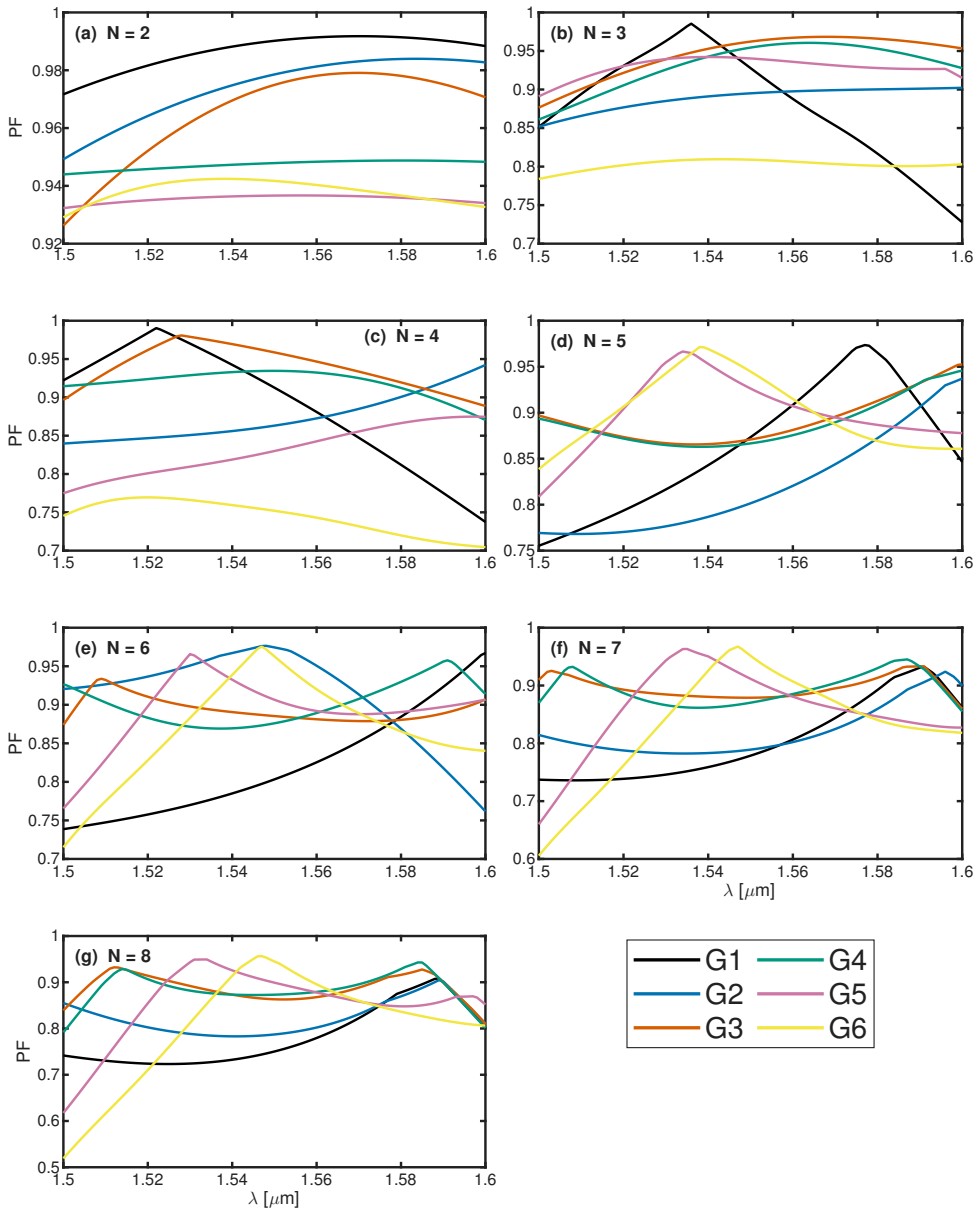


Figure 2.10: Broadband performance factor (PF) as a function of wavelength for the $1 \times N$ MMI splitters: (a) $N = 2$, (b) $N = 3$, (c) $N = 4$, (d) $N = 5$, (e) $N = 6$, (f) $N = 7$, and (g) $N = 8$. Curves G1–G6 correspond to the reference $(W_{\mathrm{MMI}}, L_{\mathrm{MMI}})$ geometries defined in Table 2.2.

into power imbalance among the output ports, causing the uniformity term to deviate from zero and directly impacting the PF.

These results highlight that, beyond the fundamental two-port case, broadband performance is primarily limited by uniformity rather than by insertion loss. Even geometries optimized to minimize loss at the central wavelength experience a reduction in PF when evaluated over a broad spectral range, due to the sensitivity of power balance to wavelength detuning. The PF analysis therefore confirms that broadband optimization of multiport MMI splitters is inherently constrained by uniformity effects, and that maintaining a PF close to unity over a wide bandwidth becomes increasingly challenging as the number of output ports increases.

Table 2.4 summarizes the final selection of representative $1 \times N$ MMI splitter geometries obtained from the combined broadband analysis of insertion loss, uniformity, and performance factor.

Table 2.4: Optimized geometrical parameters of the $1 \times N$ MMI couplers providing the best compromise in terms of performance factor (PF) among the explored W_{MMI} ranges, in accordance with the trends observed in Fig. 2.10. For each values of N, the selected multimode width W_{MMI}, length L_{MMI}, and optimized output spacing D_{opt} are reported, together with the minimum and maximum values of insertion loss (IL), uniformity (UF), and performance factor (PF) evaluated over the considered wavelength range.

Opt. case	N	W_{MMI} [μm]	L_{MMI} [μm]	D_{opt} [μm]	$\mathrm{IL_{min}}$;$\mathrm{IL_{max}}$ [dB]	$\mathrm{UF_{min}}$;$\mathrm{UF_{max}}$ [dB]	$\mathrm{PF_{min}}$;$\mathrm{PF_{max}}$
1	2	4	9.6	0.2	0.018; 0.054	0	0.972; 0.988
2	3	9	32.6	0.2	0.027; 0.143	0.034; 0.105	0.876; 0.968
3	4	13	51.6	0	0.038; 0.144	0.026; 0.142	0.899; 0.944
4	5	15	55.8	0	0.064; 0.198	0.056; 0.335	0.879; 0.952
5	6	18	67.3	0.2	0.059; 0.364	0.020; 0.215	0.883; 0.934
6	7	21	78.7	0	0.072; 0.327	0.043; 0.281	0.865; 0.933
7	8	24	90.1	0	0.090; 0.410	0.027; 0.241	0.810; 0.932

Rather than reporting all simulated configurations, only designs providing the most balanced compromise between IL and uniformity over a broad wavelength range are included for each $1 \times N$ configuration.

The optimized output spacing D_{opt} was extracted numerically for each selected geometry and does not follow a simple closed-form scaling law with either N or W_{MMI}. Nevertheless, configurations with D close to zero frequently yield near-optimal performance, although notable exceptions are observed. This behavior highlights the sensitivity of multiport MMI devices to output-waveguide spacing and motivates the tolerance and robustness analyses discussed in the following section.

2.3.6 Combiner Design Derived from the Splitter Geometry

The multiport MMI structures discussed so far were designed and optimized in the splitter configuration, where a single input field is distributed among N output ports through the self-imaging process in the multimode section. An efficient and practically attractive approach to realize the corresponding $N \times 1$ combiner is to exploit the same physical geometry by interchanging the roles of input and output ports, that is, by exciting the waveguides previously used as outputs and collecting the recombined signal at the waveguide originally used as the input.

This approach is justified by the reciprocity of linear passive waveguide devices. The multimode section implements a deterministic linear transformation between port fields, and the same transformation therefore applies in reverse propagation. However, efficient operation in the combiner configuration is not obtained by simply launching identical signals into all N input ports. If all inputs are excited with equal amplitude and identical phase, the resulting interference inside the multimode region does not, in general, lead to constructive recombination into the desired output port.

Constructive combining instead requires a specific set of relative phase offsets among the N input signals, such that the individual contributions interfere coherently at the target output. In this work, the required input phase pattern is derived directly from the splitter characterization. For each optimized $1 \times N$ splitter geometry, the complex fields at the N output ports exhibit well-defined relative phase relations imposed by the multimode interference process.

By reciprocity, imposing the same relative phase differences but with reverse sign (with respect to a chosen reference port) at the inputs of the combiner configuration enables constructive interference toward the single output port. In this way, the combiner functionality is realized without any modification of the multimode core geometry, relying solely on appropriate phase engineering of the input signals.

In the next subsection, the wavelength dependence of these inter-port phase differences is analyzed, demonstrating that the relative phases required for constructive combining remain weakly dependent on wavelength over the considered spectral range. The extracted phase relations are subsequently generalized across the explored W_{MMI} design space and summarized to provide a direct and practical design rule for MMI-based multiport combiners.

2.3.6.1 Wavelength Stability of Inter-Port Phase Relations

As discussed in the previous subsection, multiport MMI combiners can be realized by operating optimized splitter geometries in the reverse direction. In contrast to the splitting operation, however, constructive interference at the output port of a combiner cannot be achieved by exciting all input ports with identical phase. Instead, a specific set of relative phase offsets must be applied to compensate for the intrinsic phase relations imposed by the multimode interference process.

In this work, the required phase pattern is obtained directly from the splitter characterization. Owing to reciprocity, the relative phase differences evaluated at the output ports in splitter operation uniquely determine the phase offsets that must be applied at the inputs when the device is used as an $N \times 1$ combiner. Specifically, these input phases are equal in magnitude and opposite in sign to the corresponding output splitter phase differences.

Figure 2.11 reports the wavelength-dependent relative phase differences $\Delta\phi_{n,m}$ between selected pairs of output ports for optimized MMI splitters with N ranging from 3 to 8. The phase differences are evaluated over the wavelength range from 1.5 to 1.6 μm, corresponding to the C-band.

For the special case of $N = 2$, no relative phase difference exists between the two output ports. This result follows directly from the strict mirror symmetry of the 1×2 MMI splitter, which enforces identical optical path lengths and equal output phases. As a consequence, the corresponding 2×1 MMI combiner does not require phase pre-compensation, and constructive interference is naturally obtained at the output port.

For $N \geq 3$, non-zero but well-defined phase differences are observed between the output ports. A key result from Fig. 2.11 is that these phase differences remain nearly constant over the entire wavelength range under investigation. Only minor variations are observed, indicating that the relative phase relations imposed by the multimode interference mechanism are inherently broadband. To quantitatively assess the wavelength stability of the inter-port phase relations, the phase variation metric $\sigma_{\Delta\phi_{i,j}}$ is defined as

$$\sigma_{\Delta\phi_{i,j}} = \max_{\lambda} \left(\Delta\phi_{i,j}(\lambda)\right) - \min_{\lambda} \left(\Delta\phi_{i,j}(\lambda)\right), \tag{2.26}$$

which captures the maximum deviation of the relative phase difference over the considered wavelength range. For all optimized $1 \times N$ MMI splitters ($N = 3$–8), the extracted values of $\sigma_{\Delta\phi_{i,j}}$ remain below 10% of the nominal phase step, confirming the intrinsic broadband stability of the phase relations.

This wavelength stability of the inter-port phase relations is a critical property for the practical realization of multiport MMI combiners. It ensures that the phase pattern required for constructive interference does not need to be dynamically adjusted across the operational bandwidth, enabling broadband combining operation using fixed phase offsets.

It is important to note that the phase pattern required at the inputs of the combiner corresponds to the conjugate of the phase distribution observed at the outputs of the splitter. Specifically, if a relative phase difference $\Delta\phi$ is measured between two splitter output ports, the corresponding combiner requires an input phase difference of $-\Delta\phi$ between the same ports to achieve constructive interference at the output. This condition follows naturally from the reciprocity of linear passive photonic devices, where the phase evolution of the combiner corresponds to the reverse propagation of the splitter operation.

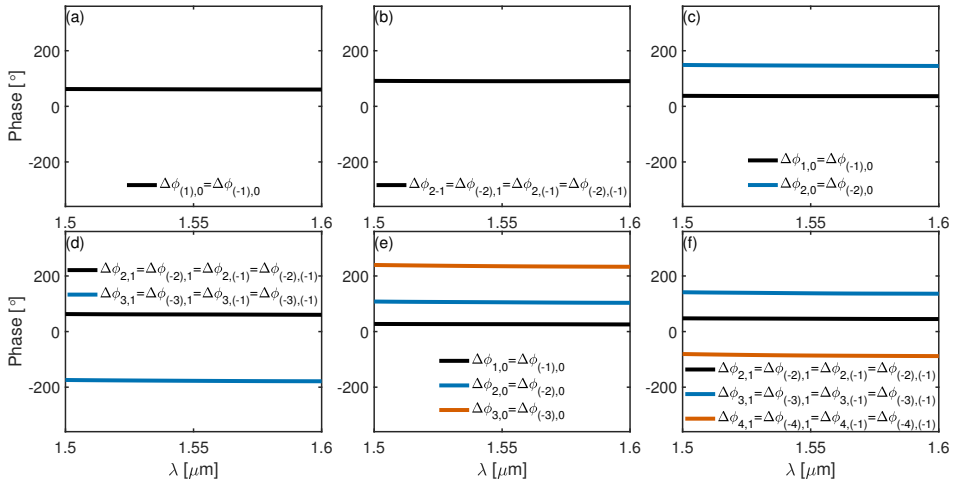


Figure 2.11: Wavelength-dependent relative phase differences between selected output ports of optimized $1\times N$ MMI splitters, evaluated over the wavelength range from 1.5 to 1.6 μm. Subfigures (a)–(f) correspond to N values from $N = 3$ to $N = 8$, respectively. For $N = 2$, no relative phase difference is observed due to the inherent symmetry of the splitter. For $N \geq 3$, distinct but nearly wavelength-independent phase offsets appear between the output ports, indicating that the phase relations imposed by the multimode interference process are intrinsically broadband. These phase differences directly define the phase pattern required at the inputs when the same structures are operated as multiport combiners.

In the following subsection, these phase relations are examined for different MMI geometries, and a compact set of phase values is identified to provide a direct and practical design rule for MMI-based multiport combiners.

Beyond coherent combining, the demonstrated wavelength-stable inter-port phase relations are particularly relevant for phase-sensitive photonic systems such as optical phased arrays (OPAs), where deterministic and broadband phase distributions are required to control the far-field radiation pattern. In this context, the $1 \times N$ MMI splitters can act as compact optical feeding networks, provided that the extracted phase offsets are either directly exploited or compensated through integrated phase shifters placed after the MMI outputs.

2.3.6.2 Output Phase Difference Across the Feasible Design Space

Beyond wavelength stability, the phase relations extracted from the splitter operation exhibit an additional property of direct relevance for combiner design. Within the feasible low-loss configurations identified in the $(W_{\mathrm{MMI}}, L_{\mathrm{MMI}})$ maps, the inter-port phase differences are found to be essentially independent of the specific multimode width and length. In other words, once a geometry belongs to the set of configurations with acceptable performance—i.e., it provides low uniformity and insertion loss—the relative phase pattern at the output ports is primarily dictated by the number of ports N, rather than by the exact values of W_{MMI} and L_{MMI}.

This observation enables a simple description of the phase pattern required for multiport combiner operation. For each value of N, the phase differences between adjacent ports can be approximated by a constant phase step, leading to a phase progression across the output ports. As representative examples, for $N = 3$ the phase step is found to be close to $\pi/3$, while for $N = 4$ it is close to $\pi/2$. The same behavior is consistently observed across the explored W_{MMI} range, provided that the geometry lies within the low-loss self-imaging regions.

The resulting phase-step values therefore provide a practical design rule. Rather than re-extracting port phases for each individual geometry, the combiner can be driven using a fixed phase pattern determined solely by the number of ports N, with the appropriate sign convention discussed in the previous subsection.

Within the optimized $(W_{\mathrm{MMI}}, L_{\mathrm{MMI}})$ design space, the relative phase differences between adjacent ports depend primarily on the total number of ports N, while exhibiting negligible dependence on the specific geometrical dimensions. The observed wavelength-induced phase variations remain limited to a few degrees, confirming that the extracted phase relations are both geometry-invariant and broadband.

Based on the numerical phase extraction performed for $N = 2$ to $N = 8$, the phase difference between port i and port $i-1$ can be described by a compact empirical rule that distinguishes between odd and even N values. Here, the port index i is defined with respect to the center of the MMI structure, assuming symmetric port placement as described in Sec. 2.3.3.

For odd-port configurations, the ports are indexed symmetrically around the central port 0, while for even-port configurations the ports are indexed as $(-N/2), \ldots, -1, 1, \ldots, (N/2)$ without a central port. The relative phase difference is defined as

$$\Delta\phi_{i,j} = \phi_i - \phi_j,$$

with the indexing chosen such that $|i| > |j|$. Due to the structural symmetry of the MMI splitter, symmetric output ports exhibit identical phase values with respect to the chosen phase reference.

$$\Delta\phi_{i,i\mp1}(N) = \begin{cases} (2|i|-1)\dfrac{\pi}{N}, & \text{for odd } N, \quad i = 0, \pm1, \pm2, \ldots, \pm(\dfrac{N-1}{2}), \\ (2|i|)\dfrac{\pi}{N}, & \text{for even } N, \quad i = \pm1, \pm2, \ldots, \pm\dfrac{N}{2}. \end{cases} \tag{2.27}$$

where the upper and lower signs correspond to positive- and negative-index ports, respectively. Equation (2.27) summarizes the observed phase relations in a form that is independent of the specific MMI geometry, provided that the structure operates within the low-loss self-imaging regime. This compact representation demonstrates that the phase pattern required for multiport combining can be predicted solely from the number of output ports N in each $1 \times N$ configuration, significantly simplifying the practical design of $N \times 1$ MMI combiners.

The phase differences obtained from this rule are consistent with the numerically extracted values for the optimized $1 \times N$ MMI configurations. Table 2.5 summarizes the adjacent-port phase differences $\Delta\phi_{i,j}$ at the design wavelength $\lambda_0 = 1.55$ μm, together with the corresponding maximum phase variations $\sigma_{\Delta\phi_{i,j}(\lambda)}$ over the 1.50–1.60 μm wavelength range.

Table 2.5: Phase differences between adjacent output ports $\Delta\phi_{i,j}$ at the design wavelength $\lambda_0 = 1.55$ μm and the corresponding maximum phase variations $\sigma_{\Delta\phi_{i,j}(\lambda)}$ over the 1.50–1.60 μm wavelength range for the optimized $1 \times N$ MMI splitter configurations.

Optimized cases	number of output ports N	$\Delta\phi_{i,j}(\lambda_0)$ [rad]	$\sigma_{\Delta\phi_{i,j}(\lambda)}$ [rad]
1	2	$\Delta\phi_{(-1),1} = 0$	–
2	3	$\Delta\phi_{1,0} = \Delta\phi_{-1,0} = \pi/3$	0.0317
3	4	$\Delta\phi_{2,1} = \Delta\phi_{-2,-1} = \pi/2$	0.0211
4	5	$\Delta\phi_{1,0} = \Delta\phi_{-1,0} = \pi/5$	0.0217
		$\Delta\phi_{2,1} = \Delta\phi_{-2,-1} = 3\pi/5$	0.0411
5	6	$\Delta\phi_{2,1} = \Delta\phi_{-2,-1} = \pi/3$	0.0470
		$\Delta\phi_{3,2} = \Delta\phi_{-3,-2} = 2\pi/3$	0.0353
6	7	$\Delta\phi_{1,0} = \Delta\phi_{-1,0} = \pi/7$	0.0308
		$\Delta\phi_{2,1} = \Delta\phi_{-2,-1} = 3\pi/7$	0.0501
		$\Delta\phi_{3,2} = \Delta\phi_{-3,-2} = 5\pi/7$	0.0334
7	8	$\Delta\phi_{2,1} = \Delta\phi_{-2,-1} = \pi/4$	0.0445
		$\Delta\phi_{3,2} = \Delta\phi_{-3,-2} = 2\pi/4$	0.0484
		$\Delta\phi_{4,3} = \Delta\phi_{-4,-3} = 3\pi/4$	0.0374

The numerical values in Table 2.5 confirm the phase progression described by Eq. (2.27). The adjacent-port phase differences are primarily determined by the number of output ports N, while the limited values of $\sigma_{\Delta\phi_{i,j}(\lambda)}$ demonstrate that these phase relations remain stable over the investigated wavelength range. The table therefore provides a compact reference for assigning the relative input phase offsets required when the same MMI geometries are operated as $N \times 1$ coherent combiners.

2.3.6.3 Ideal Combiner Operation and Insertion Loss Performance

The multimode interference structures discussed so far have been primarily analyzed in the splitter configuration. Due to the reciprocity of linear passive photonic devices, the same MMI geometries can also operate as coherent combiners when the signal propagation direction is reversed. In this configuration, the waveguides previously serving as splitter outputs are treated as combiner inputs, while the original input waveguide acts as the combiner output.

In contrast to the splitting operation, efficient combining requires not only equal input amplitudes but also a specific set of relative phase offsets among the injected signals. These phase offsets must compensate for the intrinsic phase accumulation imposed by the multimode interference process, as extracted from the splitter phase analysis discussed in the previous subsections. Before addressing the sensitivity of the combiner to non-ideal excitation or fabrication-induced perturbations, the performance of the resulting $N \times 1$ MMI combiners is first evaluated under ideal excitation conditions.

Figure 2.12 shows the wavelength-dependent insertion loss of the MMI combiners under ideal excitation conditions.

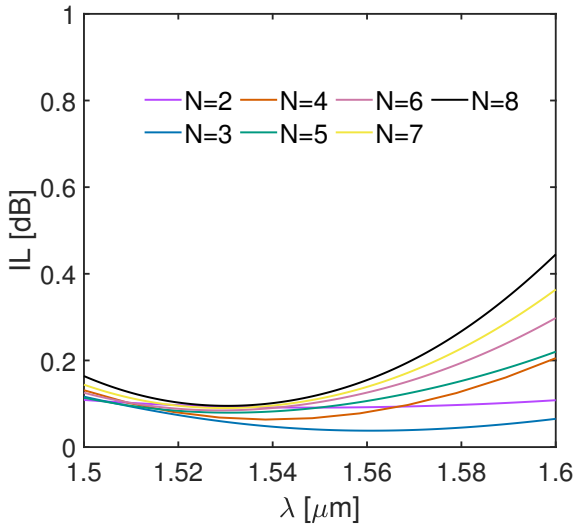


Figure 2.12: Insertion loss of the $N \times 1$ MMI combiners corresponding to the optimized splitter designs for $N = 2$ to $N = 8$, evaluated as a function of wavelength. For each case, the combiner is obtained by reversing the splitter configuration and by applying the conjugate phase offsets derived from the splitter output phase relations. All input signals are injected with equal amplitudes and ideal relative phases.

For the $N = 2$ configuration, the insertion loss remains nearly constant and close to its minimum value across the entire C-band. This behavior is expected, as no relative phase constraint exists between the two ports, and constructive interference is intrinsically guaranteed by symmetry.

As the number of combined ports increases, a gradual increase in insertion loss is observed, particularly toward the edges of the wavelength range. This trend reflects the growing sensitivity of multiport interference to residual phase dispersion, even when the nominal phase conditions are satisfied at the central wavelength. Nevertheless, for all

investigated values of N, the MMI combiners exhibit broadband operation, with insertion loss remaining well below 0.5 dB over most of the considered spectral range.

These results demonstrate that the phase-engineered MMI structures can effectively operate as coherent multiport combiners under ideal amplitude and phase excitation.

2.3.6.4 Sensitivity to Amplitude and Phase Errors in Combiner Operation

After establishing the ideal combining performance, the robustness of the MMI combiners is evaluated against deviations from the ideal excitation conditions. In practical implementations, coherent combining is affected by unavoidable amplitude and phase errors among the input signals, resulting from fabrication-induced variations and imperfections in the optical system.

The quantities $\Delta T_A(\lambda)$ and $\Delta T_{\mathrm{Ph}}(\lambda)$ quantify the variation of the combiner transmittance induced by amplitude and phase errors at the input ports. Following the definitions adopted in [82], they are expressed as

$$\Delta T_A(\lambda) = |T(\lambda) - T_A(\lambda)|\,, \tag{2.28}$$

$$\Delta T_{\mathrm{Ph}}(\lambda) = |T(\lambda) - T_{\mathrm{Ph}}(\lambda)|\,, \tag{2.29}$$

where $T(\lambda)$ denotes the transmittance calculated under ideal excitation conditions with perfect amplitude and phase at all input ports, while $T_A(\lambda)$ and $T_{\mathrm{Ph}}(\lambda)$ correspond to the transmittances obtained in the presence of amplitude and phase errors, respectively.

In particular, amplitude errors are introduced as random variations applied independently to all input ports, ranging from 0.9 to 1.1 V/m, corresponding to a $\pm 10\%$ fluctuation around the ideal amplitude value of 1 V/m. Similarly, random phase errors within $\pm 10\%$ are considered for the relative phase shifts among the input signals.

Figure 2.13 compares the sensitivity of the MMI combiners to excitation imperfections for different numbers of input ports.

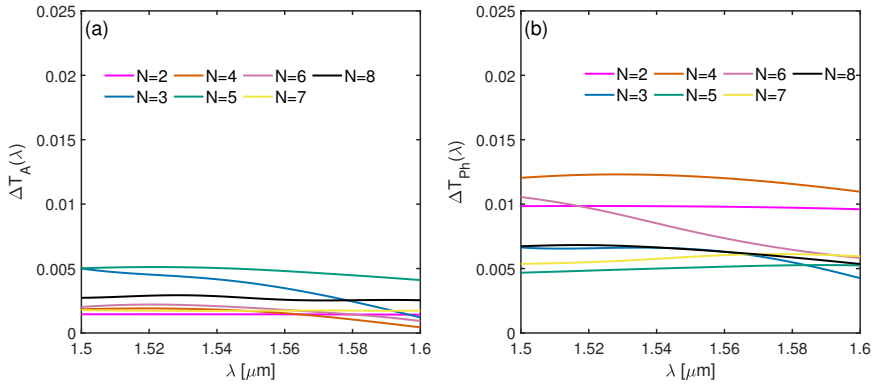


Figure 2.13: Sensitivity of the $N \times 1$ MMI combiners to input imperfections as a function of wavelength. (a) Transmission degradation induced by amplitude imbalance, quantified by $\Delta T_A(\lambda)$. (b) Transmission degradation induced by phase errors, quantified by $\Delta T_{\mathrm{Ph}}(\lambda)$. Results are reported for combiners with N ranging from 2 to 8.

Overall, both amplitude and phase deviations introduce only limited degradation over the investigated wavelength range, confirming the intrinsic robustness of the proposed MMI-based combiners.

For the $N = 2$ configuration, amplitude imbalance results in the smallest variation among all considered cases, consistent with the strong symmetry of the two-port interference process. In relative terms, the phase-related deviation appears more pronounced for $N = 2$ when compared to higher-order combiners. This behavior originates from the fact that, in the two-port case, the combining process relies on a single interference condition, making the output more sensitive to relative phase variations.

It is important to emphasize, however, that even for $N = 2$ the absolute magnitude of the phase-induced degradation remains very small across the entire wavelength range. As N increases, the relative contribution of phase and amplitude errors becomes distributed among multiple interfering paths, resulting in comparable or even reduced sensitivity per port.

Overall, the results indicate that all investigated MMI combiners exhibit low sensitivity to both amplitude and phase errors, supporting their suitability for broadband coherent combining under non-ideal excitation conditions.

2.3.7 Fabrication Tolerance Analysis

Fabrication tolerances represent a critical aspect in the practical realization of high-port-count MMI devices, particularly on high-index-contrast platforms such as thin-film lithium niobate, where etching accuracy and thickness control pose significant technological challenges. To assess the robustness of the proposed design methodology, a fabrication tolerance analysis was carried out on the optimized 1×8 MMI splitter, which represents the most demanding configuration in terms of modal complexity and device footprint.

Figure 2.14(a) and (b) report the impact of deviations in the multimode section width W_{MMI} from its nominal value.

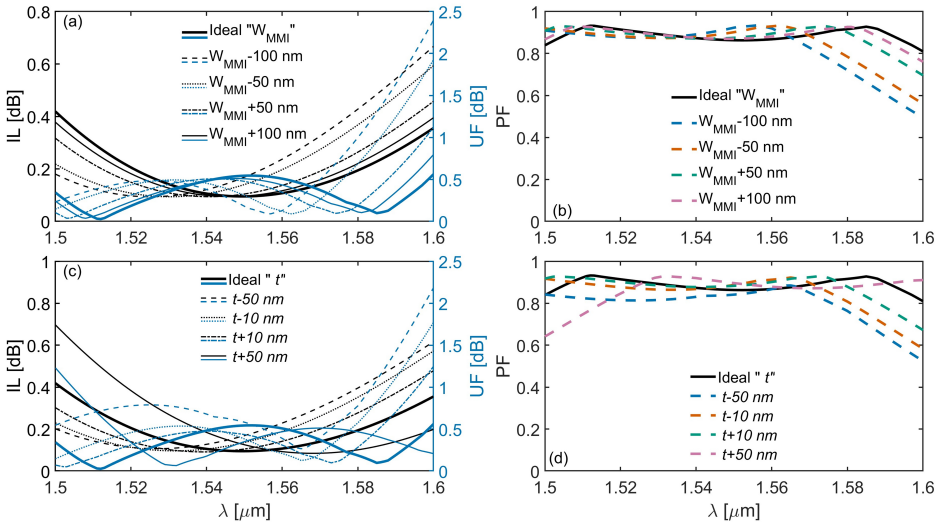


Figure 2.14: Fabrication tolerance analysis of the optimized 1×8 MMI splitter. (a) and (b) show the impact of multimode section width variations $W_{\mathrm{MMI}} \pm 50$ nm and ± 100 nm on insertion loss (IL), uniformity (UF), and performance factor (PF). (c) and (d) report the corresponding sensitivity to core thickness variations $t \pm 10$ nm and ± 50 nm. The ideal design is shown for reference in all panels.

Fabrication errors of ± 50 nm and ± 100 nm were considered, corresponding to realistic worst-case deviations in current lithographic processes. Variations in W_{MMI} primarily affect the lateral modal confinement and the self-imaging condition, resulting in a spectral shift of the device response.

When the fabricated width is larger than the nominal value, the induced spectral shift remains relatively limited. In contrast, when W_{MMI} is smaller than the ideal value, a significantly stronger spectral shift is observed, leading to a more pronounced degradation of uniformity and performance factor toward the edges of the investigated wavelength range. This behavior reflects the increased sensitivity of the self-imaging condition to reduced modal confinement in narrower multimode sections.

The impact of core thickness variations is analyzed in Fig. 2.14(c) and (d). Thickness deviations of ± 10 nm and ± 50 nm were considered, reflecting typical process-induced errors in thin-film lithium niobate platforms. Unlike width errors, thickness variations

primarily modify the effective indices of the supported modes, thereby affecting both the longitudinal interference condition and the relative phase matching among modes.

The fabrication-induced deviations do not lead to an abrupt failure of the self-imaging mechanism; however, they progressively reduce the wavelength range over which the optimized performance is preserved. In particular, variations in both W_{MMI} and the core thickness produce larger deviations in UF and PF toward the spectral edges, whereas the response remains considerably more stable around the design wavelength.

This behavior can be interpreted as a narrowing of the effective operational bandwidth under fabrication perturbations. The effect becomes particularly relevant for high-port-count MMIs, since the broadband analysis presented above already showed an increasing spectral sensitivity as N increases. Therefore, configurations with larger N, together with larger dimensional deviations, progressively lose part of their nominal wideband operating range, even though low-loss MMI operation can still be retained over a narrower spectral interval.

For instance, restricting the considered wavelength range from 1.50–1.60 μm to 1.52–1.58 μm significantly reduces the maximum variations of the investigated figures of merit. This observation highlights an important practical trade-off between fabrication tolerance and usable optical bandwidth: designs exhibiting greater sensitivity to geometrical perturbations can preserve satisfactory performance around the nominal operating wavelength, but over a reduced spectral range.

2.3.8 Conclusion

This chapter investigated multimode interference (MMI) couplers as broadband passive building blocks for optical power splitting and combining on a thin-film lithium niobate platform.

The operating principle of self-imaging was first reviewed and used to establish the geometrical and physical basis of MMI operation. A systematic design framework was then developed for multiport $1 \times N$ splitters, in which the effects of the multimode-section width, length, output-port placement, and taper geometry were analyzed through insertion-loss, uniformity, and combined performance-factor evaluations.

The numerical results showed that the MMI design space is structured by extended low-loss regions rather than isolated optima, enabling scalable multiport operation with favorable robustness to geometrical variations. Broadband analyses further demonstrated that the optimized structures maintain low insertion loss over the considered wavelength range, while output uniformity becomes the dominant limiting factor as the number of ports increases.

Beyond splitter operation, the same MMI geometries were analyzed in the combiner configuration. The extracted inter-port phase relations were shown to be weakly dependent on wavelength and largely invariant within the feasible design space, which enabled the formulation of a simple phase rule for multiport coherent combining. Under ideal excitation conditions, the corresponding $N \times 1$ combiners exhibited low insertion loss, while additional analyses confirmed limited sensitivity to amplitude and phase errors at the inputs.

Finally, the robustness of the proposed designs was assessed under fabrication-induced variations in multimode width and core thickness. Even for the 1×8 configuration, corresponding to the highest investigated $1 \times N$ configuration in this work, the results indicate that the performance degradation remains gradual and becomes more pronounced toward the spectral edges.

Overall, this chapter establishes MMI couplers as compact, broadband, and fabrication-tolerant passive components for multiport power distribution and coherent signal recombination, and provides a systematic design basis for their use in integrated photonic circuits.

The design methodologies and performance trends established in this chapter provide a comprehensive understanding of MMI-based power distribution in idealized conditions.

The following chapter focuses on the fabrication and characterization of the proposed MMI structures. This step enables a direct assessment of the agreement between simulation

and measurement, and provides insight into the impact of off-design operation and process tolerances on device performance.

Chapter 3

Design Refinement, Fabrication, and Characterization of Multimode Interference Couplers

This chapter presents the fabrication and experimental characterization of the thin-film lithium niobate (TFLN) multimode interference (MMI) couplers investigated in this thesis. After the design methodology introduced in the previous chapter, the focus here shifts to practical realization constraints, measurement strategies, and the interpretation of experimental results. Particular attention is devoted to the impact of fabrication-related deviations and off-design measurement conditions on the response of different MMI topologies. The chapter presents the fabricated chip sets, the measurement methodology, and the comparison between numerical predictions and measured performance.

3.1 Introduction

The previous chapter presented a systematic numerical design methodology for TFLN-based MMI splitters and combiners, with the representative design study primarily carried out in the C-band. The present chapter considers a distinct fabrication-oriented set of MMI devices developed for operation in the O-band on the specific TFLN platform adopted for the experimental activity. Although both studies rely on the same self-imaging principles and general design methodology, the devices investigated here were geometrically refined for their target O-band operation and fabrication constraints. The main objective is to bridge the gap between idealized numerical design and practical device characterization, by discussing the technological constraints of the adopted platform, the measurement methodology, and the interpretation of the obtained experimental responses.

In integrated photonics, the transition from simulation to fabricated device is rarely straightforward. Even when the design stage includes realistic material properties and geometrical constraints, the final device behavior may still be affected by process-dependent deviations such as thickness variations, sidewall-angle non-idealities, lithographic bias, and coupling-interface limitations. These factors are especially relevant for compact passive components, where small dimensional deviations can alter the multimode interference condition and degrade the resulting power distribution.

The measurement results reported in this chapter are aimed at providing insight into the actual robustness of different device topologies and at clarifying to what extent the design methodology remains reliable under realistic fabrication and measurement conditions.

This chapter therefore focuses on the fabricated MMI devices and their experimental behavior. After introducing the fabrication-related constraints of the adopted platform and the measurement setup, the chapter presents the measured responses of the available chip sets and compares them with the corresponding numerical expectations. Particular emphasis is placed on identifying topology-dependent trends, explaining discrepancies between simulation and experiment, and assessing the practical tolerance of the proposed MMI structures.

3.2 Experimental Overview

The work presented in this chapter was carried out within the framework of the collaboration between Politecnico di Bari, Bari, Italy, and PICadvanced, Aveiro, Portugal. During this period, the author conducted research activities at the University of Aveiro,

Aveiro, Portugal, and completed an internship at PICadvanced. The fabrication support and experimental characterization of the MMI devices were performed at the PICadvanced facilities.

3.3 Overview of Fabricated MMI Devices

The experimental characterization presented in this chapter is based on a fabrication-oriented set of multimode interference (MMI) couplers targeting operation in the O-band. The general self-imaging principles and design methodology established in Chapter 2 were used as a reference; however, the geometries considered here were not direct replicas of the C-band designs reported in that chapter. Instead, the initial dimensions were adapted and subsequently refined for the specific TFLN layer stack, sidewall geometry, optical-axis orientation, and fabrication constraints associated with the present device set. In particular, the investigated devices are fabricated on thin-film lithium niobate (TFLN) rib-waveguide platforms.

The considered structures include three representative configurations:

- 1×2 MMI coupler,
- 1×4 MMI splitter,
- 2×2 MMI coupler.

Throughout this thesis, the ports of the MMI devices are labeled using a symmetric notation with respect to the device centerline, consistent with the convention introduced in Chapter 2 Section 2.3.3.1. In particular, the output ports of the 1×4 MMI are denoted as ± 1 for the inner ports and ± 2 for the outer ports, reflecting their spatial position relative to the symmetry axis of the structure. Similarly, for the 2×2 MMI configuration, the input and output ports are labeled as $+1$ and -1, following the same symmetry-based convention. This notation is adopted to facilitate the interpretation of the multimode interference behavior and to maintain consistency between the design and experimental analysis presented in this work. Figure 3.1 illustrates the port-numbering convention adopted throughout this thesis for the investigated MMI configurations.

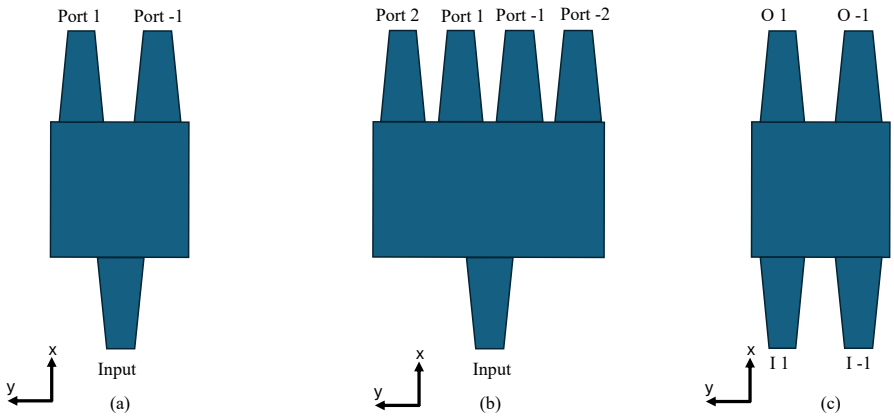


Figure 3.1: Symmetric port-numbering convention adopted throughout this thesis for the (a) 1×2, (b) 1×4, and (c) 2×2 MMI configurations.

All devices were designed targeting operation in the O-band wavelength range (1.26–1.36 μm), with the primary objective of achieving low insertion loss and balanced power distribution. The design follows the self-imaging principle discussed in Chapter 2, while

incorporating fabrication-aware constraints such as sidewall angle, rib thickness, and realistic waveguide cross-sections.

3.4 Platform Description and Design Procedure

3.4.1 Adopted TFLN Platform

The investigated devices were implemented on a thin-film lithium niobate platform based on a rib-waveguide geometry. The nominal characteristics of the platform considered during design consist of a lithium niobate slab layer of thickness

$$t_{\mathrm{slab}} = 200 \text{ nm},$$

and an etched rib section of nominal thickness

$$t_{\mathrm{rib}} = 400 \text{ nm}.$$

The sidewall angle is assumed to be

$$\theta = 55^{\circ},$$

in accordance with the fabrication specifications provided by PICadvanced, Aveiro, Portugal, during the design stage.

Under these conditions, the sidewall-induced difference between the top and bottom widths can be expressed as

$$\Delta W_{\mathrm{sw}} = 2t_{\mathrm{rib}} \cot\theta, \tag{3.1}$$

so that the bottom width of any rib section becomes

$$W^{(\mathrm{B})} = W^{(\mathrm{T})} + \Delta W_{\mathrm{sw}}. \tag{3.2}$$

Here, ΔW_{sw} denotes the total sidewall-induced width difference between the bottom and top surfaces of the rib, while $W^{(\mathrm{T})}$ and $W^{(\mathrm{B})}$ denote the top and bottom widths of the rib section, respectively. The quantities t_{rib} and θ represent the rib thickness and sidewall angle, respectively.

Equations 3.1 and 3.2 apply to the MMI region, the access waveguides, and the taper sections. In the following, the bottom width is taken as representative of the cross section and its variations are taken into account for fabrication tolerance analysis. The side-wall angle is assumed as fixed.

As illustrated in Fig. 3.2, the top width of the waveguide is defined by lithography, whereas the bottom width is determined by the etching process. As a result, variations in rib thickness directly modify the effective waveguide geometry without altering the layout dimensions.

3.4.2 Foundry-Defined Parameters and Device Optimization

The design of the investigated MMI structures was carried out within the constraints imposed by the adopted TFLN fabrication platform. Consequently, not all geometrical and material parameters were treated as independent optimization variables.

Several parameters were predetermined by the foundry and fabrication process. These include the rib thickness $t_{\mathrm{rib}} = 400$ nm, slab thickness $t_{\mathrm{slab}} = 200$ nm, and sidewall angle $\theta = 55^{\circ}$, and the anisotropic orientation of lithium niobate. These quantities were therefore fixed during the design stage and were not treated as optimization variables. In the adopted reference system, the optical signal propagates along the x-direction, and the extraordinary refractive index n_e is also assigned along the same direction. In addition, the rib and slab thicknesses are defined along the z-axis according to the layer stack of the adopted rib-waveguide platform.

Similarly, some geometrical parameters associated with the access waveguides and interface regions were selected according to the platform specifications and fabrication

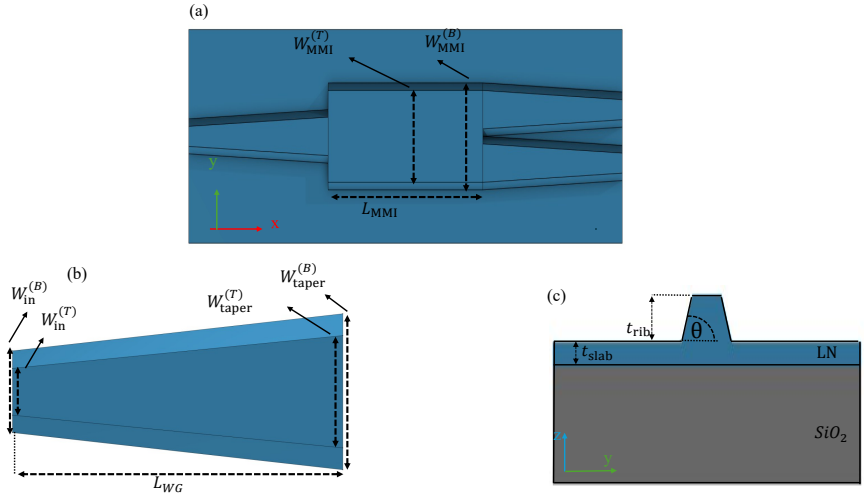


Figure 3.2: Geometrical representation of the MMI structures used for fabrication-aware analysis. (a) Top-view of the multimode section showing the distinction between top and bottom widths. (b) Tapered access waveguide geometry, including top and bottom width definitions. (c) Cross-sectional view of the rib waveguide, highlighting the slab thickness t_{slab}, rib thickness t_{rib}, and sidewall angle θ. This representation emphasizes the fabrication-induced difference between lithographically defined top widths and the effective waveguide geometry determined by the etching process.

compatibility requirements. As a result, the design degrees of freedom were the dimensions directly governing the multimode interference behavior.

Under these constraints, the optimization process mainly focused on the MMI width W_{MMI}, MMI length L_{MMI}, and taper width W_{taper}. These parameters were subsequently optimized through 3D-FDTD simulations in order to achieve low insertion loss and acceptable output power balance within the target O-band wavelength range.

3.4.3 Single-Wavelength Design Optimization at 1310 nm

The MMI devices considered in this chapter were specifically developed for operation in the O-band (1260–1360 nm). This target wavelength range was specified by the foundry for the fabricated MMI device set. Accordingly, 1310 nm, located at the center of the target wavelength range, was selected as the nominal design wavelength for the initial geometrical optimization. Performing the first optimization at the band center provides a reference self-imaging condition before assessing the spectral robustness of the resulting geometry over the complete O-band.

The geometrical refinement was performed iteratively through one-dimensional parameter sweeps. For each topology, the MMI bottom width $W_{\mathrm{MMI}}^{(B)}$ was selected from the starting design guidelines and kept fixed during this refinement stage. The MMI length L_{MMI} and taper bottom width $W_{\mathrm{taper}}^{(B)}$ were then investigated sequentially: during each sweep, the other parameter was kept fixed at its corresponding optimized value.

The initial values of the MMI section widths $W_{\mathrm{MMI}}^{(B)}$ were selected based on previously optimized TFLN MMI designs reported in our earlier work [28]. However, the present structures differ in terms of rib/slab thicknesses, sidewall angle, and optical axis orientation of lithium niobate. Therefore, the remaining geometrical parameters were refined through 3D-FDTD simulations to ensure proper self-imaging behavior and compatibility with the current platform.

The initial parameter sweeps were performed at the central wavelength of 1310 nm. In this step, the MMI length L_{MMI} and taper bottom width $W_{\mathrm{taper}}^{(B)}$ were optimized while the MMI bottom width $W_{\mathrm{MMI}}^{(B)}$ was fixed according to the starting values obtained from the previous design guidelines. The final optimized structures were then evaluated over the full O-band to verify their spectral robustness.

For the 1×2 MMI, the bottom width was fixed to $W_{\mathrm{MMI}}^{(B)} = 4\ \mu$m. Figure 3.3(a) shows the insertion loss as a function of L_{MMI}. During this sweep, L_{MMI} was varied from 10 μm to 12 μm, while the taper bottom width was fixed at $W_{\mathrm{taper}}^{(B)} = 2\ \mu$m. The minimum insertion loss was obtained for $L_{\mathrm{MMI}} = 10.6\ \mu$m, which was therefore selected as the optimized length. The taper optimization is shown in Fig. 3.3(b). In this case, $W_{\mathrm{taper}}^{(B)}$ was varied from 1 μm to 2 μm, while L_{MMI} was fixed to its optimized value of 10.6 μm. The lowest insertion loss was achieved for $W_{\mathrm{taper}}^{(B)} = 2\ \mu$m, and this value was adopted in the final design.

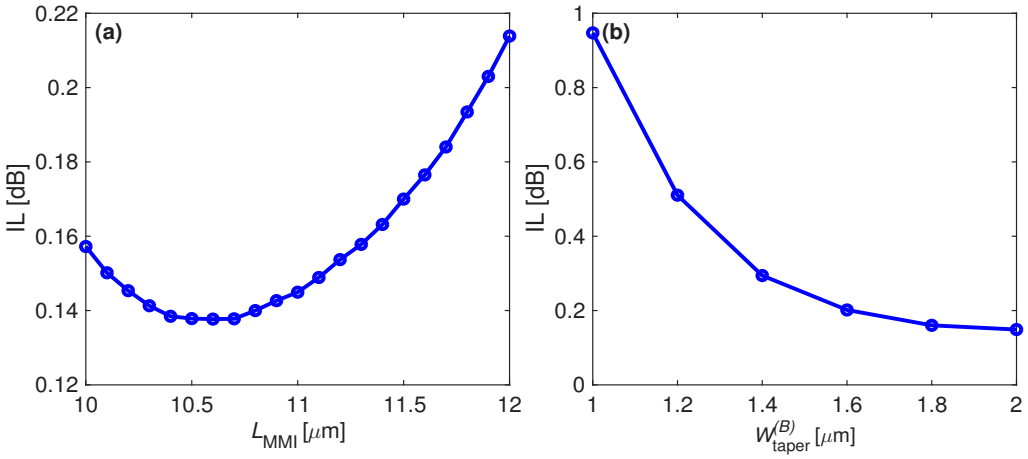


Figure 3.3: Optimization of the 1×2 MMI geometrical parameters at 1310 nm. (a) Insertion loss (IL) versus L_{MMI}. (b) Insertion loss (IL) versus taper bottom width $W_{\mathrm{taper}}^{(B)}$.

For the 1×4 MMI, the bottom width was initially fixed to $W_{\mathrm{MMI}}^{(B)} = 13\ \mu$m. In this case, both insertion loss and uniformity factor were considered during optimization, since the output power balance among the four output ports becomes important. Figure 3.4(a) shows the evolution of IL and UF as functions of L_{MMI}. During the length sweep, L_{MMI} was varied from 50 μm to 70 μm, while the taper bottom width was kept fixed at its optimized value, $W_{\mathrm{taper}}^{(B)} = 3.25\ \mu$m. The UF remains close to its minimum over the approximate range between 50 μm and 62 μm. Within this interval, priority was given to reducing the insertion loss, leading to the selection of $L_{\mathrm{MMI}} = 58\ \mu$m.

The taper bottom width optimization is shown in Fig. 3.4(b), where the MMI length was fixed to 58 μm. The taper bottom width was varied from approximately 2.4 μm to 3.25 μm. The lowest insertion loss was obtained for $W_{\mathrm{taper}}^{(B)} = 3.25\ \mu$m, which was therefore selected for the final 1×4 design.

For the 2×2 MMI, the optimization differs from the previous cases because the structure includes two input and two output waveguides, and the excitation is not centrally aligned with the MMI section. The MMI bottom width was fixed to $W_{\mathrm{MMI}}^{(B)} = 4\ \mu$m, while the remaining geometrical parameters were optimized through 3D-FDTD simulations.

In this configuration, insertion loss alone is not sufficient to evaluate the device performance, since the optical power can still be transmitted with relatively low total loss but with an unbalanced distribution between the two output ports. Therefore, the UF becomes a critical optimization parameter.

Figure 3.5(a) shows the IL and UF variations as functions of L_{MMI} at 1310 nm. During this sweep, the taper bottom width was fixed at $W_{\mathrm{taper}}^{(B)} = 2\ \mu$m.

When L_{MMI} varies approximately from 38 μm to 47 μm, the insertion loss changes moderately, from about 0.04 dB to 0.16 dB. In contrast, the UF varies much more strongly, from nearly 0 dB up to approximately 2.5 dB. This confirms that the 2×2 MMI is more sensitive in terms of power balance than total transmitted power. Based on this tradeoff, $L_{\mathrm{MMI}} = 42\ \mu$m was selected.

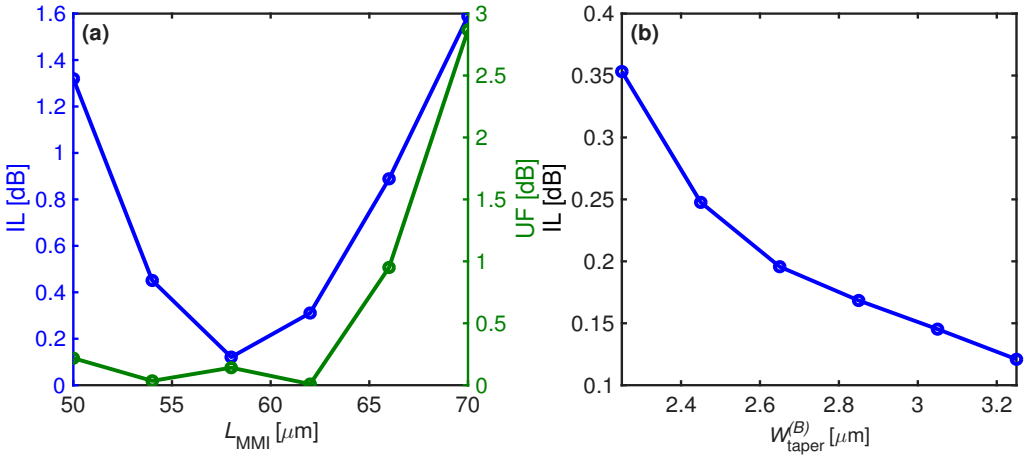


Figure 3.4: Optimization of the 1×4 MMI geometrical parameters at 1310 nm. (a) Insertion loss (IL) and uniformity factor (UF) as functions of L_{MMI}. (b) Insertion loss (IL) versus taper bottom width $W^{(B)}_{\mathrm{taper}}$.

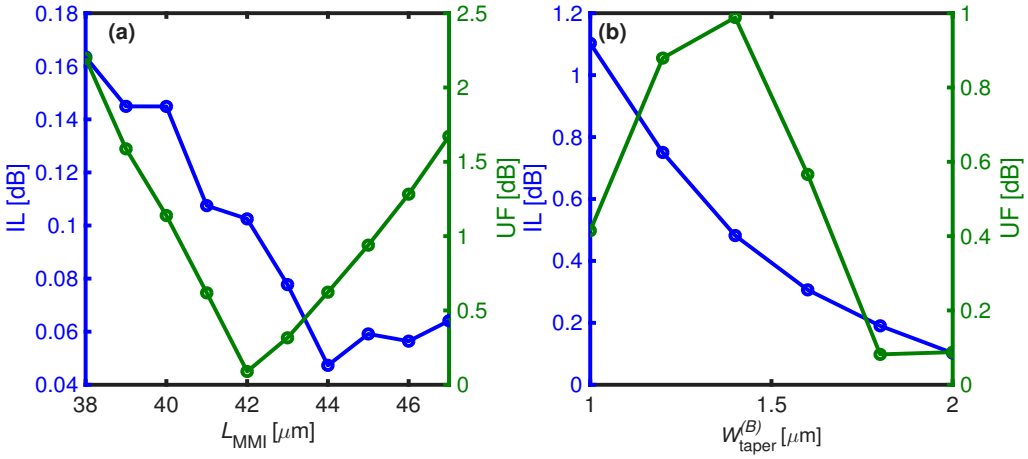


Figure 3.5: Optimization of the 2×2 MMI geometrical parameters at 1310 nm. (a) Insertion loss (IL) and uniformity factor (UF) as functions of L_{MMI}. (b) Insertion loss (IL) and uniformity factor (UF) as functions of taper bottom width $W^{(B)}_{\mathrm{taper}}$.

The taper optimization is shown in Fig. 3.5(b). In this sweep, $W^{(B)}_{\mathrm{taper}}$ was varied from 1 μm to 2 μm, while the MMI length was kept fixed at $L_{\mathrm{MMI}} = 42$ μm. For taper widths between approximately 1.8 μm and 2 μm, the UF remains below 0.1 dB, while the insertion loss remains below 0.2 dB. Considering both IL and UF, the final taper width was selected as $W^{(B)}_{\mathrm{taper}} = 2$ μm.

After determining the geometrical parameters at 1310 nm, the spectral performance of the optimized MMI structures was evaluated over the entire O-band. This subsequent broadband analysis was required to verify that the dimensions selected at the central wavelength also provide acceptable insertion loss and output power uniformity over the target wavelength range.

3.4.4 Broadband Evaluation of the Optimized Designs in the O-band

After determining the geometrical parameters at the central wavelength of 1310 nm, the optimized MMI structures were evaluated over the entire O-band in order to investigate their spectral behavior and output power uniformity under broadband operation.

Figure 3.6 illustrates the simulated spectral responses and the optical field distributions at the wavelength of 1310 nm for the designed 1×2, 1×4, and 2×2 MMI devices.

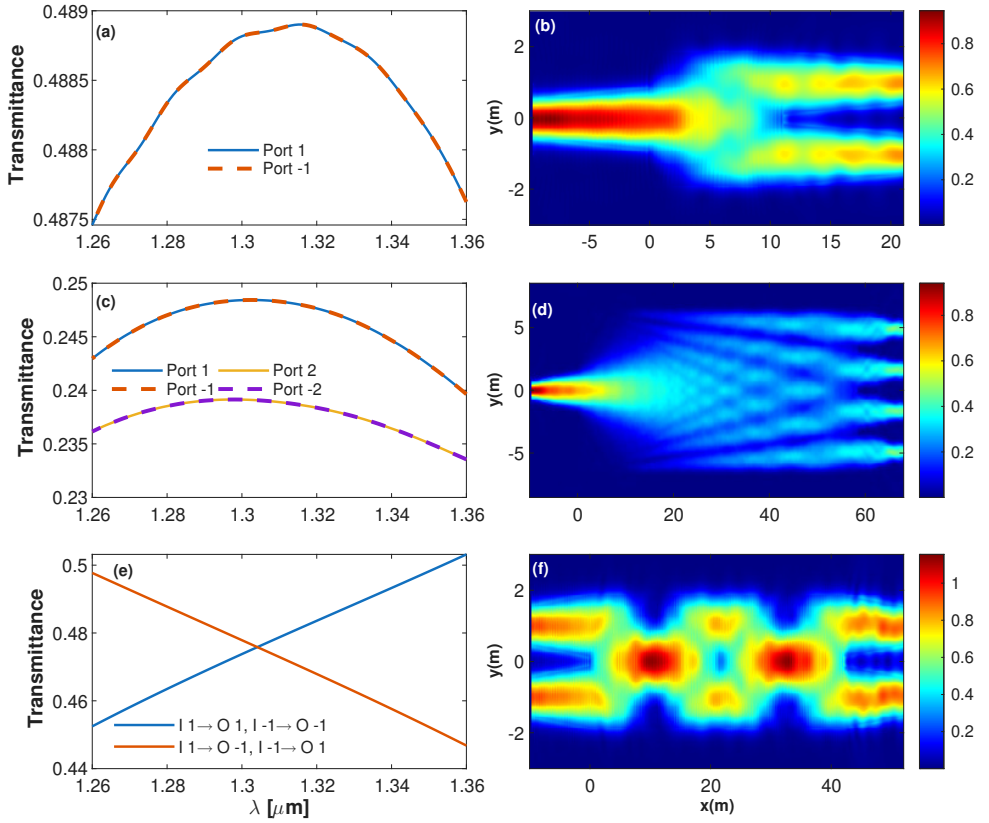


Figure 3.6: Simulated spectral responses and optical field distributions of the optimized MMI structures. (a) Spectral response of the 1×2 MMI. (b) Optical field distribution of the 1×2 MMI at 1310 nm. (c) Spectral response of the 1×4 MMI. (d) Optical field distribution of the 1×4 MMI at 1310 nm. (e) Spectral response of the 2×2 MMI. (f) Optical field distribution of the 2×2 MMI at 1310 nm.

The spectral responses are shown in Figs. 3.6(a), (c), and (e), while the corresponding optical field distributions at 1310 nm are presented in Figs. 3.6(b), (d), and (f), respectively. For the 1×2 MMI, the transmission at 1310 nm is nearly equally divided between the two output ports, with normalized transmission values close to 0.489 for each port. As observed in Fig. 3.6(a), the transmission remains relatively high across the O-band, indicating low insertion loss over a broad wavelength range. The corresponding field distribution shown in Fig. 3.6(b) confirms the formation of a symmetric self-image inside the multimode section.

For the 1×4 MMI, the maximum transmission occurs around the design wavelength of 1310 nm. At this wavelength, the outer output ports ($+2$ and -2) exhibit normalized transmission values of approximately 0.248, while the inner ports ($+1$ and -1) exhibit slightly lower values close to 0.238. As shown in Fig. 3.6(c), these transmission levels remain relatively stable throughout most of the O-band, demonstrating good spectral robustness and acceptable output power uniformity. The field distribution presented in Fig. 3.6(d) illustrates the formation of four output images along the output plane of the multimode region.

In the case of the 2×2 MMI, equal power splitting is obtained near 1310 nm, where the normalized transmission at each output port is approximately 0.476. However, compared with the previous topologies, the spectral response is more sensitive to wavelength variations. As shown in Fig. 3.6(e), even small deviations from the design wavelength, for example around 1304 nm, result in noticeable separation between the transmission curves of the two output ports. This behavior indicates increased sensitivity of the 2×2 configuration to wavelength-dependent phase variations and self-imaging conditions. The corresponding field distribution shown in Fig. 3.6(f) confirms the formation of the

expected two-fold image inside the multimode region.

Overall, the broadband analysis demonstrates that the 1×2 and 1×4 configurations maintain relatively stable spectral responses over the O-band, whereas the 2×2 structure exhibits higher sensitivity to wavelength variations, particularly in terms of output power balance.

3.5 Numerical Analysis of MMI Topologies

The numerical performance of the investigated MMI couplers was analyzed in detail and forms the basis for the interpretation of the experimental results presented in this chapter. The analysis focuses on three representative configurations, namely 1×2, 1×4, and 2×2 MMI couplers implemented on a TFLN rib-waveguide platform.

The primary figures of merit considered in the numerical study are the insertion loss (IL) and the output power uniformity (UF), as defined in Chapter 2. For convenience, they are briefly recalled here:

$$IL = -10 \log_{10}(T_{\text{out}}), \tag{3.3}$$

$$UF = -10 \log_{10} \left(\frac{T_{\text{min}}}{T_{\text{max}}} \right), \tag{3.4}$$

where T_{out} is the total transmitted power, and T_{min} and T_{max} denote the minimum and maximum normalized output powers, respectively.

The geometries analyzed in this section correspond to the finalized O-band designs described in Sec. 3.4. The simulations extending toward the C-band were not used as an additional design or optimization stage; the device dimensions remained unchanged from those selected for O-band operation.

Following fabrication, the available optical coupling interfaces enabled experimental characterization in the C-band, i.e., outside the nominal design range of the MMI structures. The finalized geometries were therefore re-evaluated numerically over this extended wavelength range for two purposes: first, to support the interpretation of the off-design experimental measurements, and second, to assess the topology-dependent robustness of the MMI structures under large spectral detuning.

Accordingly, the C-band analysis presented here should be regarded as an off-design robustness and measurement-support study, rather than as a second C-band design procedure. This distinction is particularly important with respect to Chapter 2, where the C-band was instead used as the target wavelength range for the systematic MMI design study.

3.5.1 Performance analysis in the Design Band

Figure 3.7 shows the simulated insertion loss (IL) and output power uniformity (UF) of the investigated MMI devices across the O-band under nominal design conditions.

The results indicate that all investigated MMI structures maintain relatively low insertion loss throughout the O-band, although the spectral sensitivity differs depending on the device topology and number of output ports.

Among the investigated configurations, the 1×2 MMI exhibits the most stable broadband behavior. The insertion loss remains low across the entire O-band, while the transmitted power remains nearly equally distributed between the two output ports. This behavior indicates that the self-imaging condition of the 1×2 structure is relatively robust against wavelength variations within the considered spectral range.

The 1×4 configuration exhibits slightly higher insertion loss together with increased sensitivity in output power uniformity. Nevertheless, the overall spectral response remains relatively stable throughout most of the O-band. Although moderate differences appear between the inner and outer output ports, the device preserves acceptable power balance and low-loss operation within the target wavelength range.

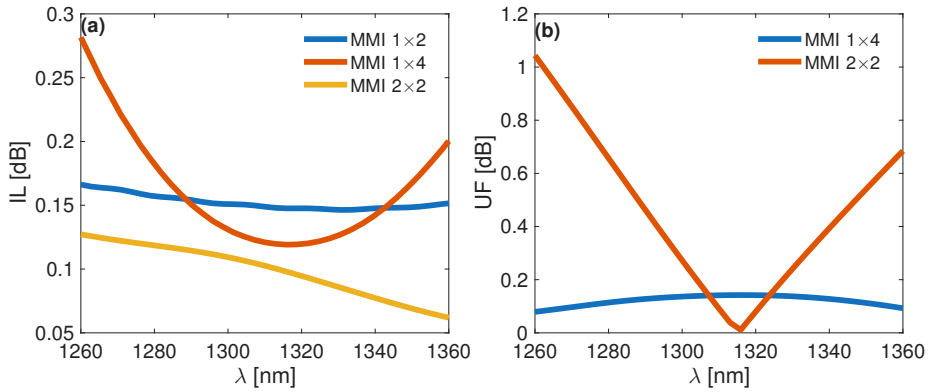


Figure 3.7: Simulated performance of the 1×2, 1×4, and 2×2 MMI couplers in the O-band: (a) insertion loss and (b) output power uniformity. The uniformity of the 1×2 MMI is not shown in (b), since ideal equal splitting leads to a nominal UF value of 0 dB.

In contrast, the 2×2 MMI exhibits a noticeably higher sensitivity to wavelength variations, particularly in terms of output power balance. While the insertion loss remains relatively stable, the UF changes more significantly as the wavelength deviates from the design wavelength, especially near the spectral edges. This behavior indicates that the interference condition in the 2×2 configuration is more strongly affected by spectral detuning compared with the other investigated topologies.

Overall, the results show that increasing the number of ports and the complexity of the multimode interference pattern generally increases the spectral sensitivity of the structures. Nevertheless, all investigated designs maintain acceptable insertion loss within the target O-band range.

3.5.2 Off-Design Spectral Response Toward the C-Band

Although the proposed MMI structures were originally designed for operation in the O-band, their spectral response was further evaluated over an extended wavelength range toward the C-band. This additional analysis provides insight into the extent to which the different MMI topologies preserve their performance outside the nominal operating range and allows a comparative assessment of their robustness under off-design conditions.

Figure 3.8 shows the simulated transmittance spectra of the investigated MMI devices over the extended wavelength range from the O-band toward the C-band. The three investigated topologies exhibit different spectral behaviors as the wavelength deviates from the design region.

Figure 3.8(a) shows the transmittance response of the 1×2 MMI coupler as a function of wavelength. It can be observed that, even when moving away from the design wavelength region toward the C-band, the transmitted power remains relatively equally distributed between the two output ports. In particular, the transmittance decreases only gradually, from approximately 48% to nearly 44% for each output port. This limited degradation indicates that the 1×2 topology maintains a relatively robust broadband behavior over the investigated spectral range.

The transmittance response of the 1×4 MMI coupler is shown in Fig. 3.8(b). In this case, the broadband performance strongly depends on the output port position. The outer ports, namely ports ± 2, preserve transmittance values close to 25% over a relatively wide wavelength range. In contrast, the inner ports, namely ports ± 1, exhibit significantly stronger wavelength sensitivity, with their transmitted power progressively decreasing to values below 10% toward the end of the analyzed spectral range. This behavior indicates that the four-fold self-imaging condition becomes increasingly perturbed under off-design operation, leading to degradation in both insertion loss and output power uniformity.

A different behavior is observed for the 2×2 MMI, as shown in Fig. 3.8(c). In this case, although the total transmitted power remains relatively stable over the

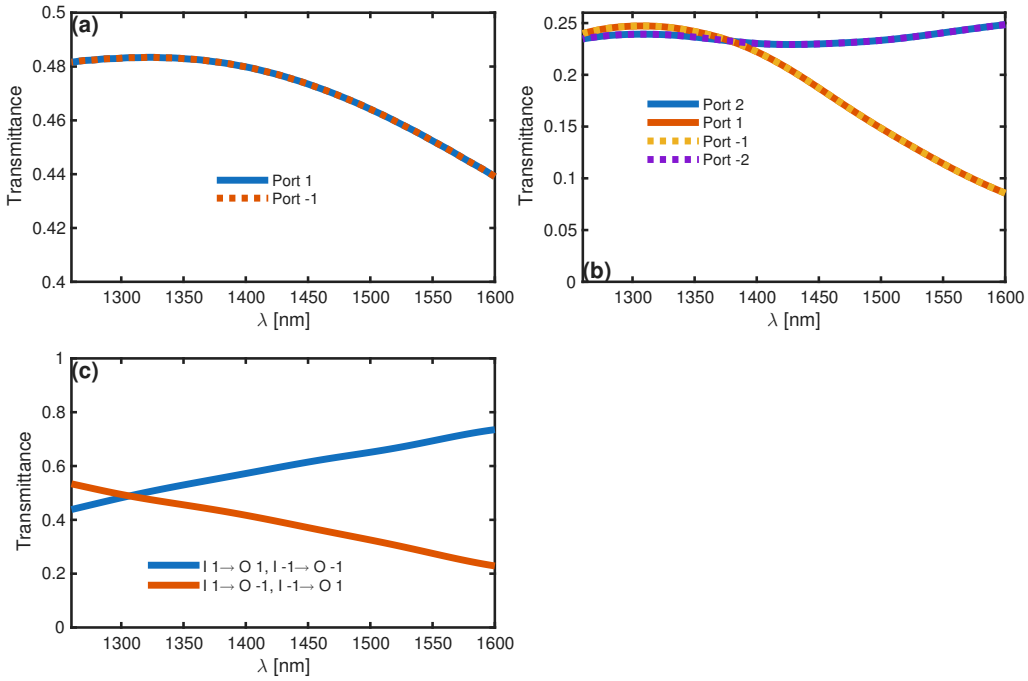


Figure 3.8: Simulated transmittance spectra of the designed MMI devices over an extended wavelength range from the O-band toward the C-band. (a) 1×2 MMI coupler. (b) 1×4 MMI coupler. (c) 2×2 MMI coupler.

investigated wavelength range, the power distribution between the two output ports changes significantly with wavelength.

As the wavelength increases from the O-band toward the C-band, the transmitted power progressively shifts toward the straight-through paths ($I1 \rightarrow O1$ and $I-1 \rightarrow O-1$). Conversely, the transmission associated with the cross-coupled paths ($I1 \rightarrow O-1$ and $I-1 \rightarrow O1$) gradually decreases over the same spectral range.

This wavelength-dependent redistribution of optical power can be further illustrated using two representative wavelength points. Around 1308.5 nm, where the UF approaches 0 dB, both output ports exhibit nearly identical normalized transmittances close to 48.9%. This corresponds to an almost perfectly balanced output distribution, while the insertion loss remains low, approximately 0.09 dB. In contrast, near 1600 nm, where the UF reaches its largest value within the analyzed wavelength range, the transmitted powers become approximately 23% and 73%, revealing a pronounced imbalance between the output ports.

As a consequence, the insertion loss varies only moderately, from approximately 0.047 dB to 0.159 dB across the investigated spectral range, whereas the UF exhibits a much stronger wavelength dependence, reaching values close to 5 dB near 1600 nm. This behavior confirms that, for the 2×2 configuration, the output power balance is considerably more sensitive to spectral detuning than the total transmitted power.

Overall, the extended spectral analysis confirms that the robustness of MMI devices is strongly topology dependent. Simpler splitting configurations, such as the 1×2 MMI, exhibit higher tolerance to wavelength detuning, whereas structures involving more complex interference conditions exhibit increased sensitivity to off-design operation and output power imbalance.

3.5.3 Combined Impact of Thickness and Wavelength Variations

3.5.3.1 Realized Fabrication Conditions

In practice, the fabricated devices may differ from the nominal design assumptions reported above. In particular, the realized rib thickness, the actual etch depth, and the coupling interfaces available on the fabricated chips can modify the expected optical response. These deviations are especially relevant when the devices are measured outside their original design band or when the fabricated chip differs from the one initially assumed during simulation.

In the present study, the experimentally characterized devices were measured under practical conditions that should be taken into account during result interpretation. These include:

- possible deviations between nominal and realized rib thickness,
- chip-specific coupling interfaces,
- measurement in a wavelength range different from the original design band,
- device-to-device variability across chips or fabrication runs.

Where appropriate, these factors are explicitly discussed together with the experimental results presented later in this chapter.

In practical fabrication processes, variations in the rib thickness are unavoidable and directly impact both the geometrical and optical properties of the device. In the considered lithium-niobate platform, the lithographic process defines the top width of the waveguides, while the bottom width is not independently controlled. Instead, it is governed by the rib thickness (t_{rib}) and the sidewall angle (θ), which is assumed to be 55° in this work.

According to the dimensional characterization and fabrication feedback obtained from the fabricated devices, the most significant deviation from the nominal design parameters was associated with t_{rib}, which was reported to vary from the nominal value of 400 nm down to approximately 300 nm. Since no comparable deviations were observed for the remaining geometrical parameters, the present analysis primarily focuses on the impact of rib-thickness variations.

As a consequence, changes in t_{rib} modify the bottom widths of the waveguide sections while leaving the lithographically defined top widths unchanged. These geometrical variations alter the effective waveguide cross-section of the MMI region, the access waveguides, and the taper sections. Consequently, the modal properties, the self-imaging condition, and the resulting optical response may deviate from those predicted for the nominal 400 nm rib geometry.

Therefore, the comparison between simulation and experiment presented in this chapter is not intended as a strict one-to-one validation of the nominal design, but rather as an interpretation of topology-dependent trends under realistic fabrication and measurement conditions.

In this section, the combined effect of rib thickness and wavelength variations on the performance of the MMI devices is investigated through two-dimensional parameter maps.

3.5.3.2 1×2 MMI: Thickness and Wavelength Sensitivity

For the 1×2 MMI configuration, the insertion loss is evaluated at a single output port. Due to the symmetric design of the device, both output ports exhibit identical behavior, and therefore the analysis of one port is sufficient.

In the ideal case of equal power splitting, the insertion loss at each output port is expected to be approximately 3 dB, corresponding to a 50/50 power division. Deviations from this value therefore indicate additional loss mechanisms.

Figure 3.9 shows the insertion loss as a function of wavelength and rib thickness, where the rib thickness is varied from 300 nm to 400 nm and the wavelength spans from the O-band toward longer wavelengths.

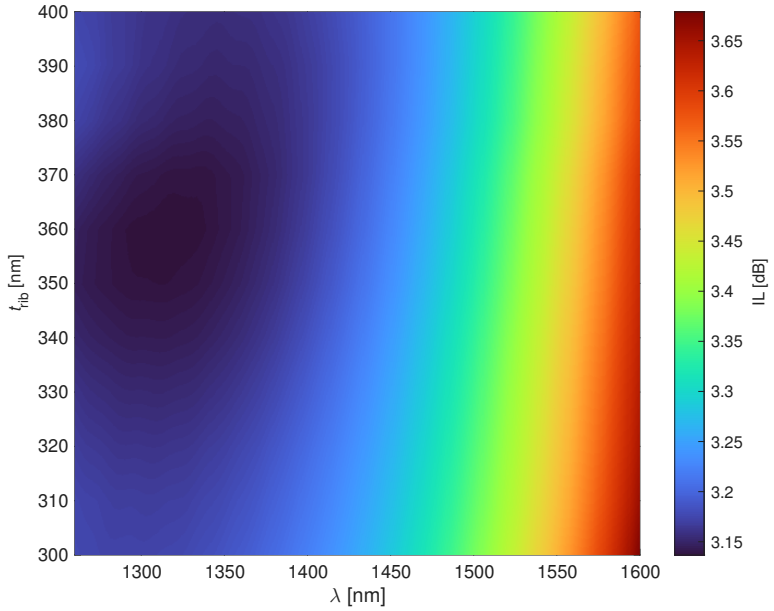


Figure 3.9: Insertion loss map of the 1×2 MMI at one output port as a function of wavelength and rib thickness, illustrating the combined effect of fabrication-induced thickness variations and spectral detuning.

As observed in Fig. 3.9, the insertion loss remains relatively stable over a broad wavelength range, even in the presence of significant thickness variations. The values remain close to the expected 3 dB level, confirming the inherent robustness of the 1×2 MMI topology.

In particular, the nearly vertical color distribution observed in the map indicates that the insertion loss is only weakly affected by rib-thickness variations within the investigated range. This behavior suggests that the spectral response is dominated more strongly by wavelength variations than by moderate fabrication-induced thickness deviations.

Within the O-band, the lowest insertion loss values are observed, indicating that the device operates close to its optimal condition within the designed wavelength range. Interestingly, a further reduction in insertion loss can be identified for slightly reduced thickness values, particularly when the rib thickness approaches $t_{\mathrm{rib}} \approx 360$ nm.

For example, at 1310 nm, the insertion loss decreases from approximately 3.20 dB for $t_{\mathrm{rib}} = 400$ nm to approximately 3.14 dB for $t_{\mathrm{rib}} = 360$ nm. However, this improvement remains relatively limited over the investigated thickness range.

Overall, for a fixed wavelength, the insertion loss exhibits only limited variation with rib thickness within the investigated range. In contrast, a stronger dependence on wavelength can be observed across the analyzed spectral range.

This behavior suggests that thickness-induced variations can locally improve the self-imaging condition within the design band, while having a limited impact outside it.

Overall, the 1×2 MMI demonstrates a high tolerance to fabrication-induced thickness variations. The insertion loss remains stable across a broad spectral range, while a local performance improvement is observed near the O-band for rib thickness values around 350–360 nm, indicating a slight shift of the optimal self-imaging condition.

3.5.3.3 1×4 MMI: Thickness and Wavelength Sensitivity

The same analysis is extended to the 1×4 MMI configuration by evaluating the insertion loss behavior of the inner ports (± 1) and outer ports (± 2), together with the output power uniformity. Owing to the structural symmetry of the device, the two inner ports ($+1$ and -1) exhibit identical responses, and the same applies to the two outer ports ($+2$

and −2). Therefore, only one representative inner port (+1) and one representative outer port (+2) are reported in Fig. 3.10.

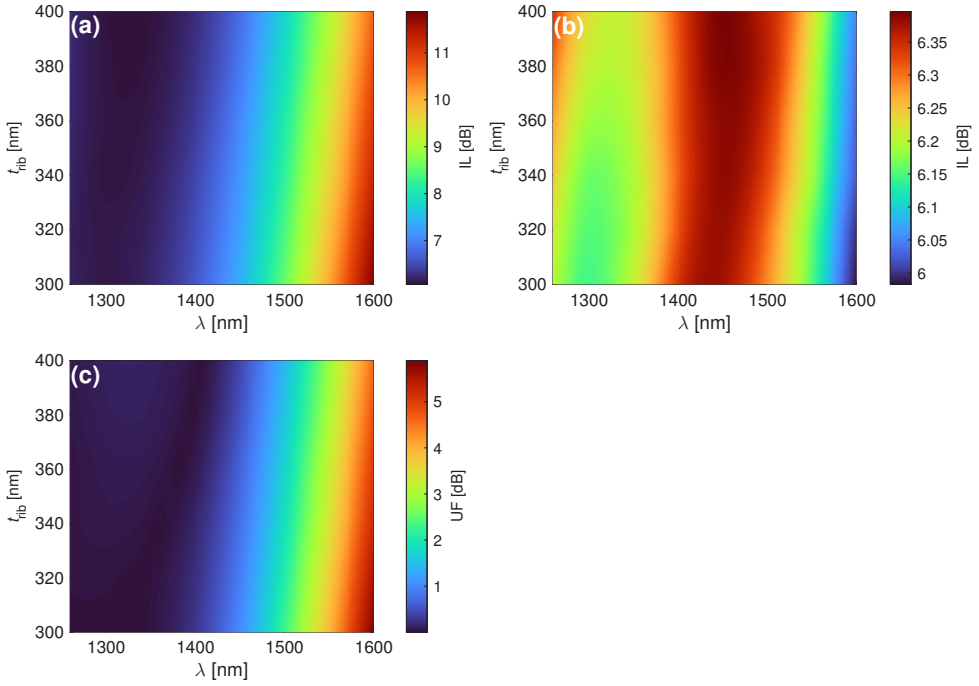


Figure 3.10: Insertion loss and uniformity maps of the 1 × 4 MMI as a function of wavelength and rib thickness. (a) Insertion loss at an inner output port (+1). (b) Insertion loss at an outer output port (+2). (c) Output power uniformity (UF) of the device.

Figure 3.10(a) shows the insertion loss behavior of one of the inner ports (+1). Due to the symmetry of the structure, the other inner port (-1) has an identical response. The inner ports of the 1 × 4 MMI exhibit a noticeably stronger dependence on wavelength variations, while the effect of rib-thickness variations remains comparatively weaker within the investigated range.

Within the O-band, the minimum insertion loss is observed near the center of the operating wavelength range 1310 nm, where the device operates close to the optimal self-imaging condition. In this region, the optimal behavior of the inner ports tends to occur for thickness values approaching the nominal design thickness. For example, at 1310 nm, the insertion loss changes only slightly, from approximately 6.13 dB for $t_{\mathrm{rib}} = 400$ nm to approximately 6.08 dB for $t_{\mathrm{rib}} = 300$ nm, confirming the relatively limited sensitivity to thickness variations near the design wavelength.

As the wavelength shifts toward the C-band, the insertion loss progressively increases, indicating degradation of the transmission efficiency under off-design operation. In this longer-wavelength regime, a more noticeable dependence on rib thickness can be observed. For instance, around 1550 nm, the insertion loss varies from approximately 9.07 dB to 10.1 dB over the considered thickness range. This behavior indicates that the inner ports become increasingly sensitive to geometrical perturbations as the operating wavelength moves away from the nominal self-imaging condition.

In contrast, the outer ports insertion loss behavior, shown in Fig. 3.10(b), exhibit a significantly more stable behavior. The map corresponds to port +2, while port −2 exhibits the same response owing to the structural symmetry of the device. The insertion loss remains within a relatively narrow range over the investigated wavelength span, indicating a more robust transmission behavior and a nearly constant power distribution close to the expected 25% splitting ratio.

The observed port-dependent sensitivity originates from the multimode nature of the self-imaging process. At the nominal design wavelength, the relative phases accumulated by the modes supported in the multimode section lead to the formation of four self-images

at the positions of the output waveguides. When the wavelength is detuned from 1310 nm, the modal propagation constants and beat lengths change, so that the relative phases accumulated over the fixed MMI length no longer correspond to the nominal four-fold self-imaging condition. Variations in rib thickness introduce an additional perturbation by modifying the modal effective indices and, consequently, the same relative phase relations.

Since the four output waveguides sample different transverse positions of the reconstructed field, this perturbation does not necessarily redistribute the optical power uniformly among them. In the present 1×4 geometry, the simulated responses indicate that spectral detuning primarily reduces the field contribution sampled by the inner ports, whereas the field lobes sampled by the outer ports remain comparatively better preserved. Consequently, ports ± 1 exhibit a stronger degradation with wavelength and dimensional variations, while ports ± 2 remain comparatively robust. This behavior is therefore a topology-dependent consequence of the perturbed four-fold self-imaging condition.

Figure 3.10(c) presents the output power uniformity (UF) of the 1×4 device. As expected, the best uniformity is obtained within the O-band, where the self-imaging condition is better satisfied. In this region, a slight improvement in uniformity can be observed for reduced thickness values. For example, at 1310 nm, reducing the rib thickness from 400 nm to 300 nm improves the UF from approximately 0.141 dB to approximately 0.001 dB, indicating an improved power balance between the output ports.

However, as the wavelength shifts toward the C-band, the uniformity progressively degrades, since the imbalance between the output ports becomes more significant under off-design operation. Although thickness variations do influence the UF behavior, their impact remains secondary compared with the intrinsic wavelength sensitivity of the multiport interference process.

Overall, the 1×4 MMI exhibits a pronounced wavelength-dependent behavior, with the inner ports showing strong sensitivity to both wavelength and thickness variations, while the outer ports remain comparatively robust. Although fabrication-induced thickness deviations affect the device performance, their influence is weaker than the intrinsic spectral sensitivity associated with the four-fold self-imaging condition.

3.5.3.4 2×2 MMI: Thickness and Wavelength Sensitivity

The thickness sensitivity of the 2×2 MMI is analyzed by examining the insertion loss associated with the straight and cross-coupling transmission paths, together with the output power uniformity. The straight transmission paths correspond to $I1 \rightarrow O1$ and $I-1 \rightarrow O-1$, while the cross-coupling paths correspond to $I1 \rightarrow O-1$ and $I-1 \rightarrow O1$. Owing to the structural symmetry of the device, each pair of corresponding transmission paths exhibits identical behavior.

Figure 3.11(a) shows the insertion loss associated with the straight transmission path ($I1 \rightarrow O1$). The insertion loss varies approximately between 1.2 dB and 3 dB across the investigated parameter space, with values close to 3.6 dB observed within the O-band, corresponding to the nominal design condition of balanced power splitting.

As the wavelength increases and moves away from the O-band region, the transmission toward the straight-through port progressively increases. However, this behavior does not indicate an overall improvement in device performance. Instead, it reflects a redistribution of optical power between the output ports, leading to a deviation from the ideal 50/50 splitting condition.

As further observed in Fig. 3.11(a), reduced rib-thickness values enhance the transmission toward the straight-through port, reinforcing the imbalance between the two output paths. This behavior indicates that both wavelength detuning and thickness reduction tend to favor the straight-through propagation path at the expense of the cross-coupling path.

As shown in Fig. 3.11(b) for the cross port, the best transmission condition is observed within the O-band, where the self-imaging condition is optimally satisfied. As the wavelength increases and deviates from the nominal operating region, the transmission toward the cross port progressively decreases.

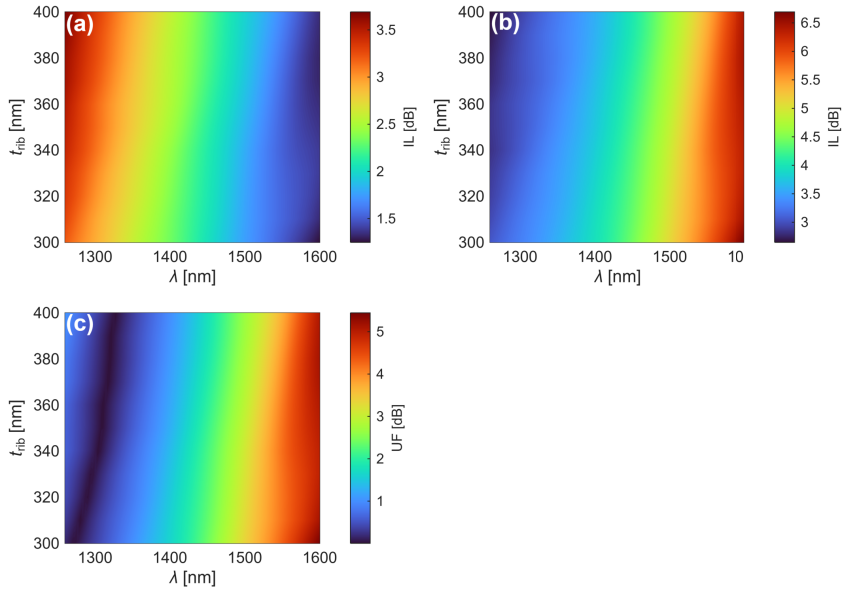


Figure 3.11: Insertion loss and uniformity maps of the 2×2 MMI as a function of wavelength and rib thickness. (a) Insertion loss for the straight transmission path. (b) Insertion loss for the cross-coupling path. (c) Output power uniformity (UF) of the device.

Similarly, reducing the rib thickness leads to degradation of the transmission efficiency associated with the cross path, while the best performance occurs near the nominal thickness of $t_{\mathrm{rib}} = 400$ nm.

Although rib-thickness variations also affect the transmission characteristics, their influence remains less pronounced than the wavelength-dependent transmission variations observed across the investigated spectral range. This behavior indicates that the dominant sensitivity mechanism of the 2×2 MMI is associated primarily with spectral detuning rather than moderate fabrication-induced thickness deviations.

Figure 3.11(c) presents the output power uniformity (UF) of the 2×2 MMI. The most balanced power distribution is achieved around the O-band, consistent with the nominal design wavelength. As the wavelength deviates from this region, the uniformity degrades significantly, indicating increasing imbalance between the output ports.

3.6 Device Layout, Fabrication and Chip Organization

3.6.1 Device Layout

Figure 3.12 shows the layout of the fabricated devices, including both the design-level implementation and the corresponding realized structures on the chip.

The main MMI devices and reference structures are explicitly labeled in Fig. 3.12(a) to facilitate their identification within the complete photonic circuit.

The fabricated chip includes both reference structures provided by the foundry and the MMI devices designed in this work. All devices are accessed through grating couplers designed for operation in the C-band, enabling vertical fiber-to-chip coupling during experimental characterization.

The input and output ports of each device are connected to specific grating couplers through routing waveguides. For the 1×2 MMI, the input signal is injected through Grating 2, while the outputs are collected at Gratings 3 and 4. For the 1×4 MMI, the input is connected to Grating 5, and the outputs are routed to Gratings 6, 7, 10, and 11. In the case of the 2×2 MMI, the input ports correspond to Gratings 12 and 13, while the outputs are connected to Gratings 14 and 15.

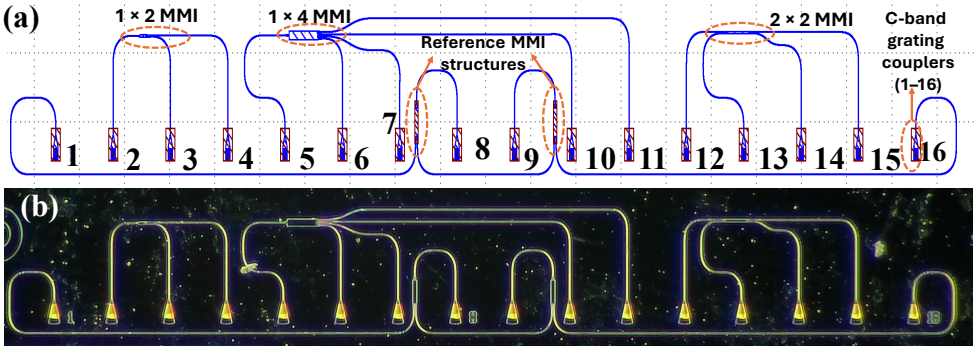


Figure 3.12: (a) Layout of the fabricated photonic circuit implemented in KLayout. (b) Optical microscope image of the corresponding fabricated chip. The figure illustrates the routing of the input and output waveguides toward grating couplers, as well as the placement of reference and test MMI devices. The 1×2, 1×4, and 2×2 MMI devices, together with the reference MMI structures, are explicitly identified in panel (a). The numbered elements 1–16 correspond to the C-band grating couplers used to access the different device ports.

In addition, two reference paths are included on the chip for calibration purposes. The first reference path connects Grating 8 to Grating 1, while the second connects Grating 9 to Grating 16. These reference structures, consisting of two 1×2 MMI splitters provided by the foundry PDK, allow the estimation of the baseline losses associated with the measurement setup, including fiber coupling and grating-coupler losses.

The baseline loss of the measurement chain was estimated by directly connecting the optical source to the optical spectrum analyzer, without the device under test (DUT) in the optical path. Using this reference configuration, the overall insertion loss of the measurement setup was found to be on the order of 27 dB. Considering an additional coupling loss of approximately 5 dB per grating coupler, the total system loss is expected to be around 37 dB. This value is in reasonable agreement with the measured response of the 1×2 reference MMI, which was found to be around 40 dB, when accounting for the nominal 3 dB splitting loss. This observation provides additional confidence in the consistency of the measurement and normalization procedure.

3.6.2 Chip Organization and Measurement Repeatability

In foundry-oriented photonic fabrication workflows, multiple nominally identical chips are often distributed across different regions of the same mask in order to evaluate process repeatability, wafer-level non-uniformity, and device-to-device consistency. This strategy is particularly useful when characterizing passive photonic components, since it enables direct comparison among replicated structures fabricated under nominally identical process conditions.

As shown in Fig. 3.13(a), diced photonic chips originating from different regions of the same fabrication mask may be organized in a labeled holder for traceable experimental characterization.

Such organization allows each measurement to be associated with a specific chip identity and original mask location.

Two identical chips containing the investigated MMI devices were fabricated for this study. Figure 3.13(b) shows the chip whose experimental results are presented in this chapter. Among the two fabricated chips, this chip exhibited the closest agreement with the numerical predictions and the most consistent experimental behavior.

Within the present experimental framework, chip indexing, controlled injection geometry, polarization adjustment, and repeated measurements were used to support the interpretation of the measured behavior of the fabricated MMI couplers.

3.7 Measurement Setup and Experimental Methodology

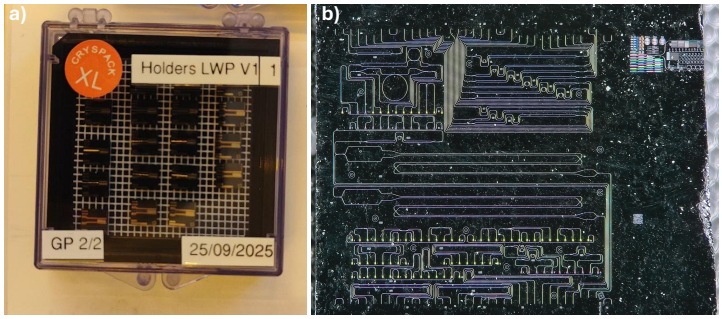


Figure 3.13: (a) Example of diced photonic chips mounted and indexed for traceable experimental characterization. (b) Optical microscope image of the fabricated TFLN chip used for the experimental characterization reported in this chapter. The chip contains multiple integrated photonic devices, including the investigated MMI structures.

Two fiber-based optical characterization configurations were considered during the experimental activities, depending on the optical coupling interface available on the photonic chip. Figure 3.14 schematically summarizes the corresponding optical paths. In both configurations, the C-band optical signal is first passed through a polarization controller (PC), while the transmitted signal is acquired using an optical spectrum analyzer (OSA) and transferred to a computer for data visualization and analysis. The main difference between the two configurations lies in the fiber-to-chip coupling interface.

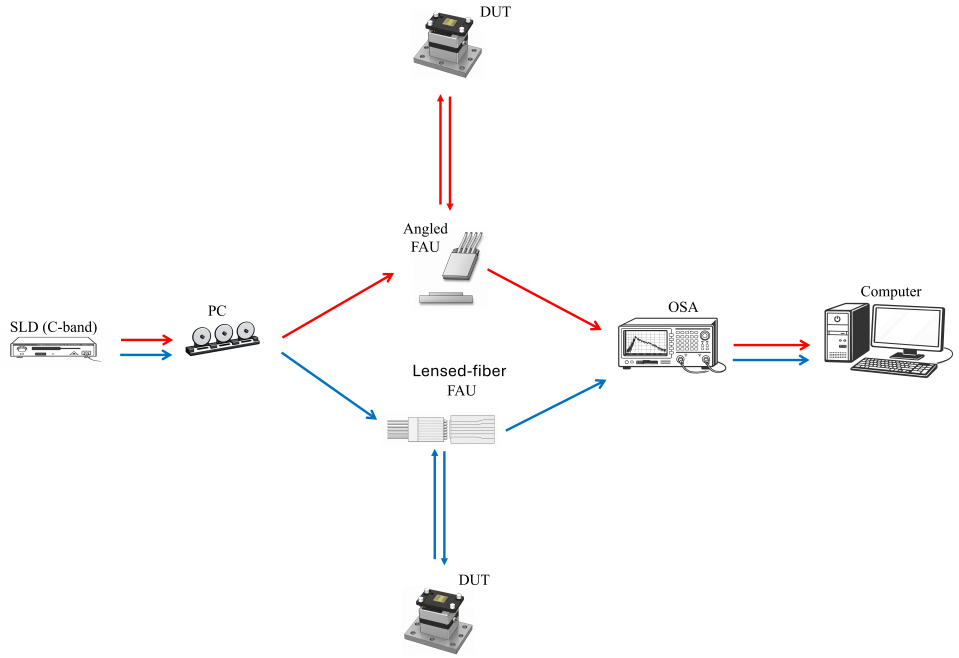


Figure 3.14: Schematic representation of the two fiber-based optical characterization configurations considered during the experimental activities. The red optical path corresponds to vertical coupling through the on-chip grating couplers using an angled fiber array unit (FAU), whereas the blue optical path corresponds to the alternative edge-coupling configuration. In both cases, the C-band optical signal passes through a polarization controller (PC) before reaching the device under test (DUT), and the transmitted signal is collected and directed to an optical spectrum analyzer (OSA). The acquired spectra are subsequently transferred to a computer for visualization and analysis. The arrows indicate the optical signal path and do not represent the physical orientation of the coupling interfaces with respect to the chip.

For the MMI devices investigated in this chapter, the experimental measurements were performed using the grating-coupler configuration shown by the red path in Fig. 3.14. In

this arrangement, the angled FAU provides simultaneous optical access to the integrated grating couplers used for signal injection and collection. The second configuration represents the alternative coupling approach available for devices providing direct access to the waveguide facets and is discussed in Sec. 3.7.3.

3.7.1 General Measurement Strategy

The experimental characterization of the fabricated photonic integrated circuits was carried out using a fiber-based optical measurement setup that enables selective access to the input and output ports of the chip. The setup is designed to support accurate fiber-to-chip alignment, polarization control, and stable acquisition of transmission spectra over the wavelength range of interest.

In integrated photonic measurements, input and output coupling plays a central role in determining the reliability of the extracted device response. For this reason, the measurement procedure was structured so as to ensure repeatable alignment, stable optical injection, and consistent acquisition across different devices and chips. The methodology adopted in this work therefore combines optical alignment tools and polarization tuning to minimize measurement uncertainty not directly related to the device under test.

3.7.2 Laboratory Setup

A fiber-based optical characterization setup used at PICadvanced during on-site research activities is shown in Fig. 3.15. The setup was used for the optical characterization of the fabricated MMI devices and it includes the chip holder, precision translation stages used for fiber alignment, and microscope-assisted visualization of the chip and fiber-to-chip coupling region. The microscope camera system provides approximately 10× magnification for visual inspection of the device under test during the alignment procedure. The chip and fiber-coupling assemblies are mounted on precision positioning stages, enabling fine adjustment of their relative position and accurate alignment at the fiber-to-chip coupling interface.

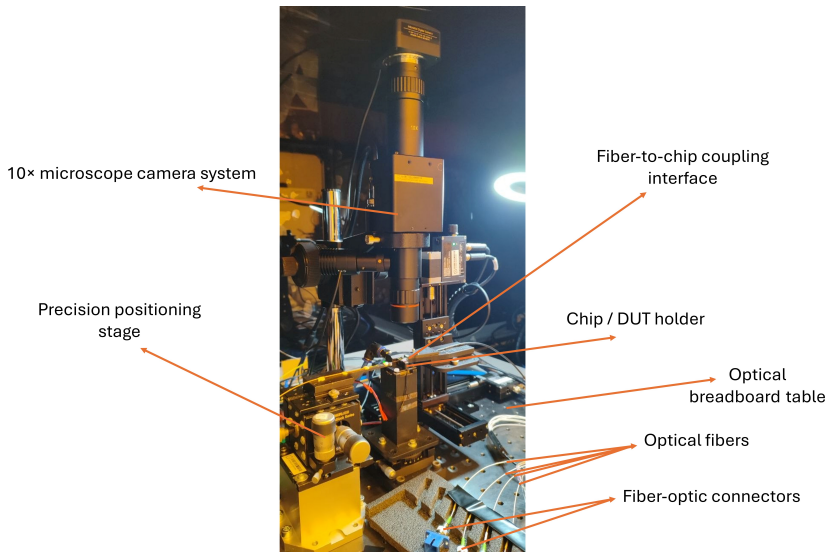


Figure 3.15: Fiber-based optical measurement setup used for the alignment and characterization of photonic integrated circuits. The setup integrates precision positioning stages and microscope-based inspection tools for fiber-to-chip alignment. The main visible components include the 10× microscope camera system, the chip/DUT holder, the fiber-to-chip coupling interface, the optical fibers and fiber-optic connectors, and the precision positioning stages used for fiber and sample alignment.

Although the exact measurement configuration can vary depending on the coupling interface and device layout, the general purpose of such a setup remains the same: to provide controlled optical injection and reliable monitoring of the transmitted signal

through the photonic component under test. For the measurements reported in this work, the complete optical characterization chain additionally included an optical source, a fiber polarization controller, and an optical spectrum analyzer for acquisition of the transmitted optical signal. These external instruments were connected to the alignment station but are not visible in Fig. 3.15.

3.7.3 Injection Configurations

To accommodate different coupling interfaces, photonic integrated circuits can be characterized using different optical injection configurations. Two representative approaches are illustrated in Fig. 3.16. The choice between these configurations is primarily determined by the optical interface implemented on the chip. Vertical coupling is appropriate for devices equipped with surface grating couplers, whereas edge coupling is used when the optical waveguides terminate at accessible chip facets.

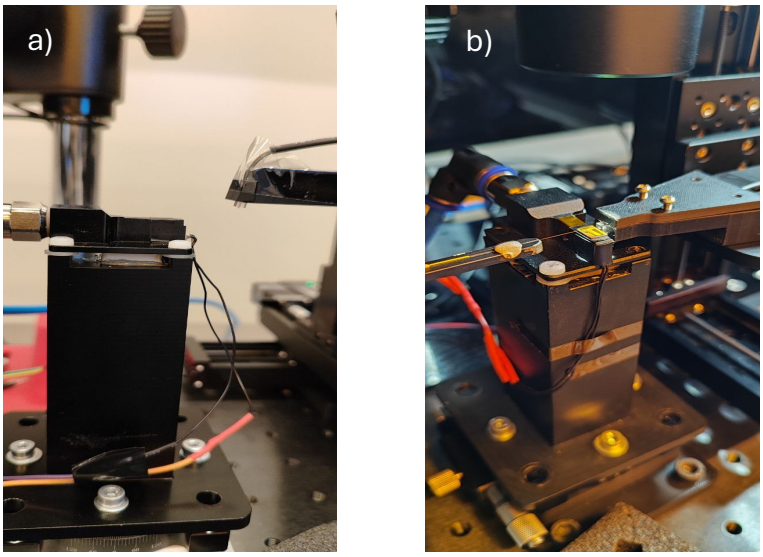


Figure 3.16: Examples of optical coupling configurations used for photonic chip characterization. (a) Vertical fiber-to-chip coupling through grating couplers. (b) Horizontal edge coupling using lensed fibers aligned with the chip facets. The appropriate coupling configuration is selected according to the chip layout and the available optical interfaces.

The first configuration employs vertical fiber-to-grating coupling, where the optical signal is coupled through surface grating couplers. In this case, the input fiber is positioned at a controlled tilt angle with respect to the chip surface in order to satisfy the grating coupling condition. The second configuration corresponds to horizontal in-plane coupling, in which the optical fiber is aligned parallel to the chip surface and directly matched to the waveguide facet.

The two approaches involve different experimental requirements. Grating-coupler access facilitates the characterization of multiple devices distributed across the chip surface without requiring direct access to the chip edge. In contrast, edge coupling provides direct in-plane excitation of the waveguide, but requires an accessible waveguide facet and accurate lateral and vertical alignment of the lensed fiber with the corresponding waveguide mode.

In the present work, the experimental characterization of the MMI devices reported in this chapter was performed using vertical fiber-to-chip coupling through grating couplers integrated on the photonic chips. This configuration enables non-invasive optical access without direct fiber-to-facet contact, while providing flexibility in addressing multiple devices on the chip. This choice was dictated by the coupling interfaces available on the fabricated MMI chip, whose input and output ports were routed to integrated C-band grating couplers. The edge-coupling configuration shown in Fig. 3.16(b) is therefore

presented as an alternative approach applicable to devices providing direct waveguide-facet access, rather than as the configuration used for the MMI measurements reported in this chapter.

However, the use of grating couplers introduces additional wavelength-dependent coupling losses and spectral filtering effects. As a result, the measured transmission spectra include both the intrinsic device response and the characteristics of the coupling interface.

For this reason, the experimental results presented in this chapter are primarily interpreted in terms of relative trends, power distribution, and topology-dependent behavior, rather than absolute insertion loss values directly comparable to ideal numerical predictions.

3.7.4 Polarization Control

Polarization control is a crucial aspect of the measurement of anisotropic or polarization-sensitive integrated photonic platforms such as thin-film lithium niobate. As indicated in Fig. 3.14, the polarization controller is placed in the input optical path between the C-band source and the fiber-coupling interface. In the adopted setup, the input polarization state is adjusted using paddle-type fiber polarization controllers, as shown in Fig. 3.17.

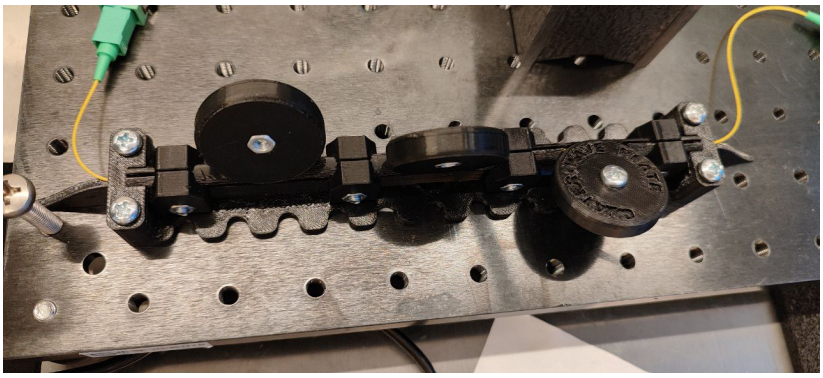


Figure 3.17: Paddle-type fiber polarization controller used to tune the polarization state of the injected light. Controlled birefringence is introduced in the optical fiber by rotating the paddles, enabling alignment of the incident field with the polarization response of the device under test.

By manually rotating the paddles, controlled birefringence is induced in the fiber, allowing the output polarization state to be continuously tuned. This procedure enables the optical excitation to be matched to the relevant polarization eigenmode of the device under test. Once the optimal polarization state is reached, the transmission measurement can be carried out without further perturbing the coupling condition.

In practice, proper polarization adjustment is essential not only for maximizing the measured transmission but also for ensuring measurement consistency across nominally identical devices.

3.7.5 Practical Measurement Considerations

In addition to alignment and polarization control, several practical factors contribute to the quality and repeatability of the measurement. These include the cleanliness of the optical fibers, the chip surface, and the coupling interfaces, as well as the mechanical stability of the setup and the reliability of the source and detector connections.

Imperfections or contamination at the fiber–chip interface may introduce additional insertion loss, back-reflections, or polarization perturbations that are not intrinsic to the device itself. For this reason, the extracted device response should be interpreted with awareness of the baseline losses and uncertainties associated with the experimental environment. In the present work, these factors are considered when interpreting the differences between numerical and experimental results.

3.8 Experimental Results

Although the proposed MMI devices were designed for operation in the O-band, the fabricated structures were experimentally characterized in the C-band using the available grating-coupler-based measurement chain. Rather than preventing validation, this off-design operating condition provides an opportunity to verify whether the topology-dependent trends predicted by the extended spectral simulations remain observable outside the nominal design band. The measured transmission was obtained by normalizing the output power with respect to a reference device available on the chip.

Consequently, the curves reported in Fig. 3.18 do not represent the raw transmission spectra. Since the DUT and reference paths were accessed through the same type of C-band grating couplers, the reference normalization partially compensates for their common wavelength-dependent response. This explains why the reported normalized transmission curves appear considerably flatter than the corresponding raw spectra. However, this normalization does not constitute a complete de-embedding of the grating-coupler response, and residual wavelength-dependent effects may remain because of differences in alignment, routing, and individual grating-coupler responses.

Figure 3.18 compares the measured and simulated transmission spectra of the second fabricated chip set for the (a,b) 1×2, (c,d) 1×4, and (e,f) 2×2 MMI configurations.

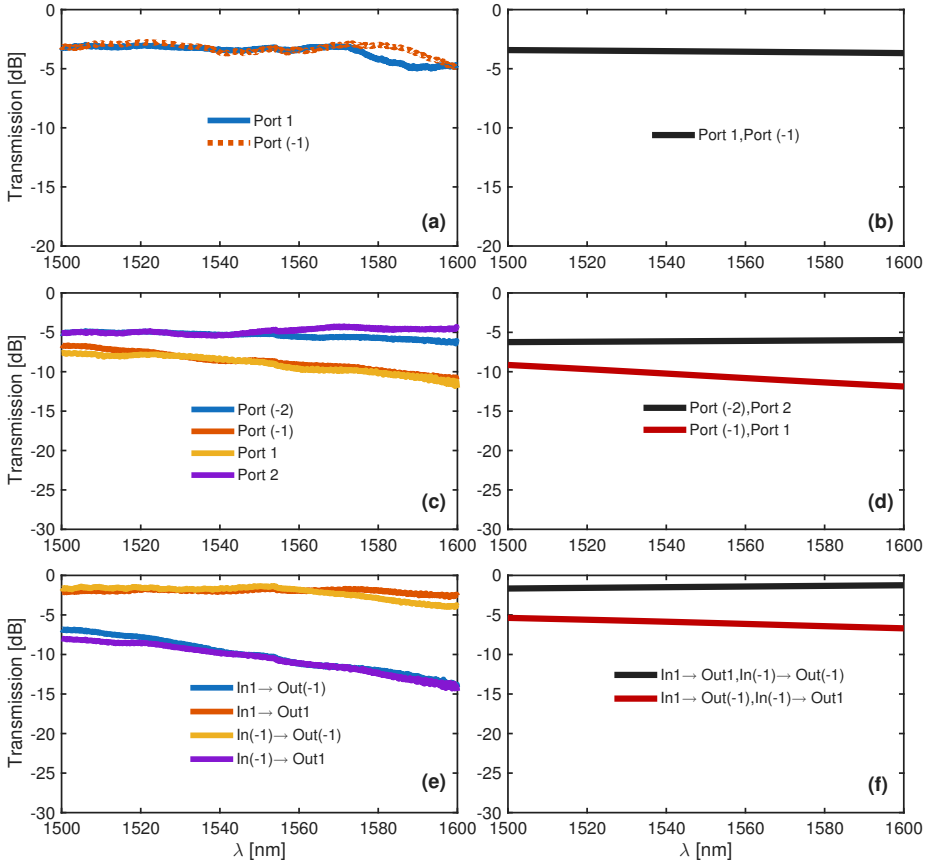


Figure 3.18: Measured and simulated transmission spectra of the second fabricated chip. (a) Measured response of the 1×2 MMI. (b) Simulated response of the 1×2 MMI. (c) Measured response of the 1×4 MMI. (d) Simulated response of the 1×4 MMI. (e) Measured response of the 2×2 MMI. (f) Simulated response of the 2×2 MMI.

For the 1×2 MMI, the measured spectra exhibit a relatively balanced response between the two output ports over the considered wavelength range and follow the general spectral trends predicted by the simulations. The insertion loss per port is observed to be around 3.5 dB near 1.55 μm, remaining reasonably close to the ideal 3 dB condition

expected for equal power splitting. This behavior confirms the relatively robust operation of the 1×2 topology, even under off-design operation in the C-band.

For the 1×4 MMI, a clear distinction between inner and outer ports is observed in both the measured and simulated spectra. The outer ports exhibit higher transmission levels, while the inner ports show a noticeable degradation, particularly toward longer wavelengths. This behavior is consistent with the numerical predictions, where the inner ports were found to be more sensitive to wavelength detuning. Although quantitative differences are present between the measured and simulated transmission levels, the measurements preserve the predicted distinction between the more strongly attenuated inner ports and the comparatively higher-transmission outer ports.

For the 2×2 MMI, the measured spectra exhibit a pronounced imbalance between the straight and cross-coupling transmission paths, confirming the strong sensitivity of this topology to the redistribution of optical power between its outputs. However, the agreement with the numerical results is primarily qualitative rather than quantitative. In particular, the relative transmission levels of the straight and cross-coupling paths differ substantially between measurement and simulation in the C-band.

This observation indicates that the experimentally observed 2×2 response remains strongly sensitive to off-design operation, but the individual path transmissions are also affected by practical fabrication and measurement conditions. Consequently, the experimental results support the predicted tendency toward strong output-power imbalance, while a direct quantitative correspondence between the individual simulated and measured transmission paths is not obtained.

To quantify the differences between the numerical and experimental responses, a direct comparison was performed at $\lambda = 1550$ nm, close to the center of the wavelength range used for the experimental characterization. Since the spectra in Fig. 3.18 are expressed in decibels, the corresponding linear transmission values were obtained using $T = 10^{T_{\mathrm{dB}}/10}$.

The relative deviation was then calculated using the simulated transmission as the numerical reference:

$$\delta = \frac{T_{\mathrm{sim}} - T_{\mathrm{meas}}}{T_{\mathrm{sim}}} \times 100\%. \tag{3.5}$$

In the numerical model, symmetry-equivalent output ports exhibit identical transmission and are therefore represented by a single simulated value. The experimentally measured responses, however, are not perfectly symmetric. For this reason, the two measured values corresponding to each symmetry-equivalent simulated response are retained separately in Table 3.1, rather than being averaged. A negative value of δ indicates that the measured transmission is higher than the corresponding simulated value, whereas a positive value indicates lower measured transmission.

Table 3.1: Comparison of simulated and measured linear transmission at $\lambda = 1550$ nm. For symmetry-equivalent ports, the single simulated response is compared separately with the two corresponding measured responses.

MMI	Output/path	T_{sim}	T_{meas}	δ (%)
1×2	Port 1	0.4432	0.4482	-1.12
1×2	Port (-1)	0.4432	0.4673	-5.45
1×4	Port 1	0.08870	0.1380	-55.60
1×4	Port (-1)	0.08870	0.1306	-47.24
1×4	Port 2	0.2447	0.3245	-32.62
1×4	Port (-2)	0.2447	0.3033	-23.94
2×2	Straight, In1–Out1	0.7109	0.6660	6.31
2×2	Straight, In(-1)–Out(-1)	0.7109	0.7315	-2.89
2×2	Cross, In1–Out(-1)	0.2580	0.09672	62.51
2×2	Cross, In(-1)–Out1	0.2580	0.09427	63.46

The quantitative comparison highlights a clear topology dependence. The 1×2 MMI exhibits the closest agreement between simulation and measurement, with relative

deviations of approximately 1.1%–5.5% for the two measured outputs. The measured asymmetry between the two ports is therefore relatively limited.

For the 1×4 MMI, larger deviations are obtained. The outer ports show relative deviations of approximately 24%–33%, whereas the inner ports exhibit deviations of approximately 47%–56%. Nevertheless, both the numerical and experimental results preserve the same qualitative port-dependent behavior, with higher transmission at the outer ports and stronger attenuation at the inner ports.

For the 2×2 MMI, the agreement depends strongly on the transmission path. The straight paths show relatively close agreement, with deviations of approximately 6.3% and -2.9% for the two symmetry-related measurements. In contrast, substantially larger deviations of approximately 62.5%–63.5% are observed for the cross-coupling paths. Nevertheless, both simulation and experiment preserve the same overall power-distribution trend at 1550 nm, with the straight paths exhibiting considerably higher transmission than the cross-coupling paths.

Overall, the comparison indicates that the 1×2 topology provides the closest quantitative agreement, whereas the 1×4 device and the cross-coupling paths of the 2×2 MMI exhibit greater sensitivity to practical deviations. The remaining discrepancies may result from the combined influence of fabrication-induced geometrical variations, port-dependent fiber-to-chip coupling, polarization and alignment uncertainty, and the normalization procedure. These effects are expected to become more significant for transmission paths whose power levels are more sensitive to wavelength detuning and fabrication perturbations.

3.9 Conclusion

This chapter presented the design, fabrication-aware analysis, and experimental characterization of 1×2, 1×4, and 2×2 TFLN rib-waveguide MMI couplers. The investigated devices were analyzed in terms of insertion loss, output power uniformity, broadband spectral response, and robustness against fabrication-induced rib-thickness variations. The results reveal a pronounced topology-dependent behavior.

Among the investigated structures, the 1×2 MMI exhibits the highest robustness, maintaining low insertion loss and nearly balanced splitting over a wide wavelength range and under realistic thickness deviations. The 1×4 MMI shows a clear port-dependent response, where the outer ports remain relatively stable while the inner ports are significantly more sensitive to wavelength detuning and, to a lesser extent, rib-thickness variations. The 2×2 MMI, although relatively stable in terms of total transmitted power, exhibits a strong sensitivity in power distribution and output uniformity, indicating that its main limitation lies in the balance between the output ports rather than in the overall transmission efficiency.

The extended spectral analysis beyond the O-band also supports the interpretation of the experimental C-band characterization under off-design operating conditions, where the measured responses qualitatively follow the topology-dependent trends predicted by the simulations. Despite the fabrication deviations and the non-ideal operating conditions, the experimental investigation confirms that meaningful validation can be achieved by focusing on topology-dependent behavior rather than on absolute performance values.

Overall, these results demonstrate that TFLN-based MMI couplers constitute compact and fabrication-tolerant building blocks for integrated photonic circuits, while highlighting the fundamental role of device topology in determining their spectral stability, robustness, and experimental performance.

Chapter 4

Design of Wavelength-Selective Add Drop Filters

This chapter presents the design and analysis of wavelength-selective add–drop filters based on grating-assisted contra-directional coupling implemented on a hybrid SiN–TFLN platform.

A systematic design methodology is developed, starting from a single-channel configuration and extending toward dual- and multi-channel configurations using superimposed gratings. The influence of key geometrical parameters on drop efficiency, crosstalk, and spectral selectivity is investigated through parametric analysis.

The results demonstrate that multi-channel wavelength routing can be achieved within a single grating section while maintaining high drop-port transmission, strong through-port suppression, and controlled inter-channel isolation. Fabrication-tolerance analysis further confirms the robustness of the proposed structures under realistic process variations.

4.1 Introduction

Wavelength-selective routing constitutes a key functionality in photonic integrated circuits (PICs), enabling wavelength-division multiplexing (WDM), channel management, and scalable optical signal processing [83]. This functionality is essential for optical transceivers, sparse-WDM access networks, on-chip monitoring, and scalable photonic interconnect fabrics [83].

In integrated photonics, wavelength routing is commonly implemented using resonant devices (e.g., microring resonators) or grating-based filtering structures. Resonant approaches offer compact footprints but inherently exhibit a periodic spectral response determined by their free spectral range (FSR), which can lead to parasitic resonances and increased sensitivity to fabrication and temperature variations [84], [85]. Consequently, multi-channel resonator-based systems often require active thermal tuning and stabilization.

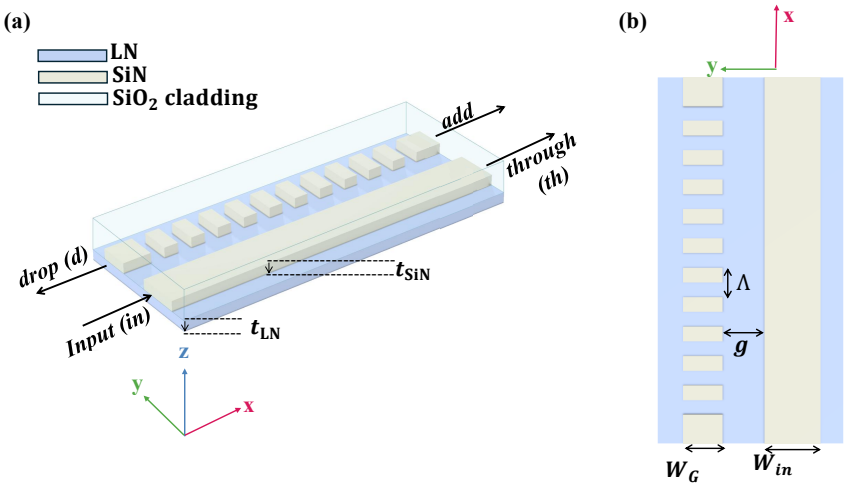
By exploiting Bragg-type phase matching between forward- and backward-propagating modes, CDC-based filters enable narrowband channel extraction with high extinction ratios and reduced sensitivity to resonance detuning [48], [86]. These properties make CDC-based add–drop filters particularly attractive for sparse-WDM routing and robust wavelength-selective operation.

In this thesis, wavelength-selective routing is achieved through the design of grating-assisted contra-directional add–drop filters on a hybrid SiN–TFLN platform, with particular emphasis on scalable multi-channel architectures based on superimposed grating concepts. This approach leverages the fabrication maturity and low propagation loss of SiN together with the low-loss and system-level compatibility of thin-film lithium niobate [87], [88].

4.2 Contra-Directional Coupling Principle

The add-drop filters investigated in this work are based on grating-assisted contra-directional coupling. Figure 4.1 shows the schematic of the single-channel grating-assisted add-drop filter employed throughout this work.

The device consists of two parallel waveguides, one of which is periodically corrugated to provide the phase-matching condition required for contra-directional coupling. Under this condition, the grating couples a forward-propagating mode in one waveguide to a backward-propagating mode in the adjacent waveguide at specific wavelengths.



(c) Fixed platform parameters

Parameter	Value
SiN thickness, t_{SiN}	300 nm
LN thickness, t_{LN}	300 nm
SiN sidewall geometry	Vertical (90°)
Upper cladding	SiO_2
n_{SiN} at 1.55 μm	1.98
$n_{\mathrm{SiO_2}}$ at 1.55 μm	1.445

Figure 4.1: Schematic of the single-channel grating-assisted add–drop filter implemented on a hybrid SiN–TFLN platform. (a) Three-dimensional view illustrating the input, through, drop, and add ports, as well as the SiN–TFLN vertical stack and the silica upper cladding, which is shown transparently for clarity. (b) Top view of the coupling region highlighting the grating period Λ, the lateral separation g, and the waveguide widths W_{in} and W_G. The fixed geometrical and material parameters employed throughout the GACDC analysis are summarized in (c).

The periodic grating structure provides the phase matching required to couple optical modes that would otherwise remain phase mismatched [89].

In a grating-assisted contra-directional coupler (GACDC), two dissimilar waveguides are placed in close proximity. Therefore, in the absence of a grating perturbation, optical power launched into the input waveguide propagates mainly toward the through port. When a periodic perturbation is introduced, however, the grating compensates for the propagation-constant mismatch and enables coupling from the forward-propagating mode of the input waveguide to the backward-propagating mode of the neighboring waveguide [48].

The wavelength at which this interaction occurs is determined by the Bragg phase-matching condition

$$\beta_{\mathrm{fwd}} + \beta_{\mathrm{bwd}} = \frac{2\pi}{\Lambda}, \tag{4.1}$$

where β_{fwd} and β_{bwd} are the propagation constants of the forward- and backward-propagating interacting modes, respectively, and Λ is the grating period. This condition represents longitudinal momentum conservation: the spatial frequency of the grating provides the momentum required to couple two counter-propagating guided waves [48], [89].

For a target wavelength λ_0, the required grating period can be written as

$$\Lambda = \frac{\lambda_0}{n_{\mathrm{eff,fwd}}(\lambda_0) + n_{\mathrm{eff,bwd}}(\lambda_0)}, \tag{4.2}$$

where $n_{\mathrm{eff,fwd}}$ and $n_{\mathrm{eff,bwd}}$ are the effective indices of the interacting modes at λ_0. This relation shows that the Bragg wavelength is governed jointly by the grating period and by the modal properties of the two coupled waveguides. Consequently, accurate extraction of the effective indices is essential, especially in hybrid platforms where material dispersion, modal confinement, and anisotropy can influence the phase-matching condition.

Away from the exact Bragg condition, the interaction is described by the phase-mismatch parameter

$$\Delta\beta = \beta_{\mathrm{fwd}} + \beta_{\mathrm{bwd}} - \frac{2\pi}{\Lambda}. \tag{4.3}$$

Efficient power transfer occurs only when $\Delta\beta \approx 0$. When the wavelength is detuned from the Bragg wavelength, the phase mismatch accumulates along the grating length and prevents coupling to the backward field. This explains the intrinsically narrowband behavior of grating-assisted contra-directional couplers.

From a physical point of view, the coupling process is distributed along the grating region. Each grating period gives a small scattering contribution, and efficient transfer is obtained only when these contributions add coherently. Therefore, the grating length and the strength of the periodic perturbation directly influence the filtering response. As established in grating theory, increasing the interaction length generally improves spectral selectivity, while the modulation strength influences the coupling efficiency and bandwidth [89].

When the Bragg condition is satisfied, optical power at the resonant wavelength is transferred from the through waveguide to the backward-propagating mode of the adjacent waveguide and exits from the drop port. At wavelengths away from resonance, the grating-assisted interaction is not phase matched, so the optical signal remains predominantly in the original waveguide and exits from the through port. This four-port operation distinguishes GACDC filters from conventional Bragg gratings, which generally operate as two-port reflective devices and may require circulators to access the reflected signal [48], [86].

A further important advantage of contra-directional add–drop filters is their free-spectral-range-free behavior. Unlike ring-resonator filters, whose responses repeat periodically with the free spectral range, a grating-assisted contra-directional coupler is governed by a distributed Bragg phase-matching condition rather than resonant recirculation. As a result, the desired add–drop response can be obtained without the periodic resonance replicas that are typical of cavity-based filters [86]. This property is particularly attractive for wavelength-division multiplexing and sparse wavelength-routing applications, where parasitic resonances can limit the usable spectral window.

The spectral response can also be engineered by modifying the longitudinal grating profile. Uniform gratings provide the simplest narrowband response, while apodized or otherwise tailored gratings can be used to control sidelobes, bandwidth, and spectral shape [89]. In integrated implementations, such control is achieved by adjusting the grating period, length, duty cycle, modulation depth, and spatial distribution of the perturbation.

The same principle can be extended to multi-wavelength operation by introducing more than one spatial period into the grating. In a two-period or superimposed grating, each grating component can satisfy a distinct Bragg condition and therefore generate a separate drop wavelength. Under suitable conditions, the drop-port response of the composite structure can be interpreted as the superposition of the responses associated with the corresponding single-period gratings [90]. This concept provides the physical basis for the dual- and multi-channel add–drop filters analyzed later in this chapter.

Therefore, the contra-directional coupling mechanism combines three key features required for the present work: wavelength-selective Bragg phase matching, four-port add–drop operation and scalability toward multi-channel filtering through superimposed grating components.

4.3 Hybrid SiN–TFLN platform for grating-assisted add–drop filters

All grating-assisted add–drop filters presented in this chapter are implemented on a hybrid silicon nitride on thin-film lithium niobate (SiN–TFLN) platform with a silica (SiO_2) upper cladding, as illustrated in Fig. 4.1.

In this hybrid configuration, the silicon nitride layer contributes to optical mode confinement and can be patterned more easily using standard electron-beam lithography (EBL) than lithium niobate. This feature, in principle, facilitates the fabrication of subwavelength gratings. This strip-loaded geometry allows the optical mode to be primarily confined within the LN layer, while avoiding direct etching of LN and thereby mitigating scattering losses induced by sidewall.

The silicon nitride and lithium niobate layer thicknesses are fixed at $t_{\mathrm{SiN}} = 300$ nm and $t_{\mathrm{LN}} = 300$ nm, respectively [87]. The SiN waveguides and gratings are fully etched through the SiN layer and are assumed to exhibit vertical sidewalls (90°), which is a reasonable approximation for standard SiN fabrication processes. The upper cladding is assumed to be silica. At the reference wavelength of 1.55 μm, the refractive indices of SiN and silica are $n_{\mathrm{SiN}} = 1.98$ and $n_{\mathrm{SiO_2}} = 1.445$, respectively, as summarized in Fig. 4.1.

In the FDTD numerical model, material dispersion is included for both SiN and LN over the entire investigated wavelength range, ensuring accurate modeling of the grating-assisted contra-directional coupling mechanism.

Also in this case, the platform parameters, including the t_{SiN}, t_{LN}, sidewall geometry, and cladding material, are kept fixed throughout the analysis. The parametric analysis therefore focuses exclusively on device parameters, including the input and grating waveguide widths (W_{in}, W_G), the lateral gap g, the grating period Λ, the grating length L, and the superimposed-grating separation Δ, as detailed in the following sections.

As illustrated in Fig. 4.1, the single-channel GACDC consists of two parallel waveguides separated by a lateral gap g. The main waveguide, of width W_{in}, connects the input and through ports and supports forward propagation along the x-direction. Outside the Bragg spectral region, the input optical power remains predominantly in this waveguide and exits through the through port.

The adjacent grating waveguide has a width W_G and contains a periodic perturbation with period Λ. Near the Bragg wavelength, this perturbation enables contra-directional coupling between the forward-propagating mode of the input waveguide and a backward-propagating mode of the grating waveguide. Consequently, the selected wavelength is transferred toward the drop port. The port at the opposite end of the grating waveguide constitutes the add port.

The single-channel device is therefore geometrically characterized by W_{in}, W_G, g, Λ, and the total grating length L. These parameters determine the Bragg phase-matching condition, coupling strength, and spectral response and are investigated in the following design analysis.

4.4 FDTD Simulation Model

The proposed grating-assisted contra-directional couplers are designed and analyzed using a full-vectorial three-dimensional finite-difference time-domain (FDTD) method implemented in Ansys Lumerical FDTD [78].

All device geometries are constructed through script-based modeling within the FDTD environment, allowing parametric control of the waveguide dimensions, grating period, and coupling region. The contra-directional grating structure is implemented by introducing a longitudinal refractive-index modulation along the grating waveguide.

For multi-channel configurations, superimposed gratings are employed. Each individual grating corresponding to a target wavelength is first implemented separately, and the final structure is obtained by superimposing these gratings within a single interaction region. This approach enables the realization of multiple Bragg phase-matching conditions in a unified device.

Optical excitation is provided using mode injection ports. Four ports are defined, corresponding to the input, through, drop, and add ports of the device. Unless otherwise specified, only the input port is actively excited, while the remaining ports are used to monitor transmitted and reflected signals. In superimposed grating configurations, additional drop and add ports are introduced to account for the extra coupling channels, as detailed in the following sections.

The transmission characteristics are extracted using S-parameter analysis. The optical power at each port is normalized with respect to the injected input power, allowing direct evaluation of through-port and drop-port transmission levels.

To ensure numerical accuracy, perfectly matched layer (PML) boundary conditions are applied in all directions to eliminate artificial reflections from the simulation boundaries. A sufficiently large simulation time is selected to guarantee that all transient fields decay and the spectral response is fully converged.

The spatial discretization (mesh) is chosen to accurately resolve both the waveguide geometry and the fine features of the grating structure, particularly in regions with strong refractive-index modulation.

This simulation framework provides a reliable and flexible approach for analyzing the wavelength-selective behavior of grating-assisted contra-directional couplers and the multi-channel configurations.

To provide a visual representation of the implemented simulation model, the three-dimensional geometry of the grating-assisted contra-directional coupler (GACDC) within the FDTD environment is illustrated in Fig. 4.2.

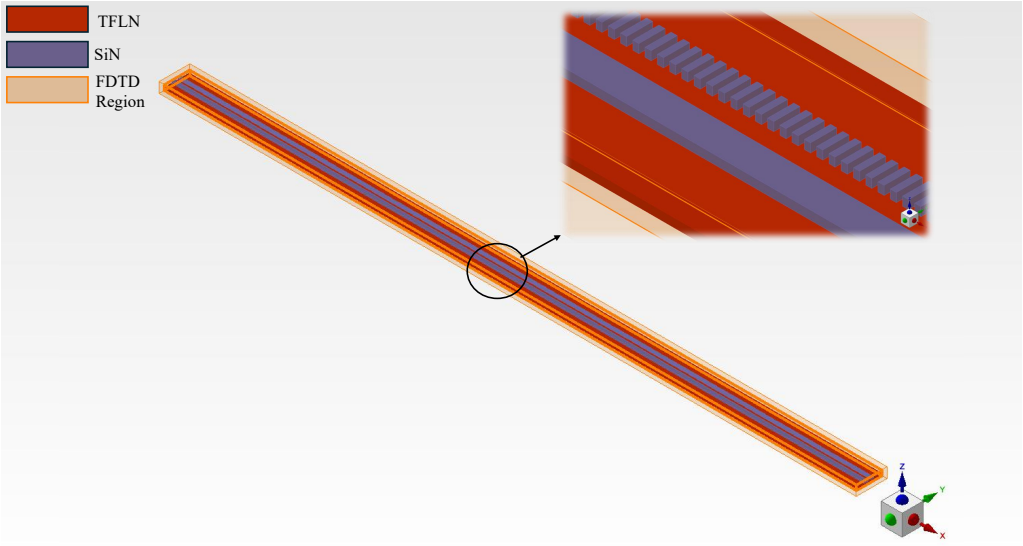


Figure 4.2: Three-dimensional view of the grating-assisted contra-directional coupler (GACDC) implemented in the FDTD simulation environment. The full device is shown within the simulation region, highlighting the longitudinal extent of the coupling structure. Due to the large interaction length, a magnified close-up is provided to clearly illustrate the grating profile and the periodic refractive-index modulation along the grating waveguide.

The structure consists of two parallel waveguides, where the grating is introduced as a longitudinal periodic modulation along one of the waveguides.

Due to the extended interaction length of the device, the full structure appears elongated within the simulation region. Therefore, a magnified close-up view is included to clearly highlight the grating profile and the periodic modulation responsible for the contra-directional coupling mechanism.

4.5 Figures of Merit for Add–Drop Operation

The performance of the proposed grating-assisted contra-directional couplers is evaluated using a set of well-defined figures of merit, consistently adopted throughout this chapter and extracted from the simulated spectral responses of the devices. These metrics quantify the efficiency, selectivity, and robustness of the wavelength-selective add–drop operation and are evaluated at the corresponding Bragg wavelength for each geometrical configuration.

- **Drop-Port Transmission**

  The primary figure of merit for wavelength extraction is the transmission to the drop port, denoted as T_d. As shown in Fig. 4.1, the drop port corresponds to the output waveguide where the selected wavelength is extracted through contra-directional coupling. This quantity represents the fraction of the input optical power that is successfully transferred to the drop waveguide at the Bragg wavelength. In the numerical analysis, T_d is obtained directly from the simulated transmission spectrum at the drop port and is expressed in decibels as

  $$T_d \text{ [dB]} = 10 \log_{10}(P_d), \tag{4.4}$$

  where P_d is the normalized optical power evaluated at the drop port. Higher values of T_d correspond to more efficient wavelength extraction. The dependence of T_d on the input waveguide width W_{in} and the grating waveguide width W_G is analyzed in the two-dimensional maps discussed later in this chapter.

- **Through-Port Transmission**

  The through-port transmission $T_{\text{th}}(\lambda)$ represents the fraction of optical power that remains in the main propagation path and is collected at the through port (Fig. 4.1) as a function of wavelength. Although the through port carries nearly all the optical power at wavelengths outside the Bragg condition, its transmission is strongly suppressed at the target wavelength. The minimum value of T_{th} at the Bragg wavelength therefore serves as a figure of merit for assessing the effectiveness of wavelength extraction in the add–drop filter.

  For an ideal add–drop filter, T_{th} should be strongly suppressed at the Bragg wavelength. It is defined as

  $$T_{\text{th}} \text{ [dB]} = 10 \log_{10}(P_{\text{th}}), \tag{4.5}$$

  where P_{th} is the normalized transmitted power at the through port. The variation of T_{th} across the design space highlights the trade-off between efficient wavelength extraction and through-port suppression.

- **Input-Port Reflection**

  The input-port reflection, denoted as R_{in}, represents the fraction of optical power that is back-reflected toward the input due to the contra-directional coupling mechanism and grating-induced perturbations. Excessive reflection can degrade the effective add–drop performance and introduce unwanted feedback into upstream components. This metric is defined as

  $$R_{\text{in}} \text{ [dB]} = 10 \log_{10}(P_{\text{ref}}), \tag{4.6}$$

  where P_{ref} is the reflected optical power measured at the input port. Its dependence on the geometrical parameters provides insight into parasitic coupling effects inherent to the grating-assisted interaction.

- **Crosstalk Between Ports**

Crosstalk quantifies the level of undesired signal leakage between different ports of the device and represents a critical figure of merit for wavelength-selective routing. The crosstalk between two generic ports i (desired) and j (undesired) is defined as

$$\mathrm{CT}_{i,j} = 10\log_{10}(P_i) - 10\log_{10}(P_j), \tag{4.7}$$

where P_i and P_j are the normalized transmitted power at ports i and j, respectively. In this work, particular emphasis is placed on the crosstalk between the through and drop ports, $\mathrm{CT}_{\mathrm{th},d}$, which directly quantifies the isolation between the transmitted and extracted wavelength channels. Lower crosstalk values indicate improved filtering selectivity and channel isolation.

- **3-dB Bandwidth**

  The spectral selectivity of the add–drop filter is characterized by the 3-dB bandwidth, denoted as $\mathrm{BW}_{3\mathrm{dB}}$. This parameter is defined as the wavelength interval over which the drop-port transmission remains within 3 dB of its maximum value. The 3-dB bandwidth provides a direct measure of the intrinsic narrowband behavior of the contra-directional coupling mechanism and is used to assess channel selectivity across the design space.

- **Distributed Coupling Coefficients**

  To establish a physical link between the numerical results and coupled-mode theory, the distributed coupling coefficients κ_{11} and κ_{12} are extracted from the simulated reflectance and drop-port transmission at the Bragg wavelength. Under the assumptions of weak perturbation and negligible propagation loss, the relations

  $$R_{\mathrm{in}} = \tanh^2(\kappa_{11}L), \qquad T_d = \tanh^2(\kappa_{12}L) \tag{4.8}$$

  hold, where L is the total grating length. By inverting these expressions, the coupling coefficients are obtained as

  $$\kappa_{11} = \frac{1}{L}\tanh^{-1}\left(\sqrt{R_{\mathrm{in}}}\right), \qquad \kappa_{12} = \frac{1}{L}\tanh^{-1}\left(\sqrt{T_d}\right). \tag{4.9}$$

  The coefficient κ_{11} characterizes the intra-waveguide coupling responsible for back-reflection, whereas κ_{12} quantifies the inter-waveguide coupling that enables power transfer to the drop port. These coefficients are not used as direct design parameters, but rather as interpretative quantities that provide physical insight into the operating regime of the optimized add–drop filters.

  Overall, the figures of merit defined in this section form the basis for the systematic design-space exploration and multi-channel extension of the proposed add–drop filters discussed in the following sections.

4.6 Single-Channel Add–Drop Filter Design

The design of the single-channel grating-assisted add–drop filter is performed through a systematic exploration of the geometrical parameter space defined by the input waveguide width W_{in} and the grating waveguide width W_G. These two parameters play a central role in determining the effective refractive indices of the interacting modes, the Bragg phase-matching condition, and the distributed contra-directional coupling strength, and therefore directly govern the redistribution of optical power among the input, through, and drop ports.

In this analysis, the grating period is fixed to $\Lambda = 422$ nm, corresponding to a Bragg wavelength around 1550 nm, and the duty cycle is set to 50% for all simulated configurations, while the gap between the SiN waveguides is kept constant at $g = 900$ nm. Consequently, the observed trends arise solely from geometrical variations in W_{in} and W_G, rather than from changes in the grating period or duty cycle.

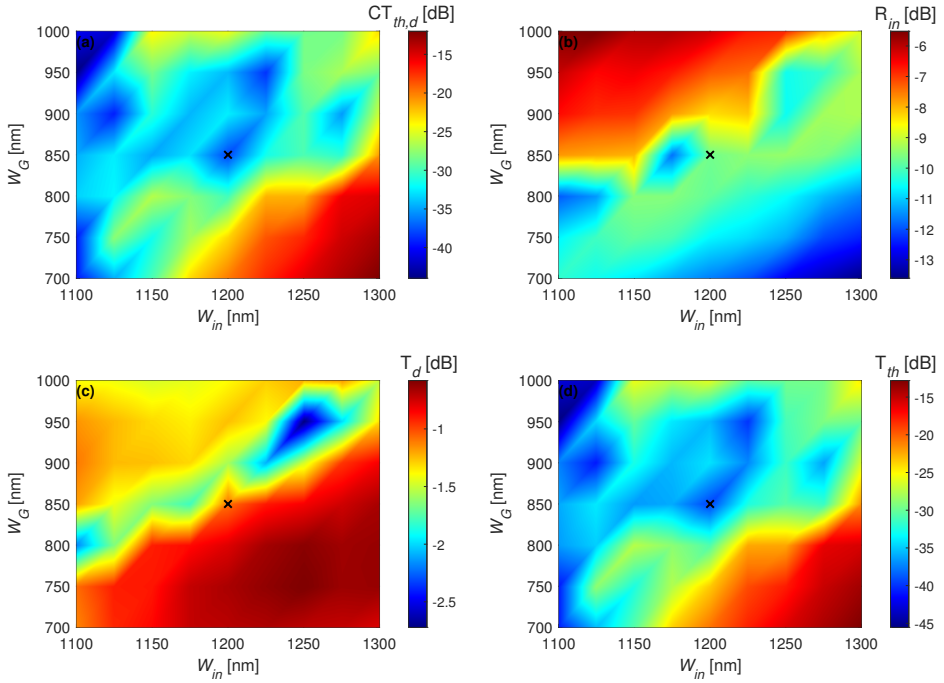


Figure 4.3: Figures of merit of the single-channel add–drop filter as a function of the input waveguide width W_{in} and the grating waveguide width W_G: (a) through-to-drop crosstalk $CT_{\mathrm{th,d}}$, (b) input-port reflection R_{in}, (c) drop-port transmission T_d, and (d) residual through-port transmission T_{th}. All quantities are evaluated at the corresponding Bragg wavelength λ_0 for each geometrical configuration. The marked point identifies the selected operating configuration resulting from the trade-off among efficient drop transmission, low crosstalk, strong through-port suppression, and negligible reflection. Adapted from [87].

Figure 4.3 reports the two-dimensional maps of the through-to-drop crosstalk $CT_{\mathrm{th,d}}$, the input-port reflection R_{in}, the drop-port transmission T_d, and the residual through-port transmission T_{th} as functions of W_{in} and W_G.

Among these metrics, the drop-port transmission T_d is treated as the dominant selection criterion, as it directly quantifies the efficiency of wavelength extraction toward the drop port. At the same time, low crosstalk between through and drop ports, strong suppression of the through-port transmission at the Bragg wavelength, and minimal reflection at the input port are design requirements.

It is important to emphasize that, for each geometrical configuration (W_{in}, W_G), all figures of merit reported in Fig. 4.3 are evaluated at the corresponding Bragg wavelength λ_0. Since variations in the waveguide widths modify the effective refractive indices of the interacting modes, the Bragg wavelength shifts accordingly.

The trends observed in Fig. 4.3 can be physically interpreted by considering the interplay between modal index matching and distributed coupling strength. An increase in the input waveguide width W_{in} generally improves modal matching between the coupled waveguides, leading to a reduction in back-reflection at the input port. Conversely, increasing the width difference between W_G and W_{in} enhances the contra-directional coupling strength, thereby promoting higher power transfer to the drop port. However, this enhancement is accompanied by an increase in the residual through-port transmission, which is undesirable for wavelength-selective filtering.

This competing behavior defines a trade-off region in the (W_{in}, W_G) design space. The operating point indicated in Fig. 4.3 is selected within this region as a balanced compromise that maximizes drop-port transmission while maintaining strong through-port suppression, low crosstalk, and negligible input reflection.

Once the operating point is identified based on the primary figures of merit, additional characteristics are examined to assess spectral robustness. Figure 4.4 reports the

corresponding Bragg wavelength λ_0, the 3-dB bandwidth $BW_{3\mathrm{dB}}$, and the extracted distributed coupling coefficients κ_{11} and κ_{12} as functions of W_{in} and W_G.

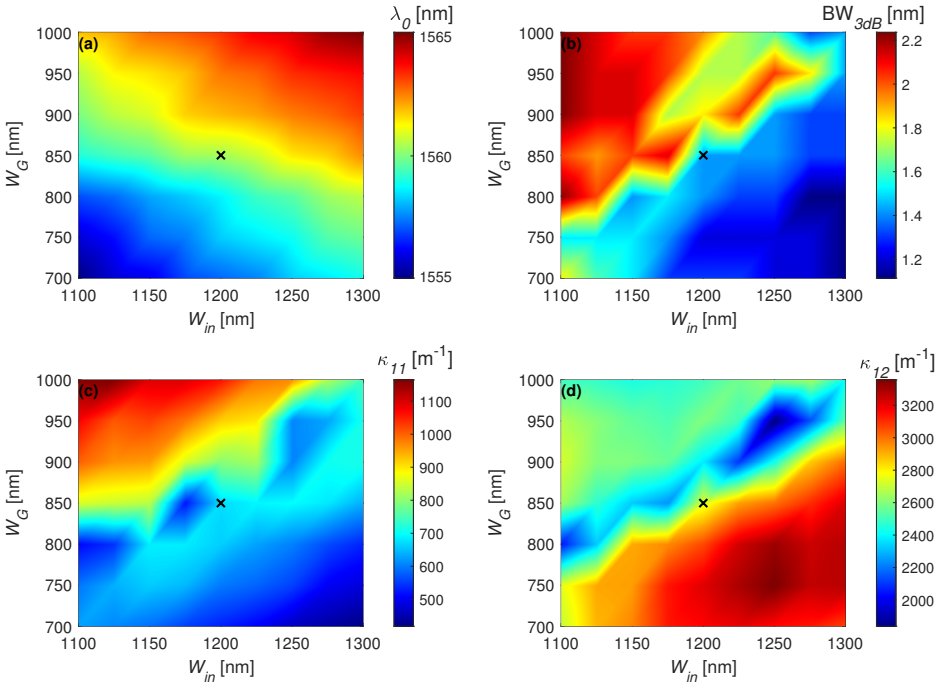


Figure 4.4: Secondary characteristics associated with the selected single-channel add–drop configuration: (a) Bragg wavelength λ_0, (b) 3-dB bandwidth $BW_{3\mathrm{dB}}$, (c) self-coupling coefficient κ_{11}, and (d) cross-coupling coefficient κ_{12}, reported as functions of W_{in} and W_G. The grating period is fixed to $\Lambda = 422$ nm. These maps confirm the limited wavelength sensitivity to geometrical variations, the narrowband filtering behavior, and the dominance of inter-waveguide coupling required for efficient add–drop operation. Adapted from [87].

The relatively weak dependence of the Bragg wavelength λ_0 on the geometrical parameters indicates limited sensitivity to moderate fabrication-induced dimensional variations.

In addition, the 3-dB bandwidth provides important insight into the spectral selectivity of the proposed contra-directional filter. As shown in Fig. 4.4(b), the extracted bandwidth values remain confined within a narrow range across the (W_{in}, W_G) design space, typically between approximately 1 nm and 2.2 nm.

This limited variation indicates that changes in the waveguide widths primarily affect the coupling efficiency and power redistribution among the ports, while the intrinsic narrowband nature of the Bragg-assisted coupling mechanism is preserved. In other words, geometrical variations modify the strength of the interaction rather than the spectral selectivity of the filter.

The observed stability of the 3-dB bandwidth confirms that the selected operating point combines efficient drop-port transmission with a well-controlled and spectrally selective response, which is essential for wavelength-routing applications.

To further validate the physical consistency of the selected operating point, the distributed coupling coefficients are interpreted within the framework of coupled-mode theory. The self-coupling coefficient κ_{11} quantifies parasitic coupling between counter-propagating modes within the input waveguide and is directly associated with back-reflection. In contrast, the cross-coupling coefficient κ_{12} characterizes the coupling between the forward-propagating mode in the input waveguide and the backward-propagating mode in the grating waveguide, which enables efficient power transfer toward the drop port.

The clear dominance of κ_{12} over κ_{11} across the selected region of the design space confirms that the device operates in a regime where inter-waveguide contra-directional coupling prevails over parasitic self-coupling. This coupling hierarchy directly explains the simultaneous observation of high drop-port transmission and low input reflection, and consistently supports efficient single-channel add–drop operation.

Accordingly, the operating point $W_{\text{in}} = 1200$ nm and $W_G = 850$ nm was selected for the subsequent device analysis and spectral characterization, as it combines high drop-port transmission with low crosstalk, suppressed through-port transmission, and negligible input reflection.

4.6.1 Optimization of the Gap between the waveguides

After identifying the optimal values of the input waveguide width W_{in} and the grating waveguide width W_G from the parametric analysis, the lateral separation g between the through waveguide and the grating waveguide is optimized to further refine the add–drop performance.

The optimization of the gap is primarily guided by the drop-port transmission T_d, which remains the dominant figure of merit for the considered contra-directional add–drop configuration. Figure 4.5 reports drop-port transmittance T_d together with the corresponding input-port reflection R_{in} as a function of the gap size g.

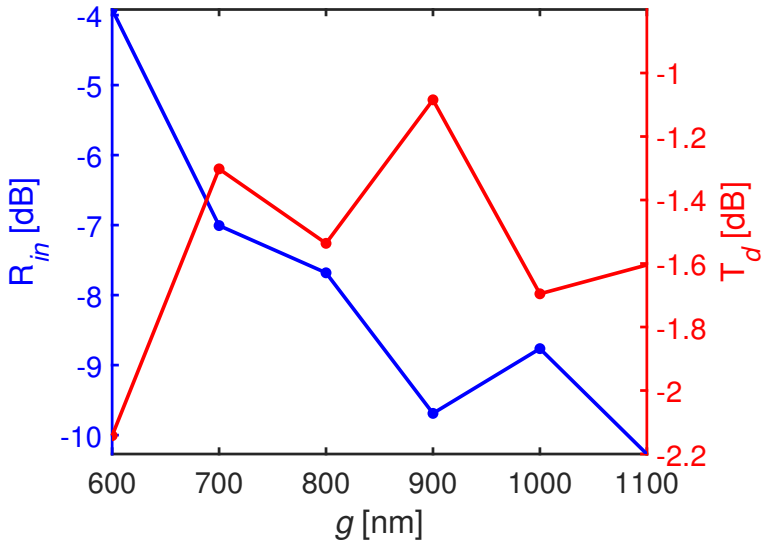


Figure 4.5: Drop-port transmission T_d and input-port reflection R_{in} as a function of the lateral gap g for the selected single-channel add–drop configuration. Reducing the gap increases the coupling strength and enhances wavelength extraction, at the expense of higher input reflection. The chosen value $g \approx 900$ nm provides a balanced trade-off between efficient drop-port transmission and negligible reflection, while exhibiting limited sensitivity to fabrication-induced variations.

As expected, reducing the lateral separation enhances the evanescent overlap between the interacting modes, leading to stronger contra-directional coupling and increased power transfer to the drop port. However, excessively small gap values simultaneously increase parasitic self-coupling mechanisms, resulting in a noticeable increase in input-port reflection. Conversely, for larger gap values, the reduced modal overlap weakens the distributed interaction, causing a progressive degradation of the drop-port transmission.

This behavior highlights the intrinsic trade-off imposed by the contra-directional coupling geometry, where both too weak and too strong coupling conditions negatively affect the overall add–drop performance. Based on the trends observed in Fig. 4.5, an optimal lateral separation of approximately $g \approx 900$ nm is selected for the considered structure. At this value, the drop-port transmission approaches its near-optimal level

while the input-port reflection remains sufficiently low to be considered suitable for practical operation.

4.6.2 Spectral Response of the single channel filter

To validate the wavelength-selective operation of the optimized single-channel add–drop filter, both its spectral response and spatial electromagnetic-field distribution at the design wavelength are examined. This combined analysis provides direct physical insight into the underlying contra-directional coupling mechanism and confirms the effectiveness of the selected geometrical parameters.

Figure 4.6(a) reports the wavelength-dependent transmittance at the through port (T_{th}) and the drop port (T_d).

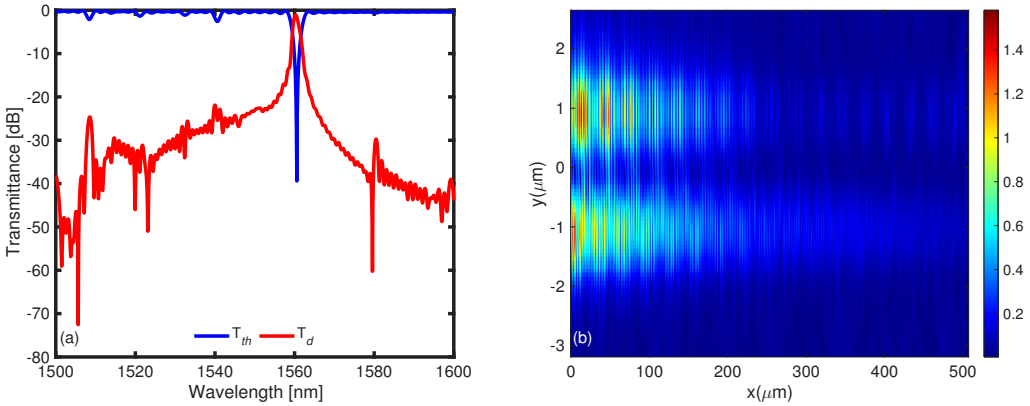


Figure 4.6: Single-channel add–drop filter performance and physical field interpretation. (a) Spectral response showing the through-port transmission T_{th} (blue curve) and the drop-port transmission T_d (red curve). A clear transmission notch at the through port and a corresponding peak at the drop port are observed at the Bragg-matched wavelength. (b) Electric-field magnitude distribution evaluated at the drop wavelength. The input signal is launched into the lower waveguide, while efficient contra-directional coupling transfers optical power to the upper grating waveguide, resulting in backward propagation toward the drop port.

At the Bragg wavelength, a pronounced suppression of the through-port transmission is observed, accompanied by a corresponding peak in the drop-port response. This complementary behavior confirms efficient wavelength-selective extraction. Outside the resonance region, the through-port transmission remains close to 0 dB, indicating that the filtering action does not introduce significant excess loss away from the target wavelength.

The electric-field distribution shown in Fig. 4.6(b), is evaluated at the drop wavelength. The optical signal is launched into the lower waveguide, which acts as the input waveguide of the structure. Within the grating-assisted interaction region, the forward-propagating mode supported by the input waveguide is progressively coupled to a backward-propagating mode supported by the upper grating waveguide.

As the field evolves along the propagation direction, optical power is transferred from the input waveguide to the grating waveguide and propagates in the opposite direction, exiting the drop port. The observed backward energy flow and spatial field localization clearly demonstrate the contra-directional nature of the coupling process.

Overall, the combined spectral and field analyses verify that the selected single-channel configuration operates as an efficient contra-directional add–drop filter. This optimized structure is used in the following as building block for the multi-channel configurations.

To facilitate a clear and consistent extension toward dual- and multi-channel add–drop architectures, the optimized single-channel filter geometrical parameters and performance metrics are summarized in Tab. 4.1 as a reference design.

Table 4.1: Reference geometrical parameters and baseline performance metrics of the optimized single-channel add–drop filter used as the building block for multi-channel architectures.

Parameter	Value
Input waveguide width W_{in}	1200 nm
Grating waveguide width W_G	850 nm
Lateral gap g	900 nm
Grating period Λ	422 nm
Number of grating periods N	1200
Grating length L	506.4 μm
Bragg wavelength λ_0	1560 nm
Drop-port transmission T_d	-1.08 dB
Through-port transmission T_{th}	-39.3 dB
Through-to-drop crosstalk $CT_{\text{th,d}}$	-38.3 dB
Input-port reflection R_{in}	≈ -9 dB

4.7 Dual-Channel Add–Drop Filter Design

Building upon the single-channel reference configuration defined in Table 4.1, the following section introduces a dual-channel add–drop filter based on superimposed grating concepts.

The dual-channel add–drop filter investigated in this work is based on a grating-assisted contra-directional coupling scheme implemented on a hybrid SiN–TFLN platform. The device configuration is illustrated in Fig. 4.7 and represents the basis for the multi-channel wavelength routing concepts discussed in the following sections.

The structure consists of a straight silicon nitride input waveguide placed in close proximity to a parallel grating waveguide fabricated on thin-film lithium niobate. Wavelength-selective coupling between the two waveguides is enabled through a longitudinal refractive-index modulation applied to the grating waveguide, which induces contra-directional coupling between the forward-propagating mode of the input waveguide and the backward-propagating mode supported by the grating waveguide.

In the dual-channel configuration, the grating region is formed by the superposition of two distinct periodic gratings characterized by periods Λ_1 and Λ_2, each designed to satisfy the Bragg phase-matching condition at a different target wavelength. As schematically shown in Fig. 4.7(b), the two individual gratings are first designed independently and are then superimposed to generate a composite grating pattern. This superimposed grating enables simultaneous wavelength-selective coupling at two distinct wavelengths, thereby realizing dual-channel add–drop functionality within a single coupling section.

From a functional perspective, the device supports four optical ports: an input port, a through port, a drop port, and an add port. At wavelengths far from the Bragg conditions associated with Λ_1 and Λ_2, optical power propagates predominantly along the input waveguide and exits through the through port with minimal interaction with the grating waveguide. At the Bragg-matched wavelengths, however, efficient contra-directional coupling occurs, and optical power is transferred to the grating waveguide and routed toward the drop port.

An important feature of the proposed configuration is that the two wavelength channels are generated by a single physical grating section rather than by cascading multiple filters. This approach enables a compact footprint and avoids additional inter-stage losses. Moreover, when the spectral separation between the two Bragg wavelengths is sufficiently large, the coupling mechanisms associated with Λ_1 and Λ_2 remain nearly independent. Under this condition, the dual-channel filter can be approximately interpreted as the combination of two single-channel filtering responses.

In the next subsection, the design criteria and figures of merit used to quantitatively evaluate the performance of this dual-channel add–drop filter are introduced, followed by a detailed analysis of its spectral response.

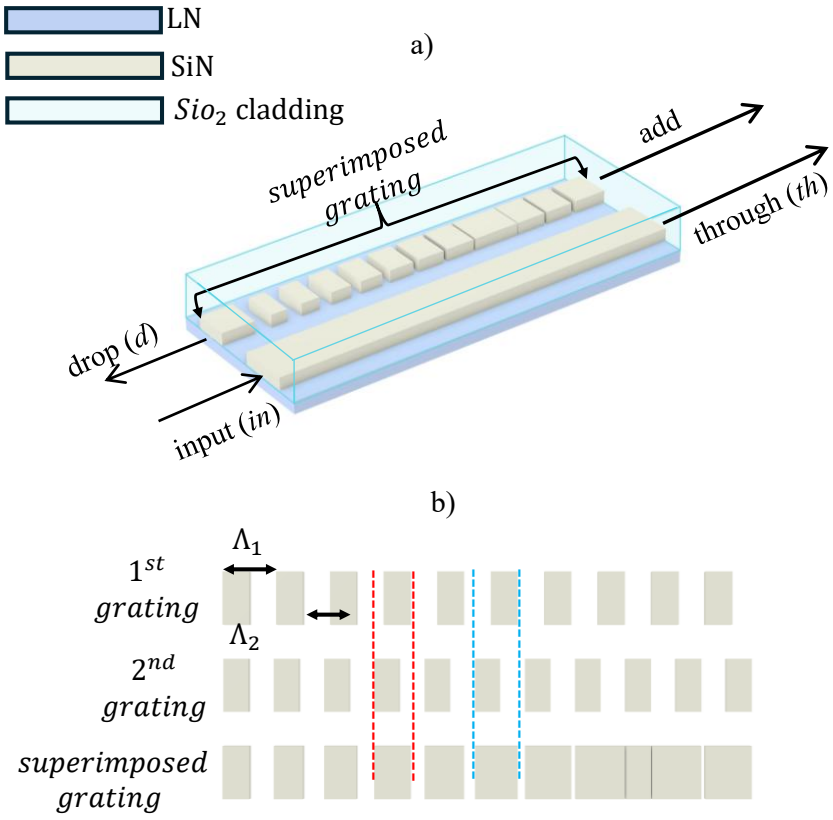


Figure 4.7: Schematic illustration of the dual-channel grating-assisted add–drop filter. (a) Three-dimensional view of the device, showing the input waveguide, the grating waveguide, and the superimposed grating section enabling contra-directional coupling. The input, through, drop, and add ports are indicated. The SiN waveguides are covered by a silica (SiO_2) upper cladding, shown transparently for clarity. (b) Conceptual construction of the superimposed grating. Two individual gratings with periods Λ_1 and Λ_2, corresponding to two distinct target wavelengths, are combined to form a single composite grating pattern that enables dual-channel wavelength-selective coupling.

4.7.1 Effect of Grating-Period Separation in Dual-Channel Operation

All results reported in this subsection are obtained by fixing $\Lambda_1 = 412$ nm, defining $\Lambda_2 = \Lambda_1 + \Delta$, and maintaining a constant grating length of $N = 1200$ periods.

A key design parameter governing the spectral behavior of the dual channel add-drop filter is the separation between the two grating periods. This parameter is defined as

$$\Delta = \Lambda_2 - \Lambda_1, \tag{4.10}$$

where Λ_1 and Λ_2 correspond to the Bragg periods associated with the first and second wavelength channels, respectively.

The parameter Δ plays a dual role in the operation of the device. First, it directly determines the spectral separation between the two dropped wavelength channels through the independent Bragg phase-matching conditions imposed by the superimposed gratings. Second, it influences the degree of interaction between the two contra-directional coupling processes, thereby affecting the achievable drop-port transmission efficiency for each channel. As a result, Δ constitutes a critical degree of freedom for balancing channel spacing and insertion loss in dual-channel add–drop filters based on superimposed gratings.

Figure 4.8 illustrates the impact of Δ on both the dropped wavelengths and the corresponding drop-port transmission levels for the two channels. As shown in Fig. 4.8(a),

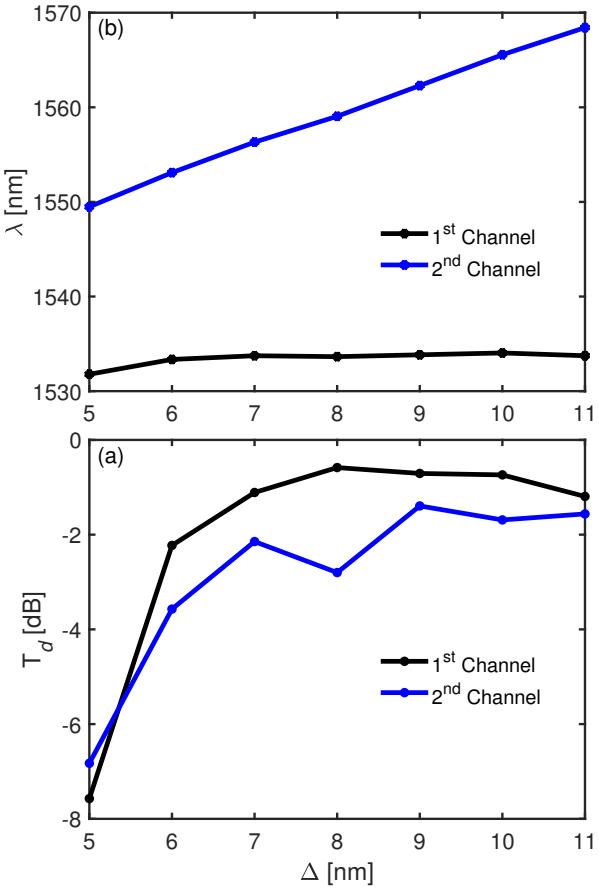


Figure 4.8: Impact of the grating-period separation $\Delta = \Lambda_2 - \Lambda_1$ on the dual-channel add–drop filter performance. (a) Corresponding variation of the dropped wavelengths, illustrating the tunability of the inter-channel spacing. (b) Drop-port transmission T_d for the first and second channels as a function of Δ. An optimal trade-off between transmission efficiency and channel separation is obtained for Δ values between 8 and 11 nm.

increasing Δ leads to a monotonic increase in the spectral separation between the two channels. This behavior reflects the independent tuning of the Bragg conditions associated with Λ_1 and Λ_2 and enables flexible control of the inter-channel spacing within a single grating section.

At the same time, Fig. 4.8(b) shows a non-monotonic dependence of the drop-port transmission T_d on Δ for both channels. For small values of Δ, the proximity of the two grating periods results in partial spectral overlap between the two coupling processes, which degrades the effective drop efficiency. Conversely, for excessively large values of Δ, the drop-port transmission of the second channel progressively decreases due to the reduced coupling strength associated with its longer grating period.

An optimal operating region is identified for Δ values between approximately 8 and 11 nm. Within this range, both channels exhibit favorable drop-port transmission while maintaining well-separated spectral responses. Based on this trade-off, a value of $\Delta = 9$ nm is selected for the final dual-channel design, corresponding to an inter-channel spacing of approximately 30 nm. This value is adopted in all subsequent simulations and analyses of the dual-channel structure.

The slightly reduced transmission observed for the second channel is attributed to its longer grating period and the corresponding decrease in the distributed coupling

coefficient, a limitation that could be mitigated by increasing the grating length or by independently tailoring the modulation strength in future designs.

4.7.2 Dual-Channel Spectral Response with Optimized Grating Separation

After identifying the optimal grating-period separation $\Delta = 9$ nm, the spectral response of the dual-channel add–drop filter is evaluated to assess the effectiveness of the superimposed grating concept under the selected operating conditions. Figure 4.9 reports the wavelength-dependent transmittance at the through port (T_{th}) and at the drop port (T_d) over the C-band.

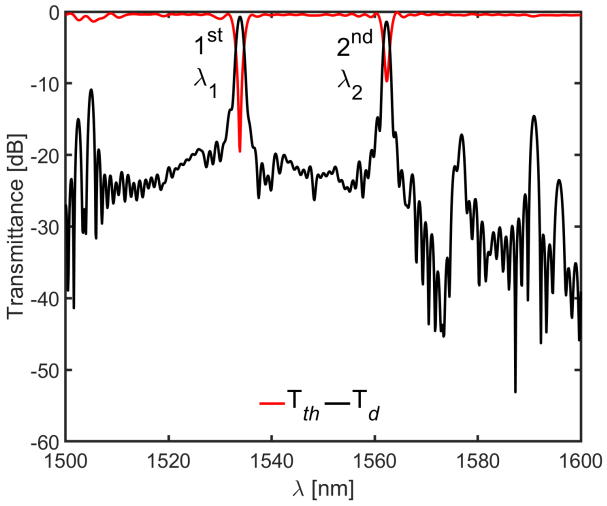


Figure 4.9: Spectral response of the dual-channel add–drop filter for the optimized grating-period separation $\Delta = 9$ nm. The through-port transmission T_{th} (blue curve) remains close to 0 dB outside the resonance regions, while two distinct transmission notches appear at λ_1 and λ_2. At the same wavelengths, the drop-port transmission T_d (red curve) exhibits pronounced peaks, confirming efficient wavelength-selective extraction for both channels.

Two well-defined resonance features are clearly observed at wavelengths λ_1 and λ_2, corresponding to the Bragg phase-matching conditions imposed by the two superimposed grating components. At these wavelengths, efficient contra-directional coupling leads to pronounced transmission minima at the through port and simultaneous power extraction at the drop port, confirming the correct operation of the dual-channel add–drop architecture.

Outside the resonance regions, the through-port transmission remains close to 0 dB across the investigated wavelength range, indicating negligible excess loss and minimal interaction with the grating waveguide. Concurrently, the drop-port transmission is strongly suppressed away from λ_1 and λ_2, demonstrating effective channel selectivity and low out-of-band crosstalk.

At the resonant wavelengths, the drop-port transmission reaches values comparable to those obtained in the corresponding single-channel configuration. This observation indicates that the superposition of two grating components does not significantly degrade the extraction efficiency of each individual channel. The slight asymmetry observed between the two resonance peaks is attributed to the different grating periods and the associated variation in distributed coupling strength, in agreement with the trends discussed in the previous subsection.

Overall, the spectral response confirms that the selected grating-period separation enables largely independent and efficient operation of the two wavelength channels within a single coupling section. This result validates the superimposed grating approach as an effective strategy for compact dual-channel wavelength-selective routing and establishes a solid basis for extension toward higher channel counts.

For clarity and to facilitate comparison with the single-channel reference configuration, the key performance metrics of the optimized dual-channel add–drop filter are summarized in Table 4.2.

Table 4.2: Summary of the optimized dual-channel add–drop filter performance for $\Delta = 9$ nm.

Metric	Channel 1	Channel 2
Bragg wavelength λ [nm]	1533	1563
Grating period Λ [nm]	412	421
Drop-port transmission T_d [dB]	-0.70	-1.39
Through-port suppression T_{th} [dB]	~ -38	~ -36
Inter-channel spacing [nm]	30	

Unless otherwise stated, all geometrical and material parameters of the dual-channel structure are identical to those of the single-channel filter optimization, ensuring a consistent design baseline. All values are extracted at the corresponding Bragg wavelengths for $\Delta = 9$ nm.

4.8 Four-Channel Add–Drop Filter Design

Following the demonstration of dual-channel operation enabled by superimposed gratings, the proposed design concept is further extended to realize four-channel wavelength-selective routing. The four-channel configuration preserves the same physical principles and design methodology established for the single- and dual-channel filters, while increasing the channel count through a symmetric architectural extension. Figure 4.10 illustrates the schematic layout of the four-channel add–drop filter.

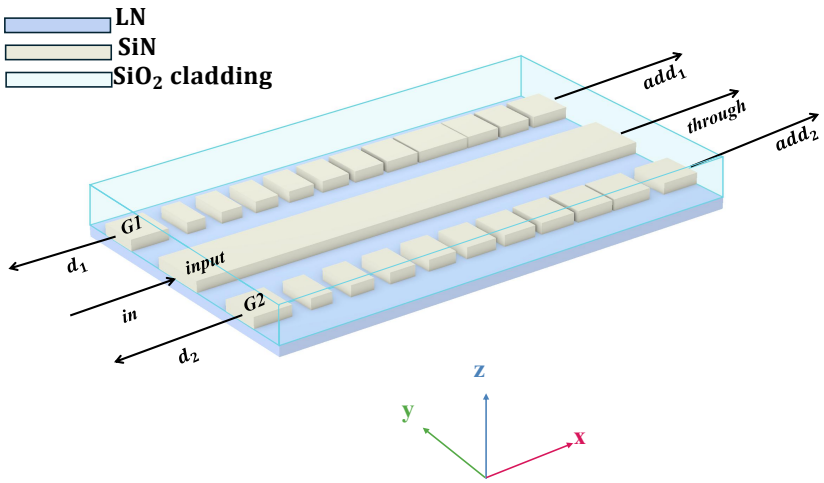


Figure 4.10: Schematic representation of the multi-channel grating-assisted contra-directional add–drop filter implemented on the hybrid SiN–TFLN platform. The device consists of a central input–through waveguide coupled to two grating waveguides, G_1 and G_2, providing the corresponding drop and add ports. The SiN waveguides are covered by a silica (SiO_2) upper cladding, shown transparently to preserve the visibility of the device geometry.

The structure consists of a central input waveguide and two grating-assisted contra-directional couplers, symmetrically placed on opposite sides of the input path. Each grating waveguide incorporates a superimposed grating composed of two distinct grating periods, enabling dual-channel contra-directional coupling on each side of the input waveguide.

As a result, the overall device supports four wavelength-selective drop channels within a single integrated structure, without requiring cascading of multiple filtering stages.

In the four-channel architecture, wavelength selectivity is achieved by two physically distinct grating waveguides, denoted as G_1 and G_2, symmetrically placed on opposite sides of the input waveguide. Each grating waveguide implements a superimposed grating composed of two distinct grating periods, resulting in a total of four effective Bragg periods and four extracted wavelength channels.

Specifically, channels λ_1 and λ_3 are generated by the superimposed grating implemented on G_1, while channels λ_2 and λ_4 are generated by the superimposed grating on G_2. Accordingly, the four wavelength channels are associated with four grating periods Λ_1–Λ_4, following the mapping $\lambda_1 \leftrightarrow \Lambda_1$, $\lambda_2 \leftrightarrow \Lambda_2$, $\lambda_3 \leftrightarrow \Lambda_3$, and $\lambda_4 \leftrightarrow \Lambda_4$.

The symmetric placement of the two grating waveguides ensures balanced coupling conditions on both sides of the input waveguide and facilitates scalable multi-channel operation. Importantly, the same geometrical parameters and grating-engineering principles optimized for the single- and dual-channel configurations are retained, allowing the increase in channel count without introducing additional design degrees of freedom.

From a functional standpoint, the device operates as a multi-port wavelength router comprising one input port, one through port, two drop ports, and two add ports. Each drop port is associated with two wavelength channels determined by the corresponding superimposed grating. At wavelengths far from the Bragg conditions, optical power propagates predominantly along the input waveguide and exits through the through port with minimal interaction. At the Bragg-matched wavelengths, wavelength-selective contra-directional coupling transfers optical power to the appropriate grating waveguide and routes it toward the corresponding drop port.

It is worth emphasizing that the four-channel architecture does not introduce new coupling mechanisms beyond those already discussed for the dual-channel case. Instead, it represents a direct and scalable extension of the superimposed grating concept, where each filtering wavelength is primarily controlled by its corresponding grating period. For this reason, the physical interpretation and design trade-offs identified for the dual-channel configuration remain fully applicable and are not repeated here.

4.8.1 Effect of Grating-Period Separation in Four-Channel Operation

To enforce an approximately uniform spectral spacing among the four extracted channels, the grating periods are designed such that the separation between the two periods within each superimposed grating is identical. The grating-period separation parameter Δ is therefore defined as

$$\Delta = \Lambda_3 - \Lambda_1 = \Lambda_4 - \Lambda_2. \tag{4.11}$$

Under this constraint, the remaining grating periods satisfy

$$\Lambda_2 - \Lambda_1 = \Lambda_4 - \Lambda_3 = \frac{\Delta}{2}, \tag{4.12}$$

which leads to an approximately uniform wavelength spacing, $\lambda_2 - \lambda_1 \approx \lambda_3 - \lambda_2 \approx \lambda_4 - \lambda_3$. This design strategy enables a predictable and evenly spaced spectral allocation across all four channels and allows the role of Δ to be systematically investigated.

The impact of the grating-period separation Δ on the device performance is evaluated by considering its influence on wavelength extraction efficiency and channel isolation. Since each side of the input waveguide contains a superimposed grating supporting two wavelength channels, the choice of Δ must simultaneously ensure efficient drop-port transmission and limited inter-port crosstalk (defined in Eq. 4.7).

Figure 4.11 reports the evolution of the drop-port transmission T_d and the corresponding through-to-drop crosstalk as functions of Δ.

As shown in Fig. 4.11, the drop-port transmission exhibits a clear dependence on Δ, with a broad maximum observed in the range between approximately 9.5 and 10.5 nm. Within the same interval, the crosstalk level remains sufficiently low, indicating that the

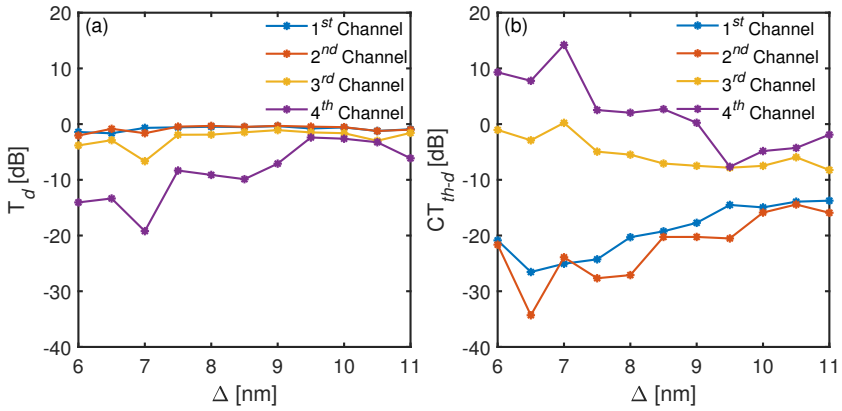


Figure 4.11: Drop-port transmission T_d and through-to-drop crosstalk as functions of the grating-period separation Δ for the symmetric multi-channel configuration based on two superimposed gratings.

superimposed gratings operate with limited mutual interference and that the extracted channels remain well isolated from the through path.

For smaller values of Δ, the reduced spectral separation between the superimposed grating components leads to increased interaction between the coupling processes, resulting in degraded channel isolation and higher through-to-drop crosstalk. Conversely, excessively large values of Δ do not provide further improvement in isolation while yielding a gradual reduction in the overall drop-port transmission.

A more detailed channel-resolved analysis reveals an important behavior that is not immediately captured by the global optimization criterion. In particular, for small values of the grating-period separation Δ, channels 1 and 2 exhibit favorable operating conditions, whereas channels 3 and 4 remain under-coupled and therefore operate away from their optimal extraction regime.

It is important to emphasize that, for channels 1 and 2, the drop-port transmission T_d remains approximately constant over the entire investigated range of Δ. The observed performance degradation as Δ increases is therefore not driven by a reduction in extraction efficiency toward the drop port, but rather by an increase in through-to-drop crosstalk. This indicates that the coupling strength for these channels remains sufficient, while the spectral selectivity with respect to the through path progressively deteriorates.

However, as Δ increases toward the globally optimal region, the operating point of channels 1 and 2 gradually shifts away from their individual optimum conditions. This effect does not significantly impact the drop-port transmission of these channels, which remains approximately constant over the investigated Δ range, but reflects the inherent trade-off introduced by the global optimization of a multi-channel structure.

Importantly, this reduction in isolation performance for channels 1 and 2 near the global design point is not a fundamental limitation of the proposed architecture. As discussed in the following subsection, the associated crosstalk penalty can be effectively mitigated by increasing the total number of grating periods N, which sharpens the spectral response and enhances channel selectivity without altering the wavelength organization imposed by Δ.

Based on this combined analysis, the interval $9.5\ \text{nm} \leq \Delta \leq 10.5\ \text{nm}$ is identified as the optimal operating region for the symmetric four-channel add–drop structure. This range provides a balanced compromise between efficient wavelength extraction, controlled inter-port crosstalk, and uniform spectral spacing, and is therefore adopted as the reference for the subsequent design steps.

4.8.2 Crosstalk Between Drop Ports in Four-Channel Operation

While the analysis of Fig. 4.11 focuses on the trade-off between drop-port transmission and through-to-drop crosstalk, an additional constraint emerges in multi-channel configurations due to crosstalk between drop ports. In particular, when multiple wavelength channels are extracted using symmetric superimposed gratings, mutual interference between the drop ports can become a limiting factor for scalability.

Figure 4.12 reports the crosstalk levels between all drop ports as a function of the grating-period separation Δ. The present analysis extends the evaluation to all extracted

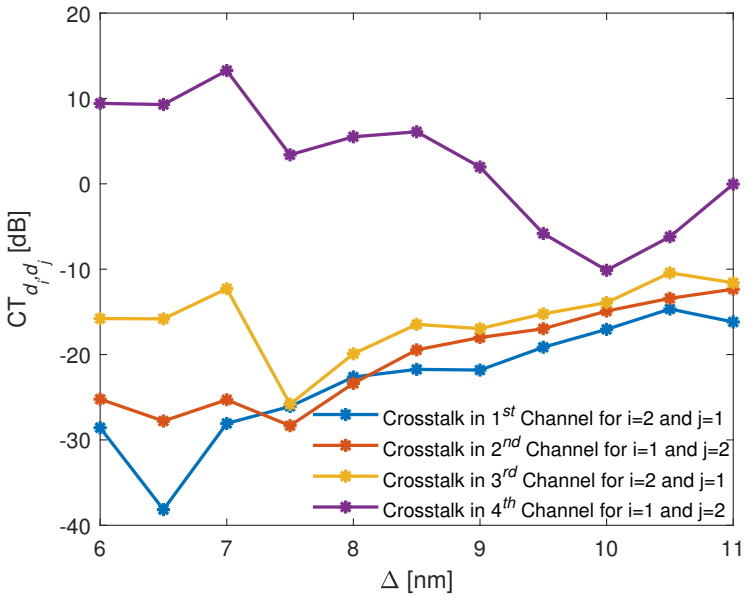


Figure 4.12: Inter-drop crosstalk as a function of the grating-period separation Δ for the symmetric multi-channel add–drop filter. Crosstalk levels are reported for all extracted channels. While the first three channels exhibit limited sensitivity to Δ and remain below -10 dB in the worst-case condition, the fourth channel shows a strong dependence on Δ and acts as the dominant limiting factor. The combined analysis identifies $\Delta = 10$ nm as the optimal operating point.

channels in order to provide a comprehensive assessment of multi-channel isolation.

As observed from Fig. 4.12, the inter-drop crosstalk associated with the first three channels remains below -10 dB over the entire investigated range of Δ, even in the worst-case condition. This indicates that, for these channels, mutual interference does not represent a critical limitation and is largely insensitive to the exact choice of Δ.

In contrast, the fourth channel exhibits a markedly different behavior. The crosstalk shows a pronounced dependence on Δ, acting as the dominant limiting factor in the selection of the grating-period separation. For values of Δ outside a narrow optimal region, the crosstalk associated with the fourth channel increases significantly, thereby constraining the usable design space.

By combining the inter-drop crosstalk trends observed in Fig. 4.12 with the transmission and crosstalk criteria identified in Fig. 4.11, a well-defined optimal operating point emerges around $\Delta = 10$ nm. This value provides a favorable compromise between high drop-port transmission, low through-to-drop crosstalk, and acceptable inter-drop isolation across all channels.

This observation indicates that, although the overall add–drop operating principle remains the same, the multi-channel configuration introduces additional inter-channel effects that slightly modify the optimal Δ value. Consequently, the optimization of Δ should be performed independently for each channel configuration rather than assumed to be universally transferable.

4.8.3 Drop Channel Wavelength and Bandwidth Stability

Beyond transmission efficiency and crosstalk considerations, drop wavelength positioning and bandwidth stability constitute additional critical figures of merit for multi-channel add–drop filters. In particular, the dependence of the channel wavelengths and their spectral spacing on the grating-period separation Δ must be carefully assessed to ensure predictable, scalable, and fabrication-robust wavelength routing.

Figure 4.13 reports the drop channel wavelength of all four extracted channels as a function of Δ, together with their corresponding 3-dB bandwidth.

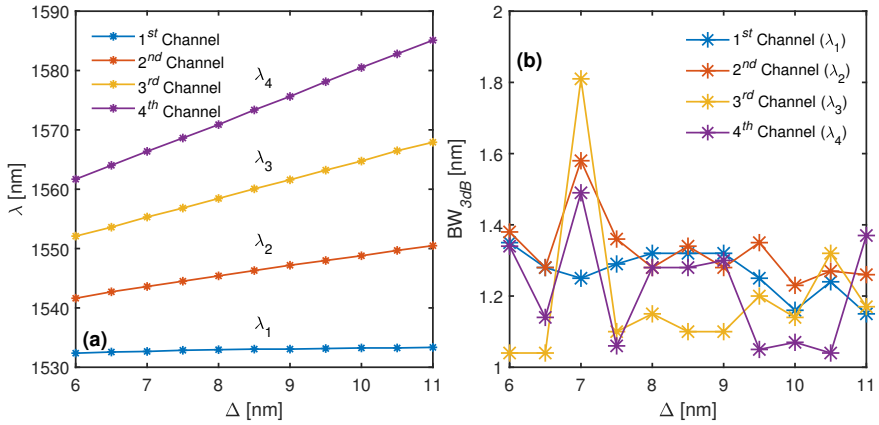


Figure 4.13: Drop channel wavelength and 3-dB bandwidth of the four extracted channels as functions of the grating-period separation Δ. For each fixed value of Δ, the wavelength spacing between adjacent channels remains uniform. The limited bandwidth values confirm the narrowband operation of the multi-channel add–drop filter.

As shown in Fig. 4.13, for any fixed value of Δ, the wavelength spacing between adjacent channels remains uniform. Specifically, the separations between channel 1 and 2, channel 2 and 3, and channel 3 and 4 are equal for each chosen value of Δ. This behavior directly reflects the imposed constraint on the grating periods and indicates that the superimposed-grating enforces a regular and predictable spectral allocation.

Although the absolute wavelength spacing increases with Δ, the channels remain uniformly spaced. As a result, the grating-period separation Δ acts as a tuning parameter that controls the spacing between the wavelength channels while preserving the overall filtering behavior. This property is particularly advantageous for wavelength-division multiplexing applications, where uniform channel spacing is a fundamental requirement.

In addition to wavelength positioning, the bandwidth analysis confirms that the proposed structure operates in a consistently narrowband regime. For all investigated values of Δ, the extracted channels exhibit 3-dB bandwidths in a limited range, although a slightly larger bandwidth is observed for $\Delta = 7$. Nevertheless, it remains within the narrowband operating regime, reflecting the inherently selective nature of the contra-directional coupling mechanism. Notably, around $\Delta = 10$ nm—corresponding to an approximately uniform channel spacing of 16 nm, as shown in Fig. 4.13(a)—the drop-port transmissions of the four channels become nearly balanced, as shown in Fig. 4.11(a). In the same region, the bandwidths of all channels also become closely matched, indicating a uniform spectral response across the device.

Importantly, variations in Δ primarily affect the absolute channel spacing, while only weakly influencing the individual channel bandwidths. This provides design flexibility, allowing Δ to be used to tailor channel allocation without significantly degrading filter selectivity or bandwidth uniformity.

Overall, the combined analysis of wavelength positioning and bandwidth stability confirms that, together with the transmission and crosstalk trends discussed in the

previous subsections, these results further support the selection of $\Delta = 10$ nm as the optimal operating point for the four-channel add–drop filter.

4.8.4 Optimization of the Number of Grating Periods

In the previous optimization steps, the total number of grating periods was fixed to $N = 1200$ in order to reduce the computational burden associated with full three-dimensional FDTD simulations. While this value is sufficient to capture the main trends of the multi-channel behavior, the interaction length related to N directly governs the strength of the distributed contra-directional coupling and, therefore, plays a critical role in determining the final drop-port transmission of each channel.

To complete the optimization of the four-channel add–drop filter, the impact of increasing the number of grating periods N is investigated while keeping all previously optimized geometrical parameters fixed. In particular, the grating-period separation is set to $\Delta = 10$ nm, and the four channels are associated with the grating periods $\Lambda_1 = 412$ nm, $\Lambda_2 = 422$ nm (forming G_1), and $\Lambda_3 = 417$ nm, $\Lambda_4 = 427$ nm (forming G_2), as discussed in the previous subsection.

Figure 4.14 reports the drop-port transmission of all four channels as a function of the total number of grating periods, with N varying from 1200 to 2000. A different behavior

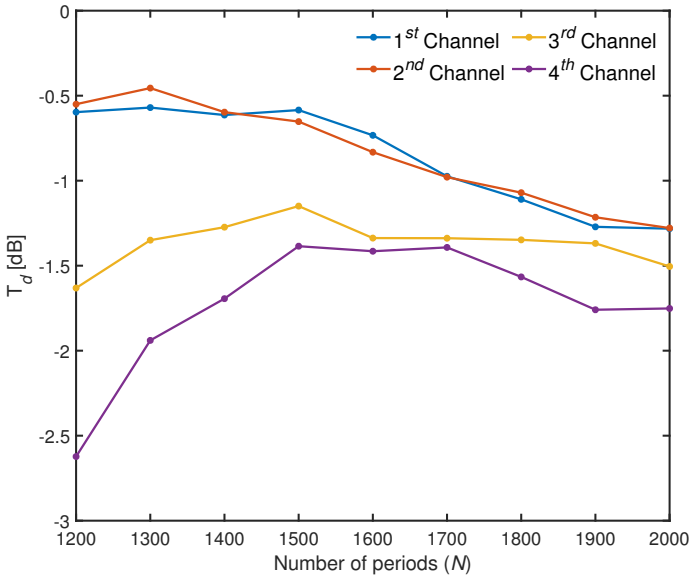


Figure 4.14: Drop-port transmission of the four extracted channels as a function of the number of grating periods N. Channels 1 and 2 exhibit stable transmission up to $N \approx 1500$, while channels 3 and 4 benefit from increased coupling strength. Beyond $N = 1500$, coupling effects lead to degradation of the first two channels without further improvement for the higher-order channels.

is observed for the different channels.

For channels 1 and 2, which are associated with the shorter grating periods, the drop-port transmission remains nearly constant as N increases, with values typically ranging between -0.5 dB and -1 dB up to approximately $N = 1500$. This indicates that, for these channels, the coupling strength is already sufficient at moderate interaction lengths and that further increasing N does not provide a significant benefit.

In contrast, channels 3 and 4 exhibit a different trend. As N increases, the drop-port transmission of these channels progressively improves, reflecting the fact that the larger grating periods associated with these channels lead to weaker coupling for a fixed interaction length. Consequently, a longer grating section is required to achieve efficient wavelength extraction for the channels associated with the larger grating periods.

However, when the number of grating periods exceeds approximately $N = 1500$, a saturation and eventual degradation behavior is observed. Beyond this point, the drop-port transmission of channels 3 and 4 no longer improves, and also channels 1 and 2 begin to experience a reduction in transmission. These results indicate the existence of an optimal grating length beyond which no further improvement in the multi-channel response is obtained.

Based on this trade-off, an optimal number of grating periods of $N = 1500$ is selected. At this value, the drop-port transmission of channels 3 and 4 is significantly enhanced, while channels 1 and 2 maintain high transmission levels without noticeable degradation. All subsequent simulations and performance evaluations of the four-channel add–drop filter are therefore carried out using $N = 1500$.

It is worth noting that, although increasing N improves the transmittance of the higher-order channels, it does not fully eliminate the residual losses observed in channels 1 and 2. This suggests the presence of additional loss mechanisms beyond incomplete coupling, such as radiation losses induced by refractive-index discontinuities at the grating interfaces, imperfect boundary conditions, and out-of-plane scattering inherent to full 3D-FDTD simulations.

4.8.5 Optimized Four-Channel Spectral Response

Figure 4.15 presents the transmission characteristics of the final optimized four-channel add–drop filter under the complete set of selected design parameters.

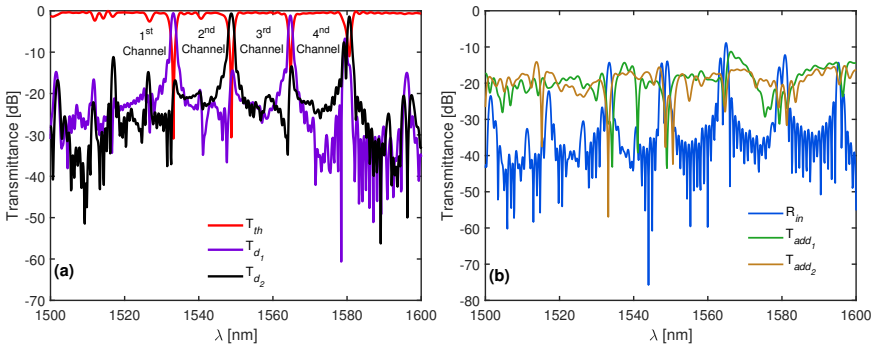


Figure 4.15: Transmission characteristics of the final optimized four-channel add–drop filter. (a) Through- and drop-port responses showing efficient wavelength-selective extraction and narrowband filtering. (b) Reflection at the input port and transmission toward the add ports, confirming controlled backward coupling and negligible unwanted add-port excitation.

The spectral response is reported in terms of through- and drop-port transmissions, as well as input-port reflection and add-port behavior, providing a comprehensive assessment of the device operation.

Figure 4.15(a) shows the through- and drop-port responses for all four channels. Four well-defined spectral peaks are observed at the drop ports, corresponding to the target wavelengths λ_1–λ_4. At these wavelengths, the through-port transmission exhibits pronounced suppression, confirming efficient wavelength-selective extraction via contra-directional coupling. Outside the targeted spectral bands, the through-port transmission remains close to unity, indicating that the filtering action is highly localized and does not introduce broadband insertion loss.

The drop-port responses exhibit narrowband behavior, consistent with the distributed Bragg-type coupling mechanism. Moreover, the uniform spectral spacing between the extracted channels confirms that the superimposed grating configuration preserves the intended wavelength allocation across the device, in agreement with the multi-channel optimization analysis discussed in the previous subsections.

Figure 4.15(b) reports the transmission toward the add ports together with the reflection at the input port. The reflection spectrum shows pronounced peaks at the

extracted wavelengths, confirming that the add–drop operation relies on a controlled backward-coupling mechanism rather than on resonant energy storage. At the same time, the reflected power remains spectrally confined to the target channels, with negligible broadband reflection elsewhere.

The add-port transmission remains strongly suppressed across the entire wavelength range, indicating minimal unwanted coupling toward the add ports under normal operation. This behavior confirms that the device operates as a wavelength-selective contra-directional coupler, rather than as a bidirectional reflector or resonant cavity.

Overall, the combined responses reported in Fig. 4.15 demonstrate that the final optimized structure achieves efficient multi-channel drop operation, strong through-port suppression at the target wavelengths, and controlled reflection consistent with contra-directional coupling. These results define the reference operating condition for the subsequent fabrication-oriented analysis.

For completeness, the optimized design parameters and performance metrics of the four-channel add–drop filter are summarized in Tables 4.3 and 4.4. The reported values correspond to the final design obtained after the combined optimization of the grating-period separation Δ and the total number of grating periods N.

Table 4.3 collects the global geometrical and architectural parameters defining the final device configuration, while Table 4.4 reports the channel-resolved spectral characteristics in terms of center wavelength, grating period, drop-port transmission, and 3-dB bandwidth. All values are reported for $\Delta = 10$ nm and $N = 1500$, which were identified as the optimal configuration ensuring a balanced trade-off between transmission efficiency, crosstalk suppression, wavelength-spacing uniformity, and bandwidth stability.

Table 4.3: Global optimized design parameters of the four-channel add–drop filter.

Parameter	**Value**
Number of channels	4
Grating-period separation Δ	10 nm
Number of grating periods N	1500
Lateral gap g	900 nm
Input waveguide width W_{in}	1200 nm
Grating waveguide width W_G	850 nm
Operating wavelength band	C-band
Coupling mechanism	Contra-directional (Bragg-assisted)

Table 4.4: Channel-resolved spectral performance of the optimized four-channel add–drop filter ($\Delta = 10$ nm, $N = 1500$).

Ch.	$\boldsymbol{\lambda_i}$ [nm]	$\boldsymbol{\Lambda_i}$ [nm]	$\boldsymbol{T_{d,i}}$ [dB]	$\boldsymbol{BW_{3\text{dB},i}}$ [nm]	$\boldsymbol{\Delta\lambda}$ [nm]
1	$\lambda_1 = 1533$ nm	$\Lambda_1 = 412$ nm	~ -0.7	~ 1.2	~ 16
2	$\lambda_2 = 1549$ nm	$\Lambda_2 = 417$ nm	~ -1.0	~ 1.2	
3	$\lambda_3 = 1565$ nm	$\Lambda_3 = 422$ nm	~ -1.2	~ 1	
4	$\lambda_4 = 1581$ nm	$\Lambda_4 = 427$ nm	~ -1.4	~ 0.9	

The approximately constant inter-channel spacing $\Delta\lambda$ reported in Table 4.4 directly reflects the imposed constraint on the grating-period differences and confirms the predictable spectral organization of the four-channel structure.

4.9 Fabrication Tolerance Analysis

4.9.1 Sensitivity to Duty-Cycle Variations

In practical fabrication processes, the duty cycle of the grating pattern cannot be controlled with perfect accuracy. Deviations from the nominal duty cycle may arise from lithographic

proximity effects, etch non-uniformity, or resist profile variations. It is therefore important to evaluate the sensitivity of the proposed multi-channel add–drop filter to duty-cycle fluctuations.

Figure 4.16 summarizes the effect of duty-cycle variations on the optimized four-channel structure. Figure 4.16(a) presents the drop-port transmission of the four wavelength channels as a function of the duty cycle. Figure 4.16(b) reports the corresponding center wavelengths of the extracted channels, while Fig. 4.16(c) shows the associated 3-dB bandwidths. In this analysis, the duty cycle is varied around its nominal value of 0.5 within the range 0.48–0.52, while all other geometrical and spectral parameters are kept fixed at their optimized values ($\Delta = 10$ nm and $N = 1500$).

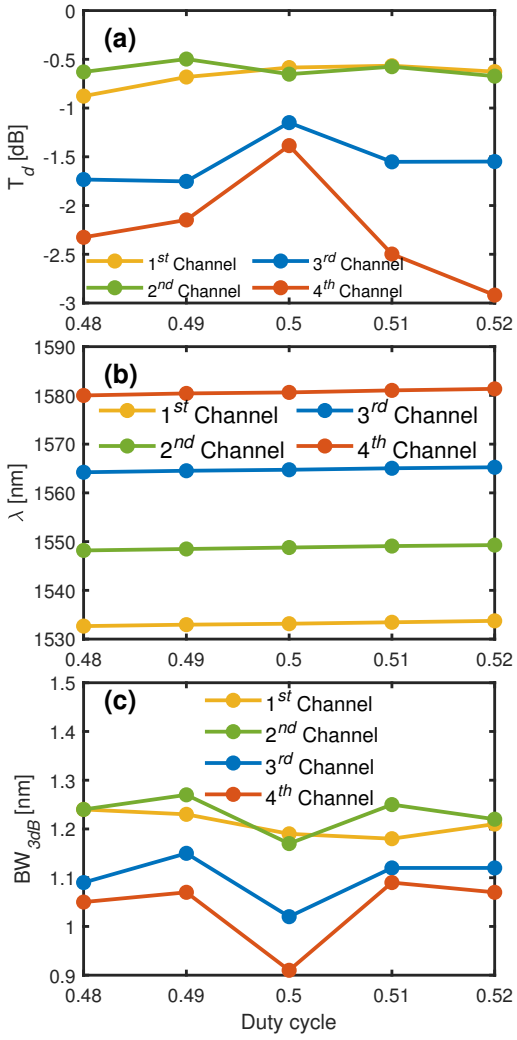


Figure 4.16: Effect of duty-cycle variations on the optimized multi-channel add–drop filter: (a) drop-port transmission of the four wavelength channels, (b) center wavelengths of the extracted channels, and (c) corresponding 3-dB bandwidths. The results confirm that duty-cycle variations mainly influence the transmission efficiency, while the spectral positions and bandwidths of the channels remain largely stable.

As observed in Fig. 4.16(a), duty-cycle variations mainly affect the drop-port transmission efficiency of the channels. Channels 1 and 2 maintain relatively stable transmission levels throughout the investigated duty-cycle range, whereas channels 3

and 4 exhibit a more pronounced dependence on the duty cycle, with their highest transmission achieved close to the nominal value of 0.5. This behavior is associated with the larger grating periods used for channels 3 and 4, which require stronger distributed coupling to achieve efficient wavelength extraction.

Figure 4.16(b) shows that the center wavelengths of all four channels remain nearly unchanged as the duty cycle varies from 0.48 to 0.52. This confirms that the spectral positions of the extracted channels are primarily determined by the grating periods, while duty-cycle variations mainly influence the coupling efficiency rather than the Bragg phase-matching condition.

The effect of duty-cycle variations on the spectral selectivity is further evaluated through the 3-dB bandwidth analysis shown in Fig. 4.16(c). Across the investigated range, all channels preserve narrow bandwidths between approximately 1 and 1.5 nm, with only limited variations observed among the different duty-cycle values. At the optimized duty cycle of 0.5, where the drop-port transmissions of the four channels become nearly balanced, the bandwidths are also similar, indicating consistent filtering characteristics among the channels.

Overall, the absence of abrupt performance degradation together with the limited sensitivity of the center wavelengths and bandwidths demonstrates that the proposed multi-channel add–drop filter exhibits robustness compatible with realistic fabrication tolerances. The results indicate that moderate duty-cycle deviations mainly introduce predictable changes in transmission efficiency without significantly affecting the spectral organization or wavelength-selective operation of the device.

4.9.2 Effect of Waveguide Thickness and Width Variations

After evaluating the sensitivity to duty-cycle variations, the robustness of the optimized multi-channel add–drop filter is further assessed under representative fabrication imperfections. In realistic fabrication processes, both lateral dimensional deviations (originating from lithography and etch bias) and vertical non-uniformities (related to film-thickness variations) may occur. These imperfections can affect both the Bragg phase-matching condition and the distributed coupling strength of grating-assisted contra-directional couplers.

Two dominant fabrication deviations are considered, as illustrated in Fig. 4.17: Symmetric dimensional deviations of ±20 nm around the nominal geometry are considered to represent both positive and negative systematic fabrication biases. Accordingly, the analyzed cases are: (i) lateral waveguide-width deviations of $\delta W = -20$, 0, +20 nm, and (ii) SiN-thickness deviations of $\delta t_{\mathrm{SiN}} = -20$, 0, +20 nm.

The selected magnitude of 20 nm provides a common perturbation level for comparing the lateral and vertical dimensional sensitivities of the device. Both signs are considered because width and thickness deviations may arise in either direction during fabrication and may produce asymmetric changes in modal confinement, Bragg wavelength, and coupling strength.

Figures 4.17(a) and (b) compare the drop-port transmission spectra obtained for the nominal geometry and for dimensional deviations of ±20 nm in the waveguide width and SiN thickness, respectively. Figures 4.17(c) and (d) show the corresponding channel center wavelengths over the complete variation range from −20 to +20 nm.

The spectral comparison in Fig. 4.17(a) indicates that lateral width deviations produce a more pronounced perturbation of the device response compared to thickness variations. In addition to inducing shifts in the channel center wavelengths, the width deviation leads to a moderate reduction in the peak drop-port transmission. This increased sensitivity is physically consistent with the fact that a lateral bias simultaneously perturbs the effective indices of the interacting modes and the lateral geometry of the coupling region, including the effective gap between the coupled waveguides. As a result, both the Bragg condition and the coupling strength are affected.

It is important to note that the lateral width variation is applied uniformly to all waveguides in the structure. In this case, the width deviation is introduced in a symmetric

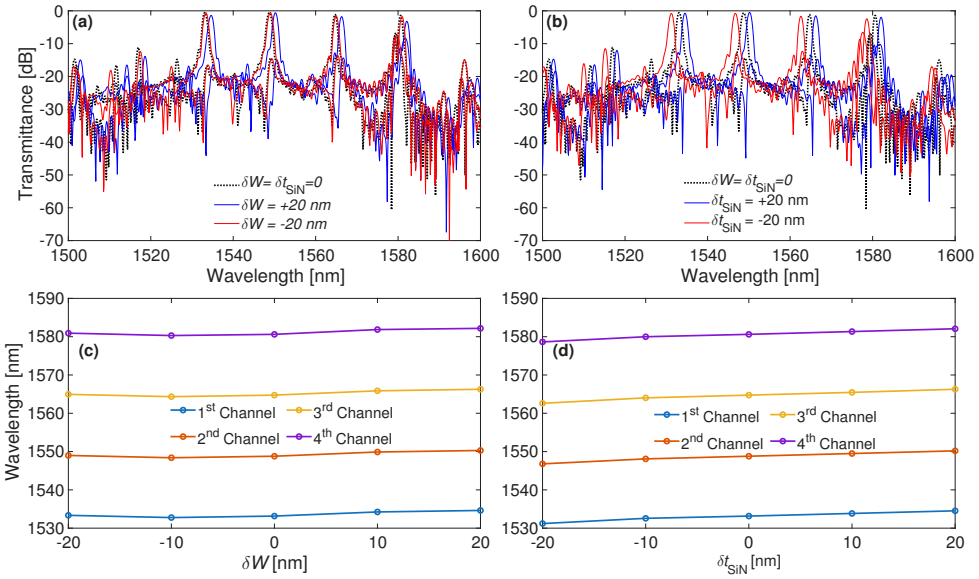


Figure 4.17: Impact of dimensional variations on the optimized multi-channel add–drop filter, based on Fig. 12 of [87]. (a) Drop-port transmission spectra for the nominal structure and for waveguide-width deviations of $\delta W = \pm 20$ nm. (b) Drop-port transmission spectra for the nominal structure and for SiN-thickness deviations of $\delta t_{\mathrm{SiN}} = \pm 20$ nm. (c) Channel center wavelengths as functions of δW over the range from -20 to $+20$ nm. (d) Channel center wavelengths as functions of δt_{SiN} over the same range.

manner, meaning that an increase of δW results in a corresponding reduction of the gap between adjacent waveguides. Consequently, a width variation of $\delta W = +20$ nm leads to an effective gap variation of $\delta g = -20$ nm, such that a nominal gap of $g = 900$ nm is reduced to $g = 880$ nm.

This assumption reflects a systematic fabrication bias, as typically observed in lithography and etching processes, where dimensional variations affect all features simultaneously rather than independently.

In contrast, Fig. 4.17(b) shows that variations in the SiN thickness have a milder impact on the spectral response. Thickness deviations primarily modify the effective-index and modal dispersion, resulting mainly in wavelength shifts, while the degradation of the drop-port transmission remains limited.

The corresponding central-wavelength shifts are summarized in Fig. 4.17(c) for lateral deviations and in Fig. 4.17(d) for thickness variations. In both cases, the wavelength shifts remain moderate and do not compromise the relative spectral ordering of the four channels. Importantly, no abrupt performance collapse, channel merging, or loss of add–drop functionality is observed within the considered tolerance range.

Overall, the results confirm that the optimized four-channel add–drop filter maintains its intended operation under typical fabrication tolerances. The observed performance degradation is gradual and predictable, with lateral width variations representing the dominant sensitivity mechanism. These findings demonstrate that the proposed architecture exhibits a level of robustness compatible with standard nanofabrication capabilities.

4.9.3 Minimum Feature Size and Edge-Spacing Constraints

In addition to dimensional deviations, practical fabrication processes impose strict constraints on the minimum realizable feature size and the minimum spacing between adjacent etched regions. Such constraints originate from the finite resolution of the lithography process, fabrication-induced dimensional deviations, and the limited accuracy with which the designed grating pattern can be transferred to the fabricated structure.

To assess the manufacturability of the proposed multi-channel add–drop filter, the impact of enforcing a conservative minimum edge-to-edge spacing of 100 nm is investigated.

This constraint effectively emulates the inability of the fabrication process to reliably resolve very narrow gaps between adjacent grating features.

Figure 4.18 reports the transmission response of the optimized four-channel add–drop filter after enforcing the minimum spacing constraint across the entire grating structure.

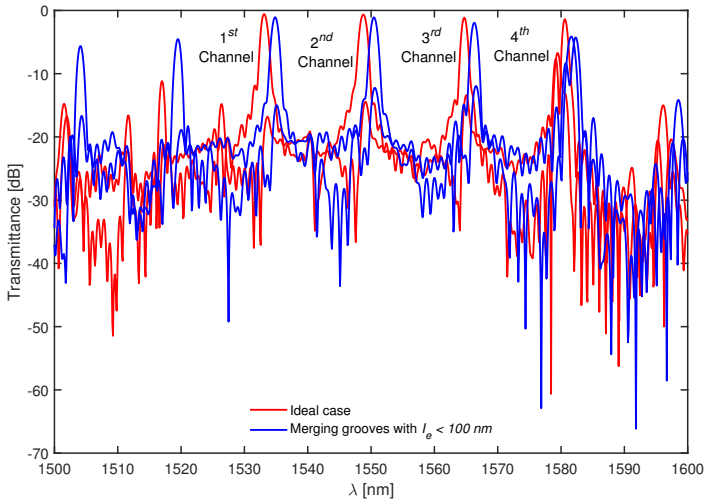


Figure 4.18: Transmission spectra of the optimized multi-channel add–drop filter for the ideal design and for the structure obtained after merging grooves with $l_e < 100$ nm, in accordance with the minimum fabrication spacing rule. The comparison shows only minor variations in insertion loss, while the channel wavelengths remain essentially unchanged.

The minimum-spacing constraint is applied to all grating segments where adjacent etched features would otherwise violate fabrication limits, effectively replacing sub-resolution regions with continuous SiN sections. This approach mirrors the fabrication scenario in which narrow grooves are merged due to lithographic and etching limitations.

As shown in Fig. 4.18, enforcing a minimum edge-to-edge spacing of 100 nm leads only to limited performance degradation. In particular, the insertion loss of the first three channels increases by approximately 0.6 dB, while the fourth channel exhibits a larger, yet still moderate, degradation of about 2.7 dB. Despite this increase, all channels preserve a well-defined spectral response and remain clearly distinguishable.

In addition to amplitude variations, a small shift in the central wavelength of each channel is observed. However, for all channels, the wavelength shift remains below 2 nm, indicating that the spectral positioning is preserved even under conservative fabrication constraints. No abrupt spectral distortion of the add–drop functionality is observed.

These results confirm that the optimized device does not rely on sub-resolution grating features to achieve its wavelength-selective behavior. Instead, the distributed Bragg coupling mechanism remains dominant and robust, even when realistic minimum feature-size and spacing constraints are enforced. The limited insertion-loss degradation and the small wavelength shifts demonstrate that the proposed add–drop filter is compatible with practical fabrication processes and exhibits strong tolerance to feature-merging effects.

4.10 Discussion

The add–drop filters investigated in this work are implemented on a hybrid silicon nitride on thin-film lithium niobate (SiN–TFLN) platform. This choice is not motivated by generic material advantages, but rather by the specific requirements imposed by grating-assisted contra-directional coupling and by the performance trade-offs identified in the preceding design analysis.

In grating-assisted contra-directional couplers, the spectral response is governed by the distributed coupling strength between forward- and backward-propagating modes.

As demonstrated by the numerical results presented in this chapter, both the achievable transmission to the drop port and the suppression of parasitic back-reflection critically depend on the balance between the self-coupling coefficient κ_{11} and the cross-coupling coefficient κ_{12}. Accurate and independent control of these coefficients requires precise engineering of the refractive-index modulation amplitude, spatial overlap, and modal confinement along the grating section.

Silicon nitride is particularly well suited for fulfilling these requirements. Its moderate refractive-index contrast with respect to the surrounding cladding enables the realization of well-defined periodic perturbations while avoiding excessive scattering or radiation loss. Moreover, the mature etching processes available for SiN allow fine and reproducible control of grating geometry, which is essential for tuning the distributed coupling coefficients. This directly supports the design strategy adopted in this work, where κ_{12} is intentionally enhanced to promote efficient wavelength extraction, while κ_{11} is kept at a controlled level to limit undesired reflection at the input port.

Thin-film lithium niobate is employed as the guiding substrate due to its intrinsically low propagation loss and favorable dispersion characteristics over the wavelength ranges considered in this study.

A key advantage of the proposed devices lies in the combination of Silicon Nitride and Lithium Niobate. The silicon nitride layer acts as the primary grating-engineering medium, where the periodic refractive-index modulation and superimposed grating profiles are defined with high geometrical precision. The underlying thin-film lithium niobate layer, on the other hand, provides optical confinement and ensures stable modal propagation throughout the interaction length. This material combination allows the improvement of both the optimization of coupling strength and the propagation loss, which would be significantly more constrained in a single-material implementation.

An all-TFLN realization of the proposed add–drop filters would impose tighter constraints on grating definition and etch-depth control, thereby limiting the accessible range of coupling coefficients. Conversely, an all-silicon-nitride platform would sacrifice the ultra-low-loss guiding properties and the long-term extensibility toward active or tunable functionalities offered by lithium niobate. The hybrid SiN–TFLN platform therefore represents a balanced and application-driven compromise that directly supports the contra-directional add–drop functionality targeted in this work.

Finally, the adopted platform naturally enables scalable wavelength routing through superimposed grating concepts. The flexibility of silicon nitride in defining multiple spatial-frequency components within a single grating section allows multiple wavelength channels to be engineered without modifying the underlying guiding structure.

4.11 Summary

This chapter addressed wavelength-selective routing in photonic integrated circuits through the design of grating-assisted contra-directional add–drop filters on a hybrid SiN–TFLN platform.

Starting from the fundamental Bragg phase-matching principle, a set of figures of merit was introduced to evaluate wavelength extraction efficiency, through-port suppression, crosstalk, and spectral selectivity. These metrics were used as a systematic design methodology, progressing from a single-channel configuration toward dual- and multi-channel architectures based on superimposed gratings.

The design-space exploration highlighted the interplay between geometrical parameters and distributed coupling strength, revealing the trade-offs required to simultaneously achieve high drop efficiency, low crosstalk, and stable spectral response. In particular, the superimposed grating approach enabled multiple wavelength channels to be integrated within a single coupling section, avoiding the need for cascaded filtering stages.

The robustness of the proposed structures was further assessed under realistic fabrication constraints, showing that the spectral behavior remains stable while performance degradation is gradual and predictable.

The results of this chapter establish a scalable framework for wavelength-selective routing based on contra-directional coupling, which can be extended toward more complex photonic architectures and system-level implementations.

Conclusions

This thesis has addressed the design, analysis, and experimental validation of passive photonic integrated circuit (PIC) components, with a primary focus on power distribution and wavelength-selective functionalities. In particular, the work has investigated multimode interference (MMI) couplers as broadband power splitters/combiners and grating-assisted contra-directional couplers (GACDC) as add-drop filters.

A central aspect of this thesis has been the adoption of a fabrication-aware design approach, where all device geometries and performance metrics were evaluated not only under ideal conditions but also in the presence of fabrication-induced variations. In this context, systematic tolerance analyses were carried out to assess the robustness of the proposed devices against variations in key parameters such as thickness, waveguide width, and grating geometry.

The thesis combines numerical design and experimental characterization through the fabrication and measurement of selected MMI devices. The experimental results, obtained under non-ideal conditions such as the use of C-band grating couplers for O-band-designed structures, provided a valuable framework for understanding real-device behavior. The results were used to interpret the impact of off-design operation, coupling inefficiencies, and fabrication deviations on device performance.

From a design perspective, a comprehensive framework for MMI couplers on the TFLN platform has been developed. Starting from the fundamental self-imaging principle, the work explored the role of geometrical parameters in determining insertion loss, output uniformity, and broadband response. In addition, the phase relations between output ports and their dependence on device geometry were analyzed, providing further insight into coherent combining behavior and wavelength stability.

The experimental investigation confirmed that MMI devices on lithium niobate exhibit inherently broadband characteristics and a relatively high tolerance to fabrication variations.

A key outcome of this work is the identification of topology-dependent robustness in MMI devices. Lower-order configurations, such as 1×2 splitters, exhibit inherently higher tolerance to fabrication-induced variations due to reduced modal complexity and more stable self-imaging conditions. In contrast, higher-order structures, including 1×4 and 2×2 devices, show increased sensitivity to both geometrical variations and wavelength detuning, particularly under off-design operation.

Furthermore, the analysis revealed that thickness variations represent one of the dominant factors affecting device performance in TFLN platforms, directly influencing effective indices and self-imaging conditions. Despite this, the devices maintain functional operation over a wide spectral range, confirming the broadband and fabrication-tolerant nature of MMI-based designs.

The thesis introduced a wavelength-selective routing strategy based on grating-assisted contra-directional coupling. A key contribution in this context is the development of a superimposed grating concept, enabling multi-wavelength extraction within a single device without the need for cascaded structures. This approach provides a compact and scalable solution for multi-channel filtering.

In wavelength-selective structures, the use of superimposed gratings enables compact multi-channel operation, but introduces additional sensitivity to fabrication constraints, particularly when the gaps between adjacent grating features approach sub-100 nm dimensions. In the investigated designs, this minimum-gap limitation was found to significantly affect the efficiency of the fourth channel, which exhibited the highest sensitivity among the considered channels. Variations in waveguide width and thickness were also observed to influence the overall channel efficiency and spectral shift, although

their impact remained less pronounced than that associated with the minimum-gap constraint. These observations highlight the fundamental trade-off between device compactness, functionality, and fabrication feasibility in advanced integrated photonic structures.

Future Work

The results presented in this thesis open several directions for further research, particularly toward the realization of fully integrated photonic systems combining passive, active, and nonlinear functionalities.

A first extension of this work concerns the integration of nonlinear optical functionalities in lithium niobate platforms. In particular, periodically poled lithium niobate (PPLN) structures will be investigated for efficient wavelength conversion based on second-order nonlinear processes such as second-harmonic generation (SHG), sum-frequency generation (SFG), and difference-frequency generation (DFG). The objective is to extend the functionality of the demonstrated passive devices toward wavelength translation and frequency conversion within the same integrated platform.

A second research direction involves the design and modeling of electro-optic devices, such as Mach–Zehnder modulators (MZMs), on the TFLN platform. In this context, future work will incorporate the co-design of optical and radio-frequency (RF) domains, enabling realistic modeling of modulation efficiency, bandwidth limitations, and electrode–waveguide interactions. Experimental realization and characterization of such devices will further bridge the gap between numerical design and practical system implementation.

Finally, a key long-term objective is the transition from device-level design to system-level integration. The combination of power-distribution components (MMIs), wavelength-selective filters (GACDC-based add–drop devices), and future active and nonlinear elements will enable the development of more complex photonic circuits. System-level analysis will allow the evaluation of performance metrics such as scalability, signal integrity, and overall functionality within integrated photonic architectures.

These directions aim to extend the present work from passive device design toward a comprehensive photonic system platform capable of power manipulation, wavelength routing, modulation, and nonlinear signal processing.

References

[1] Xiao, Z., Liu, W., Xu, S., Zhou, J., Ren, Z., and Lee, C., "Recent progress in silicon-based photonic integrated circuits and emerging applications," *Advanced Optical Materials*, vol. 11, no. 20, p. 2 301 028, 2023. DOI: https://doi.org/10.1002/adom.202301028 eprint: https://advanced.onlinelibrary.wiley.com/doi/pdf/10.1002/adom.202301028. [Online]. Available: https://advanced.onlinelibrary.wiley.com/doi/abs/10.1002/adom.202301028

[2] Su, Y., He, Y., Guo, X., Xie, W., Ji, X., Wang, H., Cai, X., Tong, L., and Yu, S., "Scalability of large-scale photonic integrated circuits," *ACS Photonics*, vol. 10, no. 7, pp. 2020–2030, 2023. DOI: 10.1021/acsphotonics.2c01529

[3] Dong, P., "Silicon photonic integrated circuits for wavelength-division multiplexing applications," *IEEE Journal of Selected Topics in Quantum Electronics*, vol. 22, no. 6, pp. 370–378, 2016. DOI: 10.1109/JSTQE.2016.2575358

[4] Mu, X., Wu, S., Cheng, L., and Fu, H., "Edge couplers in silicon photonic integrated circuits: A review," *Applied Sciences*, vol. 10, no. 4, 2020. DOI: 10.3390/app10041538 [Online]. Available: https://www.mdpi.com/2076-3417/10/4/1538

[5] Zhang, Y., Sun, D., Yu, M., Xu, Y., and Chen, Z., "Active manipulation for goos-hänchen shift of guided-wave via a metasurface of silicon-nanoscale semi-spheres on soi waveguide," *Opt. Express*, vol. 32, no. 11, pp. 19 999–20 010, May 2024. DOI: 10.1364/OE.522948 [Online]. Available: https://opg.optica.org/oe/abstract.cfm?URI=oe-32-11-19999

[6] Zhang, C., Yang, H., Cui, P., Ma, J., Huang, S., Guo, L., Li, J., Zhang, J., Wang, Y., Yin, X., Chen, W., Wu, Y., and An, J., "High extinction ratio multi-polarization states preparation based on soi integrated chips," *Optics Communications*, vol. 574, p. 131 177, 2025. DOI: https://doi.org/10.1016/j.optcom.2024.131177 [Online]. Available: https://www.sciencedirect.com/science/article/pii/S0030401824009143

[7] Henriksson, A., Neubauer, P., and Birkholz, M., "Strategies to realize ac electrokinetic enhanced mass-transfer in silicon based photonic biosensors.," *Advanced Materials Technologies*, vol. 10, no. 2, p. 2 302 191, 2025. DOI: https://doi.org/10.1002/admt.202302191 eprint: https://advanced.onlinelibrary.wiley.com/doi/pdf/10.1002/admt.202302191. [Online]. Available: https://advanced.onlinelibrary.wiley.com/doi/abs/10.1002/admt.202302191

[8] Marinis, L. de, Seigo Kincaid, P., Lucas, Y., Krafft, L., Michau, V., Cherchi, M., Karppinen, M., and Contestabile, G., "A silicon photonic 32-input coherent combiner for turbulence mitigation in free space optics links," *IEEE Access*, vol. 13, pp. 31 718–31 728, 2025. DOI: 10.1109/ACCESS.2025.3541870

[9] Wang, K., Dong, X., Köhler, M. H., Kienle, P., Bian, Q., Jakobi, M., and Koch, A. W., "Advances in optical fiber sensors based on multimode interference (mmi): A review," *IEEE Sensors Journal*, vol. 21, no. 1, pp. 132–142, 2021. DOI: 10.1109/JSEN.2020.3015086

[10] Arafin, S. and Coldren, L. A., "Advanced inp photonic integrated circuits for communication and sensing," *IEEE Journal of Selected Topics in Quantum Electronics*, vol. 24, no. 1, pp. 1–12, 2018. DOI: 10.1109/JSTQE.2017.2754583

[11] Tol, J. J. G. M. van der, Jiao, Y., Shen, L., Millan-Mejia, A., Pogoretskii, V., Engelen, J. P. van, and Smit, M. K., "Indium phosphide integrated photonics in membranes," *IEEE Journal of Selected Topics in Quantum Electronics*, vol. 24, no. 1, pp. 1–9, 2018. DOI: 10.1109/JSTQE.2017.2772786

[12] Reniers, S., Wang, Y., Abdi, S., Graaf, J. de, Zozulia, A., Williams, K., and Jiao, Y., "Highly versatile photonic integration platform on an indium phosphide membrane," *Chips*, vol. 4, no. 3, 2025. DOI: 10.3390/chips4030032 [Online]. Available: https://www.mdpi.com/2674-0729/4/3/32

[13] Mukherjee, C., Deng, M., Nodjiadjim, V., Riet, M., Mismer, C., Guendouz, D., Caillaud, C., Bertin, H., Vaissiere, N., Luisier, M., Wen, X., De Matos, M., Mounaix, P., and Maneux, C., "Towards monolithic indium phosphide (inp)-based electronic photonic technologies for beyond 5g communication systems," *Applied Sciences*, vol. 11, no. 5, 2021. DOI: 10.3390/app11052393 [Online]. Available: https://www.mdpi.com/2076-3417/11/5/2393

[14] Wu, C., Zhang, J., Wong, H., Liu, J., Qin, X., Wu, L., Bao, W., Duan, J., Zhao, B., Yang, A., and Chen, X., "Room-temperature high-performance inp/si surface-activated wafer bonding for electronic-photonic system integration applications," *ACS Applied Electronic Materials*, vol. 8, no. 6, pp. 2545–2557, 2026. DOI: 10.1021/acsaelm.6c00018

[15] Li, J., Han, L., Wang, D., Chen, M., Zhang, D., and Li, H., "Sub-hz linewidth integrated photonic microwave generation based on a low-noise hybrid inp/si3n4 comb laser," *Photon. Res.*, vol. 13, no. 11, pp. 3034–3044, Nov. 2025. DOI: 10.1364/PRJ.561151 [Online]. Available: https://opg.optica.org/prj/abstract.cfm?URI=prj-13-11-3034

[16] Runge, P., Schindler, A., Gläsel, J., Theurer, M., Fiol, G., and Schell, M., "Indium phosphide platform for high-speed optical transceivers (invited)," in *2025 IEEE Photonics Society Summer Topicals Meeting Series (SUM)*, 2025, pp. 1–2. DOI: 10.1109/SUM65312.2025.11121810

[17] Buzaverov, K. A., Baburin, A. S., Sergeev, E. V., Avdeev, S. S., Lotkov, E. S., Bukatin, S. V., Stepanov, I. A., Kramarenko, A. B., Amiraslanov, A. S., Kushnev, D. V., Ryzhikov, I. A., and Rodionov, I. A., "Silicon nitride integrated photonics from visible to mid-infrared spectra," *Laser & Photonics Reviews*, vol. 18, no. 12, p. 2 400 508, 2024. DOI: https://doi.org/10.1002/lpor.202400508 eprint: https://onlinelibrary.wiley.com/doi/pdf/10.1002/lpor.202400508. [Online]. Available: https://onlinelibrary.wiley.com/doi/abs/10.1002/lpor.202400508

[18] Xiang, C., Jin, W., and Bowers, J. E., "Silicon nitride passive and active photonic integrated circuits: Trends and prospects," *Photon. Res.*, vol. 10, no. 6, A82–A96, Jun. 2022. DOI: 10.1364/PRJ.452936 [Online]. Available: https://opg.optica.org/prj/abstract.cfm?URI=prj-10-6-A82

[19] Tan, D. T. H., Ng, D. K. T., Choi, J. W., Sahin, E., Sohn, B.-. U., Chen, G. F. R., Xing, P., Gao, H., and Cao, Y., "Nonlinear optics in ultra-silicon-rich nitride devices: Recent developments and future outlook," *Advances in Physics: X*, vol. 6, no. 1, p. 1 905 544, 2021. DOI: 10.1080/23746149.2021.1905544

[20] Wilmart, Q., El Dirani, H., Tyler, N., Fowler, D., Malhouitre, S., Garcia, S., Casale, M., Kerdiles, S., Hassan, K., Monat, C., Letartre, X., Kamel, A., Pu, M., Yvind, K., Oxenløwe, L. K., Rabaud, W., Sciancalepore, C., Szelag, B., and Olivier, S., "A versatile silicon-silicon nitride photonics platform for enhanced functionalities and applications," *Applied Sciences*, vol. 9, no. 2, 2019. DOI: 10.3390/app9020255 [Online]. Available: https://www.mdpi.com/2076-3417/9/2/255

[21] Fraser, W., Korček, R., Benedikovič, D., Horvath, C., Wang, S., Vachon, M., Ma, R., Schmid, J. H., Cheben, P., and Ye, W. N., "Single-etch silicon nitride grating couplers for multiband applications in quantum and fiber communications," *IEEE Journal of Selected Topics in Quantum Electronics*, vol. 31, no. 5: Quantum Materials and Quantum Devices, pp. 1–10, 2025. DOI: 10.1109/JSTQE.2025.3574059

[22] Cui, S., Yu, Y., Cao, K., Pan, Z., Gao, X., and Zhang, X., "Integrated waveguide coupled ultralow-loss multimode waveguides based on silicon nitride resonators," *Opt. Express*, vol. 32, no. 2, pp. 2179–2187, Jan. 2024. DOI: 10.1364/OE.507791 [Online]. Available: https://opg.optica.org/oe/abstract.cfm?URI=oe-32-2-2179

[23] Liu, F., Lv, H., Zhang, H., Liu, S., Liang, Y., Wang, H., Cong, Y., Li, X., and Guo, Q., "Design of polarization-independent 1 × 2 optical power splitter based on silicon nitride slot waveguide structure," *Scientific Reports*, vol. 15, no. 1, p. 25 288, 2025. DOI: 10.1038/s41598-025-11404-0

[24] Ishimura, S., Elfiqi, A. E., Kan, T., Takahashi, H., and Tsuritani, T., "Silicon-nitride photonic integrated waveguide for dual-polarization traveling-wave four-wave-mixing applications," *Opt. Express*, vol. 33, no. 9, pp. 19 546–19 557, May 2025. DOI: 10.1364/OE.558777 [Online]. Available: https://opg.optica.org/oe/abstract.cfm?URI=oe-33-9-19546

[25] Prousalidi, T., Syriopoulos, G., Kyriazi, E., Botter, R., Zervos, C., Poulopoulos, G., and Apostolopoulos, D., "Flat emission silicon nitride grating couplers for lidar optical antennas," *Photonics*, vol. 12, no. 3, 2025. DOI: 10.3390/photonics12030214 [Online]. Available: https://www.mdpi.com/2304-6732/12/3/214

[26] Xie, Z., Bo, F., Lin, J., Hu, H., Cai, X., Tian, X.-H., Fang, Z., Chen, J., Wang, M., Chen, F., Cheng, Y., Xu, J., and Zhu, S., "Recent development in integrated lithium niobate photonics," *Advances in Physics: X*, vol. 9, no. 1, p. 2 322 739, 2024. DOI: 10.1080/23746149.2024.2322739

[27] Vazimali, M. G. and Fathpour, S., "Applications of thin-film lithium niobate in nonlinear integrated photonics," *Advanced Photonics*, vol. 4, no. 3, May 30, 2022, https://www.spiedigitallibrary.org/journals/advanced-photonics/volume-4/issue-3/034001/Applications-of-thin-film-lithium-niobate-in-nonlinear-integrated-photonics/10.1117/1.AP.4.3.034001.pdf ; https://doi.org/10.1117/1.ap.4.3.034001. DOI: 10.1117/1.ap.4.3.034001 [Online]. Available: https://lens.org/069-533-711-861-92X

[28] Boes, A., Corcoran, B., Chang, L., Bowers, J., and Mitchell, A., "Status and potential of lithium niobate on insulator (lnoi) for photonic integrated circuits," *Laser & Photonics Reviews*, vol. 12, no. 4, p. 1 700 256, 2018. DOI: https://doi.org/10.1002/lpor.201700256 eprint: https://onlinelibrary.wiley.com/doi/pdf/10.1002/lpor.201700256. [Online]. Available: https://onlinelibrary.wiley.com/doi/abs/10.1002/lpor.201700256

[29] Li, Z., Wang, R. N., Lihachev, G., Zhang, J., Tan, Z., Churaev, M., Kuznetsov, N., Siddharth, A., Bereyhi, M. J., Riemensberger, J., and Kippenberg, T. J., "High density lithium niobate photonic integrated circuits," *Nature Communications*, vol. 14, no. 1, p. 4856, 2023. DOI: 10.1038/s41467-023-40502-8

[30] Peng, Y., Yang, S., Wu, R., and Hong, W., "Efficient optical parametric amplification in the thin film lithium niobate waveguides," *Scientific Reports*, vol. 15, no. 1, p. 2851, 2025. DOI: 10.1038/s41598-025-87524-4

[31] Lu, J., Chen, G., Su, W., Li, H., Gu, X., and Yu, H., "High efficiency and ultra-broadband suspended grating coupler on ultra-thin lithium niobate on insulator," *Opt. Express*, vol. 33, no. 13, pp. 28 226–28 232, Jun. 2025. DOI: 10.1364/OE.565933 [Online]. Available: https://opg.optica.org/oe/abstract.cfm?URI=oe-33-13-28226

[32] Chen, M., Wang, C., Jia, K., Tian, X.-H., Tang, J., Zhu, C., Gu, X., Zhao, Z., Wang, Z., Ye, Z., Tang, J., Zhang, Y., Yan, Z., Wang, X., Qian, G., Jin, B., Wang, Z., Zhu, S.-N., and Xie, Z., "High-gain optical parametric amplification with a continuous-wave pump using a domain-engineered thin-film lithium niobate waveguide," *Optica*, vol. 12, no. 8, pp. 1242–1249, Aug. 2025. DOI: 10.1364/OPTICA.565112 [Online]. Available: https://opg.optica.org/optica/abstract.cfm?URI=optica-12-8-1242

[33] Ou, S., Xue, K., Zhou, L., Lee, C.-h., Sludds, A., Hamerly, R., Zhang, K., Feng, H., Yu, Y., Kopparapu, R., Zhong, E., Wang, C., Englund, D., Yu, M., and Chen, Z., "Hypermultiplexed integrated photonics–based optical tensor processor," *Science Advances*, vol. 11, no. 23, eadu0228, 2025. DOI: 10.1126/sciadv.adu0228 eprint: https://www.science.org/doi/pdf/10.1126/sciadv.adu0228. [Online]. Available: https://www.science.org/doi/abs/10.1126/sciadv.adu0228

[34] Wackernagel, D., Kaufmann, F., Maeder, A., Grange, R., and Franck, C. M., "Design choices for an integrated optical electric field sensor in lithium niobate on insulator," *IEEE Access*, vol. 13, pp. 33 683–33 696, 2025. DOI: 10.1109/ACCESS.2025.3538846

[35] Moeini, N. and Nouroozi, R., "Effective electro-optical coefficient determination of low finesse periodically poled lithium niobate waveguide resonator," *Scientific Reports*, vol. 15, no. 1, p. 22 009, 2025. DOI: 10.1038/s41598-025-05917-x

[36] Hou, S., Hu, H., Liu, Z., Xing, W., Zhang, J., and Hao, Y., "High-speed electro-optic modulators based on thin-film lithium niobate," *Nanomaterials*, vol. 14, no. 10, 2024. DOI: 10.3390/nano14100867 [Online]. Available: https://www.mdpi.com/2079-4991/14/10/867

[37] Zhang, J., Wang, C., Denney, C., Riemensberger, J., Lihachev, G., Hu, J., Kao, W., Blésin, T., Kuznetsov, N., Li, Z., Churaev, M., Ou, X., Santamaria-Botello, G., and Kippenberg, T. J., "Ultrabroadband integrated electro-optic frequency comb in lithium tantalate," *Nature*, vol. 637, no. 8048, pp. 1096–1103, 2025. DOI: 10.1038/s41586-024-08354-4

[38] Komljenovic, T., Huang, D., Pintus, P., Tran, M. A., Davenport, M. L., and Bowers, J. E., "Photonic integrated circuits using heterogeneous integration on silicon," *Proceedings of the IEEE*, vol. 106, no. 12, pp. 2246–2257, 2018. DOI: 10.1109/JPROC.2018.2864668

[39] Xiang, C., Jin, W., Huang, D., Tran, M. A., Guo, J., Wan, Y., Xie, W., Kurczveil, G., Netherton, A. M., Liang, D., Rong, H., and Bowers, J. E., "High-performance silicon photonics using heterogeneous integration," *IEEE Journal of Selected Topics in Quantum Electronics*, vol. 28, no. 3: Hybrid Integration for Silicon Photonics, pp. 1–15, 2022. DOI: 10.1109/JSTQE.2021.3126124

[40] Boes, A., Corcoran, B., Chang, L., Bowers, J., and Mitchell, A., "Status and potential of lithium niobate on insulator (lnoi) for photonic integrated circuits," *Laser & Photonics Reviews*, vol. 12, no. 4, p. 1 700 256, 2018. DOI: https://doi.org/10.1002/lpor.201700256 eprint: https://onlinelibrary.wiley.com/doi/pdf/10.1002/lpor.201700256. [Online]. Available: https://onlinelibrary.wiley.com/doi/abs/10.1002/lpor.201700256

[41] Sahu, P. P., "Multimode interference coupler based on general interference for integrated optical and quantum optic devices: A review," *Physica Scripta*, vol. 99, no. 8, p. 085 106, 2024.

[42] Piasetzky, J., Drori, Y., Warshavski, Y., Rotem, A., Cohen, K., Oz, Y., and Suchowski, H., *Robust characterization of integrated photonics directional couplers*, 2024. arXiv: 2412.11670 [physics.optics]. [Online]. Available: https://arxiv.org/abs/2412.11670

[43] Lv, D., Wu, L., Liu, C., Li, A., Wang, R., and Wu, A., "Broadband and low-loss silicon photonic directional coupler for signal power tapping on the 3 μm soi waveguide platform," *Photonics*, vol. 10, no. 7, 2023. DOI: 10.3390/photonics10070776 [Online]. Available: https://www.mdpi.com/2304-6732/10/7/776

[44] Sattari, H., Takabayashi, A. Y., Zhang, Y., Verheyen, P., Bogaerts, W., and Quack, N., "Compact broadband suspended silicon photonic directional coupler," *Opt. Lett.*, vol. 45, no. 11, pp. 2997–3000, Jun. 2020. DOI: 10.1364/OL.394470 [Online]. Available: https://opg.optica.org/ol/abstract.cfm?URI=ol-45-11-2997

[45] Pérez-López, D., Gutierrez, A. M., Sánchez, E., DasMahapatra, P., and Capmany, J., "Integrated photonic tunable basic units using dual-drive directional couplers," *Opt. Express*, vol. 27, no. 26, pp. 38 071–38 086, Dec. 2019. DOI: 10.1364/OE.27.038071 [Online]. Available: https://opg.optica.org/oe/abstract.cfm?URI=oe-27-26-38071

[46] Elshazly, A., Bayoumi, A., Oktay, M., Kobbi, H., Magdziak, R., Subramaniam, P., Singh, N., Filipcic, M. E., Chakrabarti, M., Velenis, D., Sar, H., Verheyen, P., Absil, P., Ferraro, F., Ban, Y., Van Campenhout, J., Bogaerts, W., and Deng, Q., "Silicon photonic polarization beam splitter with low loss and high extinction ratio enabled by topic bends," *Journal of Lightwave Technology*, vol. 44, no. 6, pp. 2323–2328, 2026. DOI: 10.1109/JLT.2026.3652920

[47] Li, Y., Jung, M., Yu, Y., Han, Y., Zhang, B., and Shvets, G., "Topological directional coupler," *Laser & Photonics Reviews*, vol. 18, no. 11, p. 2 301 313, 2024. DOI: https://doi.org/10.1002/lpor.202301313 eprint: https://onlinelibrary.wiley.com/doi/pdf/10.1002/lpor.202301313. [Online]. Available: https://onlinelibrary.wiley.com/doi/abs/10.1002/lpor.202301313

[48] Shi, W., Wang, X., Lin, C., Yun, H., Liu, Y., Baehr-Jones, T., Hochberg, M., Jaeger, N. A. F., and Chrostowski, L., "Silicon photonic grating-assisted, contra-directional couplers," *Opt. Express*, vol. 21, no. 3, pp. 3633–3650, Feb. 2013. DOI: 10.1364/OE.21.003633 [Online]. Available: https://opg.optica.org/oe/abstract.cfm?URI=oe-21-3-3633

[49] Naghdi, B. and Chen, L. R., "Spectral engineering of subwavelength-grating-based contradirectional couplers," *Opt. Express*, vol. 25, no. 21, pp. 25 310–25 317, Oct. 2017. DOI: 10.1364/OE.25.025310 [Online]. Available: https://opg.optica.org/oe/abstract.cfm?URI=oe-25-21-25310

[50] Han, X., Jiang, Y., Xiao, H., Yuan, M., Nguyen, T. G., Boes, A., Ren, G., Zhang, Y., Hao, Q., Su, Y., Mitchell, A., and Tian, Y., "Subwavelength grating-assisted contra-directional couplers in lithium niobate on insulator," *Laser & Photonics Reviews*, vol. 17, no. 10, p. 2 300 203, 2023. DOI: https://doi.org/10.1002/lpor.202300203 eprint: https://onlinelibrary.wiley.com/doi/pdf/10.1002/lpor.202300203. [Online]. Available: https://onlinelibrary.wiley.com/doi/abs/10.1002/lpor.202300203

[51] Mirza, A., Sunny, F., Walsh, P., Hassan, K., Pasricha, S., and Nikdast, M., "Silicon photonic microring resonators: A comprehensive design-space exploration and optimization under fabrication-process variations," *IEEE Transactions on Computer-Aided Design of Integrated Circuits and Systems*, vol. 41, no. 10, pp. 3359–3372, 2022. DOI: 10.1109/TCAD.2021.3132555

[52] Fallahi, V., Kordrostami, Z., and Hosseini, M., "Sensitivity and quality factor improvement of photonic crystal sensors by geometrical optimization of waveguides and micro-ring resonators combination," *Scientific Reports*, vol. 14, no. 1, p. 2001, 2024. DOI: 10.1038/s41598-024-52363-2

[53] Kui, L. F. and M, R. U., "Photonic microring resonator modulated resonance response analysis," *Optical and Quantum Electronics*, vol. 49, no. 8, p. 275, 2017. DOI: 10.1007/s11082-017-1113-5

[54] Sumon, M. S. I., Ghosh, S., Vorobev, A. S., Maraviglia, N., Atar, F. B., Maddi, C., Zakaria, R., Ullman, G. T., Devarapu, G. C. R., Faruque, I. I., Dwivedi, S., Bowman, R. M., O'Faolain, L., Corbett, B., and Arafin, S., "Large area micro-transfer-printed tfln-on-sin racetrack resonators for nonlinear photonics," *IEEE Journal of Quantum Electronics*, vol. 62, no. 3, pp. 1–7, 2026. DOI: 10.1109/JQE.2026.3678154

[55] Liu, L., Xue, W., and Yue, J., "Photonic approach for microwave frequency measurement using a silicon microring resonator," *IEEE Photonics Technology Letters*, vol. 31, no. 2, pp. 153–156, 2019. DOI: 10.1109/LPT.2018.2886894

[56] Wang, J., Sheng, Z., Li, L., Pang, A., Wu, A., Li, W., Wang, X., Zou, S., Qi, M., and Gan, F., "Low-loss and low-crosstalk 8 × 8 silicon nanowire awg routers fabricated with cmos technology," *Opt. Express*, vol. 22, no. 8, pp. 9395–9403, Apr. 2014. DOI: 10.1364/OE.22.009395 [Online]. Available: https://opg.optica.org/oe/abstract.cfm?URI=oe-22-8-9395

[57] Barritault, P., Brun, M., Labeye, P., Hartmann, J.-M., Boulila, F., Carras, M., and Nicoletti, S., "Design, fabrication and characterization of an awg at 4.5 µm," *Opt. Express*, vol. 23, no. 20, pp. 26 168–26 181, Oct. 2015. DOI: 10.1364/OE.23.026168 [Online]. Available: https://opg.optica.org/oe/abstract.cfm?URI=oe-23-20-26168

[58] Ramaswami, R., Sivarajan, K. N., and Sasaki, G. H., "Chapter 3 - components," in *Optical Networks (Third Edition)*, Third Edition, Boston: Morgan Kaufmann, 2010, pp. 113–243. DOI: https://doi.org/10.1016/B978-0-12-374092-2.50011-4 [Online]. Available: https://www.sciencedirect.com/science/article/pii/B9780123740922500114

[59] Paśnikowska, A., Stopiński, S., Kaźmierczak, A., and Piramidowicz, R., "Multi-channel integrated transmitters with cyclic awg," *Journal of Lightwave Technology*, vol. 42, no. 7, pp. 2371–2384, 2024. DOI: 10.1109/JLT.2023.3339594

[60] "Wide-range and high-resolution fbg interrogator based on a silicon awg photonic chip," *Optics & Laser Technology*, vol. 194, p. 114 391, 2026. DOI: https://doi.org/10.1016/j.optlastec.2025.114391

[61] Jiao, Y., Yao, K., Lin, Q., Du, J., Zhao, Y., Ye, K., Sun, B., and Jiang, Z., "Miniaturized high-speed fbg interrogator based on a photonic awg chip," *Nanomaterials*, vol. 16, no. 2, 2026. DOI: 10.3390/nano16020089 [Online]. Available: https://www.mdpi.com/2079-4991/16/2/89

[62] Rahim, A., Hermans, A., Wohlfeil, B., Petousi, D., Kuyken, B., Thourhout, D. V., and Baets, R. G., "Taking silicon photonics modulators to a higher performance level: state-of-the-art and a review of new technologies," *Advanced Photonics*, vol. 3, no. 2, p. 024 003, 2021. DOI: 10.1117/1.AP.3.2.024003 [Online]. Available: https://doi.org/10.1117/1.AP.3.2.024003

[63] Temporiti, E., Ghilioni, A., Minoia, G., Orlandi, P., Repossi, M., Baldi, D., and Svelto, F., "Insights into silicon photonics mach–zehnder-based optical transmitter architectures," *IEEE Journal of Solid-State Circuits*, vol. 51, no. 12, pp. 3178–3191, 2016. DOI: 10.1109/JSSC.2016.2593802

[64] Huszaník, T., Turán, J., and Ovseník, L., "Utilization of 10 gbps dwdm system with duobinary modulation into passive optical network," *Journal of Communications Software and Systems*, vol. 14, no. 4, pp. 367–375, 2018.

[65] Moller de Freitas, M., Zhu, X., Isti, M. I., Arnold, J., Xue, R., Zhang, J., Yao, P., Creazzo, T., Cullen, C., Shi, S., and Prather, D. W., "Tfln mzm operating at 1-μm wavelength with low vπ and high bandwidth," *IEEE Photonics Technology Letters*, vol. 38, no. 8, pp. 555–558, 2026. DOI: 10.1109/LPT.2026.3655588

[66] Zhao, J., Wang, Y., Gao, X., Chen, W., Gao, D., Chen, L., Zhang, C., Yu, Y., Dong, J., and Zhang, X., "An ultra-efficient integrated plasmonic lithium niobate electro-optic mach-zehnder modulator," *Laser & Photonics Reviews*, vol. 20, no. 1, e01067, 2026. DOI: https://doi.org/10.1002/lpor.202501067

[67] Lee, W., Han, S., Moon, S.-R., Park, J., Yoo, S., Park, H., Lee, J. K., Yu, K., and Cho, S. H., "Coherent terahertz wireless communication using dual-parallel mzm-based silicon photonic integrated circuits," *Opt. Express*, vol. 30, no. 2, pp. 2547–2563, Jan. 2022. DOI: 10.1364/OE.446516

[68] Wang, X., Shen, W., Li, W., Liu, Y., Yao, Y., Du, J., Song, Q., and Xu, K., "High-speed silicon photonic mach–zehnder modulator at 2 μm," *Photon. Res.*, vol. 9, no. 4, pp. 535–540, Apr. 2021. DOI: 10.1364/PRJ.417107 [Online]. Available: https://opg.optica.org/prj/abstract.cfm?URI=prj-9-4-535

[69] Lian, Y., Tian, W., Sun, H., Yu, Y., Su, Y., Tong, H., Zhu, J., and Wei, Z., "High–efficiency, widely tunable mgo: Ppln optical parametric oscillator," *Photonics*, vol. 10, no. 5, 2023. DOI: 10.3390/photonics10050505 [Online]. Available: https://www.mdpi.com/2304-6732/10/5/505

[70] Niu, Y., Yan, X., Chen, J., Ma, Y., Zhou, Y., Chen, H., Wu, Y., and Bai, Z., "Research progress on periodically poled lithium niobate for nonlinear frequency conversion," *Infrared Physics & Technology*, vol. 125, p. 104 243, 2022. DOI: https://doi.org/10.1016/j.infrared.2022.104243 [Online]. Available: https://www.sciencedirect.com/science/article/pii/S1350449522002249

[71] Zhang, Y., Duan, Y., Wang, Z., Zhang, D., Zhang, J., Zhang, Y., and Zhu, H., "Continuous-wave widely tunable mgo:ppln optical parametric oscillator with compact linear cavity," *IEEE Photonics Technology Letters*, vol. 30, no. 20, pp. 1756–1759, 2018. DOI: 10.1109/LPT.2018.2868736

[72] Wei, J., Hu, Z., Zhang, M., Li, P., Wu, Y., Zeng, C., Tang, M., and Xia, J., "All-optical wavelength conversion of a 92-gb/s 16-qam signal within the c-band in a single thin-film ppln waveguide," *Opt. Express*, vol. 30, no. 17, pp. 30 564–30 573, Aug. 2022. DOI: 10.1364/OE.465382 [Online]. Available: https://opg.optica.org/oe/abstract.cfm?URI=oe-30-17-30564

[73] Wei, J., Cheng, C., Wu, Y., Zeng, C., Tang, M., and Xia, J., "Efficient and broadband all-optical wavelength conversion between c and o bands in nanophotonic lithium niobate waveguides," *Journal of Lightwave Technology*, vol. 42, no. 17, pp. 5966–5973, 2024. DOI: 10.1109/JLT.2024.3406579

[74] Soref, R., "Tutorial: Integrated-photonic switching structures," *APL Photonics*, vol. 3, no. 2, p. 021 101, Jan. 2018. DOI: 10.1063/1.5017968 eprint: https://pubs.aip.org/aip/app/article-pdf/doi/10.1063/1.5017968/19911847/021101_1_1.5017968.pdf. [Online]. Available: https://doi.org/10.1063/1.5017968

[75] Soldano, L. B., *Multimode interference couplers: design and applications*. Delft University Press, 1994.

[76] BŁahut, M. and Kasprzak, D., "Multimode interference structures-properties and applications," *Optica Applicata*, vol. 34, no. 4, pp. 573–587, 2004.

[77] Tian, W., Wang, Y., Dang, H., Hou, H., and Xi, Y., "Photonic integrated circuits: Research advances and challenges in interconnection and packaging technologies," *Photonics*, vol. 12, no. 8, 2025. DOI: 10.3390/photonics12080821 [Online]. Available: https://www.mdpi.com/2304-6732/12/8/821

[78] Lumerical Inc., *Lumerical fdtd: 3d electromagnetic simulator*, Available at https://www.ansys.com/products/optics/fdtd, Lumerical Inc., 2024.

[79] Zelmon, D. E., Small, D. L., and Jundt, D., "Infrared corrected sellmeier coefficients for congruently grown lithium niobate and 5 mol.% magnesium oxide–doped lithium niobate," *J. Opt. Soc. Am. B*, vol. 14, no. 12, pp. 3319–3322, Dec. 1997. DOI: 10.1364/JOSAB.14.003319 [Online]. Available: https://opg.optica.org/josab/abstract.cfm?URI=josab-14-12-3319

[80] Soldano, L. B., *Multimode interference couplers: design and applications*. Delft University Press, 1994.

[81] Shi, Y., Dai, D., and He, S., "Improved performance of a silicon-on-insulator-based multimode interference coupler by using taper structures," *Optics Communications*, vol. 253, no. 4, pp. 276–282, 2005. DOI: https://doi.org/10.1016/j.optcom.2005.04.078 [Online]. Available: https://www.sciencedirect.com/science/article/pii/S0030401805004475

[82] Yousefi, P., Khalid, M., Petruzzelli, V., and Calò, G., "Design of thin-film lithium niobate power splitters and combiners based on multimode interference," *Optical and Quantum Electronics*, vol. 57, no. 3, p. 198, 2025. DOI: 10.1007/s11082-025-08060-z

[83] Yariv, A., Yeh, P., and Yariv, A., *Photonics: optical electronics in modern communications*. Oxford university press New York, 2007, vol. 6.

[84] Little, B. E., Chu, S. T., Haus, H. A., Foresi, J., and Laine, J.-P., "Microring resonator channel dropping filters," *Journal of lightwave technology*, vol. 15, no. 6, pp. 998–1005, 1997.

[85] Bogaerts, W., De Heyn, P., Van Vaerenbergh, T., De Vos, K., Kumar Selvaraja, S., Claes, T., Dumon, P., Bienstman, P., Van Thourhout, D., and Baets, R., "Silicon microring resonators," *Laser & photonics reviews*, vol. 6, no. 1, pp. 47–73, 2012.

[86] Qiu, H., Jiang, G., Hu, T., Shao, H., Yu, P., Yang, J., and Jiang, X., "Fsr-free add–drop filter based on silicon grating-assisted contradirectional couplers," *Opt. Lett.*, vol. 38, no. 1, pp. 1–3, Jan. 2013. DOI: 10.1364/OL.38.000001 [Online]. Available: https://opg.optica.org/ol/abstract.cfm?URI=ol-38-1-1

[87] Yousefi, P., Khalid, M., Petruzzelli, V., and Calò, G., "Multi-channel add-drop filter using superimposed gratings in hybrid sin-tfln platform," *Optics Communications*, vol. 591, p. 132 164, 2025. DOI: https://doi.org/10.1016/j.optcom.2025.132164 [Online]. Available: https://www.sciencedirect.com/science/article/pii/S0030401825006923

[88] Yousefi, P., Khalid, M., Petruzzelli, V., and Calò, G., "Dual-wavelength add-drop filters with aperiodic gratings on a hybrid sin-tfln platform," in *2025 25th Anniversary International Conference on Transparent Optical Networks (ICTON)*, 2025, pp. 1–4. DOI: 10.1109/ICTON67126.2025.11125232

[89] Erdogan, T., "Fiber grating spectra," *Journal of Lightwave Technology*, vol. 15, no. 8, pp. 1277–1294, 1997. DOI: 10.1109/50.618322

[90] Boroojerdi, M. T., Ménard, M., and Kirk, A. G., "Two-period contra-directional grating assisted coupler," *Opt. Express*, vol. 24, no. 20, pp. 22 865–22 874, Oct. 2016. DOI: 10.1364/OE.24.022865 [Online]. Available: https://opg.optica.org/oe/abstract.cfm?URI=oe-24-20-22865